

# Cost and Risk Tool for Interim and Preventive Repair (CORTIR)

## EUDP project 64018-0507 – Final Report

Date: 11-03-2021

**Authors:** Find Jensen<sup>1</sup>, Andrei Buliga<sup>1</sup>, Theodoros Pardalakis<sup>1</sup>, Margrethe Werk<sup>1</sup>, Shahrukh Ahmed<sup>1</sup>, Javier Ozores Arconada<sup>1</sup>, Mads Borgnæs<sup>1</sup>, Christian Berggreen<sup>2</sup>, Jacob Waldbjørn<sup>2</sup>, John D. Sørensen<sup>3</sup>, Yi Yang<sup>3</sup>, Jannie S. Nielsen<sup>3</sup>, Rune Kirt<sup>4</sup>, Søren Horn Petersen<sup>5</sup>, Peder Munkholm Jacobsen<sup>6</sup>, Christian Løjtved<sup>7</sup>, Finn Thyrring<sup>8</sup>, Birgit Junker<sup>9</sup>, Nicolas Quievy<sup>10</sup>, Mathias Reding<sup>11</sup>, Yangjiao Liao<sup>12</sup>, Pierre Stephan<sup>13</sup>, Morten, Christiansen<sup>14</sup>, Hans Møller<sup>15</sup>, Gunther Auer<sup>16</sup>, Liane Persson<sup>17</sup>, Michael Pedersen<sup>18</sup>, Francisco Garcia Lopez<sup>19</sup>, Signe Lynge Olsson<sup>20</sup>, Eduardo Ramirez Rodriguez<sup>21</sup>, Christian Jeggesen Lysemose<sup>22</sup>, Tim Block<sup>23</sup>, Thomas Nedergaard<sup>24</sup>

- |                               |                                      |
|-------------------------------|--------------------------------------|
| 1: Bladena                    | 16: Acciona Energy                   |
| 2: DTU Mechanical Engineering | 17: Arise                            |
| 3: AAU Build                  | 18. Ørsted                           |
| 4: Kirt x Thomsen             | 19. ENEL                             |
| 5: Guide2Defect               | 20. Statkraft                        |
| 6: Global Wind Service        | 21. Vector Cuatro (Falck Renewables) |
| 7: ECC                        | 22. LM Wind Power                    |
| 8: CODAN                      | 23. Nordex                           |
| 9: EON (now RWE)              | 24. Vestas                           |
| 10: Engie                     |                                      |
| 11: Hofor                     |                                      |
| 12: Equinor                   |                                      |
| 13: EDF                       |                                      |
| 14: Innogy (RWE)              |                                      |
| 15: EWII                      |                                      |

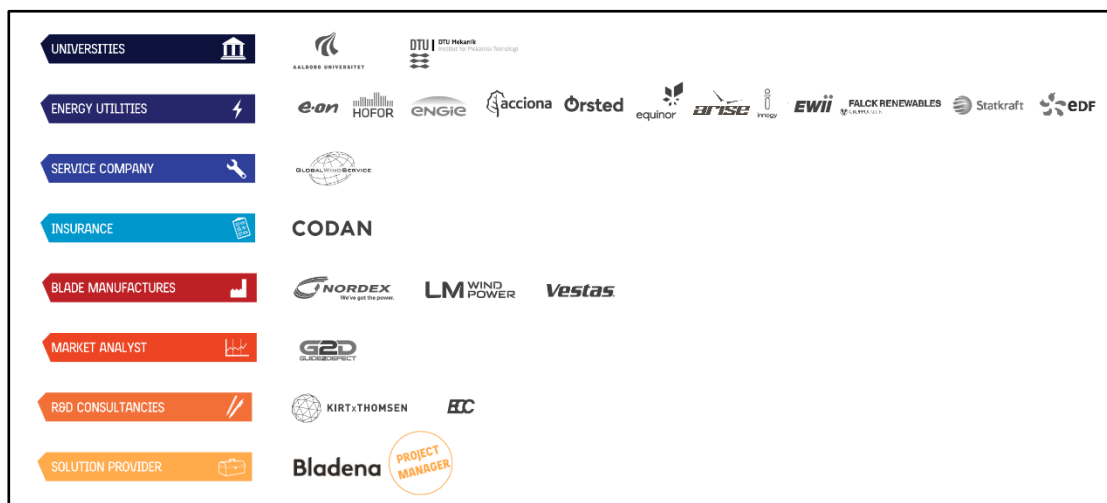


## Table of Contents

<b>1</b>	<b>Project details</b>	<b>4</b>
1.1	Acknowledgement	4
<b>2</b>	<b>Short description of project objective and results</b>	<b>5</b>
2.1	English version	5
2.2	Dansk Version	6
<b>3</b>	<b>Executive summary</b>	<b>7</b>
3.1	Value chain and WTO network Summary	8
3.2	CAR Tool Summary	9
3.3	Transverse crack – Fracture Mechanics Summary	11
3.4	Tip Solution Summary	13
<b>4</b>	<b>Project objectives</b>	<b>14</b>
4.1	Value Chain and WTO Network Objectives	14
4.2	CAR Tool Objectives	15
4.3	Transverse Crack Objectives	17
4.4	Tip Solution Objectives	17
4.5	Risk in the project	18
4.6	Milestones	19
<b>5</b>	<b>Project results and dissemination of results</b>	<b>20</b>
<b>6</b>	<b>Value Chain and WTO network</b>	<b>20</b>
6.1	Wind Industry Value Chain	20
6.2	Liability	23
6.3	WTO Network	24
6.4	Seminars and workshops	25
6.5	CORTIR Posters	29
6.6	The Blade Handbook	35
<b>7</b>	<b>CAR Tool</b>	<b>38</b>
7.1	Industry Pains	38
7.2	Uncertainty assessment	39
7.3	Risk Awareness and assessment	41
7.4	Minimal Viable Product (MVP)	43
7.5	Applied modules in the CAR Tool	43
7.6	Reliability model and fracture mechanics	44
7.7	Damage Categorization and Decision Rules	47
7.8	Cost and Risk Module	49
7.9	Field Data	50
7.10	Field Case Example	53
7.11	Graphical User Interface	56
7.12	Output	56
7.13	Results interpretation	58
<b>8</b>	<b>Transverse Cracks</b>	<b>60</b>
8.1	Large-scale testing	61
8.2	Subcomponent testing	62
8.3	Structural FEM studies	63
<b>9</b>	<b>Development of the tip solution</b>	<b>69</b>
9.1	Laboratory Test	77
<b>10</b>	<b>Utilization of project results</b>	<b>79</b>
10.1	Commercial perspectives of the Value chain	79

10.2	Commercial perspectives of the CAR Tool.....	80
10.3	Commercial perspectives of the tip solution .....	80
<b>11</b>	<b>Project conclusion and perspective .....</b>	<b>80</b>
11.1	Value Chain Conclusion .....	81
11.2	CAR Tool Conclusion .....	82
11.3	CAR Tool Roadmap .....	86
11.4	Transverse cracks and fracture mechanics Conclusion.....	92
11.5	Tip solution Conclusion .....	92
	<b>References.....</b>	<b>94</b>
<b>Appendix A</b>	<b>Abbreviations and nomenclature .....</b>	<b>96</b>
<b>Appendix B</b>	<b>CAR Tool .....</b>	<b>110</b>
<b>Appendix C</b>	<b>Reliability model .....</b>	<b>117</b>
<b>Appendix D</b>	<b>Fracture Mechanics and testing.....</b>	<b>137</b>
<b>Appendix E</b>	<b>Sub-Structural Fatigue Testing .....</b>	<b>165</b>
<b>Appendix F</b>	<b>Tip Solution .....</b>	<b>185</b>
<b>Appendix G</b>	<b>Elastic Instability and Fracture Mechanics (Light Approach) .....</b>	<b>258</b>
<b>Appendix H</b>	<b>Torsion.....</b>	<b>288</b>

# 1 Project details

Project title	Cost and Risk Tool for Interim and Preventive Repair (CORTIR)	
Project identification (program abbrev. and file)	CORTIR Project	
Name of the program which has funded the project	EUDP	
Project managing company/institution (name and address)	Bladena ApS, Banestrøget 13,1, 2630 Taastrup, DK Project Manager: Find Mølholt Jensen Mail: fmj@bladena.com	
Project partners	AAU Build DTU Mechanical Engineering Kirt x Thomsen Guide2Defect Global Wind Service ECC	CODAN E.ON (Now RWE) Engie Hofor Equinor EDF Innogy (RWE) Ewii Acciona Energy Arise Ørsted Enel Statkraft Vector Cuatro (Falck Renewables) LM Wind Power Nordex Vestas
CVR (central business register)	34208433	
Date for submission		

## 1.1 Acknowledgement

Bladena and partners would like to acknowledge the Energy Development and Demonstration Program (EUDP) for financial support under the grant number: 64018-0507 CORTIR Project.

## 2 Short description of project objective and results

### 2.1 English version

The main objective of the project has been to develop a Cost and Risk tool (CAR Tool) to support when deciding an optimal blade maintenance strategy for Wind Turbine Owners (WTO's). The goal of the CAR Tool is to support Blade's Asset Management and Wind Turbine Owners in the decision-making process with regards to criticality of defects (and risks) and thereby significantly minimize the operation and maintenance costs.

Fracture mechanics crack propagation models and cost and risk models are implemented in the CAR Tool. Based on the integrated cost and risk model it is possible for the WTO's to decide, an optimal maintenance strategy.

The main principles of the CAR Tool are based on fracture mechanics describing damage progression and on cost and reliability models. Field data and test data are used to calibrate the models.

Sub-component testing and large-scale testing with applied torsional loads are carried out to characterize crack propagation and validate numerical models and afterwards observe the propagation of cracks in a realistic blade structure. Consequently, resulting parameters from the tests are utilized in the reliability model which is integrated in the CAR Tool.

Another critical failure mode that WTO often face is the tip opening of the wind turbine blade in tip region that is caused by lightning. Therefore, an interim solution for this particular problem is also developed in collaboration with the project partners.

In the project, the Wind Turbine Owner Network (WTO Network) has been maintained and grown significantly. Now there are 50+ WTOs from all over the world in the Network. Moreover, the WTO Network meetings were held with great participation with a large part of the network showing interest or joining the meeting.

The CORTIR project is proud to have representatives from the whole wind industry value chain as partners coming together to discuss and work toward common goals.

## 2.2 Dansk Version

Hovedformålet med projektet har været at udvikle et Cost and Risk værktøj (CAR Tool) for at estimere en optimal vedligeholdelsesstrategi for vindmølleejere. Målet med CAR Tool'et er at hjælpe vindmølleejere (WTO's) i beslutningsprocessen i forhold til defekten alvorlighed (risiko) og hvordan man minimere drift- og vedligeholdelseskostninger.

Både brudmekaniske modeller af revnevækst og Cost og Risk modeller er implementeret i CAR Tool'et. Baseret på den integrerede Cost og Risk model kan en optimal vedligeholdelsesstrategi blive tilpasset af vindmøllejerne.

Det grundlæggende princip ved CAR Tool er baseret på den brudmekaniske beskrivelse af revnevækst og på cost og reliability modeller. Field data og test data er brugt til at kalibrere modellerne.

Sub-komponent testing og storskala testing med vridningslaster er udført for først at karakterisere revnevæksten og validere numeriske modeller og dernæst for at observere spredningen af brudene. De resulterende parametre fra testene anvendes i reliability modellen, som er integreret i CAR Tool'et.

En anden større kilde til vingskader, som vindmølleejere ofte står over for, er en tip skade hvor de to vingepaneller går fra hinanden grundet lynnedslag. Derfor er en midlertidig løsning på dette problem også udviklet i samarbejde med projektets partnere.

I løbet af projektet er vindmøllejernes netværk (WTO Network) også blevet plejet og har vokset sig endnu større. Nu er der 50+ vindmølleejere fra hele verdenen i netværket. Netværksmøder for vindmøllejerne er afholdt med deltagelse fra en stor del af netværket, der viste interesse eller deltog i mødet.

CORTIR projektet er stolt over at have repræsentanter fra hele vindmølleindustrien som partnere, der samles for at diskutere og arbejde sammen mod fælles mål.

### 3 Executive summary

Over the years, the size of wind turbine blades has increased. Rated power has crossed over 10 MW and blade length over 100 meters. With increased blade lengths, the loads on the blades have also drastically increased giving rise to structural challenges. The increasing number of damages leads to an increase in maintenance and repair costs and of the risk of energy production loss for the wind turbine owners (WTOs). The current situation in the wind turbine industry is that when damages and failures occur on blades, it is unpredictable in relation to Cost and Risk, unscheduled and consequently outside the operational budget.

The proposed new strategy to manage damages and failures in wind turbine blades is driven by the WTOs, whom in the recent years have begun working together in a coordinated approach, e.g. in the rapidly growing WTO group “The WTO Blade Group” strongly supported by Bladena and earlier EUDP projects (LEX and RATZ). The inclusion of the insurance company (CODAN) in the project is highly beneficial for the development of a new predictable risk based strategy. CODAN and WTOs bring valuable insight on both the cost and risk aspect of operating wind turbines and can help identify the issues with the highest priority to solve, hereby ensuring a cost-driven focus to the project.

The *Cost and Risk tool for Interim and Preventive repair* (CORTIR) project aims at benefitting the entire value chain in the wind industry; manufacturers (OEMs), wind turbine owners (WTOs), independent service providers and insurance companies. Until now each player has had individual strategies for how to handle such situations, but the shared goal is to reduce Levelized Cost of Energy (LCoE). The money fueling the entire industry comes from the sale of energy and from subsidies. As subsidies are phased out the entire wind energy business must be viable and compatible on its own, and that means critically evaluating on the costs wherever possible. In the CORTIR project focus is on the cost and risk associated with running and maintaining a wind turbine park with regards to wind turbine blades. Blade failure, blade damage repair and downtime are all costly events. In the first instance it is the WTOs who must pay, but OEMs also pay at end of warranty and as a competitive loss and insurance companies many times must pay the WTOs when they suffer a loss. This can be a game of “who pays what”, but another take on the expense is to try to bring the risk and maintenance cost of running a wind turbine park down to the advantage of the whole value chain. This is illustrated in Figure 1.

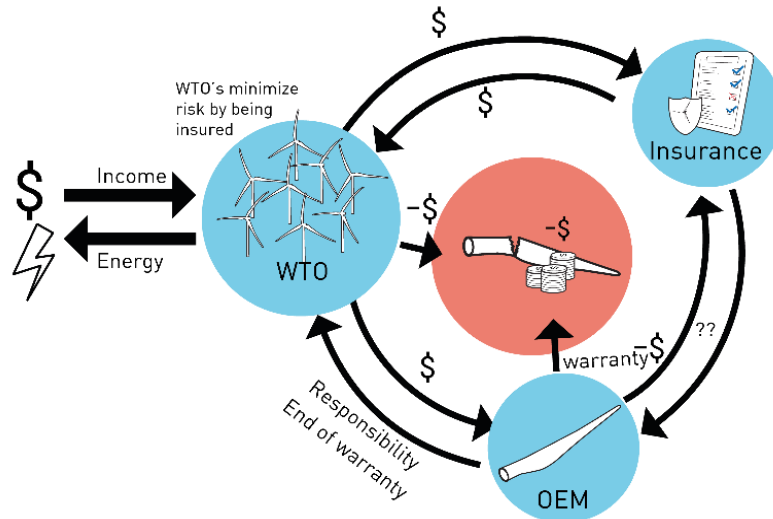


Figure 1: The WTOs are earning money by selling energy. These earnings must sustain the whole industry. The WTOs are responsible for running and maintaining the wind farms. OEMs has responsibility according to warranty contracts and ability to compete and insurance companies can be asked to pay for certain losses. In the project methods of calculating Cost and Risk for a maintenance strategy of a wind turbine field are established. Bladena has developed a Cost and Risk Tool (CAR Tool). The CAR Tool is a decision support tool mainly for the WTOs and aims to make maintenance decisions easier and more cost-efficient. The CAR Tool is based on two major research areas; the reliability model (cost and risk) developed by AAU and the fracture mechanics model developed by DTU.

A driver since the beginning of the project has been to look at reducing loss of annual energy production (AEP) due to downtime with interim or preventive repair solutions. Especially offshore or at wind farm locations with harsh winter climate with limited or no access to the blades, damages such as blade tips split open from lightning is devastating. For that reason, Bladena has developed a retrofit tip solution to prevent open tip lightning damages.

Another outcome of the CORTIR project has been the gathering of the entire value chain through quarterly seminars/workshops held at Bladena's headquarter. This has helped in building a strong relationship among the OEMs, WTOs, ISP and insurance company as well as establishing a technical common language for the value chain in wind industry.

### 3.1 Value chain and WTO network Summary

The CORTIR project - headed by Bladena - is proud to have attracted partners yet again from across the whole spectra of the wind industry value chain. Having both the WTOs, OEMs, ISPs, and insurance companies represented in the CORTIR project is priceless. The many knowledge sharing events and discussions between partners during the project have added extra focus, relevance, and substance to the project development.

The CORTIR project has successfully hosted 8 WTO seminars/workshops where CORTIR partner WTOs as well as external WTOs from the WTO-network have joined. Two external speakers, one from Wood McKenzie and one from DNV GL were invited to give a presentation and speech on “*Unplanned Repair*” and “*Lack of sufficient Certification Rules*” respectively. For internal partner presentations topics such as operation and maintenance, cost, damage tolerance, and how fracture mechanics can be applied in the industry, were presented, and discussed at the seminars.

As an important premise for communication, knowledge sharing and discussions of new ideas, dissemination of results has been highly prioritized. The CORTIR Blade handbook has been updated with the new chapters, still keeping focus on clear communication of the subjects and was nominated for a design award. Seven CORTIR NewsLetters have been sent out to partners. Press releases of most of the events have been made and the popular CORTIR Blade Handbook has been heavily distributed, both at CORTIR seminars and external events such as the conference in Berlin 2020.

To read more with regard to the growing WTO network, the project communication, outcome of seminars and workshops and analysis of the value chain, can be found in section 6 “Value Chain and WTO network” on page 20.

## 3.2 CAR Tool Summary

The CAR Tool minimum viable product (MVP) as developed in the CORTIR project is a **decision support tool** to be used by the WTOs for estimating comparative risks and costs between different maintenance strategies for a defined wind turbine site. The CAR Tool will take in user defined parameters as well as general default values. The CAR Tool is numeric and gives output results such as cost (inspection, repair, downtime etc.) and risk for the evaluated user defined maintenance strategies.

The CAR Tool aims to give answers to the industry’s needs to be accepted by the whole value chain of the wind energy industry. Therefore, experts from universities and the industry has been collaborating to consider real-life input and apply the knowledge throughout the whole development process of the tool. For that reason, CAR Tool is based on two major research cores that has been developed between Bladena, DTU Mechanical Engineering and AAU. In terms of the former, the focus is be on advanced numerical models and a series of experiments in combination with the technical knowledge and expertise of Bladena on structural issues on blades. The latter is focused on the simulation of the real-life uncertainties and risk calculations, always in relation to the knowledge and experience of Bladena from real-life cases. The combination of these two has resulted in a holistic approach regarding the maintenance strategy that needs to be applied on a wind turbine, that considers both technical and economic risk. Under this prism, the user also has a possibility to use the tool for parametrical studies and by changing multiple inputs will be able to

simulate different maintenance scenarios and adapt the tool for her special needs and characteristics.

The simulation module makes use of a Crack Propagation Rate (CPR) function to simulate damage development during blade life. This function is based on fracture mechanics and test of crack development and growth on sandwich panels at DTU.

To calculate cost and risk for a defined maintenance strategy the CAR Tool MVP consists of the two main modules; the Reliability model developed by AAU and the Fracture mechanics model developed by DTU. The CAR Tool also has the option of using field data to increase the accuracy of results. Bladena has brought this together with the experience gathered both from wind industry and other industries in a software tool, see Figure 2.

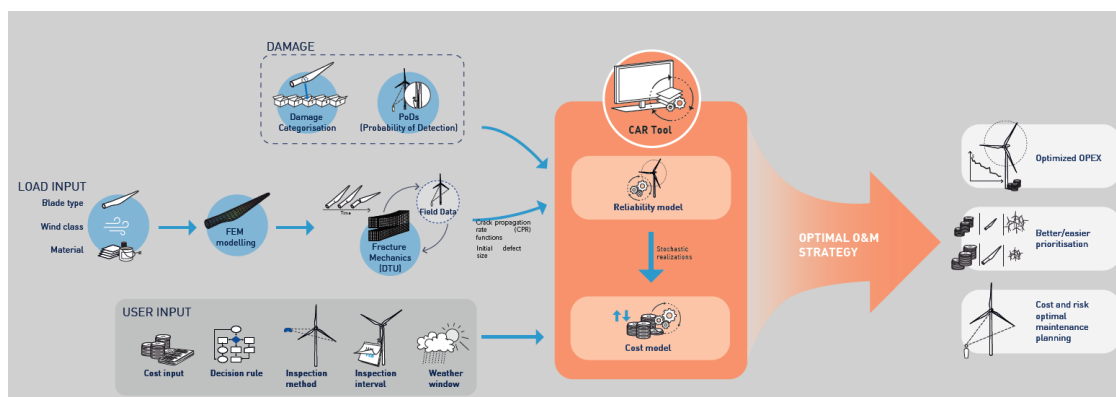


Figure 2: The CAR Tool is based on input from the field and structural understanding coupled with fracture mechanics modelling and tests. The decision support tool will provide cost-optimal maintenance strategies.

The CAR Tool minimum viable product (MVP) as developed in the CORTIR project only focus on transverse crack damages on blades, even though the CAR Tool in principle can work with any damage type which a mathematical described development and progression. DTU has done extensive testing to both validate the fracture mechanics models on crack growth in sandwich panels as well as to generate input data for the models, and study crack propagation experimentally under different scenarios. This work has provided a mathematical function describing transverse crack propagation in cyclic loaded sandwich panels and is integrated in the CAR Tool and uncertainty quantification of crack growth parameters in the crack propagation model

The user defines the evaluated wind turbine site and gets comparative cost and risk results for the evaluated maintenance strategies. The comparative results can help the user in deciding on the right maintenance decision based on willingness to take risk as well as cost and investment. Figure 3 shows a user evaluating results from CAR modelling for the considered detail with Tool to help deciding on a maintenance strategy for a wind turbine field.



Figure 3: The user can use the output from the CAR Tool to support in deciding on a maintenance decision strategy for a wind turbine park.

### 3.3 Transverse crack - Fracture Mechanics Summary

The main objective of the fracture mechanics testing to deliver the Crack Propagation Rate (CPR) function, an input function needed in the CAR tool. For this purpose, a comprehensive sub-component testing and full-scale testing campaign together with Fracture Mechanics modelling were performed with the purpose of generating simplified closed-form models and quantification of the uncertainties of the closed-form solution as well as the fracture mechanics parameters. Different blade families, load conditions and operation environments were used to identify an array of boundary conditions for testing. Figure 4 shows the setup for fatigue propagation test.

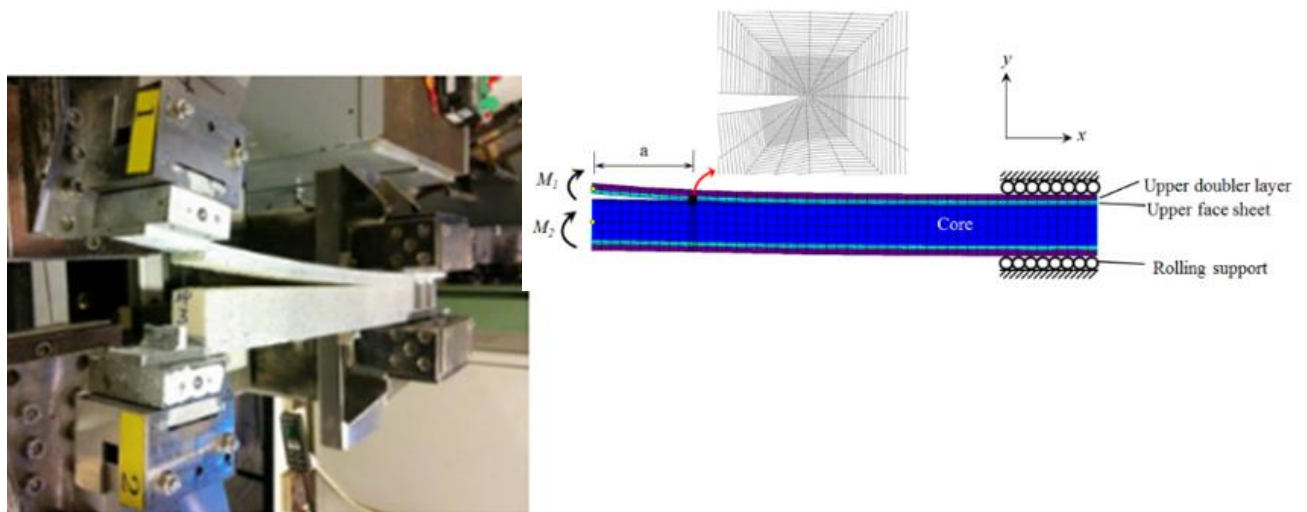


Figure 4: Illustration of the DCB-UBM laboratory fracture characterization test setup for generation of fracture toughness as well as fatigue propagation rate measurements to be used as input for computational analysis tool.

The transverse cracks are acknowledged to be one of the main structural blade failures for blades in operation today. Previous EUDP Project RATZ led to understanding of the root cause and to validation of a hypothesis describing the physics behind transverse cracks initiation and development. Main conclusion was that the torsional forces<sup>1</sup> drive the transverse crack growth and torsional testing of the blade is not included in current certification test. The “hypothesis found” in the RATZ-project has been further validated in this project.

The hypothesis refers to a 2 stages development:

1. Stage 1: Debonding of core from face sheet (skin).
2. Stage 2: Excessive fatigue bending of the debonded face sheet (local buckling of the skin) leads to high interlaminar stresses causing crack initiation and development.

Figure 5 shows how debonding of core from face sheet leads to the development of crack.

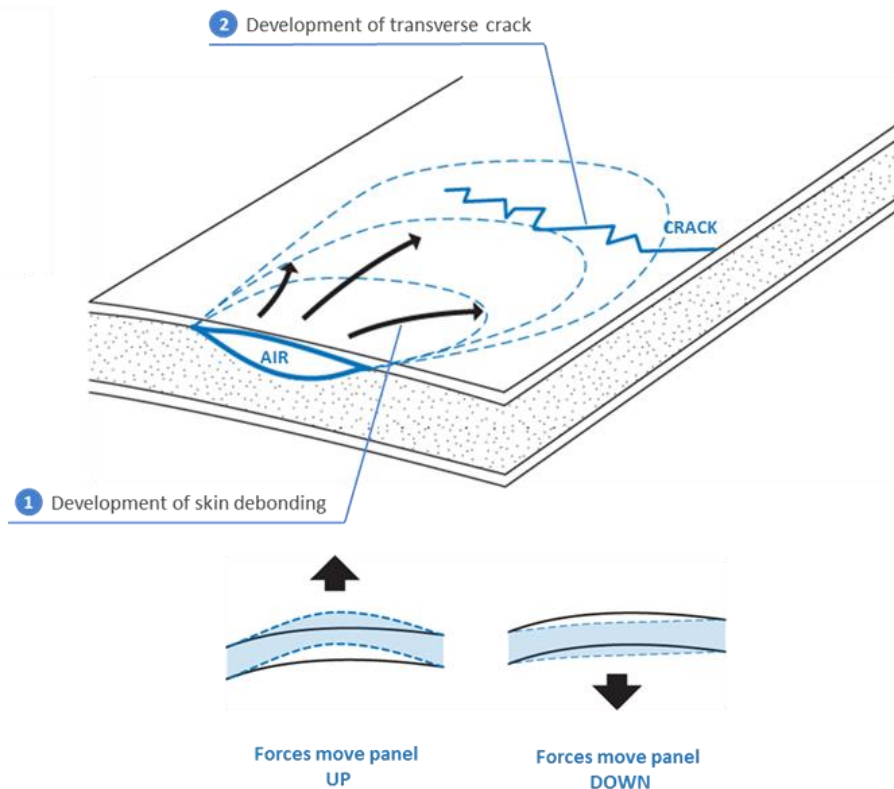


Figure 5: Phenomenon leading to development of a transverse crack due to out-of-plane deformations.

In Figure 5, it can be observed that development of skin debonding cause air particles to move in the cavity between face sheet and core which leads to crack initiation and further fatigue propagation, the hypothesis was verified in RATZ project [1]. The

<sup>1</sup> Torsional forces are a combination of edgewise and flapwise loads.

CORTIR project aims at doing in depth analysis and understanding of the link between the two development stages. Structural FEM simulations, Fracture Mechanics, sub-component testing as well as large-scale testing will be used in this study. Fracture Mechanics and Sub-component testing supports “damage prediction”, used in the CAR-tool.

Following tests were carried out on samples manufactured by GWS:

- DCB-UBM (Double Cantilever Beam loaded with Uneven Bending Moments tests) for characterization.
- 4-point bending testing on both beam and plate specimens for validation of the analysis models on simple specimen geometries, but with similar loading scenarios as in the full-scale blade geometry.
- Characterization tests on glass fiber face sheets to experimentally measure propagation rates of surface cracks observed in the field.

The results from the tests were utilized to predict the crack propagation rate (CPR) function which was then integrated into the CAR Tool. The CPR function is developed as a function of the load and with parameters which are modelled by stochastic variables to be used for the reliability (risk) calculations. The reliability of NDT inspection techniques is modelled by Probability Of Detection curves providing the probability of detecting a damage of a given size. The POD curve is integrated into the reliability and risk estimations using a Bayesian updating approach. If a damage is detected then the measurement of the actual size is also easily included in the reliability modelling.

### 3.4 Tip Solution Summary

Another issue wind turbine owners face is the tip split opening issue of the blade which occurs under lightning strikes. In this regard, a strut solution was developed to address the tip opening issue of the blade under lightning strikes. When lightning strikes the blades of a wind turbine, which are relatively thin and weak compared to the wind turbine tower, significant damage can occur. Such damage can be so extensive that the turbine can no longer operate, and the turbine must be taken out of service so that the damaged blade can be repaired or replaced which results in increased costs and downtime.

Thus, for the purpose to avoid the downtime and consequently the cost a product called struts has been developed to function as a temporary solution until a full repair is performed. Figure 6 shows the developed solution installed in a cross section of a wind turbine blade’s tip.



Figure 6: Strut solution for tip opening issue.

The feasibility of the strut solution is verified by the non-linear finite element method. A comparative analysis between a situation with and without the Strut is carried out. In addition, different materials were studied, and material testing was carried out by ECC in order to see the response of the material under high strain rates which a blade experiences under lightning strikes. Field installation of the struts were cancelled due to the unfortunate outbreak of Covid-19.

## 4 Project objectives

### Main project objectives and implementation

The project ran for two years and had 12 different work packages, all serving one purpose to provide input to CAR Tool. For ease of the project the work packages were combined into four areas which are as follows:

1. Value Chain and WTO Network
2. CAR Tool
3. Transverse Cracks
4. Tip Solution

The main objective of each area is provided in this section and steps leading to fulfillment of the goals are presented. Obstacles that hindered the project as well as milestones set prior to the project are presented as well.

### 4.1 Value Chain and WTO Network Objectives

The EUDP founded projects LEX (2015 to 2017), RATZ (2017 to 2019) and now CORTIR (2019 to March 2021) all have had the goal of bringing the wind industry together in

discussions of shared interests and ways to solve problems which has a negative effect overall on the industry. One thing everyone can agree on, is to bring the LCoE down.

It is a common practice that when damages and failures occur on blades, the associated costs and repair actions may end up as a dispute between WTOs, OEMs and insurance companies, as the cost is often not included in the operational budget. Experience from the industry indicates that each player may handle such situations with different strategies.

The aim of gathering the whole value chain has been to provide a common strategy platform for the value chain through means of seminars held regularly on a three-month interval from kick-off until the end of the project.

The CORTIR project aims to provide opportunities for different players to meet, share and learn. Two universities, AAU and DTU, are also partners and in the knowledge sharing loop.

### The WTO Network

The WTO Network has grown to 50+ WTOs from all over the world. To have a close dialog with a strong network of WTOs helps understand WTO key issues. This understanding is a driving factor in the CORTIR project and in the development of the CAR Tool.

### Knowledge sharing

In the CORTIR project knowledge sharing and learning opportunities are prioritized very high. From the start dissemination of activities, discussions and results has been planned to take place amongst other during the workshops and seminars throughout the project and through frequent NewsLetters about the project status and results. On a grander scale the Blade Handbook has been heavily and the objective of the Blade Handbook is to be both introductory and tone-setting in a shared language used in the wind industry.

### Strengthening the wind industry

By bringing key players together in a discussion about challenges and solutions in the wind industry and by taking active lead in how the industry should handle cost, risk and maintenance strategies in the future, the aim is to strengthen the wind industry and make it more competitive.

## 4.2 CAR Tool Objectives

The main objective in the CORTIR project has been to develop a Cost and Risk tool (CAR Tool). The aim of the CAR Tool is to support the decision making in Operation and Maintenance strategies and eventually contribute to business improvement of the entire value chain. The failure mode of wind turbine blade considered in the CAR Tool MVP is the occurrence of transverse cracks, but the underlying principle of the CAR Tool will be able to handle any correctly defined damage type.

The CAR Tool aims to provide solutions to the industry's requirements, subsequently solidifying its position as a reliable tool in providing support to operation and maintenance of wind turbine blades. The CAR Tool is based on two major research areas; Fracture Mechanics and as Cost and Risk models, which are developed in collaboration with Technical University of Denmark (DTU Mechanical Engineering) and Aalborg University (AAU BUILD).

The focus of fracture mechanics is on advanced numerical models sandwich face/core debond analysis and a series of experiments in combination with the technical knowledge and expertise of Bladena on structural issues on blades. The cost and risk models relied on probabilistic crack growth models, uncertainties related to crack growth based on laboratory testing and risk calculations.

The models resulting from two areas are integrated in the CAR Tool and the result is a holistic approach regarding the maintenance strategy that needs to be applied on a wind turbine, that will consider both the technical and economic risk. Under this prism, the user will also have the possibility to use the tool for parametric studies and by changing multiple inputs will be able to simulate different maintenance scenarios and adapt the tool for her special needs and characteristics.

Outcome is a decision model which provides strategies and decision rules for identifying cost-optimal decisions regarding frequency of inspections, repairs, and maintenance.

The CAR Tool can be utilized both under operation and as a tool to investigate the impact of CAPEX expenses and investments. By running different maintenance strategies through the CAR Tool, the results can give an idea of where to act to decrease the expected OPEX. This can be used as an argument for investing money in strategy changes or preventive solutions for wind turbines. See Figure 7.



Figure 7: By knowing what expenses different maintenance strategies may result in, it is easier in the earlier phase to decide on CAPEX expenses.

### 4.3 Transverse Crack Objectives

The reliability model is based on a probabilistic damage model which can predict the damage propagation based on fracture mechanics models. Whereas a cost model is developed for costs related to inspection, maintenance, and repair for transverse cracks.

Fracture mechanics is a technique where critical damages within composite materials are considered in the assessment of a structure. Concerning wind turbine blades, studies had been done on evaluating the severity of damages and getting to the root cause to avoid the damage by taking preventive measures. However, uncertainty still evolves regarding cracks being risky for the integrity of the structure. Therefore, root cause of the cracks is evaluated as well as whether the crack will lead to a critical level where the structure is compromised. Fracture mechanics modelling and testing at DTU Mechanical Engineering have been used for investigation.

Large-scale test of a blade SSP34m has been performed in DTU Structural Lab test facilities at DTU Lyngby Campus. The test are performed to investigate the blade's behavior under fatigue and torsional loads. For this purpose, face sheet debonding of blade SSP34m in the trailing edge panels at the max chord area are tested. Where a debond is created on the surface of the blade and the blade is loaded with edgewise and/or flapwise loads. Crack development is observed and used as an input to CAR Tool.

Simultaneously, two types of trailing edge panels are tested: One with a thin face sheet and other with a thicker face sheet. The following fracture mechanics tests are carried out:

1. Tensile testing of the face sheet material with a propagating crack.
2. 4-point bending testing on beam specimens.
3. Compression-tension testing of face sheet material to measure material properties and fatigue initiation threshold levels.

The purpose of the tests is to investigate the physical phenomenon found in real blades rather than a pure academic study. The results from the test are used as an input to the Cost and Risk tool.

In addition, during the project, comparison studies were also performed where results from the testing were compared with analytical results for the purpose of validation.

### 4.4 Tip Solution Objectives

The use of carbon fibre and increasing height of wind turbines and their location often make them exposed to direct and indirect lightning strikes. The wind turbine blades are equipped with lightning protection system; however, lightning damages

still occur. Therefore, making it an important issue among the wind turbine owners. The lightning causes severe damage to the blades and requires a significant cost of repairs, labor, and material.

According to one study, wind turbine in their lifetime face numerous numbers of lightning strikes, mostly at the last few meters of blades. In most cases, the tip of the blade is either completely detached or the pressure side and suction side shells are left split open. Therefore, to avoid the opening of the shells under lightning scenario, a new structural enhancement product is developed.

The product will act as an interim solution until a full repair is performed. Consequently, the extensive downtime of the turbine due to damages caused by lightning strikes is avoidable. The work included design of the solution, material testing and validation in collaboration with Engineering Consulting Cooperation (ECC), and Field demonstration of the product. However, field testing had to be cancelled due to unfortunate circumstances caused by outbreak of Covid-19.

## 4.5 Risk in the project

A series of obstacles have been faced with damages caused to the SSP34m blade in the load introduction region which caused several delays in large scale-testing. The blade was repaired two times by Global Wind Service.

Secondly, the project faced delays in the fracture mechanics testing at the Technical University of Denmark (DTU) due to change of staff at DTU. The postdoc responsible for the tests left his position before time and a new postdoc had to be found and employed, resulting in impeding of CAR Tool progression since CAR Tool heavily relied upon the results obtained from the fracture mechanics testing.

The final obstacle faced was an outbreak of Covid-19 which had a huge effect in slowing down the progression of the whole project. All the laboratory activities related to the project were put on-hold for a period of four months. However, to mitigate the problem, Bladena in collaboration with DTU developed a light fracture mechanics methodology to analytical simulate the fracture mechanics testing. Finally, the Covid-19 resulted in a cancellation of field test in Italy.

## 4.6 Milestones

Technical and commercial milestones were defined prior to the start of the project. The purpose was to keep track of the project.

### Technical Milestones

- TM1: Development of CAR-Tool (WP10)
- TM2: Cost and Reliability models (WP2)
- TM3: Sub-Component Testing (WP5)
- TM4: Root cause analysis and Structural understanding (WP6)
- TM5: Fracture mechanics testing and analysis (WP7)
- TM6: Product development (WP9)
- TM7: Pressure wave and high strain rate (material validation) (WP4)
- TM8: Field installation and support to testing
- TM9: Field data

### Commercial Milestones

- CM1: Identification and handling of market barriers for Tip Solution (WP9)
- CM2: Visualization (WP11)
- CM3: Project management (WP1)
- CM4: The Wind Turbine Owner's Blade Group (WP3)

The project had been on track until the unfortunate situation regarding Covid-19 caused a stall in the project. The fracture mechanics testing and sub-component testing were heavily affected by the Covid-19 virus since the Technical University of Denmark (DTU) had to remain closed for four months. As a consequence, Bladena in collaboration with DTU has developed a fracture mechanics approach (light approach) to evaluate the growth of transverse cracks. Main purpose of this new approach was to mitigate the tests if it could not be resumed due to Covid-19.

Furthermore, field installation of the tip solution was also heavily affected by Covid-19. The field demonstration of the Tip solution which was planned to be installed in Italy had to be cancelled. Since an alternative option could not be found a field demonstration of the solution cannot be presented to the partners.

## 5 Project results and dissemination of results

This section presents the results obtained during the project. The results are presented in the following order:

1. Value Chain
2. Development of Cost and Risk tool (CAR Tool)
3. Transverse cracks
4. Development of the tip solution

In the following section 6, 7, 8 and 9 the activities and key results under each area will be highlighted and explained.

## 6 Value Chain and WTO network

In working together with the value chain and especially with the WTO Network during the CORTIR Project, it has been important to understand where the motivation for participation, action and possible changes lies. Different parties have different interest. When looking at blade damages the main question is liability. Who has the liability for issues experienced in the field?

The first step is to understand the current situation and handling of blade related issues and to understand the players in the wind industry. Common interests must be uncovered and argued for. This is a continuing process. The CORTIR Project has started mapping interests and market values as well as improving the shared language in the wind industry and understanding of important industry aspects and has set a platform to create close collaborations between WTOs, OEMs, ISPs and insurance companies.

### 6.1 Wind Industry Value Chain

Wind energy is green energy and the world needs cost-effective environmentally friendly solutions to deliver the need for energy. That being said, the wind industry is made up of businesses and everybody needs to make money.

In the CORTIR Report focus has been on bringing costs down. This can potentially mean more money for everybody. If the cost of maintenance strategies for wind turbine fields can be brought down, the first to gain from that will be the WTOs. However, money that does not need to be paid, does not need to be fought over. Dependent on how the cost of maintenance has been reduced, the saved money might be a cost the WTOs would have otherwise asked either the OEMs or the insurance to cover.

This is why the understanding between different parties in the wind industry and the motivation change on current procedures and conceptions is important to investigate in a shared project. The main players in the wind industry are all represented in the CORTIR Project:

- **Wind Turbine Owners**
  - Acciona Energy, Arise, Enel, EDF, Engie, Equinor, Ewii, Høfor, RWE (former E.ON and Innogy), Statkraft, Vector Cuatro (Falck Renewables), Ørsted
- **Original Equipment Manufacturers**
  - LM Wind Power/GE, Nordex, Vestas
- **Independent Service Provider**
  - Global Wind Service
- **Insurance company**
  - Codan
- **Solution and knowledge provider**
  - Bladena
- **Universities**
  - DTU Mech and AAU
- **Guide2Defect and ECC**

Each player has their motivational reasons both for overall acting in the industry and for joining the CORTIR Project. For the sake of this project focus will be on wind turbine blades.

**The WTOs** have a direct interest in reducing both OPEX and CAPEX for wind turbines. The two focus areas are to optimize energy output e.g. by reducing downtime and to minimize operational cost. To take the right strategic decisions, the WTOs seek knowledge on the actual lifetime on the blades they acquire and information on the nature and amount of failures to expect during blade lifetime. For this reason, clear certification standards, testing according to realistic loading and open documentation is in the interest of the WTOs. When the decisions have been taken and turbines are operating in the field, the WTOs have several options to further increase earnings; amongst them are optimizing maintenance strategy e.g. by using new technology as NDT inspection, installing aerodynamic enhancers or preventive solutions to avoid blade failures. When failures do happen, it is important to know who has the liability. If liability can be placed on OEMs, perhaps at end of warranty, no costs are directly inflicting the WTOs.

By joining the CORTIR Project the WTOs support the growing dialogue regarding the above issues. The WTO Network is another example of a platform for the WTOs to share experiences and to work on making their needs and message clear and to be heard. Furthermore, knowledge sharing between the WTOs has proven to be very fruitful.

**The OEMs** are manufacturing and selling the blades. As a seller of a high-value product they will have to vouch for the quality and performance and to ensure their good reputation in the field in a balance against development and manufacturing expenses and production time. After end of warranty the blades are in most cases not the liability of OEMs anymore, but the good relationship with costumers is still a priority.

Some OEMs have also made a business as service providers. The OEMs will of course have a unique knowledge of their own blades which is an advantage. On the other hand, it is relevant to ask how to avoid that blade defects, damages and failures can become a business case, where profit from servicing the blades counteract the motivation to avoid blade tendencies to develop damages and failures.

As partners in the CORTIR project the OEMs makes sure that the conversation does not proceed without their input and brings important facets and considerations to the table.

**Insurance companies** have a business case everywhere things can go wrong. Especially where a lot of money are involved. When a failure occurs, the insurance company will investigate if the failure must be covered by the insurance. That does not mean, that the insurance company needs failures not to occur, if there were no failures there would be no need for insurance companies. The insurance companies often use loss adjusters to evaluate damages and place liability. The placement of liability for failures often needs an expert understanding of the root cause of the failure and the risk associated with the failure type to happen on other blades is of high interest to the insurance companies. The insurance company covers damages as a result of a sudden event. Proven design flaws are also covered by the insurance. However, damages as a result of gradually deterioration, likes those happening during normal operation, is not covered by the insurance.

In the CORTIR Project the insurance company partner (CODAN) gains knowledge about damages in the field and what can be done to prevent damages. With the development of the CAR Tool much focus has been on how to evaluate and handle risk. The estimation of risk and prediction of damages are exactly the foundation for a strong insurance business strategy. When it comes to liability this also affects insurance companies in terms of who the costumers are or how much they need insurance.

**Solution Providers**, as Bladena, has a continuing drive to provide retrofit solutions and knowledge to wind turbine owners to maximize AEP and minimize operation and maintenance cost.

Bladena participates in leading the CORTIR Project to shed light and understand the challenges facing the wind industry. As blade experts with a deep understanding of structural failures, Bladena Solutions can help decrease LCoE and risk. With Advisory Services covering all phases of blade life, Bladena can help understand and mitigate both failures and risk.

## 6.2 Liability

Liability is of key interest since this is how it is decided, who shall pay. Even if WTOs have insurance, expenses connected to damages cannot be eradicated because of deductibles. Most insurance policies include an element of own risk. Hence, regardless of insurance coverage, most events will equal cost for the WTO. Further, there will a coverage limit, both on incident level and annual level.

In deciding “*how come*” a damage or a blade failure has occurred the liability can be decided. If the “*How Come*” can be nudged a bit by good argument, perhaps the liability can be shifted.

Loss adjusters are there to uncover the “truth” on how come a blade is having a damage. In Figure 8 different damages are shown to be speculated to be in different categories of root cause for the damage. If the loss adjusters can show, with the expert help from Bladena, the *how come* of a damage, the liability can be decided.

### Wind Project Liability Options – Blade Perspective

Failure	Wear & Tear	Operation	Quality	Design	Act of God	Accident	Wilful
Leading Edge Erosion	X	X	X	X	X		
Lightning Damage		X	X	X	X		
Transverse Cracks		X	X	X			
Peeling	X		X	X			
Dust build-up	X	X					
Longitudinal Cracks, TE	X	X	X	X			
Fire		X	X	X	X	X	X
Liability	WTO	WTO	OEM/WTO	OEM	WTO	WTO	WTO

Figure 8: In the first column is a list of possible blade failures. In the top row is a listing of failure categories and the tables show which categories a certain type of failure can be associated with. The category resulting in the failure will often need expert knowledge to decide. In the bottom row the tables show whom are responsible for the different failure categories.

Dependent on the damage type and especially the cause of the damage type, different insurance options are available for the WTOs, see Figure 9.

## Wind Project Liability and Insurance options – Blade Perspective

Category	Description	Liability in warranty	Liability outside warranty	WTO Insurance Options
Wear and Tear	Naturally and inevitably degradation of the blade due to operation as per the operational procedure.	WTO	WTO	O&M cover, but only to cover unexpected peaks in cost.
Operation	Damages due to operation outside operational manual, faulty maintenance/inspections (or lack of), and faulty repairs.	Faulty Operation: WTO Others: OEM	WTO	None
Quality	Quality issues in material, workmanship, production methods, transport, storage and installation.	OEM	WTO	Extended Warranty and/or O&M Cover. Business interruption. Serial defects will only be covered until it is realised that they are serial defects. If serial, regress towards OEM
Design	Either defects due to faulty configuration/selection of turbine or serial defects	OEM	OEM	Latent Defects and Business interruption. Regress towards OEM.
Act of God	Lighting, flooding, extreme weather	WTO	WTO	All Risk and business interruption
Accident	Any accidental damages to assets.	WTO	WTO	All Risk and business interruption
Wilful	Theft, vandalism, sabotage, terrorism	WTO	WTO	Operators Risk and business interruption.

Figure 9: Most insurance policies includes an element of own risk/deductibles. Hence, regardless of insurance coverage, most events will equal cost for the WTO. Further, there will a coverage limit, both on incident level and annual level.

### 6.3 WTO Network

The WTO Network is a growing group of WTOs who are meeting and discussion shared topics of relevance. Bladena was asked in 2014 to be the coordinator of the topic “Structural blade design and testing” and has since invited WTOs to many seminars on the subject. The CORTIR Project offers an opportunity to keep creating relevant seminars and gathering WTOs for discussions and knowledge sharing.

The WTO Blade Group Network has received several new members during the time span of the CORTIR Project.

Now we have officially reached more than 50 members all registered on the member list at [www.wto-network.com](http://www.wto-network.com) with company description and logo. 9 other WTOs have shown interest to be part of the network and they have been approved by the WTO-Network Steering group but are still missing to deliver company info.

Recently, the administration in Bladena has been asked from WTO members if there (in the future) will be a message board provided online at [www.wto-network.com](http://www.wto-network.com) to be able to have a dialog directly. Until now, it has been a request from owners and operators to have a forum where you can network through meetings, seminars, and other events. Depending on the need this will, of course, be introduced. If you as a member find value in having a message board as well, please send your request to Find Mølholt Jensen ([fmj@bladena.com](mailto:fmj@bladena.com)).

## 6.4 Seminars and workshops

During project, the whole value chain in the wind industry was gathered on multiple occasions at Bladena's office in Roskilde. Several WTO seminars and workshops have been held, see Table 1.

Date	Type	Content
27 Feb. 2019	Kick-off meeting	Present the project objectives
13 May 2019	Workshop	CAR Tool, specifications
14 May 2019	Workshop	Fracture mechanics
10 Oct. 2019	Seminar the WTO Network was also invited	Value Chain & CAR Tool - Operation & maintenance - <b>Unplanned repair costs for \$8,5 billion by keynote speaker Daniel Liu, Wood Mackenzie</b>
25 Nov. 2019	Workshop	CAR Tool cost input
15-16 Jan. 2020	Mid-term meeting. The WTO Network was also invited	Value Chain & CAR Tool - Operation & maintenance - <b>Certification rules and standardization by Christopher Harrison from DNV GL</b> With WTO-Network
17-18 Juni 2020	Seminar	CAR Tool & Damage tolerance
15-16 Sep. 2020	Workshop	CAR Tool
November 2020	Seminar the WTO-Network was also invited	WTO seminar – Failures in the Field
Marts 2021	Final meeting	Sum up of CORTIR and discussion of next steps

Table 1: List of the internal largest seminars and workshops held during the CORTIR project.

Table 1 shows the larger seminars and workshops held over the course of the project, where most of the project partners participated. Results from the CORTIR Project have been presented at international events in Berlin and in Hamburg, as presented below. Moreover, quarterly fracture mechanics workshops were arranged in collaboration with DTU, where large-scale testing and sub-component testing have been the topics. Bladena and AAU, LM Wind power and Engie have actively participated in the seminars and workshops.

For the development of the Reliability module in the CAR Tool several meetings with AAU, Guide2Defect (G2D) and Bladena have been held featuring discussions of risk seen both as an academic concept and a very real consideration for the WTO, and discussions have been about how to correctly consider risk as both an input and output to the CAR Tool.

### Kick-off meeting, February 2019

In February we successfully completed the Kick-off meeting covering the whole value chain in the wind industry such as manufacturers (OEM), wind turbine owners (WTO), insurance, service providers (ISP), Universities, Sub-suppliers and were all gathered at Bladena's offices in Roskilde. At the Kick-off meeting Vestas (OEM), Codan

(insurance company), and Engie (WTO) attended a panel discussion. The CORTIR project's future plans were represented during fruitful discussion and feedback exchange, see Figure 10.



Figure 10: Kick-off meeting for the CORTIR project was well attended. Vestas, Engie, Codan, and EUDP in the panel.

### CAR Tool Workshop, May 2019

In May we successfully completed a workshop about the CAR-Tool (Cost And Risk Tool). The CORTIR project aimed to guide the decision making and provide a common strategy platform for the entire value chain. During the 2-days workshop in May 2019, there were held plenty of fruitful discussions that led to a clear consensus between the twenty represented parties.

### WTO Seminar - Operation & Maintenance, October 2019

The next CORTIR event, a 2-day seminar October 10<sup>th</sup> 2019, the partners also here had the opportunity to be involved in the continuously improving collaboration of the entire value chain. This 2-day seminar covered progress of the CAR Tool and Transverse Cracks areas, and subjects as market and trend data from an OEMs perspective regarding the development of the CAR Tool.

Daniel Liu, a principal analyst at Wood Mackenzie gave the keynote presentation. This resulted in a very insightful presentation about the recent research performed by WoodMac. According to their new research, onshore wind farm owners/operators will spend nearly €15 billion on operations and maintenance services in 2019. Of this, 57% (€8.5 billion) will be spent on unplanned repairs and correctives prompted by component failures. In the presentation, Daniel Liu dived into how the market would change and what to gain from this knowledge.

## Mid-term meeting and seminar, January 2020

January 2020 seminar was held over two days. Dr. Christopher Harrison from DNV GL was invited to present DNV GL's take on the limitations of the current certification standards. This led to a fruitful dialog between the entire value chain. What was planned to be a one-hour session ended up taking 3 hours due to the high interest from partners. The Q&A session was chaired by Nicolas Quievy, Technology Manager from Engie. Through the presentation, Dr. Christopher Harrison from DNV GL received a lot of questions, questioning the integrity of the current standards and what the plans are for improvements. His response was positive and accommodating to the input received from all participants.



Figure 11: Christopher Harrison, DNV GL present at the CORTIR Midterm Meeting.

To have a constructive dialog on what the limitations are, how to move forward and how the WTOs can help the most the WTO Blade Group Network was invited to join the seminar as the WTO members unanimously have a great interest in working together with the rest of the value chain e.g. LM Wind Power, Nordex, Codan and Global Wind Service who also were present and Codan gave a presentation. The dialog about improving the standards continued throughout the day positively.



Figure 12: The whole value chain of the wind industry was gathered at the CORTIR Midterm Meeting.

## Blades O&M Europe Forum 18 - 19 February 2020

Bladena attended the Blades Europe Forum to present the CAR Tool and how it will minimize the risk and cost associated with blade O&M. Here, Theodoros Pardalakis from Bladena presented the Cost and Risk Tool (CAR Tool). Also, a panel interview was chaired by Find Mølholt Jensen from Bladena together with Signe Olsson Statkraft, Birgit Junker, RWE and Lene Hellstern, from HOFOR discussed how the CORTIR project will revolutionize blade maintenance and repair.



Theodoros Pardalakis, Bladena present the CORTIR's CAR-Tool at the Blade O&M Europe Forum in Berlin 2020.



Find Mølholt Jensen, Bladena chair a panel interview at the Blade O&M Europe Forum in Berlin 2020. Signe Olsson Lyngne from Statkraft (picture), Birgit Junker, RWE and Lene Hellstrøm, Hofoer were represented in the panel

Figure 13: Bladena participates at the Blade O&M Europe Forum in Berlin 2020. Presenting progress in the CAR Tool development.

## Workshop, May 2020

The damage tolerance is an approach that flaws and damages exist and will propagate during operation of a wind turbine, but the structure will have the ability to sustain defects safely until a repair can be carried out. Many structural damages observed on wind turbine blades are fatigue-driven failures. The main aim is to obtain safe blades, but economically viable and this is why damage tolerance approach could be used by increasing the reliability of wind turbine blades. Thus, instead of a perfect blade, the damage tolerance approach will determine the severity of cracks, evaluating the

crack propagation and the importance of a repair in order the structural integrity of the blade to be insured in a safe for operation level. The residual strength level of the blade will be evaluated and further repairment will be determined if it is needed.

From financial perspective, the damage tolerance approach will connect repair costs with the potential risks of blade failure. The right balance between these two aspects will result in decreased OPEX. However, the overall risk strategy of each WTO and its tolerance to accepted or unaccepted damages on wind turbines is important for determining this balance. During a maintenance strategy the cost of a repair, as well as the risk of a failure due to specific damage play an important role. If the damage will be repaired, the associated risk will be decreased but the OPEX will become higher. During this phase, a damage tolerance approach will evaluate these two terms and the decision will be more qualified.

12 out of 13 WTOs participated.

### WTO Seminar, June 2020

The agenda dove more into the technical aspects of the CAR Tool regarding damage tolerance approach under the OpEx frame and the different types of field data and how they can be used.

### WTO seminar , November 2020

First fully online seminar was held for WTO members, CORTIR partners and other participants from the value chain. The goal of the seminar and the CORTIR project is to support the WTO's in the decision-making process with regards to the criticality of the damages they observe in the field and how to minimize the risk and O&M cost. To support this goal, the main subject of this seminar was blade damages and failures, since it can lead to semi-unexpected cost often outside the operational budget.

### Final CORTIR Meeting, March 2021

In the closing meeting, the project outcomes were presented to the CORTIR partners. The aim of the meeting was to present and promote the project results. This meeting presented the developments made in the CAR TOOL, findings and observations in the fracture mechanics area through testing, and solution for the Blade's tip opening issue due to lightning.strike

## 6.5 CORTIR Posters

To explain the project and its results in a simple, illustrative way a series of posters have been produced. This gives the ability to communicate the project without having to spend loads of time reading several documents explaining it. The posters have also

been collected in a booklet form called poster collection. In this way, it is possible to hand them a copy or explain it without having to pull out several large posters.

The topics of the posters are:

- CORTIR Project Overview
- Transverse Cracks
- Field Data & Inspection
- CAR Tool
- Uncertainties
- Risk: Cost & Probability
- Value Chain: Blades
- Lighting Protection

All the posters are shown on the following pages in Figure 14 to Figure 21:

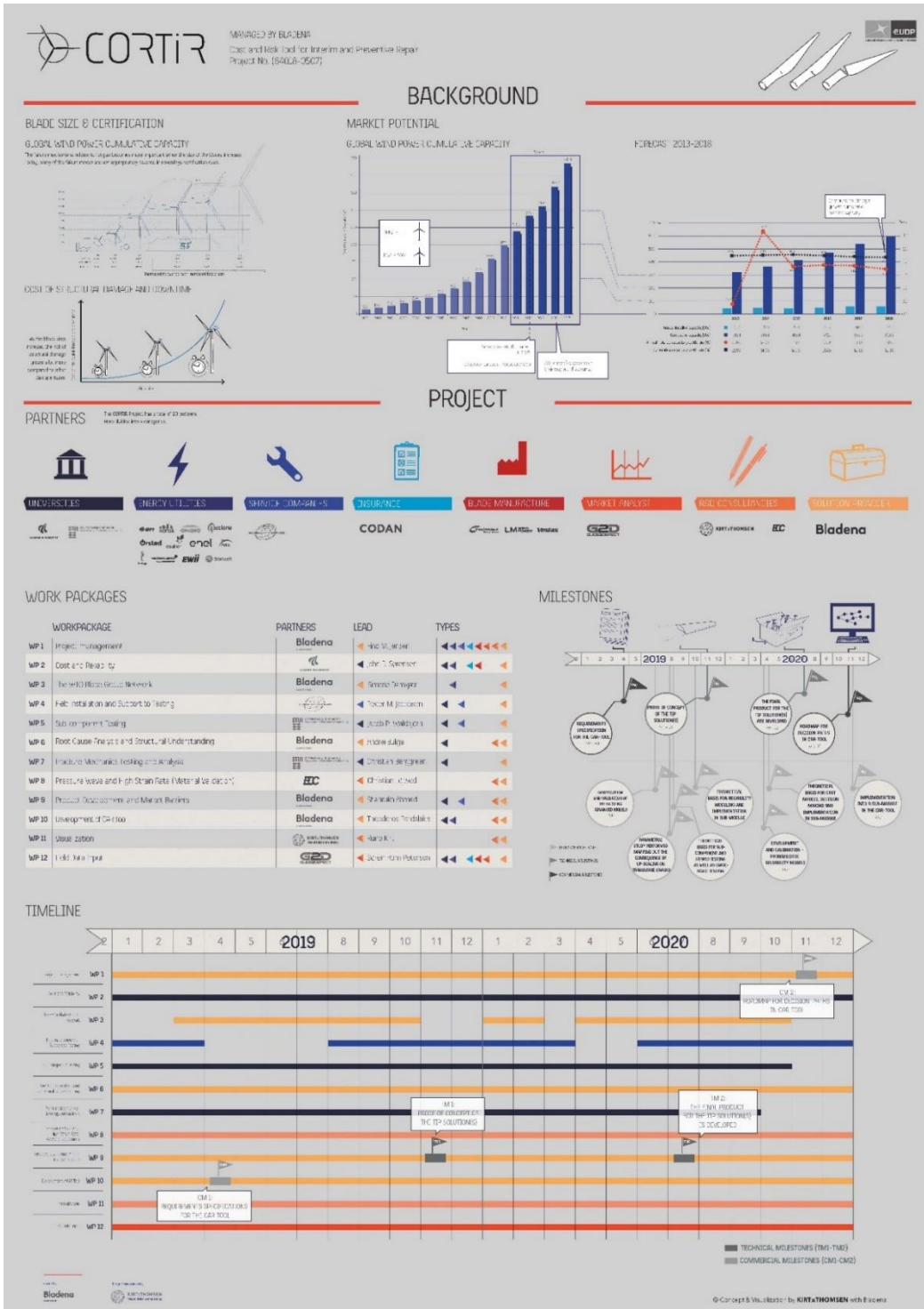


Figure 14: Poster - CORTIR Project overview

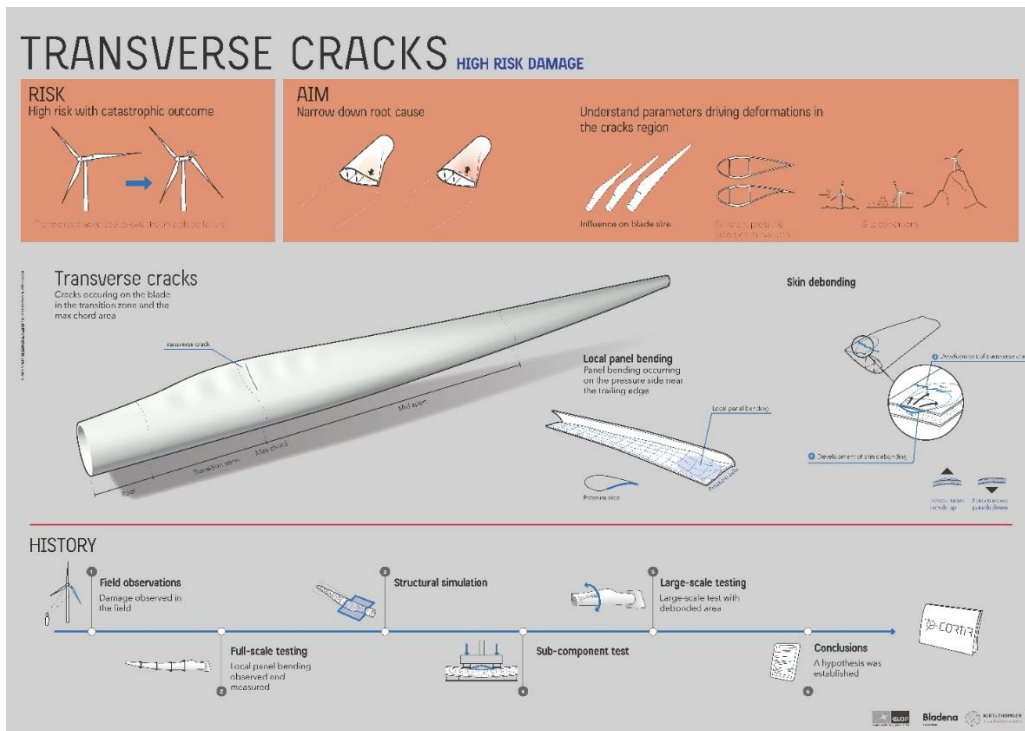


Figure 15: Poster - Transverse Cracks

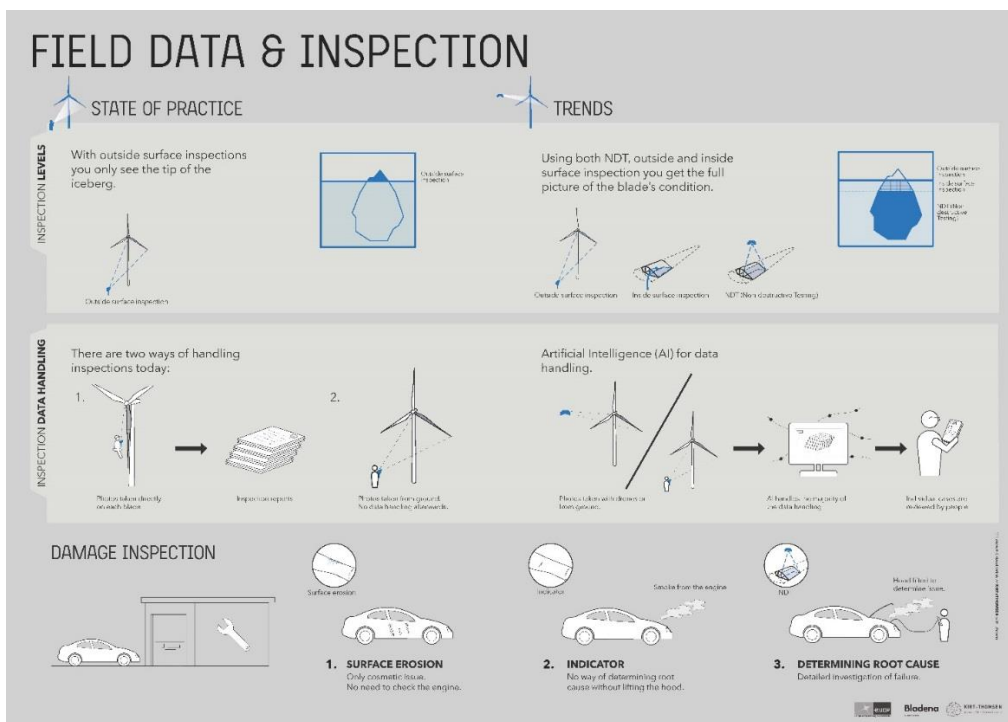


Figure 16: Poster - Field data & inspection

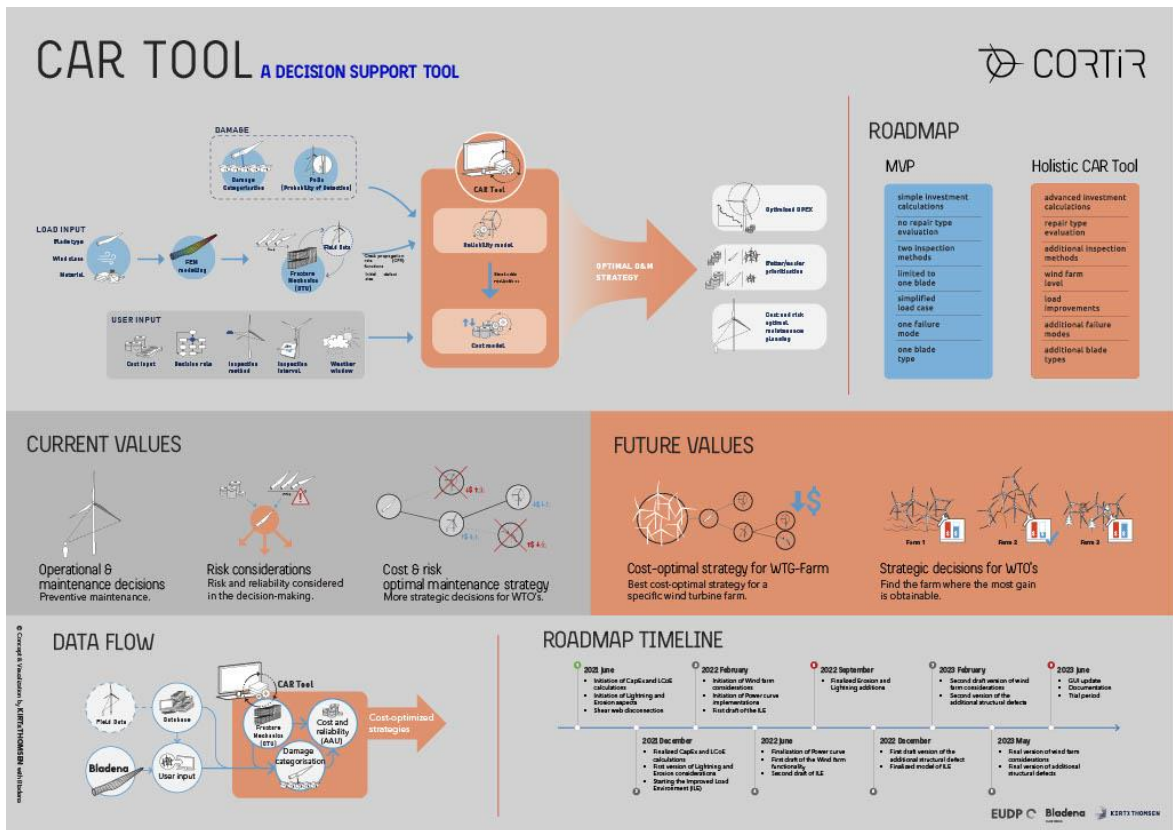


Figure 17: Poster - CAR Tool

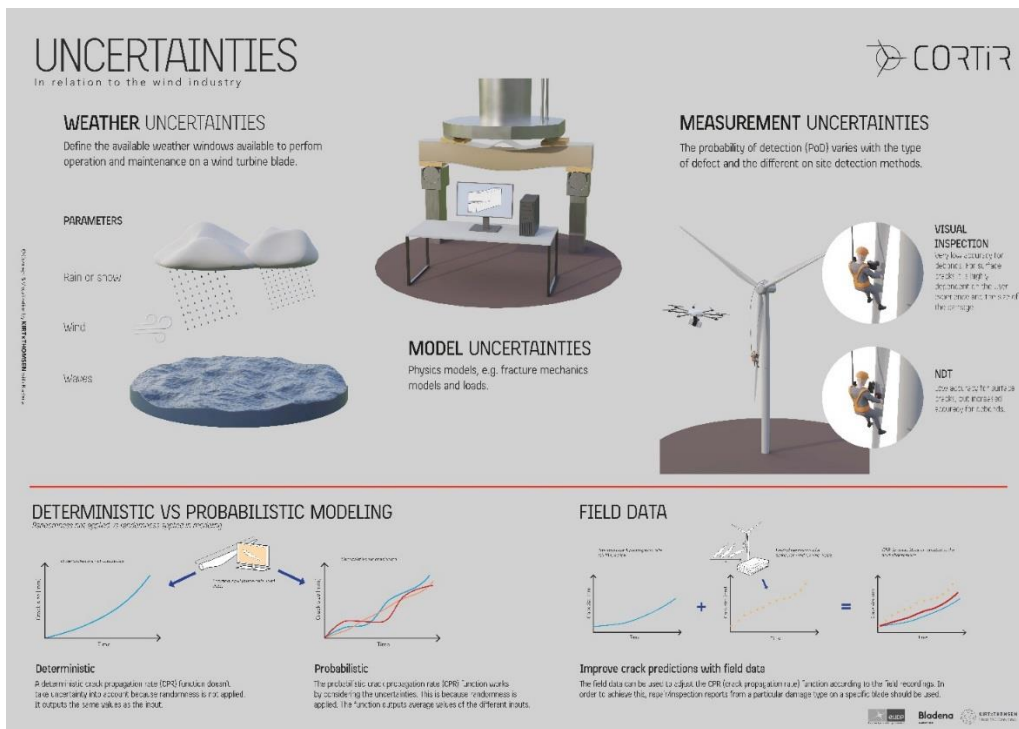


Figure 18: Poster - Uncertainties

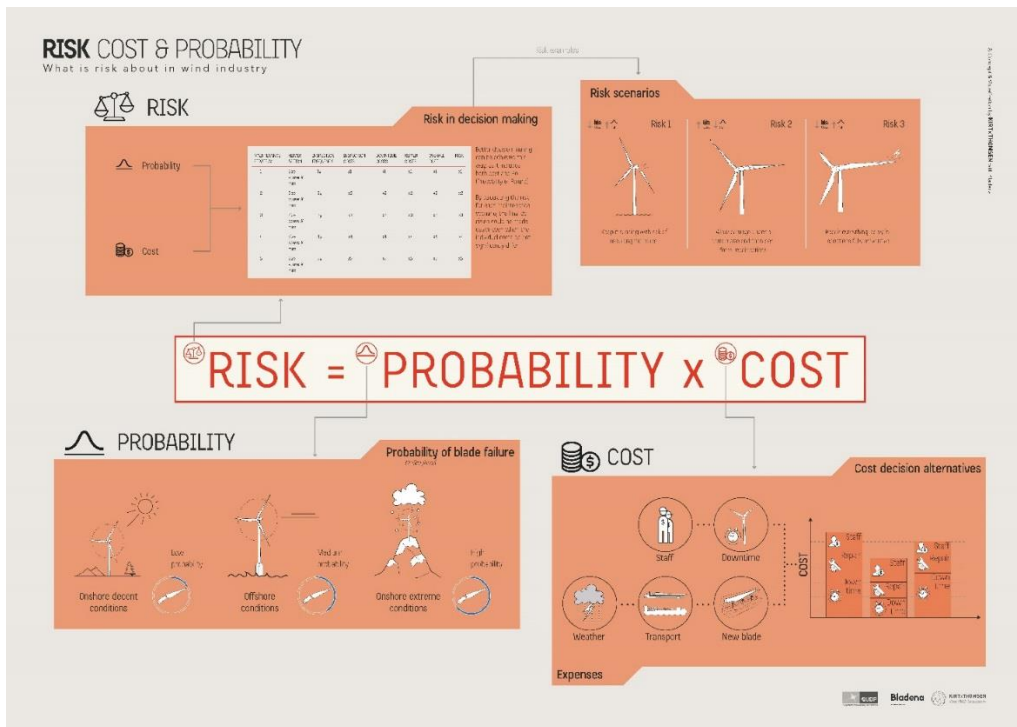


Figure 19: Poster - Risk, Cost and Probability

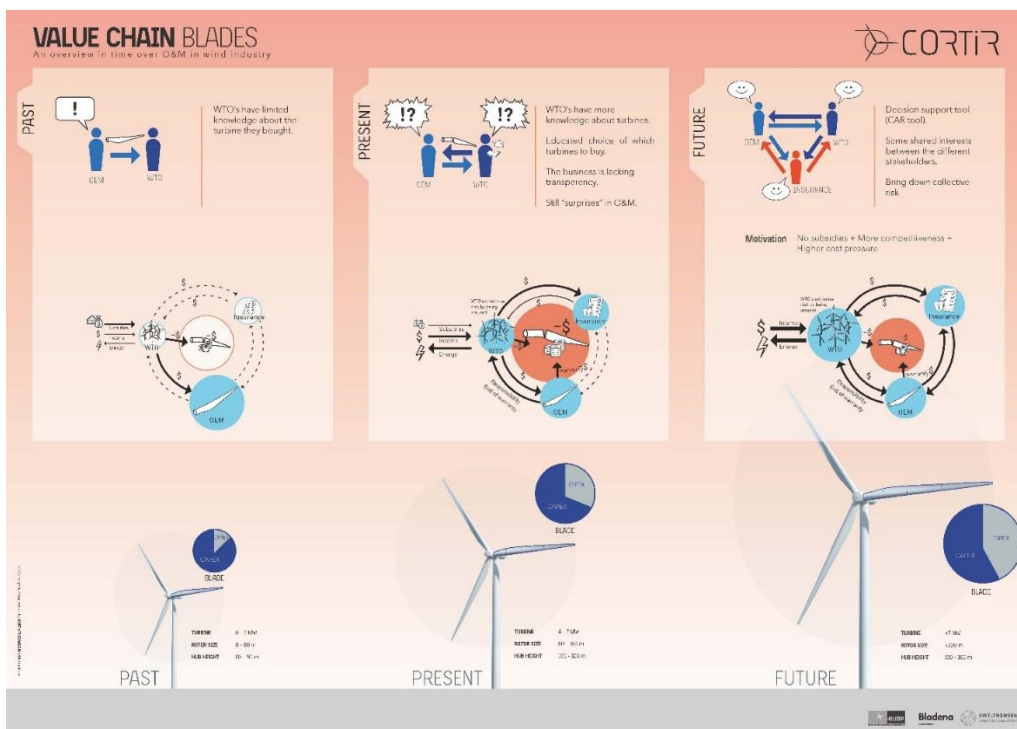


Figure 20: Poster - Value Chain, Blades

# LIGHTNING PROTECTION HIGH RISK DAMAGE

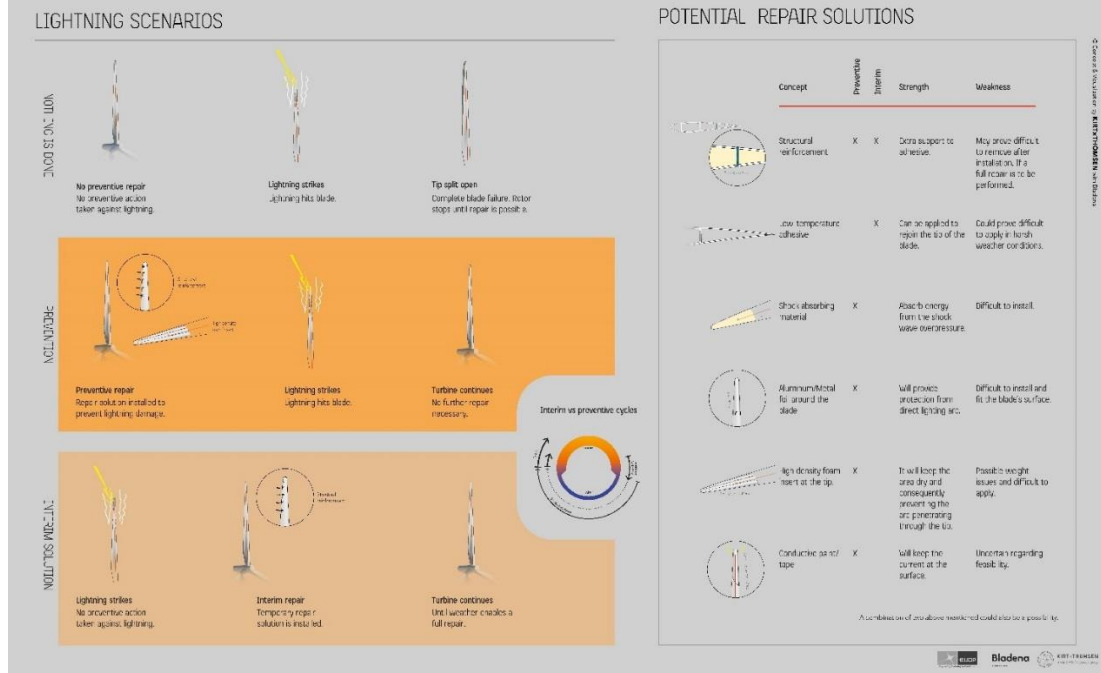


Figure 21:Poster - Lightning Protection

## 6.6 The Blade Handbook

From the former editions of the Blade Handbook, it has been obvious that such an introductory book to the wind industry in a broad variety of topics written and illustrated for easy consumption has been long overdue. For many years the industry has been using many different terms that describe the same thing. The main goal of the Blade handbook is to get a common language in the wind industry in all parts of the value chain. Furthermore, it strives to improve the common understanding of everyday blade related issues, and moreover to help newcomers to the industry get an overview.

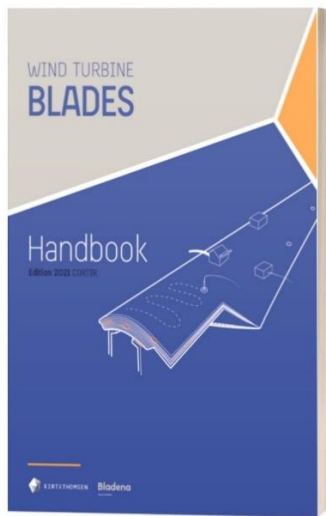


Figure 22: The new updated version of the Blade Handbook.

Generally, this version of the handbook has gone through a massive upgrade and has been taken to a whole new level. Content-wise it has been given an upgrade of over 50%. Moreover, all the previous chapters have also gone through an extensive review and have been updated to make it more comprehensive and comprehensible. Especially, the chapters regarding the market, NDT inspection, and fracture mechanics have been improved extensively. But also, the chapter about the market and the value chain have had a massive improvement. Furthermore, the handbook has also received the Nordic Swan Ecolabel, which is the official sustainability ecolabel for products from the Nordic countries.

To ensure that the updates are as accurate as possible Bladena and Kirt x Thomsen have been getting numerous inputs from a great deal of the CORTIR Partners. Especially, Aalborg University, Force Technology, DIS, Global Wind Service, Guide2Defect, DTU Mechanical Engineering, and DTU Wind Energy have contributed with many important inputs to the handbook.

### [Danish Design Award 2020 // Blade handbook one of the finalists](#)

In early February 2020 Kirt x Thomsen announced that the Blade Handbook developed within the CORTIR project was shortlisted between dozens of design solutions to be in the running of winning the Danish Design Award 2020. On the 18<sup>th</sup> of March 2020 at noon, we received the great news that the Blade Handbook now is one of the finalists to win the award within the category *Message Understood*.



Figure 23: The Blade Handbook has been nominated for a Design Award in the category *Message Understood*.

Also, The Blade Handbook has been nominated for a German Design Award 2021 and an INDEX awards 2021.



## 7 CAR Tool

The CAR Tool is a **Decision Support Tool** and can assist a wind turbine owner or site manager in strategic maintenance decision making cost and risk predictions for different applied maintenance strategies. The predictions are based on simulated blade life and applied maintenance strategy and the informed simulation of damage propagation. In the CORTIR project a minimal viable product (MVP) of the CAR Tool has been developed. The CAR Tool is developed in a collaboration between Bladena, AAU and DTU.

### 7.1 Industry Pains

In the wind industry blades are supposed to have a lifetime of 20 years or more. Some repair during the lifetime is expected but the challenge arises when the blades suffer unexpected damages where the cost of repair is not covered in the budget or when damages causes excessive amounts off downtime reducing the overall AEP. During the considerations for the maintenance strategy of a wind turbine site, several choices present themselves: The turbines could be run until failure and failed parts (including blades) be replaced, or a high frequency of inspections followed by repair might prevent serious damages. The right strategy might be to invest in using a more effective inspection method. The cost of applying a strategy and the resulting gain both in terms of run-time of the turbines, AEP and possible reduced cost from inspection and repair is difficult to guess on, and even more so if several strategies are held against each other.

#### What the CAR Tool does

Inside the CAR Tool a user defined wind site, with information regarding wind speed and market price, is subjected to different applied strategies by simulating the blade life, damage initiation and damage propagation as well as downtime from weather-related limited access to the turbine. The outcome of these different strategies can be evaluated and compared and based on the Cost and Risk results maintenance decisions can be taken with a higher confidence.

#### Definition of Maintenance Strategy

A maintenance strategy for a wind turbine park is a clear plan for how planned operation and inspection and observed damages and blade failures will be handled. The maintenance strategy delivered from the CAR Tool is described with the following three components:

- Inspection Method
- Inspection time Interval

- Decision Rules

The inspection method is a strategic decision where risk is considered. Maybe NDT methods will increase the likelihood of discovering blade damages before they turn critical, but the higher cost of inspection must be considered.

The inspection time interval off cause is dependent on the inspection method - and visa versa. The inspection interval will also be site and load dependent based on a prognosis for damage development. Again, risk is considered; for longer inspection intervals there is a higher risk of blade failures but costs on inspections are reduced.

The decision rule decides what to do when a blade damage or failure are discovered. The best decision rule and the risk attached to it is found based on many blade life simulations with different decision rules.

## 7.2 Uncertainty assessment

How to assess uncertainty it is one of the most crucial modules of the CAR Tool, thus it is essential to try and evaluate all the different uncertainty aspects and how the CAR Tool can be used by every user even when the input includes great uncertainty. Two different approaches are used here:

The theoretical basis for the cost-optimal decision making approach in CAR Tool is so-called pre-posterior Bayesian decision theory. A correct implementation of the decision making tool requires that the different types of uncertainties are modelled and implemented. In addition to the uncertainty modelling also formulation of decision rules for selection of repair options and cost modelling are essential as described in previous sections in this report.

The following types of uncertainties should be included where relevant:

- Physical uncertainty modelling inherent uncertainties which cannot be removed. This includes uncertainties related to the parameters in the Crack Propagation Function and the initial damage size. These uncertainties are modelled using the results from the tests performed by DTU and information from the literature.
- Measurement uncertainty related to the tests being performed. These are in this project assumed to be negligible compared to the other uncertainty sources.
- Statistical uncertainty due to a limited number of tests. In this project is used the procedure in IEC 61400-1:2019 on modelling statistical uncertainty by using Bayesian statistics.
- Model uncertainty accounts for uncertainty in the applied models for loads and resistances. General information related to model uncertainties for fatigue load follows from the background document to IEC 61400-1:2019.

The uncertainties related to the CPR function are modelled and included in the decision making methodology such that the total expected costs during the lifetime of a blade can be estimated and used as basis for the decision making. Here it is important to note that it is the expected value that is needed and that this expected value is estimated using possible realizations / outcomes of the uncertain parameters.

Further, uncertainty related to the inspections are modelled. First the probability to detect a defect / damage / crack of a certain size is modelled by a Probability Of detection (POD) curve. Next, if a crack is detected the uncertainty related to measurement accuracy is also modelled by a stochastic variable. In CAR Tool POD curves are implemented to model inspections of critical transvers crack locations with the possibility to be extended to cover multiple and spatially distributed inspections using uncertainty models similar to those used in the offshore industry.

The total expected costs can also be understood as the expected risk related to a certain chosen inspection plan, a set of decision rules for repair and a cost model. The expected risk can be calculated by different numerical procedures:

- Simulation based: a large number of lifetime simulations are performed where realizations of the uncertain parameters are generated. This is the primary approach in CAR Tool.
- Bayesian Networks: since the theoretical basis for the decision making is a Bayesian approach an efficient way to estimate the expected risk is to apply Bayesian Networks. This approach is used in this project to support the development of the simulation based approach in CAR Tool.

In addition to the above uncertain parameters related to the CPR function and the inspections also other input parameters may be only approximately known. This includes parameters such as:

- Parameters used to model costs related to inspections, repair, lost production;
- Real rate of interest used for discounting;
- Parameters used to model the uncertain variables, i.e. expected values and standard deviations of the stochastic variables.

In CAR Tool there are two main approaches to model and assess uncertainty.

1. Advanced probabilistic models: AAU has vast experience in modeling uncertainty through advanced numerical models combined also with knowledge from other industries in similar projects. The uncertainties related to the fracture mechanics models (CPR function) and inspections (POD curves) are modelled by probabilistic models and implemented in CAR Tool.
2. Parametric studies through sensitivity studies: the user has the possibility to make relative comparisons between different maintenance scenarios and numerical inputs which includes changing cost input parameters and rate of interest. By changing specific inputs, trends can be observed which can further

support the user how to approach each wind turbine according to his own needs. Parametric studies also allow to model and quantify the Value Of Information (VOI) of e.g. new inspection methods with associated POD curve and cost model.

See also section “7.13 Results interpretation”.

### 7.3 Risk Awareness and assessment

The CAR Tool operates not only with cost calculations but also with risk estimation. The willingness to take risk can vary between owners and reflect on which maintenance strategy is the right choice. Risk is defined as:

$$RISK = CONSEQUENCE * PROBABILITY$$

where consequences are measured in cost. The expected risk correspond to the total expected costs during the lifetime or the remaining lifetime if decision making is performed during the operational phase of the wind turbine.

If operation would always go according to plan, there would be no risk no matter how expensive the plan is. However, damages and service during blade life not in the budget constitute a cost and together with the probability that unforeseen damages will happen is a risk for the wind turbine owners. The CAR Tool helps to calculate the risk of the overall maintenance strategy associated to these damages and their connected necessary service actions. In addition, it can also estimate the risk of having to repair damages that belong to specific damage categories.

Loss of AEP due to waiting time for repair or downtime due to weather or blade failure can be a significant contribution to the risk on some wind sites and for some maintenance strategies. The OPEX cost is increasing with the increasing length of blades, further increasing the risk.

With the CAR Tool the risk awareness can be improved. In Figure 24 two trajectories for risk awareness are depicted, with and without the use of CAR Tool. In the past where blades were much smaller, the probability of failure was low as was the risk awareness (acknowledgement of potential damages and process to reduce or eliminate those damages). For that reason, thorough blade inspection was not necessary and counting the blades was sometimes enough. Today the industry is aware that blades get damaged and they can fail. More resources are put into discovering the blade's state, mainly by various visual inspection methods. The CAR Tool can show the risk of undiscovered internal damages based on the user's input resulting in an increased risk awareness. At the same time, this will increase the awareness of how important it is to use an appropriate inspection method (e.g. NDT methods), together with a correct inspection interval, a correct decision rule, and in

general, a correct customized maintenance strategy. Figure 24 shows a graphical representation of the risk awareness.

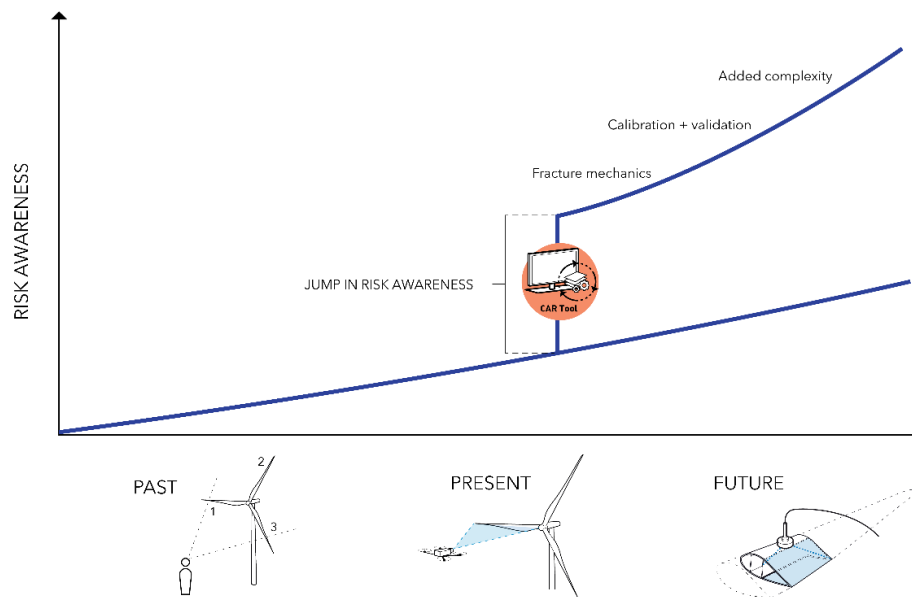


Figure 24: The risk awareness increases as the wind industry matures and blade damages continues to happen more frequently. To know more about the actual state of the blades and reduce risk the inspection methods get more thorough. With the use of the CAR Tool a “jump” in risk awareness can be expected. This may further push on the progression in inspection methods and possibly call for the use of NDT inspection methods in the future.

With the use of CAR Tool Countermeasures can be taken to reduce risk by:

1. Knowing what to expect and put the cost in the budget.
2. Applying the best maintenance plan.

The risk assessment is an additional series of calculations that will further support the final decision. Cost calculations can give an overall estimation of the most cost-beneficial strategy, but it is also important to address the risk that each decision may introduce to the whole decision making. For instance, although a given maintenance strategy may be the most cost-optimal, it may also include increased risk that may eventually expose the overall maintenance strategy. Therefore, it is essential that every cost calculation is to be also supported by a risk assessment to have a more holistic approach towards the final decision.

Because of the increased complexity of the issues that CAR Tool will address, Bladena’s belief is that the tool should not exclusively be based on strict research and scientific principles, but it should also incorporate all the knowledge from the industry. This is achieved by initially, creating a strong background with solid theoretical principles coming from academy. Later on, multiple examples will be created to evaluate different scenarios and ensure that during the entire development phase, the industry’s needs and limitations are well addressed and incorporated as inspiration for a more realistic solver. Bladena will collect feedback

from partners and will perform sensitivity analysis and assessment of the outputs obtained. This will ensure that the CAR Tool will include all the knowledge that is shared among the partners but also it will give the possibility to different members of the value chain to use the tool according to their own needs and availability of input data.

## 7.4 Minimal Viable Product (MVP)

Under the scope of the CORTIR project a Minimal Viable Product (MVP) of the CAR Tool has been developed. The MVP version of the CAR Tool covers the concept of the tool and the methods applied. The CAR Tool MVP is a working software with an interactive Graphical User Interface (GUI) and can simulate and analyze different maintenance strategies based on user-selected input. The output of the CAR Tool MVP is a results report specifying comparative differences between the analyzed maintenance strategies with results given in overall cost, risk profile and operational hours of the turbines.

The CAR Tool MVP is however in this first release limited to analyzing transverse crack damages in the max chord area on the pressure side.

### The CAR Tool, MVP version:

- Working software with all theoretical models in place
- Interactive GUI
- Auto-generated results report
- Limited to transverse crack damages
- Load assumption

Future releases of the CAR Tool will include more damage types in the order where the theoretical work and test data of each damage type becomes available. As the CAR Tool will never be capable of accurately capturing and analyzing the complexity of reality, simplified input and simplifying assumptions are integrated in the tool. These can change and be expanded upon in next versions based on user feedback and benchmarking of the CAR Tool against field case studies.

See also Appendix B for assumptions, limitations, future versions of CAR Tool, future perspectives of CAR Tool.

## 7.5 Applied modules in the CAR Tool

The CAR Tool operates on 4 main modules:

1. The Reliability Model including the uncertainty model and fracture mechanics
2. Damage categorization

### 3. The Cost and Risk Model

The CAR Tool makes use of the four modules when simulation blade life and analyzing different maintenance strategies.

#### Overview of the applied models in the CAR Tool

When the user starts using the CAR Tool, the program is asking for a number of inputs describing the blade type, site conditions, cost of actions and time and cost of logistics. This is collectively called “user input”. The CAR Tool is simulating blade life and adding cost as events and logistics are simulated. Some events, as blade repair and blade replacement are decided by the inputted set of decision rules. The blade damage (transverse crack) is simulated based on fracture mechanics and evaluated in the damage categorization module for the decision rules to use. See Figure 18.

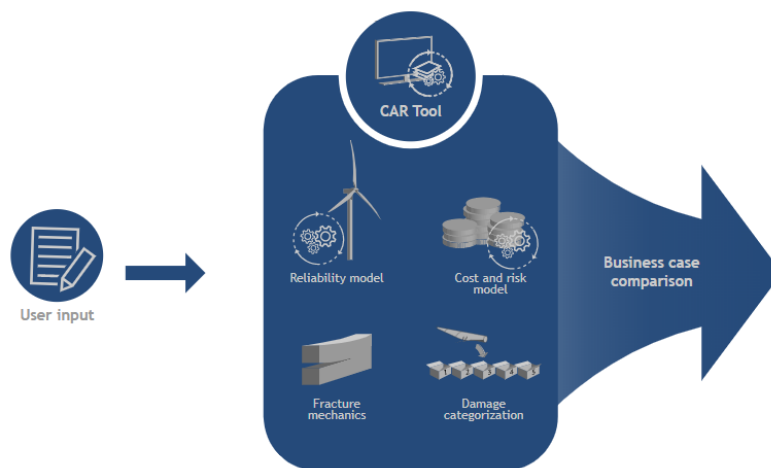


Figure 25: The CAR Tool takes user input and treats it through the four internal modules: Reliability model, Fracture mechanics, damage categorization and Cost model and Risk model. Output from the CAR Tool can be used as a business case comparison.

The modules will be further explained in the next sections.

## 7.6 Reliability model and fracture mechanics

The Reliability Model is developed by AAU and is an approach used to estimate the probability of damage being in a certain category and the probability of collapse. The method is built to handle uncertainties in a reliable way due to the probabilistic nature of events happening during blade life, e.g.: How fast does a damage grow? Is a damage detected at inspection? Will there be delay in getting access to the turbine when needed? The reliability model takes in input from fracture mechanics to simulate the damage growth of transverse cracks on the blade together with the chosen maintenance strategies. The visual examples on blade life simulation can be found in Figure 27 page 47.

The consideration of uncertainties inside this reliability model follows the description provided in subsection 7.2. This uncertainty approach includes the analysis of uncertainty in several areas that are combined, involving mainly: physical modellings (initial defect size and CPR function), performance of the testing, and inspection methods (for more details see 7.2). The idea inside the CAR Tool is to consider this uncertainty approach together with a stochastic model where probabilities are interconnected based on the particular events that take place, in order to conclude in a final expected cost or risk with its corresponding values of P10, P50 and P90.

A more detailed description of the Reliability model can be found in Appendix C.

### The Crack Propagation Rate Function

The CPR function is developed by DTU and describes the Crack Propagation Rate (CPR) of a crack in the outer layer of a sandwich panel. The CPR function is used in the CAR Tool to simulate the growth of a transverse crack in the pressure side panel, max chord area of a wind turbine blade. The fracture mechanics theory applied and extensive test program done by DTU to define and quantify the CPR function can be read about in section “8 Transverse Cracks” and in Appendix D.

The CPR function simulates the damage growing in size over time or load cycles. The Paris’ Erdogan Law is used to describe the crack growth:

$$\frac{da}{dN} = C(\Delta G)^m$$

where  $\frac{da}{dN}$  is the speed of the crack growth (crack length over load cycles) and  $C$  and  $m$  are probabilistic material parameters.  $G$  is the stress intensity factor depending on the load.  $a_0$  is the initial crack size. If the crack development after detection of a crack is considered then  $a_0$  is the measured crack size.

In the CAR Tool the damage is initiated with an initial size which is very small, since there is no such thing as a perfect blade. From here the damage will grow. However due to probabilistic factors which stems from material properties no damage will grow in the exact same way. Some transverse cracks will grow faster than others. These probabilistic properties are built in the CPR function by applying probabilistic properties to the parameters  $C$  and  $m$ .

### Transverse cracks develop in two step

It has been seen in the CORTIR project that transverse cracks in the pressure side panels max chord area develop as a two-part failure . First, a debond between the face sheet skin and the core material happens due to buckling in the panel. The debonded area will grow and when it reaches a certain size a crack will start to

develop in the outer skin. The outer skin crack will be the first visual indicator of a larger failure underneath. The development and connection between damage type, debond and transverse surface crack, can be seen in Figure 26.

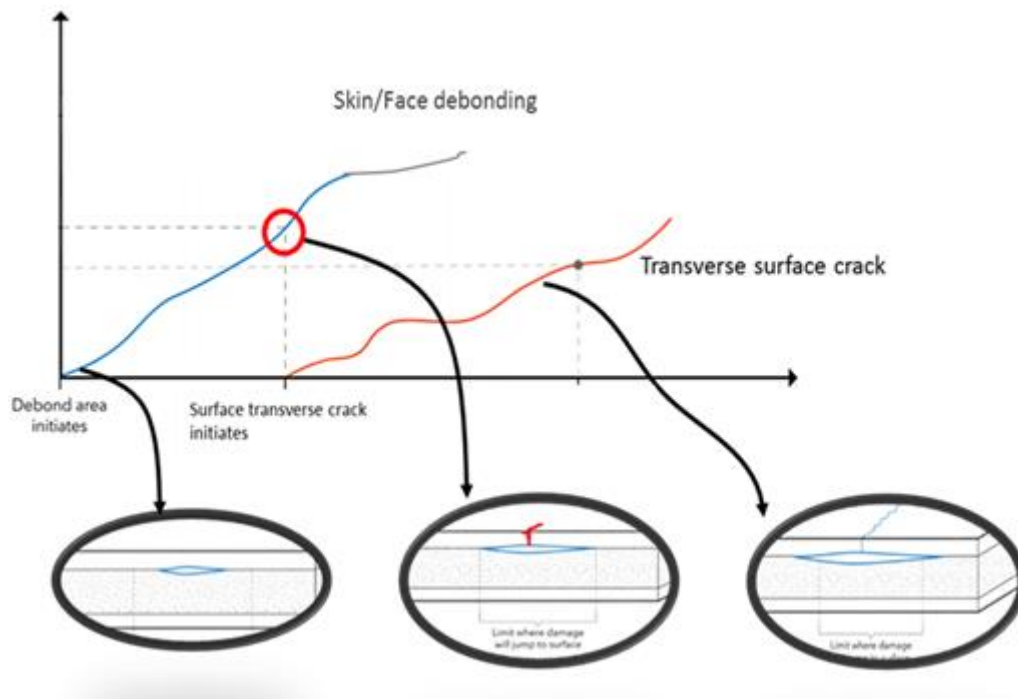


Figure 26. Damage growth of transverse crack and debond (y-axis) vs time (x-axis). The blue line represents the growing debond between the core material and the skin [face sheet]. When the debonded area reach a critical level the damage jumps to the skin and start as a small surface crack represented by the red line. It is only the surface crack which can be detected by visual inspection. To detect skin-debond NDT methods must be used.

The CPR function takes the full damage, both the debond phase and the surface crack growth, into account and the CAR Tool simulates both the debond and the surface crack damage using the CPR function.

For more detail on the CPR function see Appendix D.

### Blade life simulation

A simple example of a CAR Tool blade life simulation is presented in Figure 27. The example is showing the simulated damage propagation (length of transverse crack) over time, simplified to only the transverse surface crack. The different events and related cost the applied maintenance strategy can result in are marked in the figure.

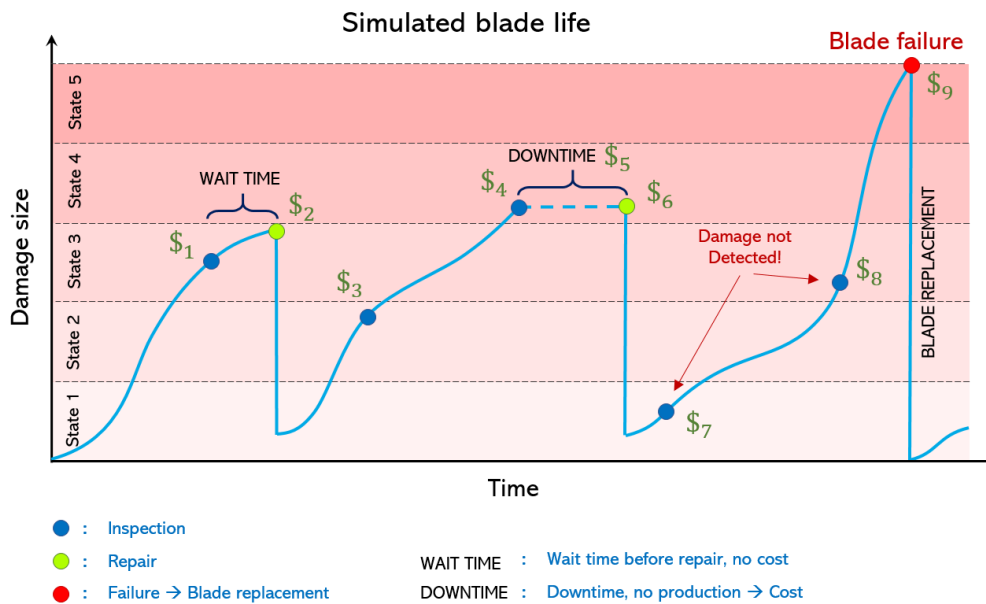


Figure 27: The figure shows a realization (one of many instances of the whole simulation) of the transverse crack damage development (the CPR function) on a blade. Different scenarios that could happen during the simulated blade life are shown on the graph. According to the selected decision rule in this strategy detected damages are repaired at damage state 3 and above. The turbine is stopped at an observed damage state of 4 and above, and the blade are replaced if the damage reaches total failure (above state 5). Inspections, repairs, blade replacements and downtime all cost money. For the two cases of repair the blade is assumed repaired to a defined repair level, which are not a perfect state. At the last damage progression, the damage fails to be detected two inspections in a row and the blade is not repaired, resulting in blade failure. The parameter Probability of Detection (PoD) decides whether a damage is discovered at inspection.

The simulation in Figure 20 represents a cost,  $\$_{sim}$ , that is the accumulated costs of the whole simulation:

$$\$_{sim} = \$_1 + \$_2 + \$_3 + \$_4 + \$_5 + \$_6 + \$_7 + \$_8 + \$_9$$

The example is an introduction to blade simulation within the CAR Tool. A more advanced example taking its root in a field case study can be found on page 49.

The CAR Tool also manage damage states, which are defined by the size of the damage and used by the decision rules. Both damage states and decision rules will be explained in the following sections.

## 7.7 Damage Categorization and Decision Rules

Damage categorization and decision rules are a fundamental part in the reliability model to evaluate which action or event happens next in the blade life simulation.

### Damage categorization

The damage is being categorized in six categories, where the first five are the increasing size of the transverse crack and the last category is blade failure. A damage

category encompasses all damage sizes inside a specific length interval, where the first and last value of the interval are called threshold values. The threshold values have been taken from the values based on the G2D database, Bladena knowledge and field experience. In Figure 28 is shown a transverse crack which in this figure grows from the trailing edge and towards the leading edge.

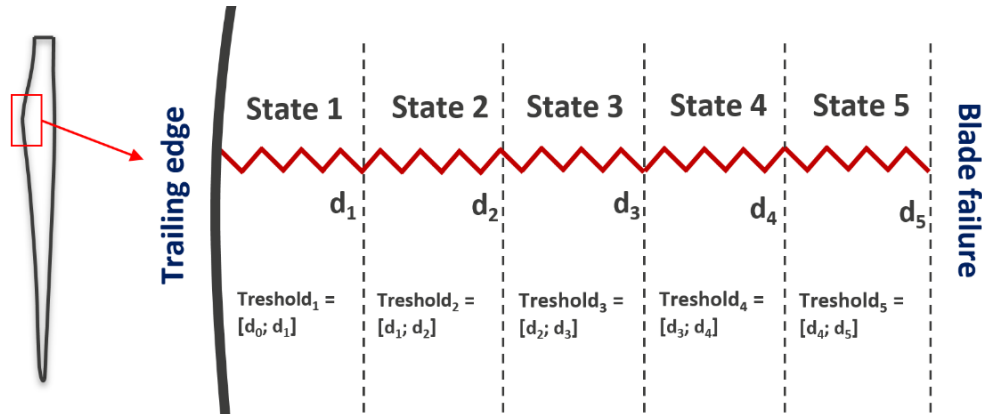


Figure 28: Damage propagation drawing.

When a transverse crack is observed on the blade, the length of the damage is used to categorize it into one of the five defined damage states or as a blade failure. All damages bigger than damage state 5 is categorized as blade failure. The damage states are used when applying decision rules to a maintenance strategy.

## Decision Rules

The decision rules describe different possible strategies. When applying a decision rule to a maintenance strategy it is pre-decided which action to take at the discovery of a transverse crack based on the damage state of the crack. Decision rules can be very straightforward as in Figure 29 or as complex as needed.

	Decision rule 1	Decision rule 2	Decision rule 3	Decision rule 4	Decision rule 5	Decision rule 6
Damage state 1	Repair when possible	No action	No action	No action	No action	No action
Damage state 2	Repair when possible	Repair when possible	No action	No action	No action	No action
Damage state 3	Repair when possible	Repair when possible	Repair when possible	No action	No action	No action
Damage state 4	Stop turbine and repair	No action	No action			
Damage state 5	Stop turbine and repair	No action				
Blade failure	Replace blade	Replace blade				

Figure 29: In this table an example of six decision rules are defined. Decision rule 1 is the extreme case where all damages are repaired as soon as they are detected. Decision rule 6 is another extreme of not doing any repair

and replacing the blades when they fail. In this set of decision rules, for damage state 4 and 5, there is an option to stop the turbine until repair is made, resulting in costly downtime.

Decision rule 1 in Figure 29 can be seen as a low risk strategy (a strategy more likely to result in long term success) whereas decision rule 6 possibly is very high risk since at no time repair is being made. This however depends on the related cost which will vary due to inspection method and site conditions. In the end the CAR Tool output will have calculated the cost and risk for different maintenance strategies.

## 7.8 Cost and Risk Module

During blade life there are planned cost and un-planned cost. Planned cost is covered by the budget and accepted, but un-planned cost covers an unknown proportion of the OPEX and of the AEP loss, therefore unplanned costs are seen as a risk. The risk can be quantified by the following equation:

$$RISK = COST * PROBABILITY$$

The risk is measured by the cost of the unplanned event and the probability that said event will happen. This is the question the CAR Tool is designed to answer.

Of course, the calculation of this risk also has its own uncertainty, taking into account among other things, the standard deviation of the costs. Therefore, as part of the assessment in the selected maintenance strategy, Bladena will inform about the percentiles P10, P50 and P90, quantifying the range of the expected risk.

### Cost model

The CAR Tool takes in user input as well as default (but adjustable) values for the cost of inspection, repair, blade failure and replacement and the price of AEP. During the blade life simulation these cost values will be applied and used in the final cost of a maintenance strategy. This final expected cost can be used as a comparative value against other maintenance strategies and in a business case.

### Risk Model

The cost of events and frequency of events are used to quantify a risk. In the past not much thought was put into prediction risk in a wind turbine project. This was not necessary as blades were small and not prone to failures and the associated cost *IF* failure happened were reasonably small. This has changed as blades and wind projects have grown in size. Still, risk is difficult to predict. The CAR Tool is a new approach to risk assessment.

The following are some benefits of using CAR Tool:

1. Uncertainties related to fracture mechanics model based on extensive tests and uncertainties related to inspections are modelled
2. Risk is quantified as the total expected lifetime costs for a given choice of inspection strategy and decision rules for repair strategy.
3. Reduce cost by using the estimated risk (including P10, P50 and P90) as decision support such that the most cost-optimal strategy for planning inspections and repair can be chosen.

## 7.9 Field Data

Fracture mechanics is the field that inside CAR Tool generates the different scenarios of damage propagation over time. Therefore, it can be argued that all the resulted maintenance strategies are highly dependent on the accuracy of the actual damage propagation. In addition, since a prediction of the future always includes increased uncertainty, it becomes apparent that any available information about real-life observations should be utilized towards a more reliable prediction. For that reason, CAR Tool has the feature of implementing field data from inspection campaigns and utilize them for the improvement of the numerical models.

Field data is utilized in CAR Tool to improve the final output of CAR Tool. In this project, data regarding structural cracks located at the max chord area of the blade is considered. Two types of field data are utilized in CAR Tool: 1) the damage propagation over time and 2) the initial size of a given damage. Implementation of field data in CAR Tool and limitations are presented in this sub-section.

### Implementation

The field data aims to provide real life data to CAR Tool to provide more accurate predictions. With respect to the damage propagation, the format of a typical data point is represented by a pair of  $(x, y)$  where  $x$  corresponds to the damage size at a given time instant  $y$ . The parameters of the damage propagation model can be updated based upon the on-site inspection records and/or the laboratory test results. Unless otherwise specified, the Paris-Erdogan law (Appendix B) is the basic form of the damage propagation model. The uncertainty of  $C$  should be quantified at least, and the uncertainties of the other parameters can be qualitatively investigated through sensitivity studies. The following approach is used to load the Data in the CAR Tool:

- Damage propagation model parameters are indirectly updated through curve fitting (Appendix B). Through the utilization of the field data, a mathematical method is defined in order to find the right values of the parameters  $C$  and  $m$ , that lead the solution of the Paris-Erdogan function to go through the defined data points. The methodology followed from a mathematical point of view, has been to fit a differential equation.  $C$  and  $m$ , are the parameters

that must be found, and field data (so date of damage observation and damage size) are introduced as variables into the equation.

- The code runs until it finds the C and m parameters that define a CPR function that adapts to the field data with an uncertainty below some specific values. The chose parameters are used for planning the inspections and repair strategy for the remaining lifetime. In this way, the parameters can be considered updated.

It is an option to use field data in the CAR Tool to improve the CPR function with real-life data. There should preferably be a certain amount of observations to feed the CAR Tool to use field data. But even if only one observation is available, this could be an observation and measurement of a transverse crack discovered at blade inspection. This one data point can be used to adjust the CPR function, understanding data point as the measurement of the crack, together with the date of the measurement. In Figure 30, the process of adjusting the CPR function based on a field observation is shown.

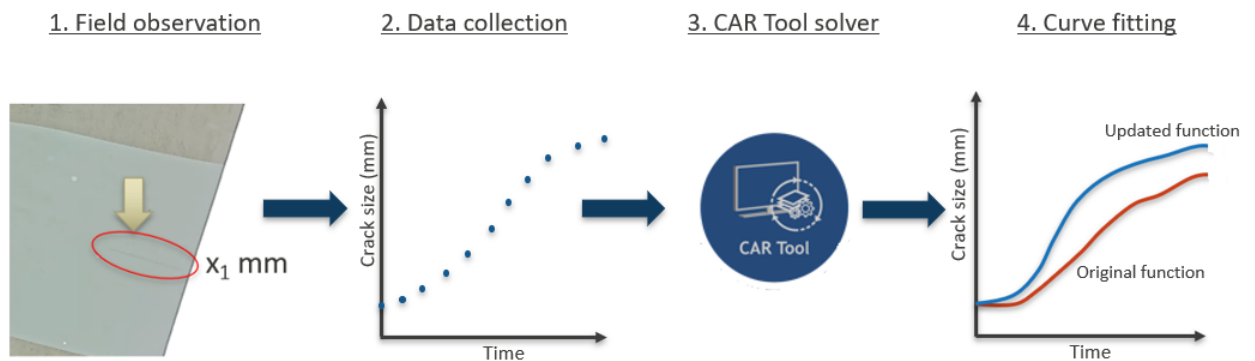


Figure 30. Description of how field data will be used. Initially, a damage is detected and together with its size measurement and date, it is collected and introduced inside the CAR Tool Solver. The CAR Tool will use this data to modify its original CPR, adapting it to the specific characteristics found on these field observations.

The data sample size (number of data points) for one specific blade it is likely to be inadequate from field inspections. Therefore, new ways were considered in order to increase the overall number of data points, see Table 2.

Data type	Data source	Notes
Damage propagation over time	Blade A	Minimum of 5 data points. Ideally, >10 data points. The more the better
Damage propagation over time	Blade A, B, C from the same turbine	Alternative to increase the data points
Damage propagation over time	Turbine A and the neighboring	The selected turbines should be located on the same row on the wind farm

Initial damage size and Turbine's operational hours during the first detection	First detection of the - under investigation- damage	-
Date and factory of manufacturing	When and where each blade was manufactured	By knowing this information, we can ensure statistical independency. If available

Table 2: Overview of the required data.

Table 2 shows a way to increase data points by considering data points of all three blades on the same turbine. Plus, considering the blades that are installed in the neighboring turbines in the wind farm layout as long as they experience similar loading conditions and develop similar defects.

### Field case

For a field case study, qualitative data was provided by Engie from three of their wind farms for four consecutive years. The data included blade visual data (pictures), analyzed for structural cracks. The purpose was to analyze the pictures and observe if the cracks have propagated over the years.

Analysis of the pictures yielded one key finding which is the recurrence of the crack after a repair is performed without removing the root cause, as seen in Figure 31.



Figure 31: Showing development of crack after previous crack was repaired.

The observations were given as input to the CAR Tool. In addition, information regarding the crack length was also provided by ENGIE which was used to update the damage propagation model. Figure 32 shows how data is implemented in the CAR Tool.

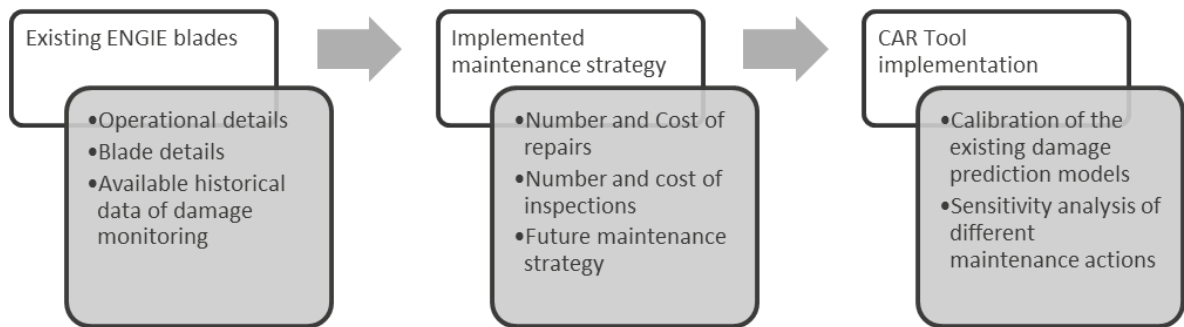


Figure 32: Process diagram showing the use of data in CAR Tool.

## 7.10 Field Case Example

An example of the application and utility of field data inside the CAR Tool is described in the current subsection.

As it has recently been explained, with the goal of improving and validating the CAR Tool, ENGIE provided to Bladena a group of data points (Figure 31) where the development of a crack had been tracked. According to the definition of field data point, the available information allowed to know with accuracy both the date of the measurement, as well as the size of the damage.

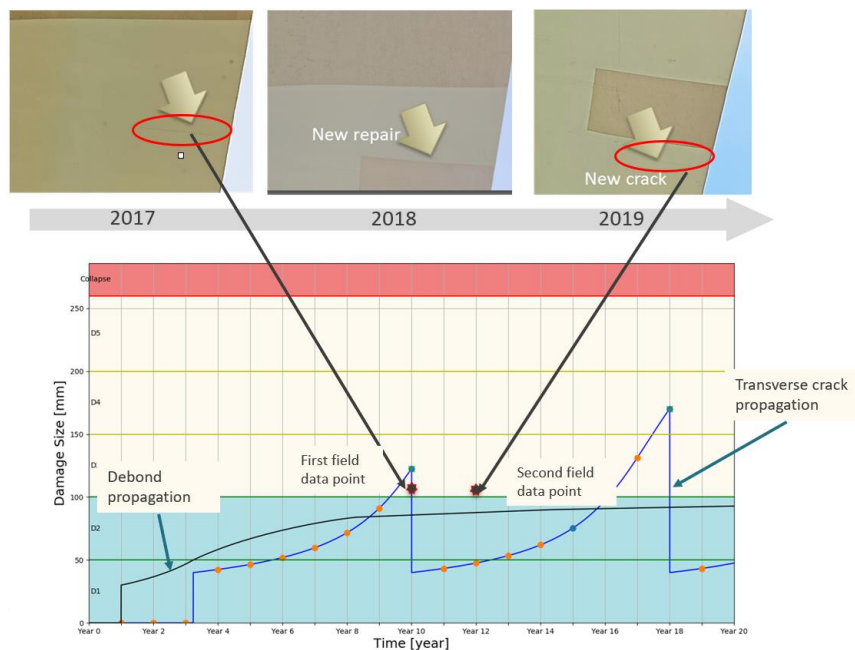


Figure 33. Simulation of a crack propagation together with field data points.

After customizing the CAR Tool so that the particular conditions of the crack, blade, site and ENGIE's O&M strategy could be represented inside the tool, Bladena decided

to perform a simulation of the crack propagation. The result of it can be observed in Figure 33.

The black line represents how the debond is estimated to propagate during the lifetime, growing gradually from 0 mm and leading to the creation of a crack after a minimum size has been achieved (It has been seen in the CORTIR project that transverse cracks in the pressure side panels max chord area develop as a two-part failure . First, a debond between the face sheet skin and the core material happens due to buckling in the panel. The debonded area will grow and when it reaches a certain size a crack will start to develop in the outer skin. The outer skin crack will be the first visual indicator of a larger failure underneath. The development and connection between damage type, debond and transverse surface crack, can be seen in Figure 34.

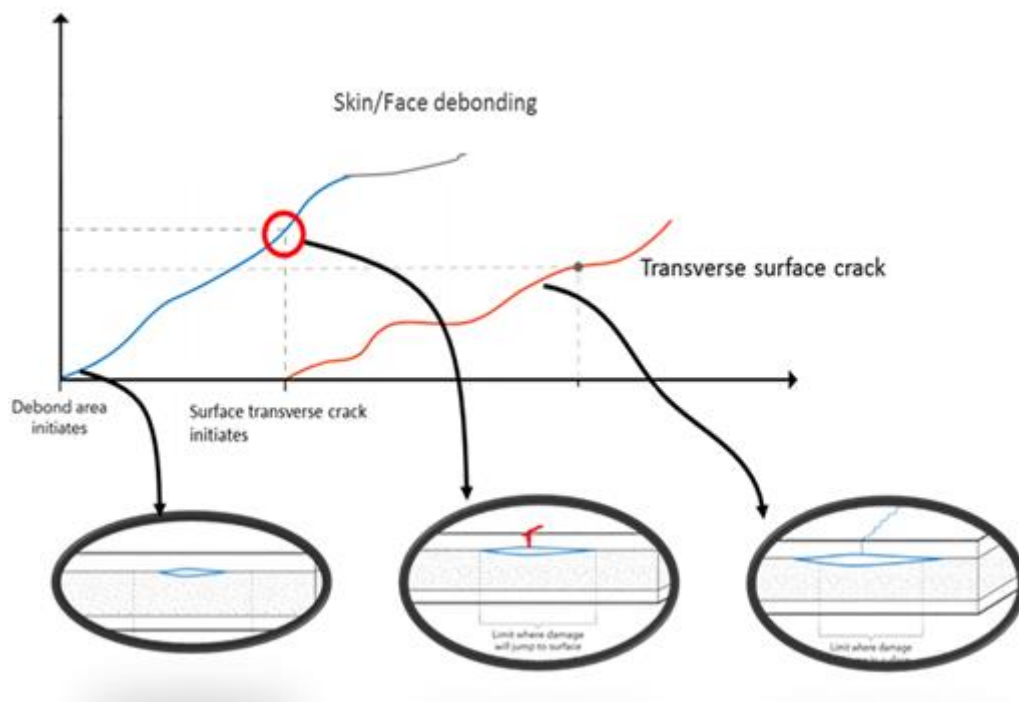


Figure 34. Damage growth of transverse crack and debond (y-axis) vs time (x-axis). The blue line represents the growing debond between the core material and the skin [face sheet]. When the debonded area reach a critical level the damage jumps to the skin and start as a small surface crack represented by the red line. It is only the surface crack which can be detected by visual inspection. To detect skin-debond NDT methods must be used.

From this moment, the transverse crack or blue line appears, and grows until it is detected and repaired in year 10, according to the predefined decision rule established by ENGIE.

At this point, making use of several assumptions explained in the appendixes (mention corresponding appendix), the crack was simulated for the remaining lifetime. By comparing this output with the real field data, it could be seen that the prediction of the damage by the CAR Tool after the first repair at year 10, was far from reality.

Taking this information into account by following the implementation from subsection 7.9, the curve was adapted concluding with a new crack propagation (red line) which is meant to gather the special characteristics of both the blade and site of the crack found by ENGIE.

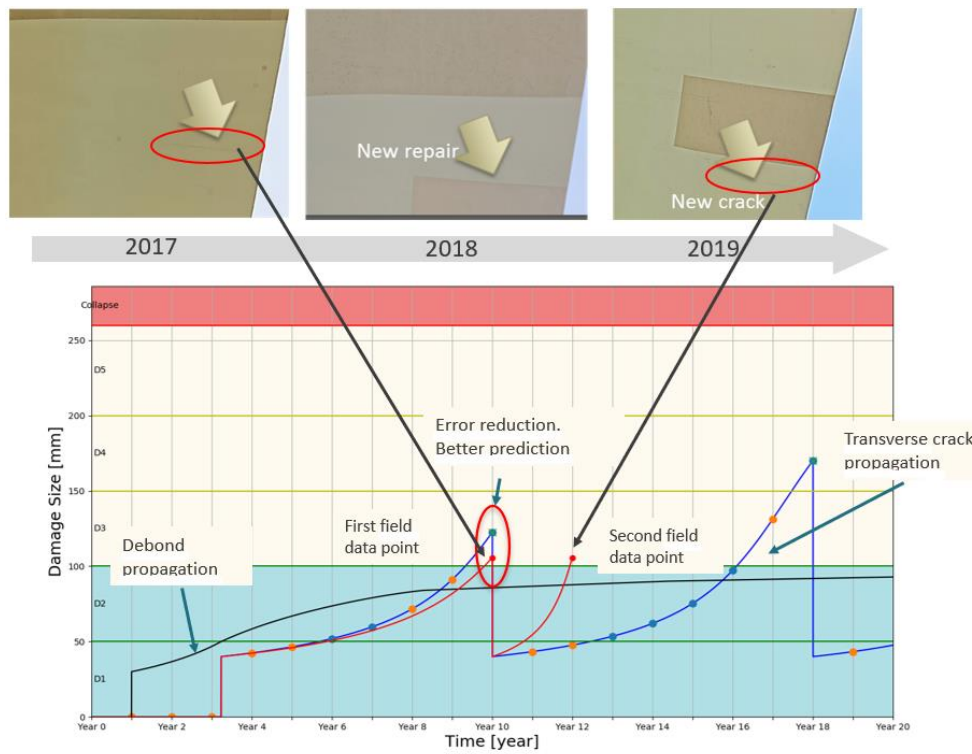


Figure 35. Original propagation (blue) and fitted propagation (red) after field data application

The example above helps to understand the benefits of applying field data.

On one hand, field data helps to identify the strengths and weaknesses of the CAR Tool, which is considered an essential information for an initial development phase like the current one. In this particular example, the prediction of the crack until the first repair turned out to be close to the reality, however, wrong assumptions seem to have been taken after this point, as the blue and red line (original and new propagation) differ from the first repair at year 10.

On the other hand, this fact can lead to further investigation about different areas of interest. For instance, seeing the obtained results, it would be relevant to study: the consequences of different types of repairs, the intrinsic relationship between the debond size and the transverse crack size; and the particular characteristics of the ENGIE example which may have led to that clear divergence.

In any case, it is proved how suitable it is to work with real field data that allows to modify the propagation of the crack simulated inside the tool.

## 7.11 Graphical User Interface

The CAR Tool is equipped with a user-friendly graphical user interface (GUI). The GUI is used to set up the different maintenance strategies to be analyzed. The user is guided through the different choices and variables which must be defined. Most variables come with a choice of default values, but the user can insert her own values either for more relevance or as a part of a parametric study.

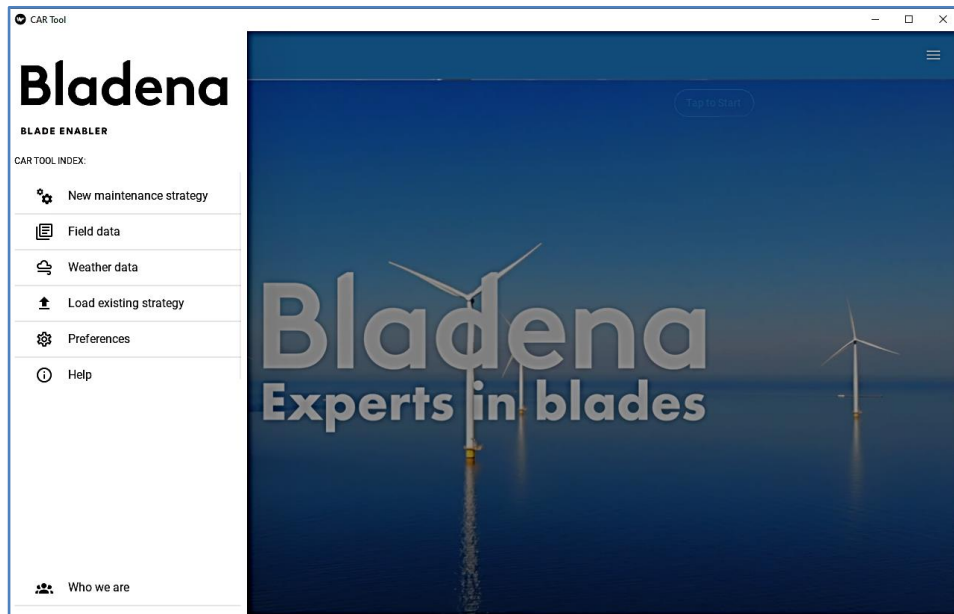


Figure 36: The CAR Tool GUI guides the user in setting up a case with different maintenance strategies to be analyzed and compared.

## 7.12 Output

The CAR Tool automatically generate a results report when the analysis is done. Cost results for the different maintenance scenarios can be studied and compared in many ways, e.g. as in the pie charts in Figure 37 where the different cost contributions can be seen.

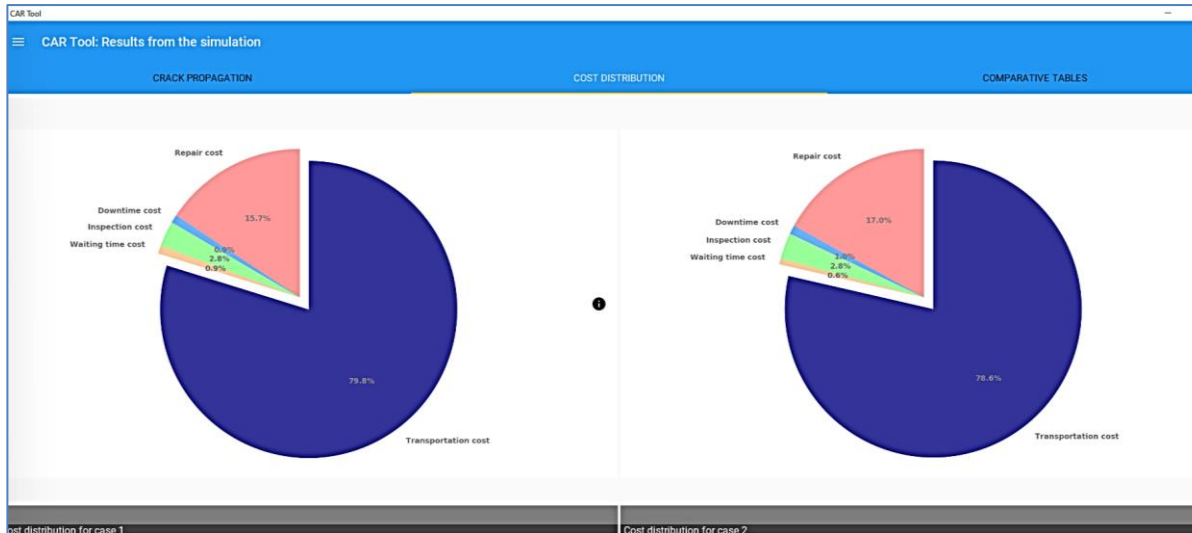


Figure 37: The pie charts are showing how much each cost contributes the overall cost of the maintenance strategy. For both these strategies transportation cost far outweighs the cost of repair, downtime, inspection and waiting time all together.

Another way to compare and evaluate results are looking at comparative tables as the one seen in Figure 38.

Simulation	Total cost [€]	Cost_rep [€]	Cost_down [€]	Cost_insp [€]	Cost_wait [€]	Cost_transp [€]
Case 1	85862	21600	1231	1800	1231	60000
Case 2	37625	10800	615	800	410	25000
Case 3	67225	14400	615	1800	410	50000

Figure 38: Comparative table of cost results for different analyzed maintenance strategies.

### Grid plots

The concept of grid plots (Figure 39) allows the comparison of several variables at the same time for a multiple number of simulations. In the example shown, in the y-axis, the decision rule is compared with the inspection interval (x-axis). The scale color located to the right side refers to the total cost, and it allows a fast interpretation of the expected cost of the different possible combinations for the primary variables.

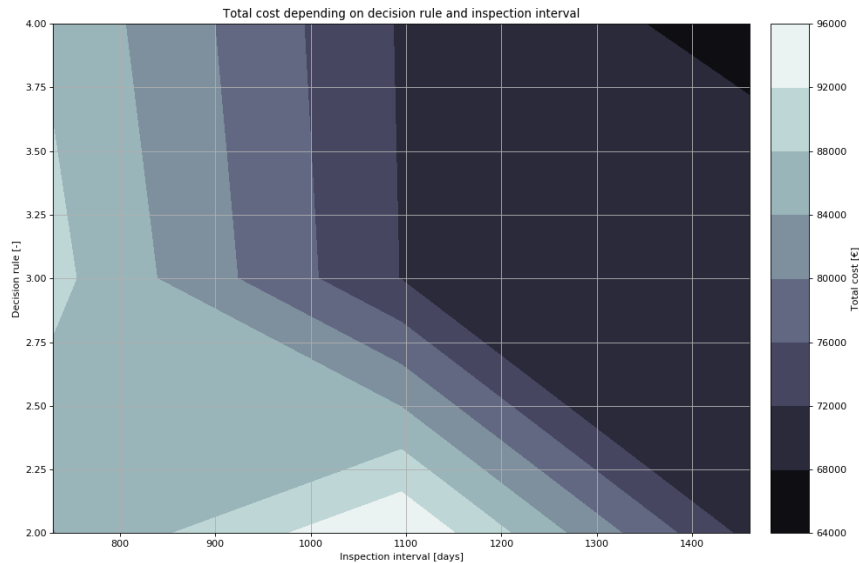


Figure 39: Grid for decision rule vs inspection interval, with a total cost in scale color.

## 7.13 Results interpretation

### Trends and parametric studies (user-controlled evaluation)

The CAR Tool is simulation blade life using assumptions and relevant input. For this reason, uncertainty is integrated in the CAR Tool results. But even if very accurate results are unreasonable to expect, the analysis and results from several strategies with different values of the input parameter will be able to show a trend which the user can be guided by when choosing the preferred maintenance strategy.

For the minimal viable product (MVP) of the CAR Tool a set of maintenance strategies where a number of input parameters differ between them, can be analyzed. The results will show trends in the resulting cost over blade lifetime, operation hours, number of failures or other failure criteria. A trend could be that increasing the inspection interval reduce overall cost. However, trends can be tricky, as shown in Figure 40.

1) Three analyzed strategies with different inspection intervals.



2) Continuous graph showing cost vs inspection interval.

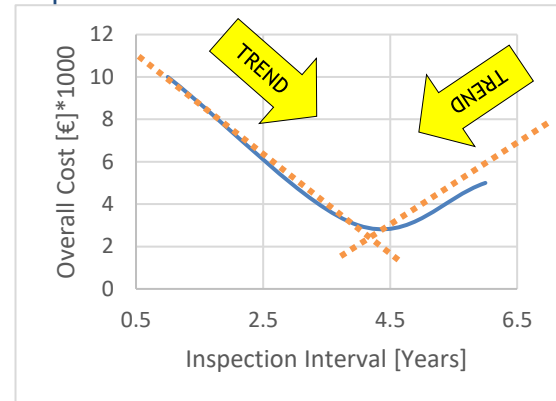


Figure 40: LEFT - A trend can be observed based on 3 analyzed maintenance strategies with different inspection intervals. According to the trend, increasing time intervals between inspection leads to a decrease in overall cost over the blade lifetime. RIGHT - The graph shows inspection interval vs overall cost. The optimal inspection interval has been found at the lowest point of the graph to be 4½ years. The trends suggest increasing or decreasing inspection intervals depending on the analyzed data and if it is for more or less than 4½ years inspection interval.

Sensitivity studies will show which parameters have the most effect on the results. Parametric studies will investigate which parametric values gives the optimal maintenance strategy. In Figure 41 three parametric studies are performed on top of each other working towards finding the optimal strategy.

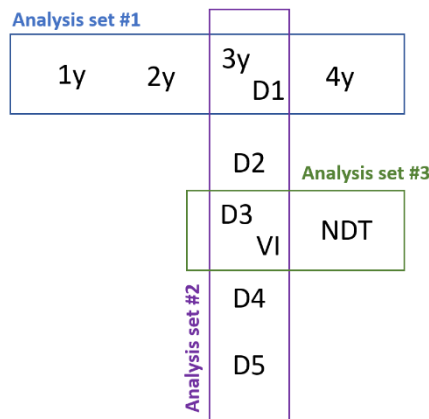


Figure 41: In analysis set#1 all parameters are the same except for variation in inspection interval, and an inspection interval of 3 years is found to be best. Analysis set #2 has the inspection interval of 3 years for all analysis but are introducing different decision rules. Decision rule 3 (D3) is found to be best. In analysis set #3 visual inspection hold up against NDT inspection method. Continuously the maintenance strategy has been improved.

The user will be looking for *trends* instead of *accuracy* by an intelligently interpretation of comparative analysis result. These trends will give a clear indication of the pros and cons of different maintenance options.

Which way leads to the mountain?

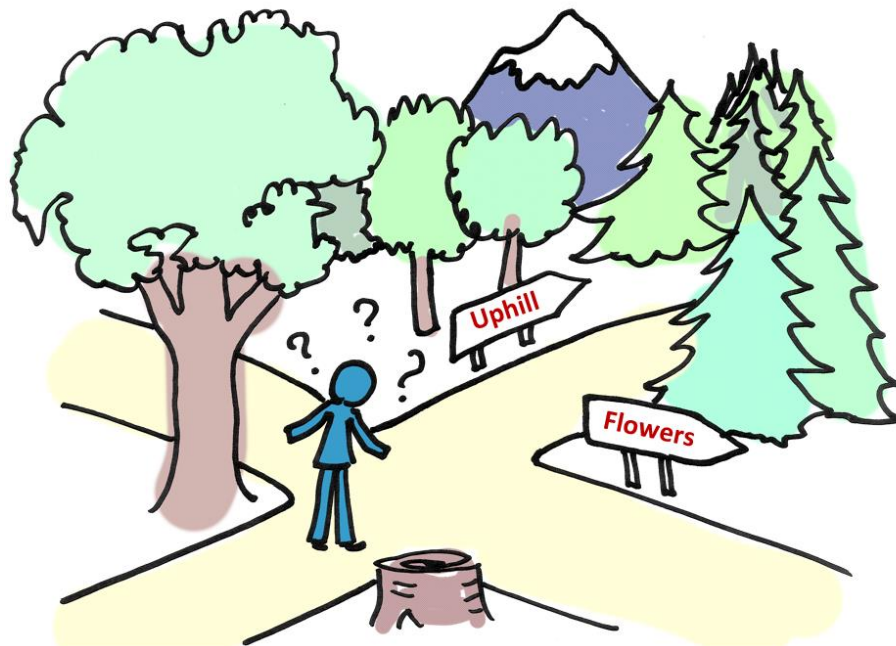


Figure 42: This forest hiker does not know the way to the mountain top but will likely follow the trend of going uphill where possible.

## 8 Transverse Cracks

In wind turbine blades, where composite materials are heavily used in manufacturing the blades and the two shells are connected through adhesive joints, prediction of failure and crack propagation is of great interest for the entire wind turbine industry. Initiation and propagation of cracks can be predicted using subcomponent and large-scale testing. The purpose of investigating crack development has been to provide relevant input to CAR Tool.

Previous EUDP Project, RATZ, led to understanding of the root cause and to validation of a hypothesis describing the physics behind transverse cracks initiation and development.

The hypothesis refers to a 2 stages development:

1. Stage 1: Debonding of core from face sheet (skin).
2. Stage 2: Excessive fatigue bending of the debonded face sheet (local buckling of the skin) leads to high interlaminar stresses causing crack initiation and development.

This section will present the use of large-scale testing and subcomponent testing to initiate a transverse crack.

## 8.1 Large-scale testing

The purpose of large-scale testing was to observe the crack growth on a 34-meter blade in the test facility of DTU. Firstly, a debond was manually created between the outer face sheet and core in the trailing edge panel on the pressure side, see Figure 43 large area covering this defect was rebuilt, creating the boundary conditions for the debond to further expand (debond propagation).



Figure 43: Defect introduced between the core and face sheet in transition zone area.

The damage was introduced in an area where the highest panel bending was measured when combined loading was applied (edgewise and torsional loads). This initiated the debond to propagate since the face sheet is subjected to additional localized bending which resulted in a transverse crack initiation. The idea was to investigate if the debond leads to crack propagation.

The large-scale test was planned in two phases:

- 1) A disbond under the face sheet (skin) was introduced and a superficial repair solution was applied. (Relative thin face sheet thickness). This simulates a patch repair solution.
- 2) The face sheet (skin) thickness is increased to a layup sequence (thickness) more adequate for medium blades sizes, keeping the 500mm disbond under the face sheet.

## 8.2 Subcomponent testing

Simultaneously with large-scale testing, two types of trailing edge panels are tested: One with a thin face sheet and other with a thick face sheet. Following fracture mechanics tests are carried out:

1. Tensile testing to characterize the face sheet material.
2. 4 Point Bending (PB) testing on the face sheet materials
3. Single Edge Notched Tension (SENT) tests on face sheet material

### Tensile test

Tensile testing is a technique where the sample is subjected to a controlled tension until failure. The properties measured of the material/sample from the test are tensile strength, breaking strength, and maximum elongation. Furthermore, fatigue tensile testing is carried out to identify fatigue initiation.

### 4-point bending test

4-Point Bend (PB) test is used to characterize the material subjected to pure bending loads (symmetric 4 PB).

### Single Edge Notched Tension (SENT) test

SENT test are used for testing fatigue and damage development in pure tension.

In the course of the project, laminate (assembly of layers of fibrous composite layers), composite beam and composite panel were tested using tensile, 4PB and SENT testing techniques.

For this, a comprehensive sub-component testing program together with Fracture Mechanics modelling was started with the purpose of generating simplified closed-form models that are easy to implement in probabilistic analyses. Different blade families, load conditions and operation environments will be used to identify an array of boundary conditions for testing.

The tests were carried out using a unique test setup specifically designed for fatigue propagation, suitable for multiple modes of loading.

The series of tests will be used to validate the numerical fracture mechanics against experiments by implementing the Fracture Mechanics models in Finite Element environment. As an output, the models will be used for higher scale validations.

Bending tests of trailing edge panels will be used for purposes such as characterizing the static and fatigue bending stiffness, fracture propagation rates as well as matrix cracking degradation, stiffness loss and fatigue limit.

The necessary trailing edge panels were delivered by Global Wind Service (GWS) as specified by DTU Mechanic.

Advances on the Fracture Mechanics and sub-component testing in the 1st phase were done using specifically manufactured samples, with the purpose of observing the phenomenon rather than getting accurate response. This phase concluded that there has to be a certain face sheet (skin) thickness in order to generate crack growth.

Phase 2 of the sub-component and large-scale testing refers to sub-component testing program continuing with real blade samples rather than specifically manufactured samples.

In phase 2 samples from the LM 58.7m blade were tested using the following:

- DCB-UBM tests for characterization.
- 4-point bending for validation on simple geometry.
- Characterization tests on glass fiber facesheet.

The purpose of this was to further advance towards the physical phenomenon found in real blades rather than a pure academic study.

A specific workshop dedicated to Fracture Mechanics took place in DTU Mechanical in Lyngby where the Fracture Mechanics group in LM took an active role in giving feedback and comments on the overall approach in respect to fracture mechanics usage in the CORTIR project.

### 8.3 Structural FEM studies

During the project, Bladena and DTU have been in a continuous dialogue regarding the exchange of boundary conditions of investigation. The purpose of exchanging boundary condition was to verify that the fracture mechanics model is working properly. First step is to verify the Fracture Mechanics model by obtaining similar results as the results obtained from the global FEM blade model where no debond/defect has been introduced. In Figure 44 the extraction of local boundary conditions in FEM is shown.

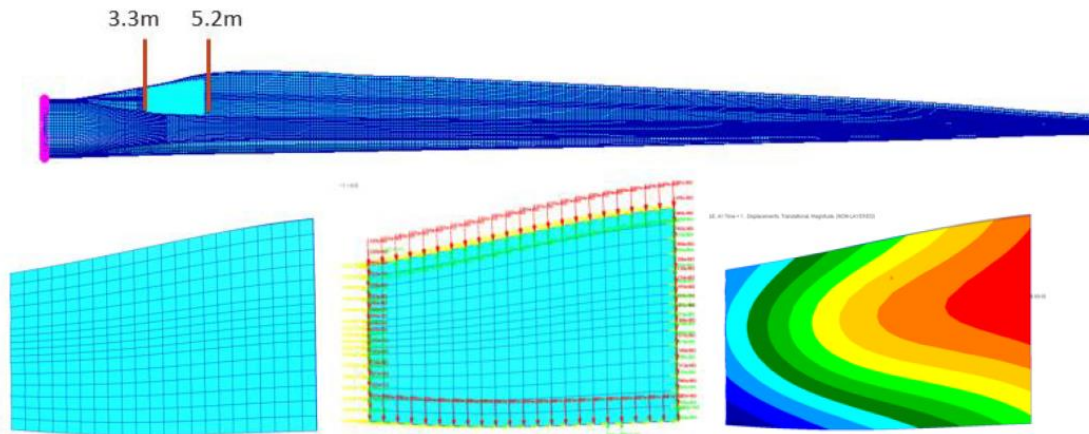


Figure 44: Extraction of local panel boundary conditions (displacements) from the global blade model. Top: Full FEM blade model of SSP34 with identification of investigated panel. Bottom from left: 1) Investigated panel. 2) Local boundary conditions along the edge of panel obtained from a global load case. 3) Deformation of panel due to local boundary conditions.

Initial global FEM blade models with debond between outer face sheet and core was made. These models and methodologies, in order to simulate a debonded area in the global FEM model, still need to be further discussed in order to determine validity. The initial global FEM models with a simulated debond at the investigated panel is shown in Figure 45.

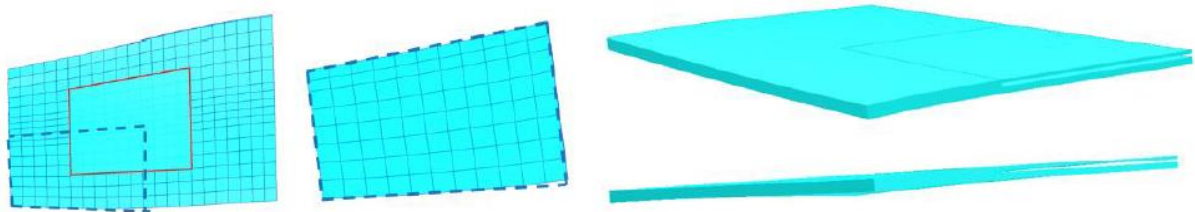


Figure 45: From left: 1) Investigated panel with a debonded area between the face sheet and core (red square). 2) Snip of investigated panel. 3) Illustration of gap/debond between face sheet and core.

Due to initiating a debonded area in the FEM model the model must take contact between face sheet and core into account. Focus has been on implementing the contact correctly by investigating and analyzing more simpler geometries in order to verify correct implementation. The effect of applying (and not applying) contact to the FEM model is shown in Figure 46.

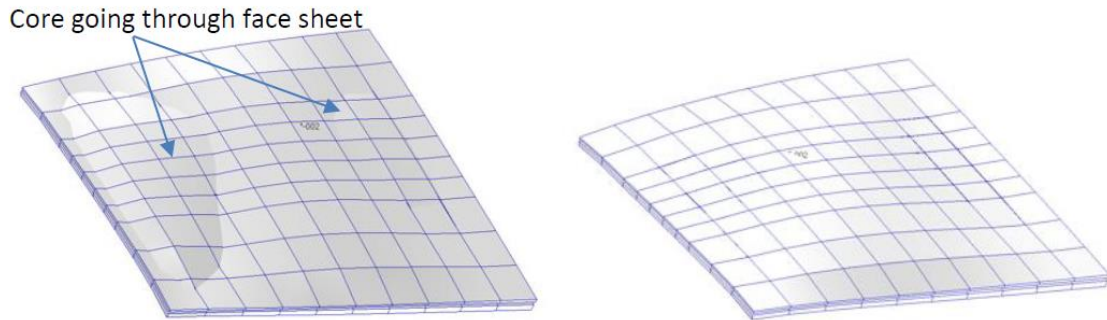


Figure 46: From left: 1) Debonded area without contact between the face sheet and core - the core is going through the face sheet. 2) Contact added to model and core is not going through face sheet.

By applying debond and contact in FEM changes the strain distribution at the debonded area and boundaries close to. In Figure 47, the contact forces on the core are shown as it is pressed against the face sheet in certain areas. Also, the longitudinal strain distribution of the investigated panel from 3.3m-5.2m is shown with a squared debond area.

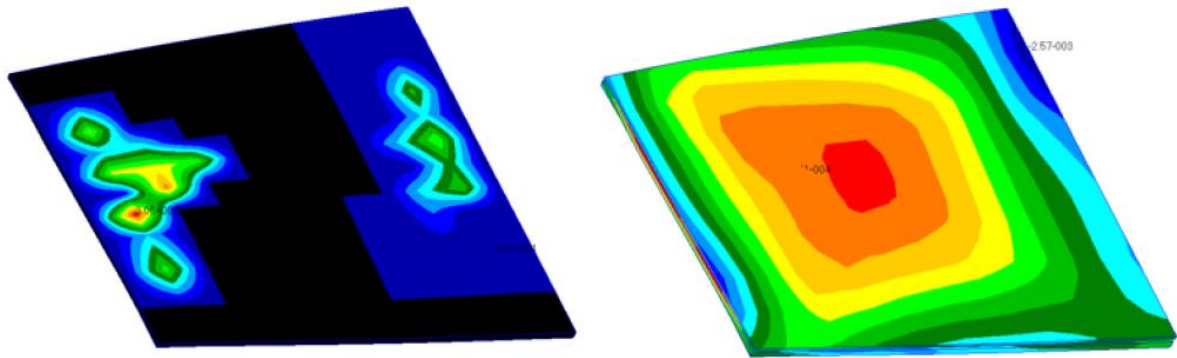


Figure 47: From left: 1) Contact forces on the outer surface of the core as it is pressed against the debonded face sheet at some locations. 2) Longitudinal strain distribution of debonded (squared) area. Red color indicates the largest strains.

From Figure 47 the longitudinal strain distribution of a debonded squared area is illustrated and the maximum is occurring at the center of the debonded area. Introducing debond areas of different magnitude, sizes, positions under various loads applied to the blade will affect the force distribution (strains and deformations) of the investigated panel. This will have a direct impact on the Crack Propagation Rate (CPR) function.

Moreover, the numerical studies and developments conducted by Bladena in the duration of the project have also focused on further developing the elastic instability approach, which is now used as an input to the CAR tool.

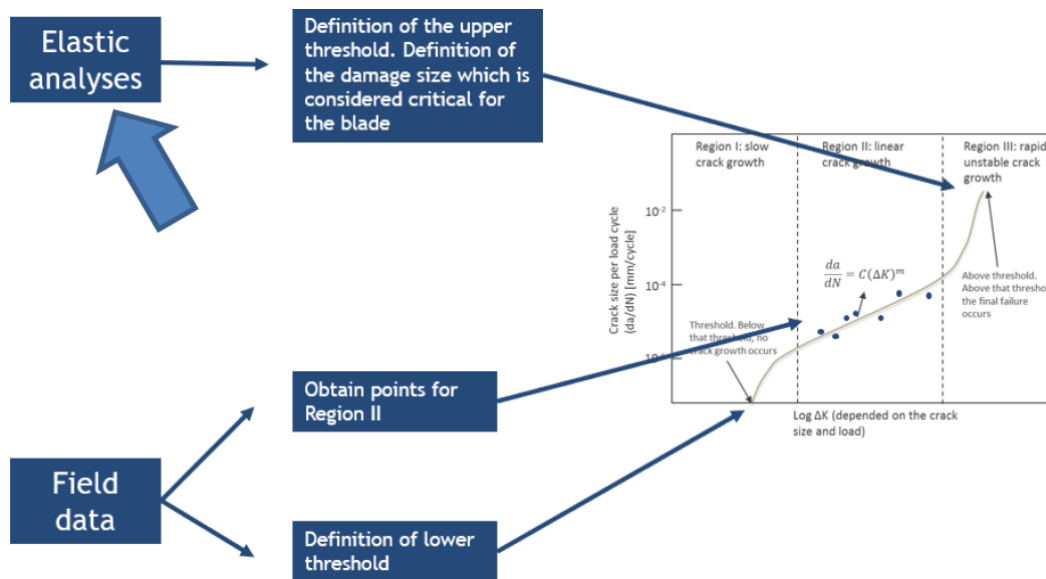


Figure 48: Overview and procedure of the elastic instability method

The scope of the elastic instability analysis is to provide information when structural damage is critical for the blade. Discussions of how to use elastic instability analysis together with the damage tolerance approach were initiated on the workshop 4<sup>th</sup> of June. In Figure 48, it is shown how the elastic instability analysis can be used to define an upper threshold of damage before it leads to the structure to become unstable and/or collapse. In Figure 48 the example is given for crack growth (e.g. transverse crack on a wind turbine panel). Using field data and reported transverse crack damages together with forthcoming obtained crack growth development in panel face sheets (based on sub-component test at DTU). The main idea is to be able to provide a well-defined estimate for the severity of the crack using the upper threshold obtained through elastic instability analysis - and give a technical opinion regarding the further development of the crack (if located in the stable region, where the *Paris Law* is assumed valid) and thereby also the effect on the lifetime of the blade.

For this, a new failure mode, which occurs more and more on blades in operation, is used as a case study. The failure mode is the disbonding of the shear web(s) from the spar cap in the load-carrying structure. It is a high-risk failure, as it affects the blade capacity to carry load.

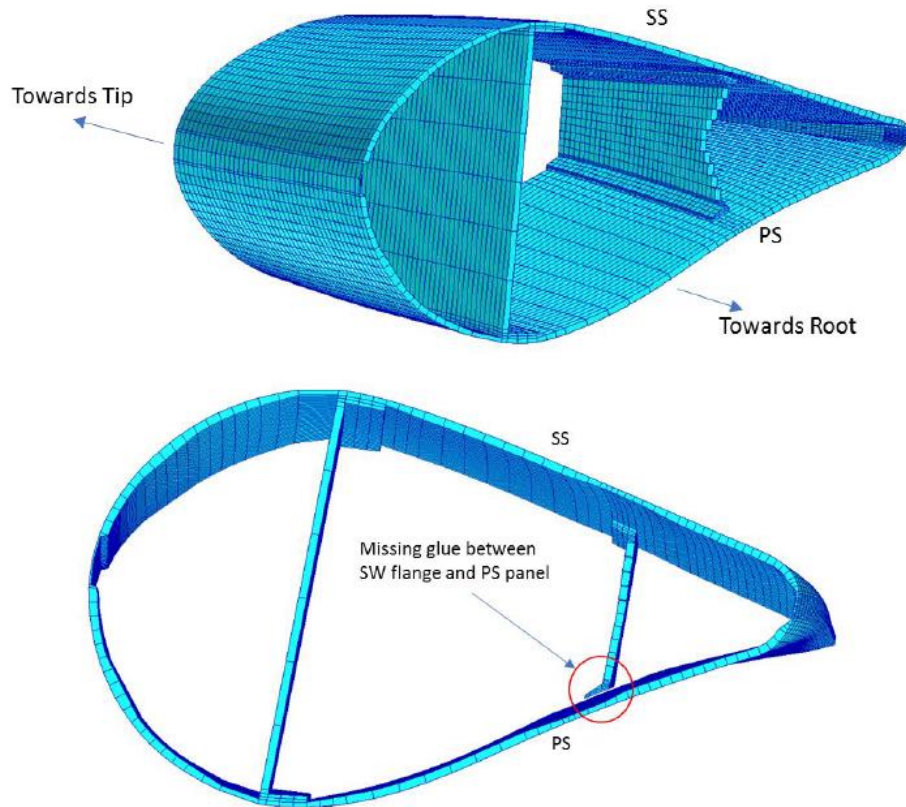


Figure 49: An aft. shear web disbond from pressure side panel at fishmouth region modeled using FEM. The aft. shear web start position is approx. 10m from the root.

In Figure 49 a FEM modeled blade section is shown with a simulated shear web disbond from the pressure side adjacent spar cap. The disbond has been created by removing the bondline/glue connecting the spar cap and aft. shear web. ‘Touching’ contact has been introduced between the aft. shear flange and pressure side panel in order to allow sliding between the two structures if they should come into contact during simulations. The length of the aft. shear disbond used in the initial FEM simulations is approximately 5m going from 10m to 15m towards the tip of the blade (blade length +60m).

The elastic instability analysis and method are presented and illustrated in Figure 50. First, the physical blade that is intended to be investigated for a structural damage (e.g. disbond of the shear web) is re-engineered and modeled in FEM. The blade is re-engineered as an ‘intact’ model meaning no damages/defects are introduced - this is the *reference model*. The purpose of the reference model is to compare results (deformations, strains, etc.) with a *defect model*. The defect model is a FEM model based on the re-engineered reference model; however, a certain damage(s)/defect(s) is introduced in this model. The elastic instability analysis is then performed by comparing the two models (reference vs. defect) in terms of different global- and local results under the same loading condition.

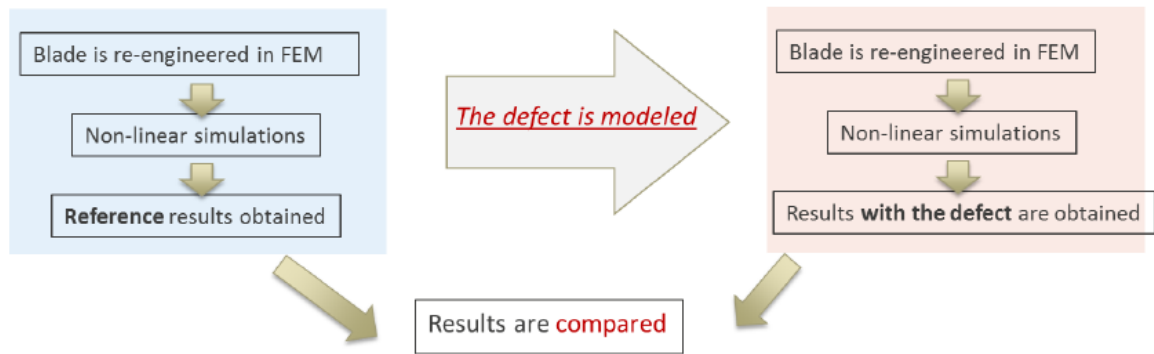


Figure 50: Overview and procedure of the elastic instability method.

Initial FEM studies regarding elastic instability have been conducted for a 5m aft. shear web disbond as illustrated in Figure 49. The elastic instability analyses have mainly been focusing on the global response (tip deflection, root torsional moment, etc.) differences between the intact blade and the damaged blade. Studies of more localized effects (bondline peeling stresses and panel deformations) due to damage introduction have been initiated. Below in Figure 51, the flapwise tip deflection is shown for the reference model and the model with 5m aft. shear web disbond (Disbond 1).

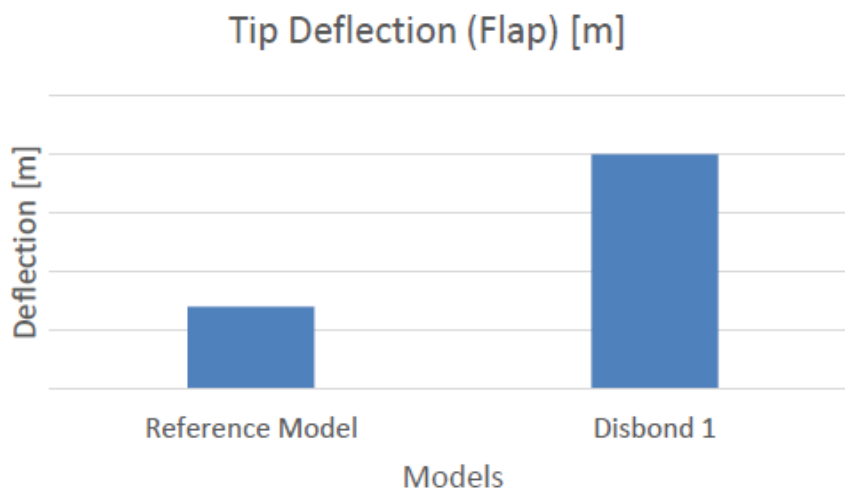


Figure 51: Flapwise tip deflection comparison between Reference Model (intact blade) and Disbond 1 Model (damaged, 5m aft. shear web disbond)

It is seen from Figure 51 that an aft. shear web damage going from 10m-15m (from the root) of a +60m blade has an effect of the global stiffness and response of the blade. This methodology (elastic instability) has a lot of potential when it comes to providing technical opinion on certain damages/defects that are present on blades in operation.

## 9 Development of the tip solution

### Design and implementation

The purpose was to develop a new structural enhancement product for damages occurring at the tip region of the blade. The product will work either as a temporary or a long-term reinforcement to avoid damage propagation leading to extreme failures as well as reduce downtime of the turbine and thus keeping the levelized cost of energy (LCOE) down. Figure 52, shows the stages involved in the development of the product.

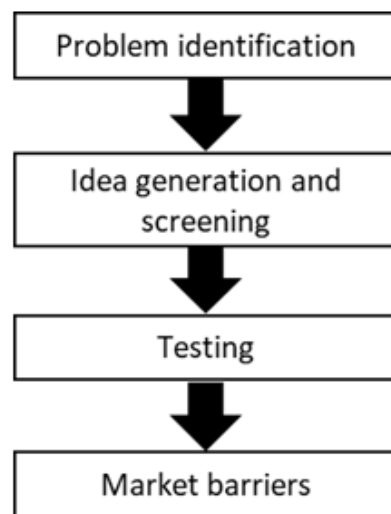


Figure 52: Process diagram for product development

### Problem identification

A study was conducted to determine the effects of lightning strikes on the blade of a wind turbine by (ECC) which resulted in a broad understanding of lightning strikes and damages caused by lightning. ECC has developed a Gap-Energy-Release (GER) approach and a schema to estimate the pressure variation. The GER approach is a technique using the time domain to calculate the energy release for a given spark gap and current distribution and can be used to calculate the overpressure propagation within a given blade profile.

Once the overpressure is estimated, Bladena, in collaboration with ECC, has researched different types of materials that can perform under extreme conditions and are able to resist high temperatures. ECC created a test-setup able to simulate the effect of the shock wave overpressure (rapid increase in air temperature) on the material inside the blade. The materials which exhibited excellent characteristics (in terms of mechanical properties, wear of the material, ability to manufacture, and

cost) were sent to ECC for testing. Meanwhile, Bladena had been working on developing a preventive and interim solution for the tip opening issue of the blade.

### Idea generation and screening

The primary function of the product will be to protect the structure, while maintaining aerodynamic and noise requirement.

Brainstorming resulted in the following ideas:

Concept	Function
Installation of another conductive path around the blade.	It will provide an area of protection for the vulnerable section.
Use of conductive paint around the tip region.	It will provide a conducting path to carry current to the conductor and hence to ground.
Reinforcing the structure with glass fibre struts.	Installing the bars would provide support to the adhesive at the tip.
Filling the tip region with expandable foam.	To reduce the moisture in the blade and maintain dryness.
Shock-absorbing material inside the tip of the blade.	To reduce the blast wave effect.
Use of adhesive.	Joining the tip shells with adhesive after it has been opened by a lightning strike. It can also be combined with glass fibre bars for extra strengthening.

Table 3: Ideas generated

After a thorough discussion with the partners and technical experts, a solution for the tip was finalized from the different possibilities. It was decided to proceed with a mechanical quick-fix solution, using glass fiber bars to prevent the blade's tip

opening issue and to keep the two shells intact. The following were the main reasons which lead to the final decision:

- 1) Every manufacturer uses different material in producing blades and solution which works for one blade might not necessarily work for the other.
- 2) The solution should be easy to install.
- 3) It should not interfere with the existing system.
- 4) It should be a mechanical quick fix solution.

Thus, taking all the factor into consideration, glass fiber (Durostone EPR-S1) struts were finalized as either interim and/or preventive solution.

### Material Testing

The reinforcing strut developed by Bladena is currently manufactured from glass fiber reinforced polymer Durostone EPR-S1 supplied by the German company Rochling. The material is a good fit for the tip solution since it combines a low electrical conductivity with high mechanical strength. However, the material has only been tested under quasi static loading i-e. at low strain rates. Since the struts are subjected to high dynamic loads during lightning strike, therefore the response of the struts under high loads is of great interest.

### Material testing method

When a material is subjected to rapid loading resulting in high strain rates which must be taken into consideration. Table 4 shows the various methods used to measure the investigate the material response of materials under different strain rates.

Strain rates [ $s^{-1}$ ]	State	Test machines/Techniques	Typical physical scenario
$10^{-4} - 10$	Static/Quasi-Static	Mechanical testing machines e.g. Instron	Extrusion
$10 - 10^2$	Quasi-static	Hydraulic testing machines	Sheet metal forming operations
$10^2 - 10^4$	High Strain rates	Hopkinson bar techniques	Forging, bullet impacts, explosion
$10^4 - 10^6$	Very high strain rates	Flyer-/Taylor impact-/Pressure	Plastic explosives, rocket weapons

Table 4: Table showing various testing methods and techniques for different strain rates.

In this case, Hopkinson bar technique is employed for testing the glass fiber reinforced composite material which is used in manufacturing of the struts. Appendix E provides the properties of the material as described by the manufacturer.

## Results:

The results obtained for durastone EPR-S1 are presented in this section. The high strain rate torsional tests of the Durostone EPR-S1 samples involved measuring the fracture stress of over 30 test samples at strain rates ranging from approximately 750/s to 5,000/s. The results of these tests, plotted with the fracture stresses measured at low strain rates, are shown in Figure 53.

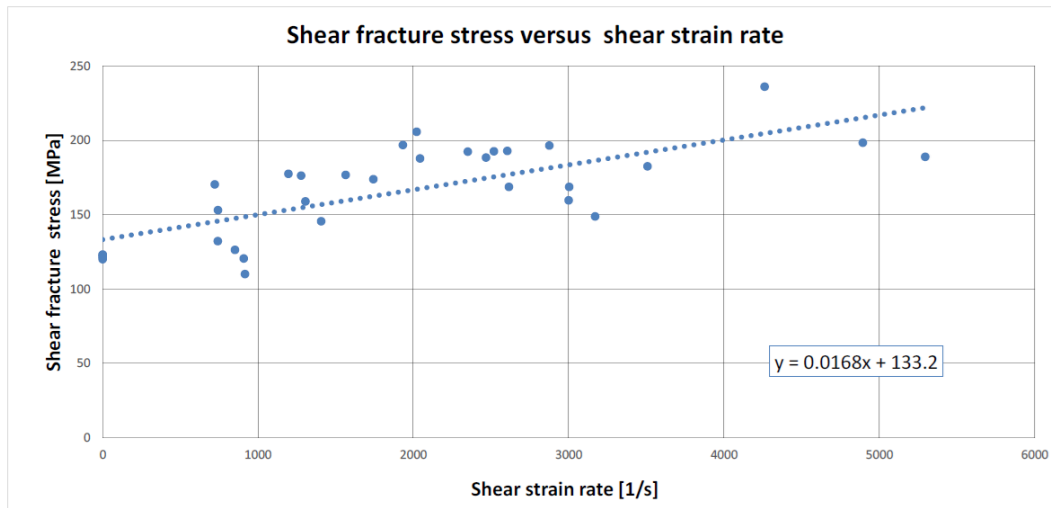


Figure 53: Plot showing the reliance of fracture stress on strain rate.

In Figure 53, the slope of the fracture stress-strain rate curve is approximately 0.016 indicating only a slight increase of shear stress with strain rate i.e. the fracture stress of the Durostone EPR-S1 test material exhibits a low strain rate sensitivity.

Shear strain rates of approximately 5,000/s correspond to the upper limit of the shear strain rates that can be achieved using the torsional split Hopkinson bar used for the tests described in this report. In view of the high amplitude impact loads resulting from a lightning strike determining the strain rate at which adiabatic shearing occurs in the Durostone EPR-S1 would be of great interest and should be determined in the future, possibly by developing methods to extend the strain rate range of torsional Hopkinson bars.

The torsional fracture stress data obtained through experiments was then converted to tensile stress fracture data based on Von Mises yield criteria and the hypothesis of incompressibility of solid (Keriguinas 1977)<sup>2</sup>.

$$\sigma_{von\ mises} = \sqrt{3} \times \tau \text{ and } \dot{\epsilon}_{eq} = \frac{\dot{\gamma}}{\sqrt{3}}$$

Until proven otherwise, it is assumed that same ratio applies to the Durostone EPR-S1 material, as further investigation is outside the scope of this project.

It should therefore be noted that a factor of  $\frac{1}{\sqrt{3}}$  is used to convert torsional strain rates into tensile strain rates. It can be seen from Figure 54, that tensile strain rates resulting from this conversion range up to a maximum of approximately 3,000/s, meaning that the Durostone EPR-S1 can withstand tensile loads at strain rates up to 3000/s.

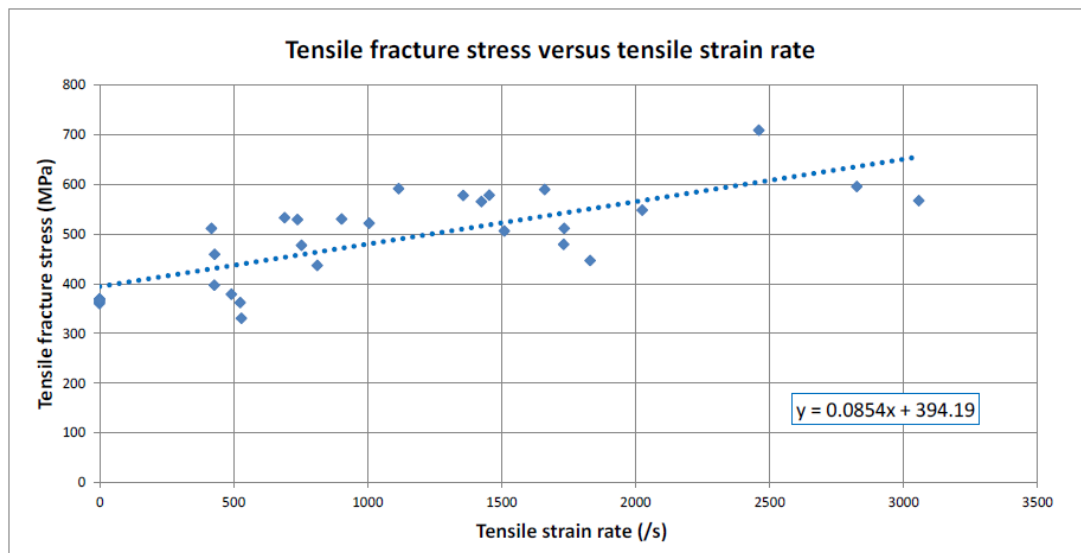


Figure 54: Tensile fracture stress versus tensile strain rate.

The material was tested at both low strain rates and high strain rates. The low strain rate tensile tests showed that the tensile fracture strength of the Durostone EPR-S1 test material was approximately 369 MPa which corresponds reasonably closely with the tensile strength value of 400 MPa quoted in the data sheet supplied by the manufacturer. Low strain rate torsional test showed that the shear fracture strength of the Durostone EPR-S1 material was approximately 122 MPa.

<sup>2</sup> Further information is given in: The Relationship Between Tensile Strength and Shear Strength in Composite Materials Subjected to High Strain Rates, by Chi-Yuen Chiem and Zeng-Gang Liu, published in April 1988 in the Journal of Engineering Materials and Technology.

Under high strain rates, the Durostone EPR-S1 only showed a small increase in the ability to withstand impact loads. However even at shear strain rates of over 5,000/s (corresponding to tensile strain rates of approximately 3,000/s) the Durostone EPR-S1 material shows no signs of the onset of adiabatic shearing (failure occurring due to deformation under high strain rates) making it particularly well suited for the manufacturing of wind turbine blades support struts.

## Structural Simulations

Structural simulations using geometric non-linear Finite Element method (FEM) were used to study the phenomenon and to verify the feasibility of the proposed tip solution. In Figure 55, the “problem” is defined in FEM where TE panels in the tip region are loaded out-of-plane using a pressure distribution load.

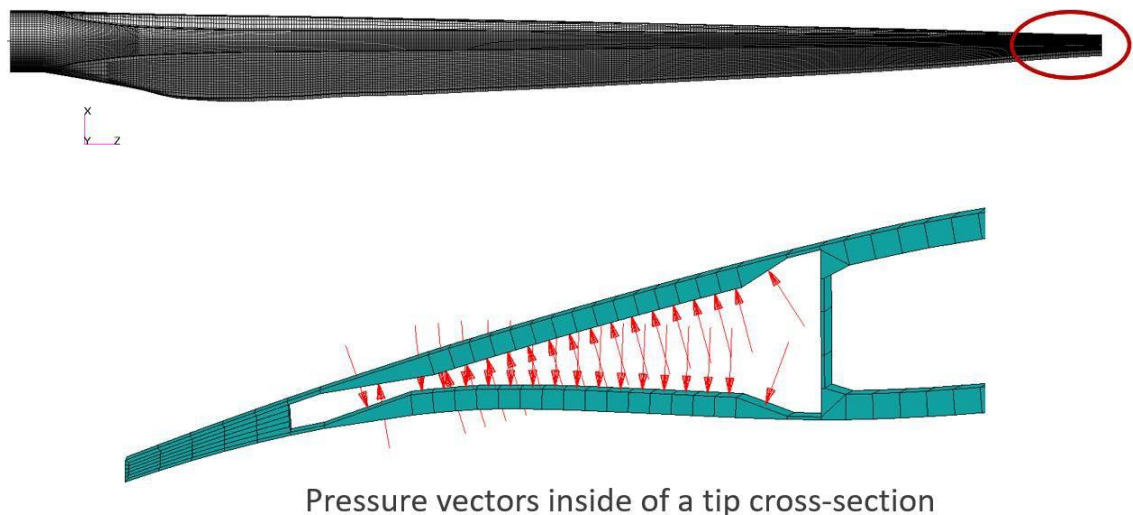


Figure 55: Structural simulations using geometric non-linear FEM.

Geometric non-linear FEM simulations were carried out with the scope of making a comparative analysis between a situation *with* and one *without* the struts installed in the blade, see Figure 56: Comparison analysis of a situation with and without Struts at the tip region. From left to right. Figure 59 a) Simulation without struts. Figure 59 b) Simulation with struts.

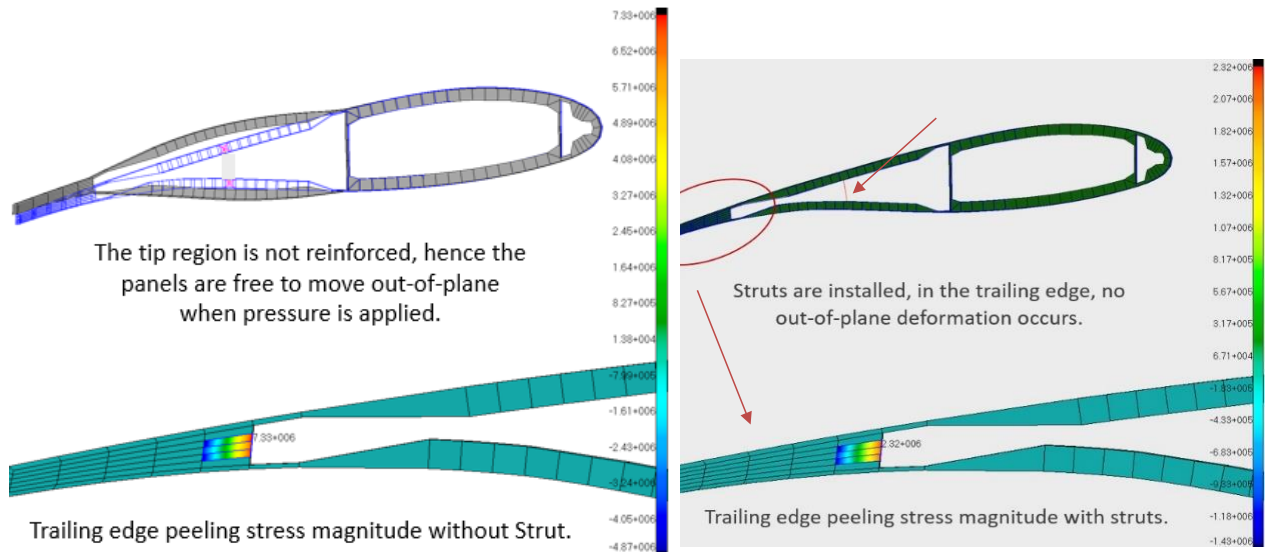


Figure 56: Comparison analysis of a situation with and without Struts at the tip region. From left to right. Figure 56 a) Simulation without struts. Figure 56 b) Simulation with struts.

In Figure 56: Comparison analysis of a situation with and without Struts at the tip region. From left to right. Figure 56 a) Simulation without struts. Figure 56 b) Simulation with struts. the effects of installing the tip solution are shown. There are two main findings:

- 1.) The tip solution reduces the peeling stresses in the adhesive bondlines adjacent to the installation location.
- 2.) The tip solution limits the out-of-plane deformation of the TE panels.

### Peeling stress reduction

Peeling stresses in the adhesive bondlines were post-processed for the comparative analysis. The results have verified the assumption that when struts are installed in the blade and internal pressure is applied in the tip region, the peeling stress level in the TE adhesive bondline is reduced by 70%.

The peeling stress reduction translates directly into reduced risk for TE opening when this kind of load situation occurs.

### Out-of-plane bending of panels reduction

Localized out-of-plane bending on the TE panels is noted when the struts are installed. This indicates that the proposed tip solution is an excellent choice for preventing damages(cracks) on the panels themselves, as it removes the root cause.

**Mention:**

The comparative analysis technique is an excellent method to tackle the limitations of elastic FEM when dealing with composites. The technique relies on studying the effect of a single parameter change, rather than to predict when failures occur.

It is well known that the biggest limitations of elastic FEM when dealing with composites is that there are no reliable failure criteria, hence failures cannot be predicted.

In the current analysis, the effect of reducing the out-of-plane deformation of the TE panels due to the Struts installation was considered as *the variable*.

In addition, the direct of the tip solution installation is the reduction of the peeling stresses in *all* adjacent adhesive bondlines, see Figure 57.

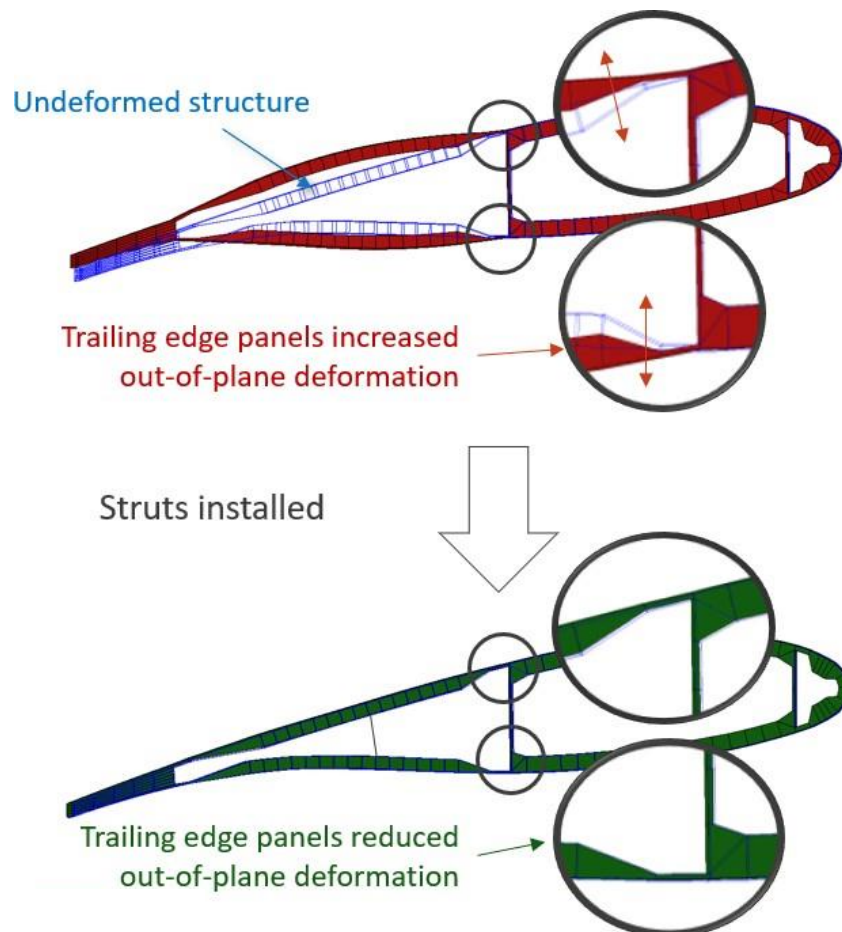


Figure 57: Reduction of TE panel out-of-plane deformation will have a direct impact on reducing the peeling stresses in all adjacent bondlines.

In Figure 57 the impact of the strut solution to adjacent bondlines is clearly visualized.

## 9.1 Laboratory Test

The reinforcement strut was tested in the field at a small scale to validate the functionality of the struts. Comparison testing was carried out on 1-m Blade's tip specimens. Firstly, a specimen was tested to find the maximum amount of energy required to completely separate the suction and pressure sides. Afterwards, comparison testing was performed.

### Test Specimen

- 1-meter blade tip specimens.
- 2 specimens without the struts and one with the struts.
- Struts were installed by making a 14mm drill hole and using 16mm machine tap to create thread inside the holes. Adhesive was applied in the holes and the struts were screwed in. A total of 4 struts were installed.



Figure 58: Test Specimens utilized for testing. All specimens were of length 1 meter. Two specimens without the struts were tested and one with the struts.

### Procedure

The goal of the test was to assess the benefits of the reinforcement struts on the tip specimen compared to the specimen without the struts. The experiment was conducted in the field where explosive material was placed inside the specimens and detonated to replicate the shockwave phenomenon inside the tip cavity.

## Results

Table 5 shows the results from the tests.

Specimen nr	Model	Energy discharged [KJ]	Result	Picture
1	Without Strut	102	Complete separation. Specimen split in three pieces.	
2	Without Strut	3	Trailing edge opening of upto 50mm.	
3	With Strut	3	Trailing edge opening of upto 30mm.	

Table 5: Test Results with and without the struts installed.

Table 5 shows the test results from the field experiment. The results of the experiments with and without the struts are visible. Comparison test showed that the reinforcement struts added additional strength to the specimens, trailing edge opening is reduced by 40 % with the struts as well as pressure and suction side shells stay intact due to the strut connection.

## 10 Utilization of project results

Throughout the project, solutions to wind turbine blade issues have been created, and large-scale test methodology has been investigated in collaboration with partners. In addition, an operation and maintenance tool CAR Tool has been developed to support the WTOs in developing inspection and maintenance strategies.

This section presents how the project results will be utilized and benefit the company commercially, both immediately and in the long run.

### 10.1 Commercial perspectives of the Value chain

The close collaboration with partners in the CORTIR Project has given a chance for Bladena to increase the understanding of the industry and the needs different partners might have. In recent years, Bladena has worked with the blade's life from project development to lifetime extension, see Figure 59. Each phase has its challenges, and Bladena has developed and structured an extensive set of Advisory Services to apply for each phase. By listening to and understanding the customer's situation, Bladena can describe the actual need and understanding what needs to be done. With the Advisory Services in mind, Bladena can offer knowledge and solutions to the customer's issue.

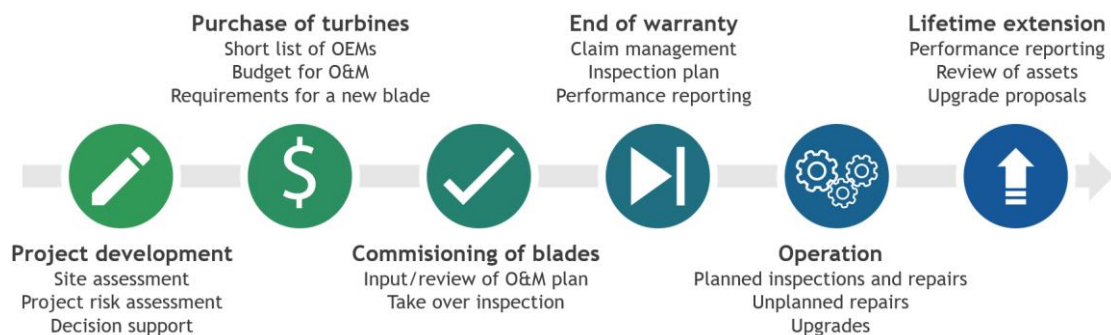


Figure 59: The process diagram shows the phases of a wind turbine from the project development to lifetime extension. Bladena has a structured approach to Advisory Services, which can be applied under each phase according to customer needs.

The set of advisory services has been upgraded and implemented in the company's new business model. Through a process of expert consultations, a range of services have been introduced fitting in with the customer-focused culture. Some examples of the services include defect analysis, damage assessment, root cause analysis (RCA), field measurements, or the increasing lifetime of the blade. The advisory services intend to grow the Bladena business.

## 10.2 Commercial perspectives of the CAR Tool

The CAR Tool is proven to be an essential part of the Bladena's business approach. The CAR Tool is already implemented in many of the above-mentioned Advisory Services as a tool. The learnings about Risk and the developed way to handle Risk will be applied directly with CAR Tool analysis. By a direct risk assessment of operational options, decisions, and investments, CAR Tool can be used as a tool to create strong business proposals or to identify possible value propositions together with customers.

A future version of the CAR Tool with the capability of including all the most frequent blade failure modes and advanced loading is attracting a lot of interest from the industry. The CAR Tool can, in principle, accommodate all that and more, but the resources to upgrade the CAR Tool to a more advanced level must be found and justified.

## 10.3 Commercial perspectives of the tip solution

The product developed in the project will undergo proof of concept in order to demonstrate the feasibility of the product. Once it has passed the demonstration phase, an effective marketing strategy will be developed to ensure that the product is brought to the market and revenue can be generated from the product.

# 11 Project conclusion and perspective

The Cost and Risk (CAR Tool) tool has been developed over the project period from January 2019 to March 2021 to support the decision-making in operation and maintenance strategies and eventually contribute to the business improvement of the entire value chain. The project has resulted in the development of CAR Tool minimal viable product where only one failure mode of the wind turbine blade is considered, which is transverse crack in the max chord area. The CAR Tool is based on two major research areas; Fracture Mechanics and Cost and Risk models, which are developed in collaboration with the Technical University of Denmark (DTU MEK) and Aalborg University (AAU BUILD).

Furthermore, several workshops and seminars were held during the project, where the whole value chain took part. Through the project, partners in the project, consisting of Bladena, Universities, G2D, ECC WTOs, OEMs, ISPs, and insurance companies have worked together successfully. Additionally, the foundation of strong communication between the universities and the industry was established. Future research topics were discussed as well as recognizing the need for a cost optimizing tool. Moreover, the damage growth propagation phenomenon was investigated by means of sub-component testing and large-scale testing. The breathing/pumping

behavior of the gauge zone is evaluated with an implemented artificial debond initiated between the outer face sheet and core material.

The following sections will present the main results achieved in the individual areas of the project.

## 11.1 Value Chain Conclusion

The ambition to create closer collaboration between WTOs, OEMs, ISPs, and insurance companies (and certification bodies) has been fulfilled. In the many workshops and seminars, important issues have been discussed, and a shared understanding has been reached. Topics agreed and understood have been added to the CORTIR Blade Handbook. Communication between universities (DTU and AAU) and the industry has been very fruitful. There is a common understanding of the future direction for research activities, e.g., future perspectives for the CAR Tool.

During the project, the question about liability has been investigated. Blade damage can fall in different categories that will affect the liability level and insurance options see Figure 60.

CATEGORY	DESCRIPTION	LIABILITY IN WARRANTY	LIABILITY OUTSIDE WARRANTY	WTO INSURANCE OPTIONS
<b>WEAR AND TEAR</b>	Natural and inevitable degradation of the blade due to operation as per the operational procedure.	WTO	WTO	O&M cover, but only to cover unexpected peaks in cost.
<b>OPERATION</b>	Damages due to operation outside operational manual, faulty maintenance/inspections (or lack of), and faulty repairs.	Faulty operation: WTO Other: OEM	WTO	None.
<b>QUALITY</b>	Quality issues in material, workmanship, production methods, transport, storage and installation.	OEM	WTO	Extended Warranty and/or O&M Cover. Business interruption. Serial defects will only be covered until it is realised that they are serial defects. If serial, regress towards OEM.
<b>DESIGN</b>	Either defects due to faulty configuration/selection of turbine or serial defects.	OEM	OEM	Latent Defects and Business interruption. Regress towards OEM.
<b>ACT OF GOD</b>	Lighting, flooding, extreme weather	WTO	WTO	All risk and business interruption.
<b>ACCIDENT</b>	Any accidental damages to assets.	WTO	WTO	All risk and business interruption.
<b>WILFUL</b>	Theft, vandalism, sabotage, terrorism	WTO	WTO	Operator's risk and business interruption.

Figure 60: Wind project liabilities and insurance coverage options, p.101 in the CORTIR Blade Handbook.

The insurance companies send out loss adjusters to investigate blade damages, leading to an understanding of which category the damage falls in. If the damage is shown to fall in a different category than first assumed, this can mean a liability shift.

Bladena, under the developed Advisory Services, has several offers to investigate and explain how come damage can be found on a blade. These services are valuable for WTO's who want to understand how come they experience damages or failures and perhaps want to know the risk of experiencing many more damages of the same kind in their wind park if preventive action is not taken.

### Knowledge sharing platform for the wind turbine owners

Throughout the development process, the WTOs have shown a high interest in the CAR tool. All external meetings have attracted great participation from the entire value chain. They have resulted in valuable inputs from the WTOs (the end-user). Also, the partners have been providing profound data and knowledge at all meetings and seminars. This has led to an advanced innovative technology platform. CAR Tool has been developed to fit the industry's needs perfectly.

Real-life cases simulated in CAR Tool were presented at the meetings. Here the partners were able to see what output the CAR Tool gives after analyzing a scenario. These outputs would guide the operators to plan their maintenance and eventually help them reduce their OPEX. This got all the WTOs' interest, and they are eager to try out the tool.

Even though there have been challenges such as COVID-19, the tool's development went great, and all milestones were reached in time.

## 11.2 CAR Tool Conclusion

During the CORTIR Project Bladena, AAU and DTU have developed a decision support tool covering cost and risk, called CAR Tool. The CORTIR project aimed to be ready at the project end with a working tool to evaluate different maintenance strategies for wind turbines and the ability to compare the pros and cons. An obvious con is higher cost, but the user might also consider the strategies' level of risk.

As a result of the project, the CORTIR partners will have a chance to visualize the CAR Tool's potential benefits on the decision-making. The results will involve maintenance strategies that can be preventive, scheduled, risk-based, or corrective. I.e. corrective maintenance can lead to disputes between WTOs, OEMs, and insurance companies since the corrective maintenance is based on the principle of Run to Failure. Based on a wide range of different scenarios, and decision alternatives, the CAR tool will propose the most cost-efficient wind turbine operation and maintenance execution options, using reliability modeling, damage growth rate modeling, risk

management and more. This will benefit the whole value chain, minimize the number of disputes over failures on blades, and keep the LCOE minimum for the WTOs.

## Risk, uncertainty, and decision-making - The CAR Tool “Philosophy”

Bladena has together with partners through workshops and seminars and structured investigations and try-outs of the CAR Tool principle. With applied theory, learned much about risk assessment and how to respond to risk.

Different parties might wish to apply a different risk profile in their management of wind turbine parks. A *risk profile* can be seen as a willingness to take the risk. Some businesses might be willing to take more risk for the chance of bigger gain, but there is also the chance of more significant loss. This is because precaution can be taken, or if the event happens, a plan can be already in place, or at the very least, the event will not come as a surprise if it happens.

All values and parameters considered have some degree of uncertainty. Even the fact that some aspects of reality is represented with a parameter and some are not (e.g. aging of the blade is not represented) offers uncertainty. Of course, when the input has uncertainty, the same can be said for the output. The way to handle uncertainty lies in the comparative method of evaluation results and looking at trends forming when one parameter value is changed. The method assumes equal uncertainty for all similar analysis legitimizing the direct comparison of results and the ability to conclude for which choices or maintenance strategies cost and risk are the lowest.

## Decision Support Tool

The current MVP version of the CAR Tool works as a decision support tool mainly intended for the WTOs. Based on output results the user can compare the evaluated maintenance strategies. The tool is currently able to provide a wide set of figures and tables in relation to: main sources of expenses, risk and cost of each maintenance strategy, risk and probability of repair at each of the default damage categories, economic indexes like Net Present Value (NPV), Internal Rate of Return (IRR) and Payback Time (PBT), and cumulative cashflows. Some of these results are shown in the following figures:

Simulation	Decision rule	Insp. interval [day]	Total cost [€]	Δ (Total Cost) [%]	Final risk	Δ (Final risk) [%]	IRR	PBT	NPV
Case 1	2	385	€291,450	0.0	189,268	0.0	0.26	3.97	€1,093,989
Case 2	3	730	€65,921	-77.0	39,907	-78.0	0.28	3.58	€1,205,463
Case 3	5	730	€25,671	-91.0	15,967	-91.0	0.28	3.57	€1,230,843

Figure 61: Final comparison table with risk, cost and economic indexes per strategy. This table can be understood as the most relevant one for the current MVP CAR Tool as in a visual and fast way, it allows to identify the main differences between the studied maintenance strategies.

Simulation	Total cost [€]	Cost_rep [€]	Cost_down [€]	Cost_insp [€]	Cost_wait [€]	Cost_transp [€]
Case 1	85862	21600	1231	1800	1231	60000
Case 2	37625	10800	615	800	410	25000
Case 3	67225	14400	615	1800	410	50000

Figure 62: As an integrated part of analysis in CAR Tool costs are found for the different events during the simulated blade life. In this case the cost contributions are shown on the main posts; Cost of repair, cost of downtime, cost of inspection and cost of waiting for turbine access. But the cost can just as easily be broken down to smaller sections, e.g. within the cost of repair both the cost of salary to workers, and the cost of renting a ship for offshore repair, are considered.

	Simulation	Case 1	Case 2	Case 3
Overall risk	Overall Risk P50	185,268	39,907	15,967
	Overall Risk P10	185,268	39,907	15,967
	Overall Risk P90	185,268	39,907	15,967
Risk DC1	DC1 Risk P50	-	-	-
	DC1 Risk P10	-	-	-
	DC1 Risk P90	-	-	-
Risk DC2	DC2 Risk P50	65,985	-	-
	DC2 Risk P10	65,985	-	-
	DC2 Risk P90	65,985	-	-
Risk DC3	DC3 Risk P50	10,515	0	-
	DC3 Risk P10	10,515	0	-
	DC3 Risk P90	10,515	0	-
Risk DC4	DC4 Risk P50	0	15,957	-
	DC4 Risk P10	0	15,957	-
	DC4 Risk P90	0	15,957	-
Risk DC5	DC5 Risk P50	0	0	8,170
	DC5 Risk P10	0	0	8,170
	DC5 Risk P90	0	0	8,170
Collapse Risk	Collapse Risk P50	0	0	0
	Collapse Risk P10	0	0	0
	Collapse Risk P90	0	0	0
		DR:2, Insp.Int: 12 months	DR:3, Insp.Int: 24 months	DR:5, Insp.Int: 24 months

Figure 63. Risk distribution by damage category and by maintenance strategy. Values for the P10, P50 and P90 are provided as an indication of the expected uncertainty. In the example shown above, only one simulation has been computed by maintenance strategy, therefore, there are no differences between the percentiles P10, P50 and P90.

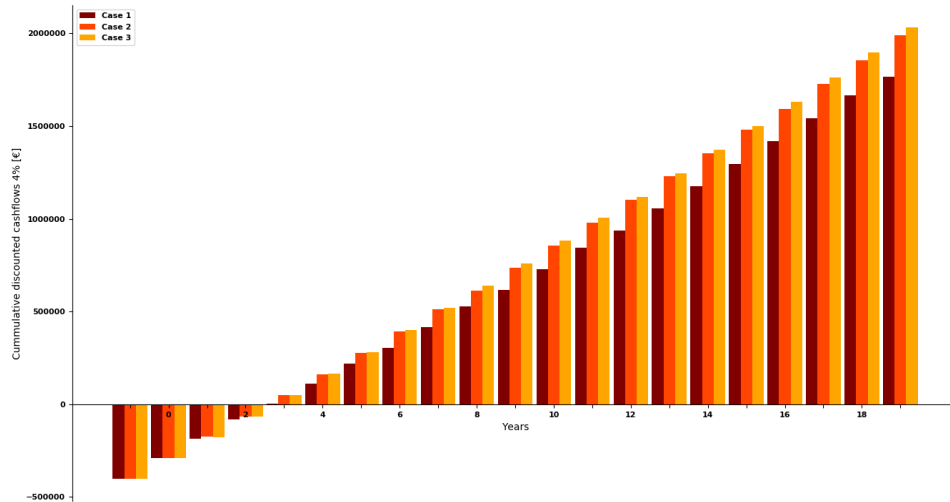


Figure 64. Cumulative discounted cashflows per maintenance strategy representing the expected economic balance for the users during the simulated years (20 for the example above)

## The CAR Tool MVP - User-friendly software tool

The CAR Tool methodology is built upon the main understanding that:

$$RISK = CONSEQUENCE * PROBABILITY$$

where *CONSEQUENCE* is measured by “cost” and *PROBABILITY* is an estimation of how often “cost” can be expected to happen. The cost is simply a sum up of expenses during blade life. The hard part is to predict *when* and *how often* events demanding money to be paid, happens. For the CAR Tool MVP, the *PROBABILITY* is found by using probabilistic input values and a approach using blade life simulation.

Within the scope of the CORTIR Project, the CAR Tool MVP has been developed as a software with a user-friendly interactive GUI. The tool embodies the methodology of simulating blade life over a chosen amount of years and with specified conditions applied and can be used to evaluate Cost and Risk for maintenance strategies of wind turbine farms. The CAR Tool MVP is a numerical tool with a built-in mathematical model - based on fracture mechanics - of the initiation and progression of damage development. The tool gives comparative results with magnitudes on Cost and Risk (including P10, P50 and P90) to the user defined maintenance strategies. A maintenance strategy is defined by a set of parameters, such as *inspection interval* or *decision rules*, and by changing one parameter at the time for a maintenance strategy it is easy to do parametric studies in the search for the optimal strategy. The CAR Tool MVP is limited to analyzing transverse crack damages in the max chord area.

The CAR Tool MVP:

- Simulates damage growth of transverse cracks in the max chord pressure side area during blade life
- Numerical tool based on fracture mechanics (the CPR function)
- Takes in probabilistic values for blade life simulation parameters and uncertainties related to inspections
- Provide the cost-optimal combination of inspection strategy (inspection method and inspection time interval) and repair strategy (by decision rules for repair to be performed after detection of a damage at an inspection)
- Good for comparative analysis
- Good for parametric studies
- Good for sensitivity studies of parameters
- Auto-generated results report

The CAR Tool is used with the understanding that accuracy in results is in any case a very high bar to set, and the most valuable results information comes from comparisons of results, parametric studies, and sensitivity studies of parameters. It is easy to compare different maintenance strategies by e.g. giving another inspection interval, inspection method or another decision rule. Using parametric studies and sensitivity studies can be added to the analysis of different maintenance strategies and all results can be easily visualized in tables and graphs.

The same approach can be used for all kinds of blade failures, if the blade failure is described with a CPR function and damage categorization.

### 11.3 CAR Tool Roadmap

The principle and all basic workings of the CAR Tool has been established during the CORTIR Project. The CAR Tool MVP has proven to work and can be used for parametric studies of trends in maintenance strategies, within the limitations given in the CORTIR Project. These limitations have mainly been to build into the CAR Tool in a simplified environment. The CAR Tool is now ready to be further developed and expanded into a more holistic tool. A holistic CAR Tool will look at the blade on a turbine and be able to consider multiple damage types, different inspection methods and complex decision rules taking the above into consideration. Further, system extensions to consider all blades on a turbine and all turbines in a wind farm is an obvious next step which also opens up for using inspection results from one blade to assess the risks at other blades in a wind farm.

A holistic CAR Tool will also be much more nuanced when it comes to load modelling. This will include understanding the wind farm, the layout of turbines and geographical considerations influencing the collected load on the blades. Field data will be an option to improve accuracy of damage propagation and to be able to optimize

maintenance strategy on historical data. In order to choose between strategies, financial indexes such as Return of Investment (ROI), Net Present Value (NPV) and Pay Back Period (PBP) will be even better integrated in and communicated with the CAR Tool. CAPEX, OPEX, LCoE and AEP production will all be a part of the analysis and results to be evaluated on.

If the industry has a need for a further developed CAR Tool, Bladena has a strong plan on how to go forward and develop the CAR Tool.

There will be many more structural damages to add. For that reason, a template in how to implement a new damage type needs to be addressed. When the CAR Tool considers the most frequent and critical damages at the same time, intelligent inspection and repair strategies linking the needs associated with damages, can be defined.

### Adding Damage Types to CAR Tool

CAR Tool must be able to handle several damage types. The most critical damage types will be developed first, but there is a certain principle to how a damage type is defined and integrated in the CAR Tool that will only vary on a few points between damage types. Therefore, a template for adding damage types can be defined and optimized while working on adding the first three new damage types.

Adding an extra damage type has basically three major conditions:

1. A mathematical expression (a damage specific CPR function and a set of damage states) of the damage initiation and progression must be used in the CAR Tool in the reliability module.
2. Probabilistic models of the uncertainties related to the parameters in the fracture mechanics model.
3. Data, either from field observation or tests must be gathered to make the mathematical expression of the damage initiation and progression.

For new damage types, the template for adding damage types will give clear instructions to what mathematical expression of the damage initiation and progression should include and which kind of input and output will be given and needed by the CAR Tool.

### Leading Edge Erosion

One of the most common damage type overall is leading edge erosion. A very important step towards a more holistic version of the CAR Tool is to add more damage types. Leading edge erosion is a widespread and serious problem and is arguably more often cause for inspection than structural damages. Leading edge erosion is not load related but Revolution per Minut (RPM) and site and weather conditions will be driving factors. Definitions for damage growth of leading edge erosion might include a

damage categorization based on field experience provided by partners, as well as a customized methodology to estimate the risk due to erosion. It is essential to include leading edge erosion in the next version of the CAR Tool.

For leading edge erosion different kinds of visual inspections will work and already the inspection strategy of when to use which method, frequency and which damage will drive the inspection need, is getting complicated. All the more reason to get the computer to crush through the numbers.

### Lightning damages

Another damage type which has a huge impact on downtime and AEP for hard-to-access turbines is lightning. Lightning is very dependent on wind farm location and type of turbine and thus need to be included in the future development of the CAR Tool.

In the CORTIR frame a retrofit solution to minimize the impact of lightning damage to the blade tip has been developed. The retrofit solution can also be used as an interim repair, but more cost-efficient use need to be further investigated e.g using the future version of the CAR Tool.

Lightning damage do not resemble neither damage progression of cracks nor of leading edge erosion. Lightning simply happens and the damage is instantaneous. The mathematical expression for lightning damage in the CAR Tool will most likely be simply a probability for lightning to strike paired with a probability for the lightning protection system of the blade to have done its job.

Rope is currently the only inspection method to inspect the lightning receptors, and there are different strategies (and laws) for how often these must be checked.

### More Structural Damages

There are several structural damage types to be added to the CAR Tool. This could e.g be de-attachment of shear web bond lines from spar caps, opening of trailing edge, damage due to mid span panel buckling, root-transition failures. Common for them all is that they are load driven, and the CPR functions will be similar to the one developed in the CORTIR Project for transverse cracks in the max chord area.

### New Standardized Damage Categorization

Many times, different damages can be observed on the blade and the decision whether to repair them or not is usually based on the industry's current practices and solely on the size of the damage. However, from a structural point of view, each damage has a different criticality level and weighting factor regarding the structural integrity of the blade. During the next development phase of the CAR Tool, a criticality level evaluation will be established, aiming to provide to the industry a deeper insight on when a damage should be repaired. However, this time, the repair

decision will be based on the structural impact of the damage to the integrity of the blade and not only on the size of the damage.

## Wind Farm Considerations

The three damage types mentioned above; structural damages, leading edge erosion and lightning strikes are all in some way dependent on the wind farm site and conditions. The latter two has to do with weather environment. Structural damages on the other hand is all about load. In order to consider a whole wind farm the layout of the wind turbines and the wake effects in different parts of the farm must be included in the analysis, see Figure 65.



Figure 65: The layout of the wind turbine affects the loads on the different turbines. In this figure the last row (row 7) has much more turbulence and at the same time less power production than the first rows of turbines.

Input to the wind farm considerations could be given as wind roses, see Figure 66, for different sections of the wind farm and with geographical data describing the environment conditions. Also, turbulence with wake increases by at least a factor of 2 as well as the fatigue loads increase.

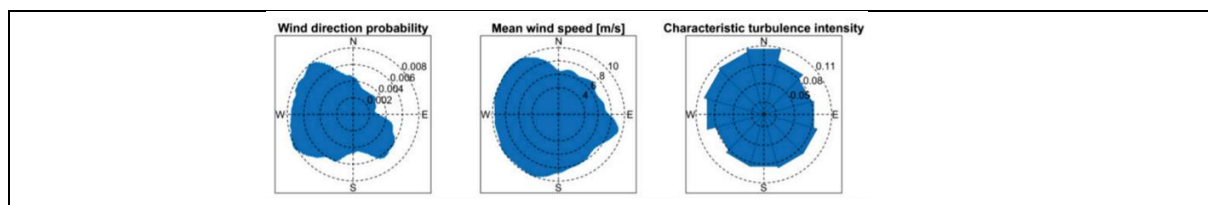


Figure 66: Wind roses representation of wind direction, mean wind speed, turbulence intensity.

So wind farm considerations can be divided in two aspects: The wind and load conditions, climate, accessibility of turbines and lightning conditions and the layout of the turbines including the wake effect variance amongst the fleet. Of course all the above-mentioned damage types are affected by the site conditions. Lightning damages might only be relevant for some wind sites, leading edge erosion will have different characteristics and progress based on site conditions and structural damages are a product of loads. When considering the layout of wind turbines on a wind farm the CAR Tool will have to evaluate the blade life differently according to the wake effect.

## Load Modelling

The load modelling in the CAR Tool will get an extensive update. Deeper investigation will be done in order to provide a more accurate but also viable approach. A more complex loading scenario, closer to real field conditions will be analyzed. In addition, further considerations in relation to wind farms will also be studied, with the corresponding wake effects. Even though the methodology to follow still has to be determined, making use of wind classes could be a first approach.

## Blade Life Measuring unit(s)

In relation to load can be introduced different ways to judge the “age” of a blade. As an example: Two blades might fail in the same way, but one blade fails after eight years and the other blade fails already after 4 years. One blade is twice as old as the other when looking at time (years). However, what if the age of the blade is measured not in time but in load cycles? What if we also consider RPM, load level, power production, turbulence, response to DLCs (Design Load Case) with fatigue loads, etc. By measuring the blade life in different units, it opens up for a better ground to evaluate between blades and between maintenance strategies.

## Field Data

With the use of field data in the CAR Tool the accuracy in prediction failure progression will be increased. WTOs can choose to use their own field data. The field data will have to live up to the requirements defined by Bladena and can be communicated as numbers in a .csv file. WTO databases with field data must be extracted and meet the Bladena template for field data in order to be used directly in the CAR Tool.

With the use of field data for the past many years, historical data will help fine-tuning the WTO maintenance strategy based on actual findings. Also, in the case that this collection of field data fits the Bladena’s specifications, it will be considered as a statistically homogeneous dataset, that will help to test and to reassess the internal fracture mechanic model, improving the risks calculations of the CAR Tool.

## Business Indexes

In the CAR Tool results are ultimately evaluated in currency. This is through both for the overall cost of the maintenance strategy and for the Risk-number attached to it. To address the business evaluation integration on OPEX, CAPEX, LCoE and AEP production will be made more visible.

With CAPEX included in the CAR Tool, LCoE can be used as an effective tool to compare maintenance strategies. CAPEX covers both the original expenditure for the wind farm and later investments.

$$LCoE = \frac{CAPEX + OPEX}{AEP}$$

With CAPEX, OPEX and LCoE considered both single investments and investment strategies can be evaluated. This will be useful in deciding whether investing in more advanced inspection equipment as NDT or if investment in damage preventive solutions as blade structural enhancers will be profitable.

Business indexes as Return of Investment (ROI), Net Present Value (NPV) and Pay Back Period (PBP) will be useful tools to estimate the business case of each wind site with different applied strategies.

## Continuous Improvement of Inspection methods

The inspection methods to choose from in the CAR Tool must include all the most common inspection types for both visual inspection and NDT inspection. Each inspection has pros and cons both in terms of costs, logistics and effectiveness against different damage types. To encompass all this information and select the right inspection strategy, the decision rules will have to be expanded and some strategies might use a combination of different inspection methods.

## Timeline for further CAR Tool development

The next step of the CAR Tool including several damage types and wind farm conditions can be developed in the span of the next three years, from 2021 to 2023, if a suitable project to encompass the CAR Tool is found. During the three years relevant updates to the GUI and output format will be made along with added code to include the new CAR Tool capabilities. Relevant testing of new features and training of users for both the CAR Tool MVP and the next step CAR Tool will be addressed.

The time plan constitutes the road map for the next step CAR Tool. The roadmap with sub-goals and planning can be seen in Figure 67.



Figure 67: CAR Tool roadmap describes how the progress of the Next step CAR Tool is visualized to span the next three years.

It should be noted, that the above roadmap is prone to adjustments according to the available funding of the next development project. Therefore, although Figure 67

illustrates the full overview of the future CAR Tool development, the individual milestones can be adjusted due to funding modifications and availability.

## 11.4 Transverse cracks and fracture mechanics Conclusion

Data has been collected from large-scale testing and sub-component testing for three purposes: 1) To find the crack propagation rate (CPR) in the sandwich panels. 2) Investigate damage development in skin (face sheet) under pure tension and pure bending as well as provide input to FEM models. 3) Investigate damage development during torsional loading of a 15m blade section. The primary objective of this effort was to produce comprehensive data to provide input to CAR Tool and use the data for comparative studies.

Following conclusion from the project are noteworthy:

- Design of large-scale test and testing procedure were also optimized during the project. Importance of load optimal introduction area was investigated in collaboration with DTU.
- For large scale testing, the localized buckling occurring on the actual face sheet caused increased stress levels that ultimately led to the initiation of 2 transverse cracks, as confirmed by the GWS when the new layup was applied.
- Sub-component testing of multiple core materials provided essential input to CAR Tool. The coefficient  $C$  and  $m$  of the CPR function (appendix D) were extracted by means of testing and CPR function was implemented in the CAR Tool to help envisage a complementary strategy. Consequently, making the output of CAR Tool more reliable and consistent.
- Results of the sub-component testing were further used in verification of the FEM simulations.
- FEM technique (such as elastic instabilities) was also utilized during the project to investigate the phenomenon leading to the transverse cracks on the wind turbine blade. The contact between skin and core was modelled and different circular debond sizes were investigated. The results helped in providing technical opinion on damages and the results were verified by means of testing.

## 11.5 Tip solution Conclusion

The process of designing the tip solution began by identifying the need of a tip retrofit solution in the market. Next, evaluation of the pool of ideas was completed in collaboration with the project partners and a product in the form of struts was finalized which met the needs of the industry in current situation. In addition, material selection and testing were also done in collaboration with the project partner (ECC) who took full responsibility of investigating the material.

Following can be concluded from the work done in tip solution area:

- A broad understanding of lightning strikes and the probability for unintended damages on wind turbine blades has been established in collaboration with ECC.
- The interim tip solution presented here can be easily installed on a wind turbine blade.
- The solution will help to keep the suction side and pressure side intact during a lightning strike.
- Analytical analysis showed that it reduces peeling stresses drastically at the tip region.
- The aim was to develop a preventive and/or interim solution for the tip split opening issue. The struts concept, analytically, satisfies the requirements for a preventive and/or interim solution. However, proof of concept for the solution could not be demonstrated due to the unfortunate situation regarding covid-19.
- Material testing proved that the chosen material (Fiberglass) has the strength of withstanding high temperatures and forces while keeping its mechanical properties (appendix E).

## References

- [1] "Project Report: Root Area Transition Zone - RATZ and Reduction O&M cost of WT blades, Energy Development and Demonstration Program (EUDP) RATZ project, 64015-0062," 2019.
- [2] DNV-GL, "Standard DNVGL-ST-0376: Rotor blades for wind turbines," DNV GL AS, 2015.
- [3] F. M. Jensen, "Ultimate Strength of Large Wind Turbine Blade," Department of Civil Engineering, Technical University of Denmark, Kgs. Lyngby, 2008.
- [4] C. IVS, "Guide2Defects," Guide2Defect, 06 January 2016. [Online]. Available: [www.guide2defect.com](http://www.guide2defect.com). [Accessed 17 December 2018].
- [5] F. Jensen, M. Werk, A. Buliga, T. Pardalakis, C. Berggreen, J. Waldbjoern, J. D. Sørensen, Y. Yang and T. Lindby, "Root Area Transition Zone - RATZ and Reduction O&M cost of WT blades," Energiteknologisk udvikling og demonstration (EUDP), Copenhagen, Denmark, 2019.
- [6] J. P. Waldbjoern, A. Buliga, C. Berggreen and F. M. Jensen, "Out-of-plane deformations of double-curved trailing edge sandwich panels in the root transition zone of a 34m wind turbine blade," *Composite Structures*.
- [7] P. Brøndsted and R. P. Nijssen, *Advances in wind turbine blade design and materials*, Woodhead Publishing, 2013.
- [8] "Data Report: Full-scale test of a LM58.7m blade with edgewise fatigue loading," Energy Development and Demonstration Program (EUDP) RATZ project, 64015-0062, Roskilde, 2019.

- [9] "Data Report: Full-scale test of a LM58.7m blade with combined static loading," Energy Development and Demonstration Program (EUDP) RATZ project, 64015-0062, Roskilde, 2019.
- [1  
0] "Data report: Full Scale Test SSP 34m blade, Combined static load," Energy Development and Demonstration Program (EUDP) Experimental Research, Phase 2 , Risø, 2010.
- [1  
1] F. M. Jensen, "Ultimate strength of a large wind turbine blade," Risø DTU, PhD Thesis, 2008.
- [1  
2] F. M. Jensen, "Floor™ Patent owned by Bladena Aps". Patent WO 2008.086205, 2008.
- [1  
3] A. B. C. B. F. M. J. Jacob P Waldbjørn, "Multi-axial large-scale testing of a 34 m wind turbine blade section to evaluate out-of-plane deformations of double-curved trailing edge sandwich panels within the transition zone," <https://journals.sagepub.com/eprint/XHMXWCNZAK6WE8WJZ7DG/full>, 2020.

# Technical Terms

## Acoustic Emission

It is a family of non-destructive testing (NDT) technique where a sound is monitored using the piezoelectric sensor and acoustic emission sensors. The function of acoustic emission is to detect specific damages, origin, severity, and potential growth.

## Adhesive:

A material that binds the blade components together by surface attachment. In general, it is used to bind the shear webs from the spar caps and suction side and pressure side shells together in the TE and LE regions (cf. Bondline).

## Aerodynamic forces

Forces caused by the wind flow over wind turbine blades.

## Bi-directional fibers

Composites in which fibers are aligned in two directions.

## Blade's radius

The blade's radius is obtained by measuring the distance from the blade root to the region of interest (see also. Blade length and Rotor Radius).

## Blade length

Distance from root to tip.

## Box bar design

Load-carrying box (Shear webs and spar caps construction). During manufacturing, the shear webs and spar caps are designed as a box, and the two shells are coupled on the box.

## Bondline

The adhesive layer between different blade components.

## Breathing

Blade panel relative deformations induced by loads in operation.

## Buckling

Buckling is a non-linear phenomenon which is the inability of the blade to have a linear response between loads and deformations. A common region for the blade to buckle is mid-span, TE region. Blades in operation are not allowed to buckle, however in static full-scale testing they are allowed to buckle.

### **Camber line**

Aerodynamic reference line with the same distance to suction surface and the pressure surface.

### **Coordinate System**

A reference system representing points in space by coordinates (numbers) from an origin.

### **Collapse**

Separation of the blade from the hub or critical damage to the blade which cannot be repaired.

### **Combined loading**

A mix of two or more loads. In the wind industry, the mix of edgewise and flapwise loads. It is commonly used as combined loading. Torsional loads are included in this formulation as well.

### **Crack propagation rate (CPR)**

Change in crack length per load cycle.

### **Cross Section Shear Distortion (CSSD)**

The localized cross-sectional local deformation where the aerodynamic profile exhibits shear localized deformations cross-sectional wise. It consists of pure torsion and pure distortion.

### **Cohesive Failure:**

The terminology “cohesive failure” is usually used to point out that the failure occurs within a material, e.g. an adhesive layer. It can be recognized from the fracture surfaces in that adhesive will be attached to both surfaces. Failure to take place along the interface between adhesive layer and the substrate material is denoted as “adhesive failure”.

### **Cohesive Zone:**

To accurately characterize such damages, it is convenient to introduce a specialized material model, called a cohesive law. This is a simplified relation that links the tractions (stresses) transmitted between the two crack faces and the displacement

between them; thus, it is called traction-separation relation and is the fracture process zone's mathematical representation.

Cohesive laws need to be experimentally measured for materials and interfaces. The correct deduction and implementation of these laws enable the accurate prediction of cracked composite structures' behaviour. These are conveniently introduced in numerical Finite Element tools and simulate a crack's propagation in a structure under loads.

### Chord length

The distance from LE to TE.

### 25% Chord

The point on a chord line which is  $\frac{1}{4}$  of the chord length away from the LE.

### C-Web

A relatively small shear web installed close to the blade's trailing edge to provide additional stability against buckling and breathing.

**CMB:** Condition-Based Maintenance.

**CORTIR:** Cost and Risk Tool for Interim and Preventive Repair

**CSSD:** Cross Section Shear Distortion

**CVI:** Close Visual Inspection.

### Defect

A flaw in a wind turbine blade formed during the blade manufacture (see also. Manufacturing flaw).

### Damage

Irreversible breakage of materials or interfaces, e.g., the formation of cracks (from manufacturing defects), caused by external loads.

### Damage category (DC)

Damage category is a term used to quantify the severity of a defect/damage.

### Digital X-ray

Digital radiography is a form of X-ray imaging, where digital X-ray sensors are used instead of traditional photographic film. Advantages include time efficiency through bypassing chemical processing and the ability to digitally transfer and enhance images.

## **Downtime**

The time during which a wind turbine is not producing electricity.

## **Delamination**

Crack initiation or growth between two layers within laminate.

## **Debonding**

Crack growth between the interface of the two different materials (e.g., adhesive/laminate interface).

**DC:** Damage Category.

**EUDP:** Energy Technology Development and Demonstration Program.

## **Edgewise load**

Loads in the edgewise direction, causing edgewise global deformation.

## **Elastic instability approach**

The method uses the elastic FEM structural simulation tool to identify the impact that certain structural defects/damage types and sizes have on the blade, from a structural point of view. The method uses a comparative analysis approach when a blade with a defect is compared with one without the defect.

**FEM:** Finite Element Method.

## **Failure**

The loss of an intended function of a component (blades) of a wind turbine and or a wind turbine due to excess loads.

## **Flatback**

It is the blunt trailing edge of an airfoil. Usually, it is a continuation of the transition zone flatback towards max chord and mid-span in some cases.

## **Flutter**

Flutter is an aerodynamic instability of blades which occurs when the torsional and flapwise eigenfrequencies are the same causing resonance.

## **Fracture**

Fracture is the separation of a loaded structure (or material) by the growth of a crack, i.e., forming new crack surfaces.

## **Fatigue**

The process in which damage accumulates under multiple load cycles, resulting in weakening or damaging the material.

### Finite Element Method (FEM)

A tool used to simulate the structural behaviour of blades.

### Field case study

The field case study is a method of carrying out a detailed examination of information from the field.

### Fracture process zone

A fracture can occur by a sharp crack tip or by a long fracture process zone. In both cases, the zone where the material (or interface) fails is called the fracture process zone. Fracture by a crack tip is called small-scale fracture process zone, while fracture involving a long fracture process zone is called large-scale fracture process zone. For a large-scale fracture process zone, such as delamination crack growth along the layers, it may not be possible to identify a defined crack tip, but there are two distinct regions: A zone where the material is beginning to be damaged and has reduced strength and a second region where intact fibres behind the damage front bridge the crack. Typically, fracture involving a small-scale fracture process zone is modelled using linear-elastic fracture mechanics, while fracture involving a large-scale fracture process zone is modelled using cohesive zone modelling.

### Flapwise load

Loads in the flapwise direction driven by wind causing flapwise bending.

**G2D:** Guide 2 Defect.

**GVI:** General Visual Inspection.

### General Visual Inspection (GVI)

Quick scanning of the blades using human senses such as vision, touching or any non-specialized equipment. This type of inspection is done from within a touching distance of the wind turbine.

### Global deformation

Deformation seen on blades at blade length-scale level.

**ISP:** Independent Service Provider.

### Interlaminar fracture

Failure mode found in composite laminates. It is the separation of layers within the laminated pile of a composite. This leads to interlaminar stresses which are the cause of the actual failure.

### **Independent Service Provider (ISP)**

An independent company specialized in carrying out services related to blades.

### **Kissing Bond**

Kissing bond is an adhesive bond defect where the two materials are not attached (joined) through the bondline. Visual inspection shows a wrong indication that there is a bondline between the materials, where in reality there is no adhesion

**LE:** Leading Edge.

**LTT:** Leading Towards Trailing.

### **Leading edge (LE)**

The front edge of a wind turbine blade directing towards the incoming wind.

### **Load-carrying shells**

Load-carrying shells blade design have spar caps embedded in the aerodynamic shells.

### **Local panel bending**

To and fro motion of the panel relative to the blade. It is localized out of plane bending of the panel.

### **Leading edge towards trailing edge (LTT)**

The term used to define the direction of the load.

### **Local deformation**

Deformation which turbine blade components experience at a much smaller scale compared to global deformation. For example, breathing is a local deformation, and tip deflection is a global deformation.

### **Manufacturing flaws**

Defects in wind turbine blades due to the faulty manufacturing process (see also. Defect).

### **The Markov model**

In probability theory, a Markov model is a stochastic model used to model randomly changing systems. It is assumed that future states depend only on the current state, not on the events that occurred before.

### Material strength

It is a measure of a material's ability to withstand an applied load without failure. It is measured as the maximum load per cross-section area.

### Max chord region

The region of the blade with a maximum distance between the TE and leading edge. In most cases, this is the region with the largest curvature on the pressure side and is a critical area for TE splits and cracks on TE panels.

### Mean wind speed

Average wind speed over a 10-minute time interval.

### Mid-span region

The section of the blade between the Max Chord region and 2/3 of the blade length.

### NDT (Non-Destructive testing)

A group of qualitative methods to identify abnormalities in a material without causing any damage. The most common NDT methods for blade testing are visual testing (VT), manual ultrasonic testing (UT), acoustic emission (AE), radiographic testing (RT) and thermographic testing (TT).

### NDE (Non-Destructive Evaluation)

A group of quantitative methods to describe material abnormalities or material properties without causing any damage. For example, the location, size, shape and orientation of a flaw or elastic property of a material.

NDE methods are often characterized by:

- A reference block with artificially made “flaws” to calibrate the method.
- An automated scanner or robot to move a sensor.
- Signal processing of the recorded data (E.g. Phased array, Fast Fourier Transform, Hilbert transform).
- Evaluation of data using rule-based methods (i.e. artificial network, Machine Learning).

The most common NDE methods are Vision systems, Automated ultrasonic testing (AUT), Computed tomography (CT) and Active dynamic thermography (ADT).

### NREL

National Renewable Energy Laboratory.

## Out-of-plane deformation

Deformation occurring perpendicular to the surface.

## O&M

Operation and Maintenance.

## Parameter (all type of CAR Tool input are “parameters” - no “variable”)

In relation to CAR tool parameter is a numerical input used in the CAR Tool to accommodate user inputs.

## Parametric study (sensitivity study)

A parameter study relates to a situation where one value depends on several parameters, and the dependency of parameters is explored systematically by varying one parameter at a time while keeping the others fixed.

## Peeling stress

Peeling stresses are stresses ahead of a crack tip acting in the direction normal to the crack plane.

## Probability of Detection (PoD)

A statistical method utilized to evaluate how well an inspection method detects a defect/damage. The figure below shows a PoD curve. The figure shows the probability of detection increases as a damage size increases.

## Post-processing (of results)

Results interpretation.

## Pressure side (PS)

It is the side of the blade which has high pressure. Usually, it is the more curved side of the blades.

## PM

Preventive Maintenance.

## PoD

Probability of Detection.

## Re-engineering

In wind turbine industry, re-engineering is a term used to describe the process of examining and understanding a blade to see the important structural parameters in

order to enhance or duplicate the blade when the information about the original drawings and/or manufacturing process is not available.

### **Rotor Radius**

Distance from the rotor to the tip of one blade in the axial direction.

### **Root**

The circular part of the blade connected to the hub using bolts. Typically, a thick laminate to accommodate the bolts.

### **Relative Thickness**

Thickness as percentage of the chord.

### **Sandwich panel**

A panel that is made of three layers: outer skin, a core and inner skin. Each of the skins can be made of multiple layers.

### **Shear web**

Supporting beams connecting the load-carrying shells (spar caps) which increases the flapwise stiffness.

### **Shearography**

Shearography is a non-destructive technique to find damages that are not visible from the outside. The method works by using coherent light or coherent soundwaves to provide information about the quality of different materials in non-destructive testing and defect detection.

### **Shells**

The SS and PS shells are large aerodynamic panels designed to transfer aerodynamic forces that define the blade capacity to extract energy from the wind.

### **Simulation**

The use of a (numerical) model to predict a structure's behaviour or a component under loads.

Synonym: Modelling

### **Skin debonding**

Skin debonding refers to the detachment of the skin from the core material.

Synonym: Face sheet debonding

### **Spar caps**

Part of the blade with the primary function being to keep the blade's global shape in the flapwise direction. The PS cap works in tension and SS cap works in compression.

### **Sub-component test**

Test procedure where part of the blade is subjected to loads in a control environment.

### **Suction side (SS)**

Suction side is a low-pressure side of the wind turbine blade. It is the side facing tower during operation.

### **Trailing Edge (TE)**

Thin edge of the blade directing opposite the direction of the incoming wind.

### **Transition zone (TZ)**

Region of the blade where the geometry of the blade changes from circular to an aerodynamical shape.

### **Transverse strains**

Normal strains in the transverse direction of a blade

### **Tri directional fibers (TRIAX)**

Composites in which fibers are aligned in three directions.

### **Thermography**

Thermographic inspection refers to the non-destructive testing of parts, materials, or systems by imaging the thermal patterns at the object's surface.

### **Thickness (aerodynamic profile)**

The distances between the outer surfaces of the suction side and the pressure side.

### **Tip region**

Part of the blade close to the tip, depending on the blade size different lengths can be considered.

### **Torsional operational loads**

Load component resulting from the combination of flapwise and edgewise loads where the flapwise application point is in the aerodynamic center.

### **Trailing edge Towards Leading edge (TTL)**

Abbreviation/term used to describe the direction of loads.

### **Turbulence (wind)**

Atmospheric turbulence is the set of apparently random and continuously changing air motions that are superimposed on the wind's average motion.

### **Twisting (structural)**

A deformation mode which is typically used for beam-like specimens. The cross-section is rotated around the beam's longitudinal axis (see also twist).

### **Aerodynamic Twist**

The difference in angle between a chord line and a reference chord line.

### **Technology Readiness level**

It is used to assess the development level of a product.

### **Ultrasonic**

Ultrasonic testing (UT) is a family of non-destructive testing techniques based on the propagation of ultrasonic waves in the object or material tested.

### **Unidirectional (UD) layers**

In composite material, Unidirectional layers mean that the fibres are aligned in primarily one direction.

### **Wrinkles**

Wrinkles is a failure mode in which a thick layer buckles locally, usually due to local shear stresses or compressive stresses.

### **Wind Turbine (WT)**

Energy generating machine which converts kinetic energy (wind) to electrical energy.

### **Wind Farm (WF)**

A group of wind turbines installed in the same area to produce electricity.

## **Business and Financial Terms**

### **Annual energy production (AEP)**

The amount of energy produced on a yearly basis.

### **Benchmark (validation, comparison)**

A standard or point of reference against which things may be compared.

### **Business case**

In relation to the CAR Tool, business case is the output of the CAR Tool showing the expected commercial benefits of different actions.

### **Capex (Capital Expenditures)**

The money the company spends acquiring or upgrading its physical assets.

### **Cash flow**

The total amount of money that goes into and out of a business.

### **Capacity Factor (CF)**

Capacity Factor is the average power generated divided by the peak power.

### **Condition-based maintenance (CBM)**

A maintenance strategy that monitors the actual condition of an asset to decide what maintenance needs to be done.

### **Corrective maintenance (CM)**

Maintenance tasks that are performed in order to repair or restore failures.

### **CORTIR**

An EUDP project called “Cost and Risk Tool for Interim and Preventive Repair” headed by Bladena.

### **Critical technology elements (CTE)**

The technological elements on which the system depends on to meet the operational requirements.

### **Cost of Equity**

It is the financial return investors expect to see.

### **Cost of capital**

It is a percentage of return expected by investors who provide capital.

### **Decision rule (DR)**

The decision rule defines the actual maintenance actions for a specific damage observed at an inspection, accordingly to the severity category.

### **Discount cash flow (DCF)**

Discount cash flow is a analytical method of determining the value of an asset based on its future cash flow (see def. valuation).

#### **EUDP**

Energy Technology Development and Demonstration Program.

#### **Failure Rate**

The average failures of a component during a year.

#### **Guide2Defect (G2D)**

A Danish company (spin-off from Bladena) which has a blade database of failures from the field.

#### **GWH**

Gigawatt-hour

#### **IEC**

International Electrotechnical Commission.

#### **ISO**

International Organization of standardization.

#### **Key performance indicator (KPI)**

It is a measurable value that demonstrates how effectively a company is achieving key business objectives or projects.

#### **Levelized cost of energy (LCOE)**

Measures lifetime costs divided by energy production. Calculates the present value of the wind turbine and its operating costs over an assumed lifetime.

#### **Mean Down Time (MDT)**

The average amount of hours that AWT does not generate power.

#### **MTBF**

Mean Time Between Failures.

#### **MTTF**

Mean Time to Failures.

#### **Mean Up Time (MUT)**

The average operational hours of a wind turbine.

#### **MVP**

Minimal Viable Product.

#### **MWH**

Megawatt-hour

#### **NREL**

National Renewable Energy Laboratory.

#### **O&M**

Operation and Maintenance

#### **OpEx (Operational Expenditures)**

The money the company spends on day-to-day basis in order to run a business (wind turbine/wind farm).

#### **Owners requirement**

Additional specifications added to the existing certification requirements found in standards today requested by wind turbine owners.

#### **Rated Power (Prated)**

The highest amount of power a wind turbine has its peak power.

#### **Preventive Maintenance (PM)**

A regularly performed maintenance to decrease the chance of failure of a component of wind turbine.

#### **Power purchase agreement (PPA)**

A contract between a company willing to sell electricity and the one which is looking to buy electricity.

#### **Power tax credit (PTC)**

It is a tax credit for electricity generated using qualified energy resources.

#### **ROI**

Return on investment is a ratio between net profit and cost of investment. A high ROI means the investment's gains compare favorably to its cost

#### **Risk**

Risk is defined as the likelihood of an event to happen multiplied by the respective consequences.

### Strategy

An approach towards success. In relation to CAR tool, strategy refers to the maintenance strategy, a set of rules describing when to inspect, repair etc.

### Upfront investment

An initial investment.

### Value proposition

A value proposition is a promise of value to be delivered, communicated, and acknowledged.

### Value chain

The Value Chain in the Wind Industry consists of three parties: Wind Turbine Manufacturers (OEMs), Wind Turbine Owners (WTOs) and Insurance Companies.

### Valuation

Valuation is a analytical process of determining the current (or projected) worth of an asset or company.

## Appendix B      CAR Tool

### Assumptions in CAR Tool

The development of the CAR Tool is a process that involves the interconnection of several areas of study like fracture mechanics, Finite Element Model, testing and application of statistical considerations.

As a result, assumptions are necessary to be made in order to progress in the project. Assumptions are due to either:

- Lack of available information: the mentioned area of fracture mechanics applied to the creation of a transverse crack in a wind turbine blade, is a novel ongoing research topic, where the very first results have allowed to establish the first theories. These theories must be confirmed, and so, they lead to a wide set of assumptions that are considered internally in the CAR Tool. The most relevant of them will be mentioned in the current section

- Simplification of concepts: assumptions are also valid to simplify and apply concepts, which must be first understood in a simple way, before the complete and complex consideration is approached.

The assumptions made so far, can be divided in three areas:

## Fracture mechanics

### *1. Paris-Erdogan law*

The Paris-Erdogan law has been assumed to represent the propagation of a transverse crack through a blade. This law is used in other industries inside civil engineering where cracks are taken into account, as a result, it has been considered correct to make use of it for this application.

So, the Paris- Erdogan is used to formulate the Crack Propagation Rate (CPR) function

### *2. Constant load input*

A simplify load consideration assumes a constant stress value as the driver of the damage initiation. In reality, the loading conditions of a blade are much more complicated and future improvements will be addressed in this relation in further versions of the CAR Tool.

### *3. Debond before a crack*

The fracture mechanics theory establishes that initially, the whole panel starts to get deformed, leading to a debond between the outer face sheet and the core material. At some point, the concentrated stresses around the defected area may lead to the cracking of the surface, as the interface may not be able to bear more deformation..

### *4. Initial crack size*

Once the debond has overpassed the minimum theoretical size to allow the creation of the crack, this crack from the very beginning will have a size.. This assumption has a fundament based on the fracture mechanic approach, but it is also based on numerical fundamentals, as it is necessary from a mathematical point of view, to count with an initial defect size to solve the Paris-Erdogan law

### *5. Visual inspections do not detect debonds*

It is assumed that visual inspection methods like drones or rope access, are not capable of detecting internal debonded areas. So, in the case a crack is detected through a visual inspection, and it has been decided to repair it, the debonded area will not be repaired

### *6. Non-Destructive-Testing (NDT) methods detect debonds*

For the detection and consequent repair of a debond, preventing so the expansion of a crack, it is assumed that WTOs or ISPs have to make use of NDT methods

### *7. Non perfect debond repair*

By analyzing field cases where the development and repair of transverse cracks has been tracked, it has been seen that on some occasions the repair crack appears again after a period of time that can be as low as 2 years.

An assumption to explain these facts is that during the repair process, the debond (considered as the root cause of the crack) was not perfectly corrected, therefore in a short period of time the area continued getting debonded until the accumulated stress led to the creation of a new crack.

#### **General development:**

##### *1. Filtering of field data*

In the case the users have available field data to introduce in the CAR Tool, the methodology followed will be to create stochastically a set of CPR functions filtering those which get closer to the available data. By doing so, the right value of the parameters that are included in the CPR function mentioned above will be obtained.

It is assumed that a stochastic CPR function that goes through the field data used as a reference will be found.

##### *2. New inspection interval*

In the case that a crack has been detected and it is getting close to the preselected size where the users would be interested in repairing it, it is assumed that the inspection interval will be reduced in order to guarantee not to overpass the maximum level of risk redecided in the customization of the maintenance strategy. The users will be able to select this new inspection interval.

#### **Probabilistic framework:**

##### *1. Parameter C from the Crack Propagation Rate formula*

It has been assumed that it follows a lognormal distribution, which must be confirmed with the characterization testing that is being carried out as part of the project.

##### *2. Parameter “Initial defect size” distribution*

It has been assumed that it follows a continuous exponential distribution. Again, testing is ongoing confirming this initial assumption.

##### *3. Probability of Detection (POD) from the inspection methods*

The probability of detection of the different inspection methods come from feedback received from WTOs and ISPs. These numbers are assumed to be correct for the

current CORTIR Phase 1. Actually, in the future CORTIR Phase 2, some studies will be conducted to validate these PODs and confirm new ones

## Limitations in the CAR Tool

The limitations can be divided in two groups, depending on whether they belong strictly to the functionalities of the tool, so to the Minimum Valuable Product (MVP), or if they belong to the communication between the users and the tool, so to the GUI.

### MVP LIMITATIONS

#### *1. Cost calculations:*

In order to establish the cost model, Bladena has gathered information from the CORTIR partners identifying the different sources of costs during the O&M activities. As a result of this, a set of variables has been defined from which the users will have the option to choose, customizing their own costs or making use of the default ones established internally.

However, further details should be included in relation to some specific costs, and a wider number of WTOs should be approached to understand the possible differences in the sources of costs between each user.

So far just a limited number of variables in relation to cost have been introduced inside the cost calculation model. The CAR Tool should be able to represent the reality that any of the potential users faces in everyday O&M conditions. Therefore, the cost model will be reviewed and improved for future versions, meaning that more variables will be introduced covering sources of costs that so far are not taking into account.

#### *2. Fracture mechanic approach for the crack propagation:*

The physical model that establishes the basis to simulate the propagation of the transverse cracks, is based on studies applied to a single particular blade model. This blade has its own layout, material characteristics, and geometry, so the results from this fracture mechanic approach are expected to vary from blade to blade.

Actually, some of the parameters used for the formulation of the physical model already consider the material properties. So, it can be said that the Crack Propagation Rate formula used for the CAR Tool already allows some kind of flexibility to adapt to different blades. However, it must be recognized that there are still limitations that can be summarized as:

- The fracture mechanic approach should be confirmed by testing a different blade model

- Research must continue with the goal of finding and confirming a numerical model that takes into account the different properties from a wide set of blades, so that its application can be extended to other blades

### *3. One specific damage type: transverse cracks*

The above fracture mechanic approach is based exclusively on 1 single damage type: transverse cracks on the max chord area of the blade.

The more damage types are considered for the calculation of cost and risk, the more the CAR Tool will be able to simulate the reality on field conditions. For further versions, it is planned to include leading edge erosion, lightning and shear-web disbonding. The final objective is to become the tool as holistic as possible, representing all the possible sources of damage that trigger the decision at designing a maintenance strategy.

### *4. Single inspection method for the whole wind turbine lifetime*

One of the variables that the users can choose from, is the inspection method. This is considered as an essential factor as maintenance strategies perform very different depending on it. However, in the current CAR Tool MVP, the inspection method selected for the year 0 of the simulation, will keep constant for the rest of the years.

By consulting WTOs and ISPs it has been discussed that this does not correspond to the reality, as the common practice is to perform different inspection methods for the same damage, but with different frequency each method, e.g: visual inspection every 2 years and internal inspection every 3 years.

This problem will be solved in future versions of the CAR Tool

### *5. Weather window most accurate approach is not available yet*

Weather window has proved to have a big influence on the waiting time costs and in some cases on the downtime costs. Its consideration has been included in the CAR Tool calculations from the beginning, however, there are several ways of considering it for the final calculations of risk and cost.

The first of these methods is to make use of available historical databases about wind speed and about a set of wave parameters for offshore conditions. From a theoretical point of view, it is recommended that a minimum of 10 years of historical data is necessary to guarantee a small deviation in the established trend for the prediction of the weather window in the following years. By relying on this method, average weather windows and waiting times per month could be concluded and applied inside the CAR Tool, reducing the uncertainty of the forecasting.

For the current MVP version, these computations have been done for 1 specific location for which the required data was available. However, Bladena is aware of the

difficulties to obtain this information, as a result, a second method has been proposed.

This second methodology is based directly on the input received from WTOs, which will introduce a vector with 12 values, representing each of them the expected waiting time per month. In the case that the users do not have access to this data either, a default Bladena's vector will be implemented. This vector has been carefully obtained after receiving feedback from several ISPs and WTOs.

Summing up, currently only the second methodology is offered in the MVP. For future versions, the first option will also be available to those users which own the necessary meteorological historical data. Clear instructions will be given by then on how to introduce this information, as it will have to be in a specific format that can be understood by the CAR Tool.

#### *6. Number of years of simulation limited to 20*

The simulations that are considered inside the CAR Tool represent a 20 years lifetime for the analyzed maintenance strategy

#### *7. Short variety of wind turbines offered*

For the current MVP, only 3 single WTs are offered for the selection of the users: Vestas V80, Enercon E-40 and GE 1.5.

The wind turbine is related to a particular power curve, which is used for the estimation of revenue and losses, which at the same time will be involved in final cost, risk and cashflows calculations.

A wider number of options will be considered in future versions.

#### *8. Revenue at selling the energy.*

One important variable in order to estimate the risk and cost of a specific maintenance strategy is the the profit that the WTOs get whenever they sell the energy that they produce. Different approaches are used by WTOs including market trading and fixed Feed in Tariffs (FiT). For simplification, the Feed in Tariff methodology has been used for the internal calculations assuming a constant value. This value has been decided after consulting a set of FiT for WTOs located in Denmark, UK and Taiwan.

### **GUI LIMITATIONS**

#### *1. Computational time*

In order to reduce the uncertainty in the final calculations, the program should run a considerable number of times each of the planned maintenance strategies that will be simulated.

This implies that in some cases, like in the “Trend analysis” section of the GUI, the computational time is high oscillating between 30 minutes and some hours.

An optimization phase of the program has to be conducted aiming to reduce this time. This is expected to be implemented in future versions of the CAR Tool.

## *2. Strict format to introduce data inside the tool*

The purpose of every GUI is that the users can interact with the program selecting options and introducing data. For the current GUI, this introduction of information has to follow a specific format, as if not followed, the CAR Tool will not be able to understand properly the input leading to errors in the calculations. Whenever this happens, the program automatically stops working and it will exit the interface.

Because of this, in the CAR Tool GUI manual clear instructions in relation to this topic are provided.

It must be said that in some exceptional cases, the CAR Tool is able to recognize the error that the user is having, and it pops up a warning message explaining why the information is introduced in a wrong format. As a result, the users can simply change whatever it is suggested, without needing to exit the interface as the program will continue working without errors.

The objective for future versions, is the GUI to assist the user to identify the errors and make the proper corrections.

## *3. Slow introduction of data*

In the case that several strategies must be compared at the same time by the CAR Tool, and the users want to customize each of the variables of these maintenance strategies without selecting any of the Bladena’s defaults options, then the whole selection process might be a bit time consuming.

Both the GUI and the CAR Tool MVP are ongoing tasks which are not finalized yet. Apart from the limitations and assumptions mentioned above, an implication of this is that there might be potential bugs or errors in the code.

Its consequence is that at some point, the program simply stops running and the users are exited from it.

## *4. Potential bugs*

Both the GUI and the CAR Tool MVP are ongoing tasks which are not finalized yet. An implication of this is that there might be potential bugs or errors in the code. Its consequence is that at some point, the program simply stops running and the users are exited from it.

It has been checked that on some occasions, when the users are selecting the different options inside each of the variables, there is the possibility that if the

options are selected by doing double click repeatedly without waiting for the program to process the selection, the code will maybe have an error and the user will be exit from the GUI. This is considered as an internal bug, that will be solved in future versions

The code has been reviewed several times, however, it might be possible that there are other sources of errors which have not been detected yet. If this is the case, these errors will not be common, but for the current CAR Tool MVP and current GUI version, Bladena cannot guarantee that other errors might appear at other unexpected moments.

## Future CAR Tool versions

Many different adaptations, features and modules have been left for the future due to lack of time. Future work concerns a more holistic approach with focus on accuracy. Currently, the CAR Tool only addresses the transverse crack in the max chord region of the blade. Going forward, the following will be added to CAR Tool to give it a more holistic approach:

- 1) Leading Edge Erosion
- 2) Lightning damages
- 3) Shear Web Disbonding
- 4) CAR Tool internal functionalities
- 5) Risk Assessment Application

## Appendix C      Reliability model

### Background Information

This appendix is intended to elaborate on the methodologies used for reliability modelling and risk assessment. More technical details can be referred to the relevant technical reports issued for Work Package 2 (WP2, Reliability and Cost Models).

### Reliability Model

#### Overview

This section is intended to briefly present the framework of a probabilistic crack propagation model for transverse cracks based upon the deterministic fracture mechanics model obtained from Work Package 7 (WP7) and the laboratory test results from WPs 5& 7. The reliability model focuses on investigating the stochastic crack growth development with time, and serves as a basis for simulating the realizations of crack propagation, which is the input to the cost and risk assessment. The model

and statistical uncertainties will be studied in the reliability model. In addition, the inspection/ measurement uncertainty, represented by probability of detection (PoD), will be taken into account as well.

Several rounds of brainstorm and/ or expert review meetings have been held to investigate the failure mechanisms causing the transverse cracks. Some conclusions have been drawn based upon the following fundamental assumptions:

- It is assumed that the concerned deterioration of the maximum chord zone on wind turbine blades starts with an initial imbedded defect, then advances to a delamination.
- At some point in time the delamination reaches a critical size, and a crack occurs on the surface and propagates transversely.

These assumptions discretizes the damage propagation into two major stages, namely stage 1) the ‘in-plane’ delamination and stage 2) the transverse crack propagation on the surface.

In principle, the reliability model can be applied to any type of failure, as long as a close-form/ analytical equation characterizing the crack propagation covering both phases can be obtained.

### Simplified Crack Propagation Model

The Paris-Erdogan model describes the relation between the increment of crack size  $a$  per each stress cycle,  $N$  and the stress intensity factor range ( $\Delta K$ ) or the energy release rate ( $\Delta G$ ). The generic expressions are formulated with respect to  $\Delta K$  or  $\Delta G$  in Eqs. (1) and (2) **Invalid source specified..** The right hand side of (1) and (2) is also denoted as the CPR (Crack Propagation Rate) function.

$$\frac{da}{dN} = C[\Delta K(a, \Delta S)]^m, \quad a(N=0) = a_0 \quad (1)$$

$$\frac{da}{dN} = C[\Delta G(a, \Delta S)]^m, \quad a(N=0) = a_0 \quad (2)$$

where  $C$  and  $m$  are the material specific parameters.  $a_0$  is the initial defect size and  $\Delta S$  is the applied stress range. Generally, both the numerical analysis and analytical solutions can be used to formulate  $\Delta K$  or  $\Delta G$ . The unit of  $C$  is  $[L]^{1-m/2}[MPa]^{-m}[cycle]^{-1}$  according to dimensional analysis. The symbol “L” refers to the length unit. “L” is used instead, because there is another parameter “m” in the CPR function.

The crack propagation per one stress cycle ( $\Delta N=1$ ) is given by Eq. (3) or (4)

$$\Delta a = \Delta N C[\Delta K(a, \Delta S)]^m \quad (3)$$

$$\Delta a = \Delta N C[\Delta G(a, \Delta S)]^m \quad (4)$$

### Discussion on Uncertainties

## Model and Statistical Uncertainties

In principle, the stochastic variables involved in the fracture mechanics model presented in Section A2.2 include the material parameters ( $C$  and  $m$ ), the initial defect size ( $a_0$ ) and the stress range ( $\Delta S$ ) in  $\Delta K$  or  $\Delta G$ . In CORTIR, part of uncertainties can be integrated, as presented below.

### Material parameters ( $C$ and $m$ )

The uncertainty of these parameters can be quantified through the laboratory tests (coupon-level tests) or alternatively by calibration to observed crack growths. Statistical analyses should be performed to fit the probabilistic distribution(s) against the test results. Based upon the knowledge in welded steel structures,  $C$  and  $m$  may be correlated for the transverse cracks in composite materials. The probabilistic distribution of  $C$  must be fitted at least.

### Initial defect size ( $a_0$ )

The uncertainty of  $a_0$  can be quantified by two approaches. Approach 1 is to collect the 1st inspection reports of wind turbine blades of the similar types and fit these inspection outcomes (if detected) to a probabilistic distribution (Normal, LogNormal or exponential distribution). Approach 2 is to use engineering/ manufacturing experience, which stems mainly from the quality control documents provided by typical manufactures.

### Stress range

There is only one load case considered, namely a load case where the stress ranges are due to gravity through rotation of the blades.  $\Delta S$  can be considered a constant (deterministic, i.e. no uncertainty) term.

## Inspection Uncertainty

Nowadays, visual inspection is the most common non-destructive testing (NDT) method used in inspections of WT blades. Due to the uncertainty associated with any NDT, information is needed about the probability of detection (PoD) of a damage with a given damage size. The PoD is used to quantify the ability of an NDT procedure for detecting a damage with a given size [2]. If a crack is detected it is assumed that the uncertainty related to measuring the size is negligible.

## Curve Fitting

This subsection is intended to elaborate on how to fit the parameters of the CPR function defined in Section A2.2. The parameters to be fitted include two model parameters ( $C$  and  $m$ ) and the initial defect size ( $a_0$ ). In analogy to curve fitting performed for welded steel structures, S-N curve is also fitted for information.

## Fitting CPR Function Parameters

### Fitting $C$ and $m$

Take logarithm base 10 on both sides of Eq. (1) to obtain the linear relationship between  $\log_{10}(da/dN)$  and  $\log_{10}(\Delta K)$ , as expressed in Eq. (5).

$$\log_{10} \left( \frac{da}{dN} \right) = m \log_{10}(\Delta K) + \log_{10}(C) \quad (5)$$

Generally, modelling uncertainty should be taken into account by introducing a by a Gaussian random variable, i.e.  $\varepsilon$  with zero mean and a finite constant variance ( $\varepsilon \sim N(0, \sigma_{err}^2)$ ). Let  $Y = \log_{10} \left( \frac{da}{dN} \right)$ ,  $X = \log_{10}(\Delta K)$  and  $b = \log_{10}(C)$ . The linearized crack propagation model with uncertainty considered can be re-formulated by Eq. (6). The geometry function in  $\Delta K$  is assumed to be unity.

$$Y = mX + b + \varepsilon \quad (6)$$

Because of the limited number of observations, statistical uncertainty should be considered as well. The Maximum Likelihood approach **Invalid source specified**. is used to take into account the statistical uncertainty. Given  $k$  independent observations of the crack lengths and the corresponding cycles, the likelihood function can be expressed as Eq. (7).

$$L(C, m, \varepsilon|X) = \prod_{i=1}^k \frac{1}{\sqrt{2\pi\sigma_{err}}} \exp \left\{ -\frac{[Y_i - (mX_i + b)]^2}{2\sigma_{err}^2} \right\} \quad (7)$$

For the sake of fitting the unknown parameters, natural logarithm is taken on both sides of Eq. (7) to obtain the log-form of likelihood function as given in Eq. (8).

$$\ln[L(C, m, \varepsilon|X)] = \sum_{i=1}^k \left\{ -\frac{[Y_i - (mX_i + b)]^2}{2\sigma_{err}^2} \right\} - \frac{k}{2} \ln(2\pi\sigma_{err}) \quad (8)$$

$m$ ,  $b$  and  $\sigma_{err}$  are three parameters to be fitted. The covariance of these parameters can be expressed as the Hessian matrix with second order derivatives of the Log-Likelihood function, given in Eq. (9).

$$\mathbf{C}_{m,b,\sigma_{err}} = \left( \begin{array}{ccc} \frac{\partial^2 \ln[L(C, m, \varepsilon|X)]}{\partial m^2} & \frac{\partial^2 \ln[L(C, m, \varepsilon|X)]}{\partial m \partial \log_{10}(C)} & \frac{\partial^2 \ln[L(C, m, \varepsilon|X)]}{\partial m \partial \sigma_{err}} \\ \frac{\partial^2 \ln[L(C, m, \varepsilon|X)]}{\partial \log_{10}(C) \partial m} & \frac{\partial^2 \ln[L(C, m, \varepsilon|X)]}{\partial \log_{10}(C)^2} & \frac{\partial^2 \ln[L(C, m, \varepsilon|X)]}{\partial \log_{10}(C) \partial \sigma_{err}} \\ \frac{\partial^2 \ln[L(C, m, \varepsilon|X)]}{\partial \sigma_{err} \partial m} & \frac{\partial^2 \ln[L(C, m, \varepsilon|X)]}{\partial \sigma_{err} \partial \log_{10}(C)} & \frac{\partial^2 \ln[L(C, m, \varepsilon|X)]}{\partial \sigma_{err}^2} \end{array} \right)^{-1} \quad (9)$$

The entries of the covariance matrix can be re-written as:

$$\mathbf{C}_{m,b,\sigma_{err}} = \begin{bmatrix} \sigma_m^2 & \rho_{m \ln(C)} \sigma_m \sigma_{\ln(C)} & \rho_{m \sigma_{err}} \sigma_m \sigma_{\sigma_{err}} \\ \rho_{m \ln(C)} \sigma_{\log_{10}(C)} \sigma_m & \sigma_{\log_{10}(C)}^2 & \rho_{\log_{10}(C) \sigma_{err}} \sigma_{\log_{10}(C)} \sigma_{\sigma_{err}} \\ \rho_{m \sigma_{err}} \sigma_{\sigma_{err}} \sigma_m & \rho_{\log_{10}(C) \sigma_{err}} \sigma_{\sigma_{err}} \sigma_{\log_{10}(C)} & \sigma_{\sigma_{err}}^2 \end{bmatrix} \quad (10)$$

### Fitting $a_0$

Given the material parameters obtained from Section A2.4.1.1 and the stress range, the crack length is a function of the initial defect size and the cycle number  $N$ , as expressed in Eq. (11).

$$a(N) = \left[ a_0^{1-m/2} + (1 - m/2)C(Y\sqrt{\pi}S)^m N \right]^{1/(1-m/2)} \quad (11)$$

For each pair of crack length and the cycle in a given data set, the initial defect size can be calculated based upon Eq. (11). The arithmetic mean of these calculated initial defect sizes can be assumed the unbiased estimation of the initial defect size for this given data set.

## Fitting S-N Curve

The generic S-N is given by Eq. (12).

$$\log_{10}(N) = -m \log_{10}(\Delta S) + \log_{10}(a) \quad (12)$$

where  $N$  is the number of cycles.  $\Delta S$  is the stress range.  $\log_{10}(a)$  is the intercept of the S-N curve at the N axis.

Generally, modelling uncertainty should be taken into account by introducing a by a Gaussian random variable, i.e.  $\varepsilon$  with zero mean and a finite constant variance ( $\varepsilon \sim N(0, \sigma_{err}^2)$ ). Let  $Y = \log_{10}(N)$ ,  $X = \log_{10}(\Delta S)$  and  $b = \log_{10}(a)$ . The linearized crack propagation model with uncertainty considered can be re-formulated by Eq. (13).

$$Y = mX + b + \varepsilon \quad (13)$$

The rest of curve fitting is the same as Section A2.4.1.1.

## Demonstration Cases

### Overview

The basic information on the test set-up is summarized in Table . DTU MECH have conducted 19 coupon tests for two directions (9 tests for Directions 0 and 10 tests for Direction 90). The sketches in Figure show the loading directions and the coupon dimensions. It should be noted that there is a numerical problem with four data sets for Direction 90, when curve fitting is performed. Therefore, these data sets will not be used in this case study.

The stresses can be directly calculated from the applied forces in Table and used in curve fitting. For each test, a constant stress range is applied. The peak stress refers to the calculated stress. The stress valley refers to zero.

Because of different mechanical properties of the two directions (Direction 0 and Direction 90), the crack propagates in different paths. In the 0 degree, crack kinks from beginning to 45 degree, but in the 90 degree specimens, crack goes horizontally until the very end when it kinks to 45 degree and test is terminated. Therefore, the fitted CPR functions (model parameters,  $C$  and  $m$ ) for two directions will be significantly different.

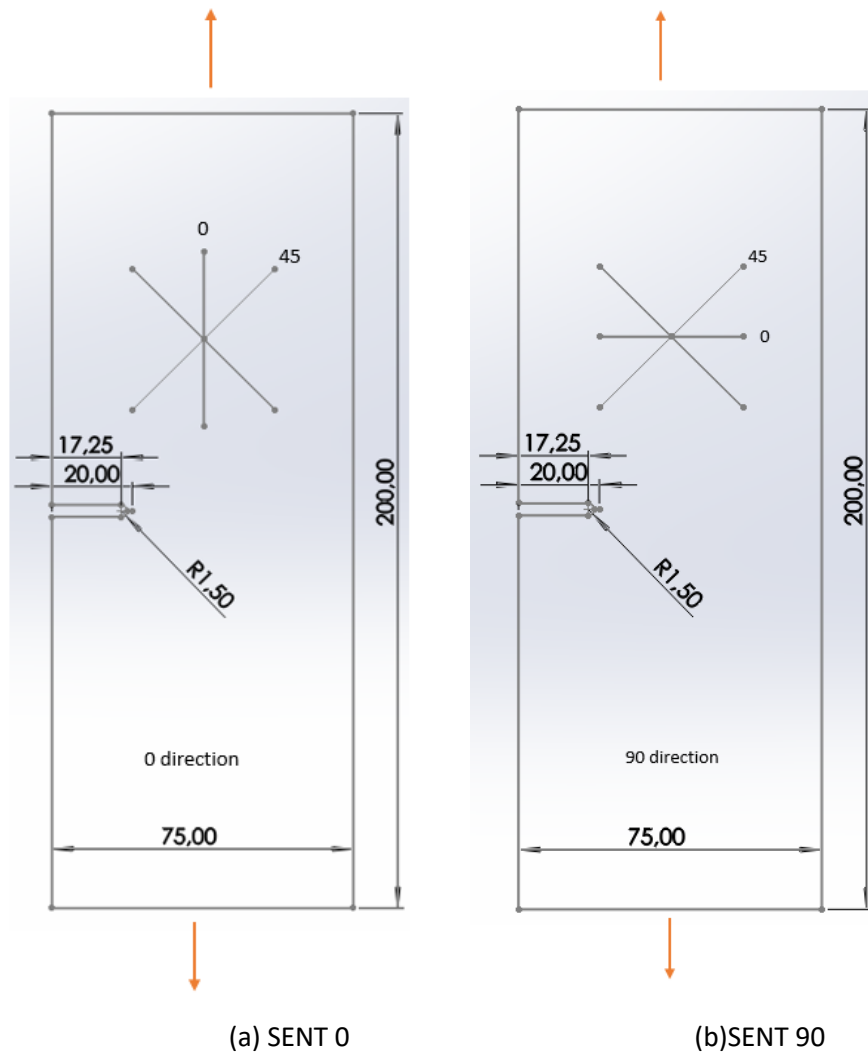


Figure 1 Schematic of Loading Condition for Test Coupons

Table 1 Basic Information of Test Set-up

Test No.	Average Coupon Thickness [mm]	Applied Force [kN]	No. of Cycles to Failure [-]
SENT-0-03	2.16	7.8	243100
SENT-0-04	2.24	9	47850
SENT-0-05	2.16	7.0	342550
SENT-0-08	2.25	6.7	2151750
SENT-0-09	2.22	7	1028800
SENT-0-10	2.23	8.5	100950
SENT-0-12	2.20	8.5	96850
SENT-0-14	2.26	7.0	508450
SENT-0-16	2.14	7.8	210800
SENT-90-04	2.29	9.0	242295
SENT-90-07	2.39	8.1	513246
SENT-90-08	2.44	8.1	645850
SENT-90-09	2.47	8.0	663679

SENT-90-11	2.49	8.6	904500
SENT-90-12	2.51	9.0	380950

## Curve Fitting of $C$ and $m$

There are two options for curve-fitting, as briefly explained as follows:

Option 1 - For one loading condition (namely Direction 0 or 90), all the test data are merged and used for curve fitting.

Option 2 - For one loading condition (namely Direction 0 or 90), curve fitting is separately done for each group of test data.

### Option 1:

For Direction 0, the fitted model parameters and the uncertainties are summarized in Table 2 and

Table 3. For Direction 90, the fitted model parameters and the uncertainties are summarized in Table 4 and

Table 5.

**Table 2 Summary of Results for CPR function - mean and standard deviations (Direction 0)**

Mean			Standard Deviations		
$\mu_m$	$\mu_{\log_{10}(C)}$	$\mu_{\sigma_{err}}$	$\sigma_m$	$\sigma_{\log_{10}(C)}$	$\sigma_{\sigma_{err}}$
4.346	-14.618	0.678	1.034	2.662	0.101

**Table 3 Summary of Results - coefficient of correlations (Direction 0)**

Coefficient of Correlations $\rho$		
$\rho_{m\log_{10}(C)}$	$\rho_{m\sigma_{err}}$	$\rho_{\log_{10}(C)\sigma_{err}}$
-0.999	$1.236 \times 10^{-7}$	$-3.093 \times 10^{-7}$

**Table 4 Summary of Results for CPR function - mean and standard deviations (Direction 90)**

Mean			Standard Deviations		
$\mu_m$	$\mu_{\log_{10}(C)}$	$\mu_{\sigma_{err}}$	$\sigma_m$	$\sigma_{\log_{10}(C)}$	$\sigma_{\sigma_{err}}$
1.926	-9.091	0.656	0.953	2.168	0.124

**Table 5 Summary of Results for CPR function - coefficient of correlations (Direction 90)**

Coefficient of Correlations $\rho$		
$\rho_{m\log_{10}(C)}$	$\rho_{m\sigma_{err}}$	$\rho_{\log_{10}(C)\sigma_{err}}$
-0.9983	$5.687 \times 10^{-6}$	$-5.876 \times 10^{-6}$

For Direction 0, the fitted  $\log_{10} [da/dN] \sim \log_{10} [\Delta K]$  curve is shown in Figure 2. For Direction 90, the fitted  $\log_{10} [da/dN] \sim \log_{10} [\Delta K]$  curve is shown in Figure 3.

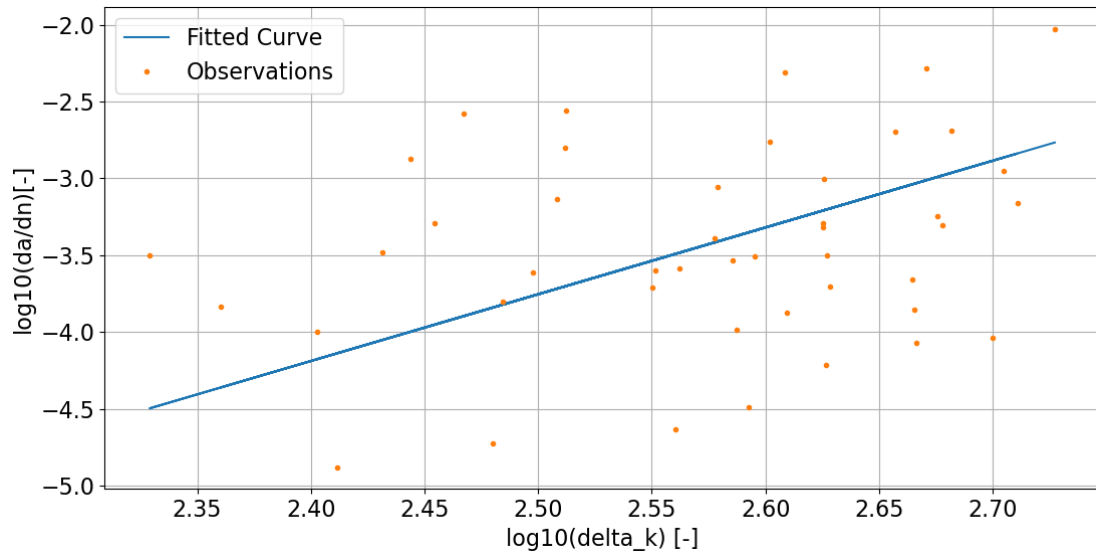


Figure 2 Fitted  $\log_{10} [da/dN] \sim \log_{10} [\Delta K]$  Relationship – Direction 0

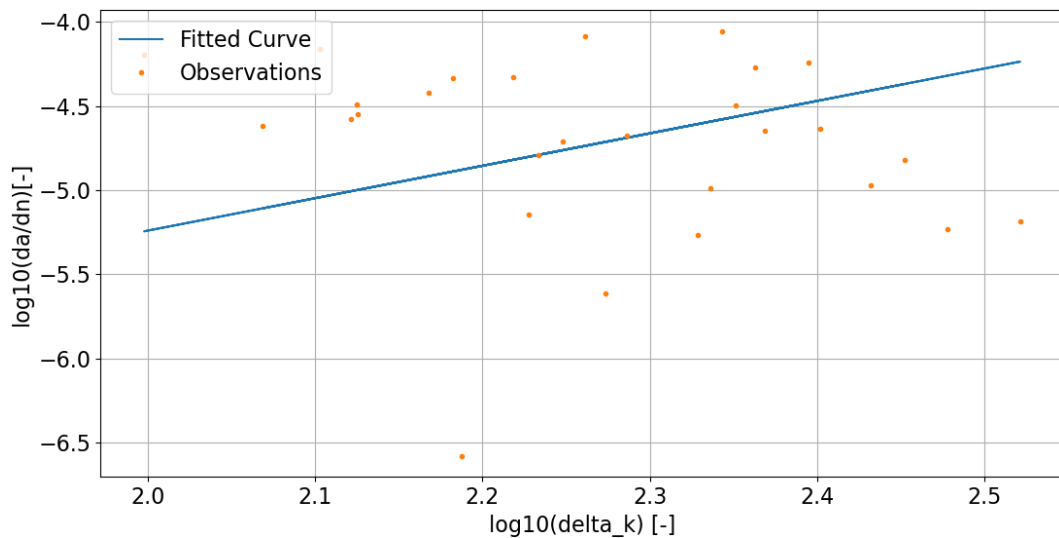


Figure 3 Fitted  $\log_{10} [da/dN] \sim \log_{10} [\Delta K]$  Relationship – Direction 90

**Option 2:**

For Direction 0, the fitted model parameters and the uncertainties are summarized in Table 6 and Table 7. For Direction 90, the fitted model parameters and the uncertainties are summarized in Table 9 and Similar to the case of Direction 0, take the arithmetic mean of  $\mu_m$ ,  $\mu_{\log_{10}(C)}$  and  $\mu_{\sigma_{err}}$  obtained in Option 2. Then, the mean values of the fitted CPR function parameters for two options are compared and given in Table 11.

**Table 11 Comparison of Means Values of CPR Function Parameter of Two Options (Direction 90)**

	$\mu_m$	$\mu_{\log_{10}(C)}$	$\mu_{\sigma_{err}}$
Option 1	1.926	-9.091	0.656
Option 2	1.991	-9.172	0.434

**Table 6 Summary of Results for CPR function – mean and standard deviation (Direction 0)**

Data Set	Mean			Standard Deviations		
	$\mu_m$	$\mu_{\log_{10}(C)}$	$\mu_{\sigma_{err}}$	$\sigma_m$	$\sigma_{\log_{10}(C)}$	$\sigma_{\sigma_{err}}$
SENT-0-03	3.055	-11.485	0.196	0.780	2.041	0.0739
SENT-0-04	1.652	-7.238	0.312	1.580	4.059	0.156
SENT-0-05	2.628	-10.212	0.187	0.770	1.957	0.0834
SENT-0-08	8.760	-26.746	0.370	3.741	9.614	0.151
SENT-0-09	5.510	-17.622	0.236	0.819	2.074	0.106
SENT-0-10	3.919	-12.944	0.290	1.475	3.863	0.145
SENT-0-12	6.352	-19.264	0.315	2.206	5.749	0.158
SENT-0-14	2.505	-10.104	0.154	0.769	1.985	0.0688
SENT-0-16	4.563	-15.009	0.0613	0.284	0.738	0.0274

**Table 7 Summary of Results for CPR function – coefficient of correlations (Direction 0)**

Data Set	Coefficient of Correlations $\rho$		
	$\rho_{m\log_{10}(C)}$	$\rho_{m\sigma_{err}}$	$\rho_{\log_{10}(C)\sigma_{err}}$
SENT-0-03	-0.9994	$1.280 \times 10^{-5}$	$-1.319 \times 10^{-5}$
SENT-0-04	-0.9992	$1.922 \times 10^{-5}$	$-1.886 \times 10^{-5}$
SENT-0-05	-0.9992	$1.041 \times 10^{-5}$	$-1.073 \times 10^{-5}$
SENT-0-08	-0.9999	$-2.748 \times 10^{-6}$	$2.753 \times 10^{-6}$
SENT-0-09	-0.9987	$-5.492 \times 10^{-6}$	$6.358 \times 10^{-6}$
SENT-0-10	-0.9992	$1.095 \times 10^{-5}$	$-1.072 \times 10^{-5}$
SENT-0-12	-0.9996	$-1.560 \times 10^{-6}$	$1.746 \times 10^{-6}$
SENT-0-14	-0.9994	$-1.263 \times 10^{-5}$	$1.262 \times 10^{-5}$
SENT-0-16	-0.9992	$2.262 \times 10^{-5}$	$-1.990 \times 10^{-5}$

Since two fitting options are used, it is of interest to compare the results of two options. Take the arithmetic mean of  $\mu_m$ ,  $\mu_{\log_{10}(C)}$  and  $\mu_{\sigma_{err}}$  obtained in Option 2. Then, the mean values of the fitted CPR function parameters for two options are compared and given in Table 8.

**Table 8 Comparison of Means Values of CPR Function Parameter of Two Options (Direction 0)**

	$\mu_m$	$\mu_{\log_{10}(C)}$	$\mu_{\sigma_{err}}$
Option 1	4.346	-14.618	0.678
Option 2	4.327	-14.514	0.236

**Table 9 Summary of Results for CPR function – mean and standard deviation (Direction 90)**

Data Set	Mean			Standard Deviations		
	$\mu_m$	$\mu_{\log_{10}(C)}$	$\mu_{\sigma_{err}}$	$\sigma_m$	$\sigma_{\log_{10}(C)}$	$\sigma_{\sigma_{err}}$
SENT-90-04	1.591	-8.051	0.208	0.745	1.759	0.0931
SENT-90-07	0.586	-5.917	0.275	1.543	3.553	0.138
SENT-90-08	3.259	-12.212	0.369	2.481	5.672	0.165
SENT-90-09	3.912	-13.497	1.183	5.441	11.697	0.592
SENT-90-11	2.132	-9.847	0.412	1.666	3.766	0.214
SENT-90-12	0.463	-5.508	0.158	0.589	1.310	0.0792

**Table 10 Summary of Results for CPR function – coefficient of correlations (Direction 90)**

Data Set	Coefficient of Correlations $\rho$		
	$\rho_{m\log_{10}(C)}$	$\rho_{m\sigma_{err}}$	$\rho_{\log_{10}(C)\sigma_{err}}$
SENT-90-04	-0.9986	$-8.711 \times 10^{-6}$	$6.948 \times 10^{-6}$
SENT-90-07	-0.9924	$3.200 \times 10^{-6}$	$-3.042 \times 10^{-6}$
SENT-90-08	-0.9996	$6.320 \times 10^{-6}$	$-5.916 \times 10^{-6}$
SENT-90-09	-0.9987	$4.600 \times 10^{-7}$	$-2.599 \times 10^{-7}$
SENT-90-11	-0.9990	$-8.672 \times 10^{-6}$	$8.711 \times 10^{-6}$
SENT-90-12	-0.9981	$5.542 \times 10^{-6}$	$-6.058 \times 10^{-6}$

Similar to the case of Direction 0, take the arithmetic mean of  $\mu_m$ ,  $\mu_{\log_{10}(C)}$  and  $\mu_{\sigma_{err}}$  obtained in Option 2. Then, the mean values of the fitted CPR function parameters for two options are compared and given in Table 11.

**Table 11 Comparison of Means Values of CPR Function Parameter of Two Options (Direction 90)**

	$\mu_m$	$\mu_{\log_{10}(C)}$	$\mu_{\sigma_{err}}$
Option 1	1.926	-9.091	0.656
Option 2	1.991	-9.172	0.434

### Estimation of $a_0$

According to Eq. (10), the mean and standard deviation of the initial defect size,  $a_0$ , are 1.98mm and 1.30 mm.

### Fitting of S-N Curve

For Direction 0, the S-N fitting results are summarized in Table 12 and

Table 13. For Direction 90, the S-N fitting results are summarized in Table 14 and Table 15.

**Table 12 Summary of Results for S-N Curve - mean and standard deviations (Direction 0)**

Mean			Standard Deviations		
$\mu_m$	$\mu_{\log_{10}(C)}$	$\mu_{\sigma_{err}}$	$\sigma_m$	$\sigma_{\log_{10}(C)}$	$\sigma_{\sigma_{err}}$
10.895	23.600	0.181	1.381	2.303	0.0605

**Table 13 Summary of Results for S-N Curve - coefficient of correlations (Direction 0)**

Coefficient of Correlations $\rho$		
$\rho_{m\log_{10}(C)}$	$\rho_{m\sigma_{err}}$	$\rho_{\log_{10}(C)\sigma_{err}}$
0.9997	$7.605 \times 10^{-6}$	$7.465 \times 10^{-6}$

**Table 14 Summary of Results for S-N Curve - mean and standard deviations (Direction 90)**

Mean			Standard Deviations		
$\mu_m$	$\mu_{\log_{10}(C)}$	$\mu_{\sigma_{err}}$	$\sigma_m$	$\sigma_{\log_{10}(C)}$	$\sigma_{\sigma_{err}}$
5.615	15.067	0.146	2.184	3.640	0.0598

**Table 15 Summary of Results for S-N Curve - coefficient of correlations (Direction 90)**

Coefficient of Correlations $\rho$		
$\rho_{m\log_{10}(C)}$	$\rho_{m\sigma_{err}}$	$\rho_{\log_{10}(C)\sigma_{err}}$
0.9999	$-9.247 \times 10^{-6}$	$-9.380 \times 10^{-6}$

## Lifetime Simulation of Crack Propagation

### Overview

The simulation-based method is used in the CAR tool. The stochastic parameters in the simplified crack propagation model are sampled from the pre-defined ranges, the upper and lower bounds of which will be determined through the engineering judgement. The purpose of setting up these bounds is to make sampling within some reasonable ranges which most likely realizations of the stochastic variables fall in.

With the specified stress ranges and the initial defect size, the code can virtually drive the initial defect to grow and decide what to do based upon the pre-chosen decision rules. In analogue to artificial intelligence, the decision rules serve to train/guide the code to automatically decide what to do, if the simulated damage reaches a certain category; and to restore the damage to a pre-defined post-repair state after repair.

A concrete example, as shown in **Error! Reference source not found.**, illustrates the working philosophy. In this example, the visual inspections are conducted every year and the decision rule DR4 is chosen. DR4, as one of decision rules, specifies that repair is only done, if the detected damage is equal to and more severe than damage category 4. The red circles represent the inspection detects the damage. Since DR4 is chosen, if and only the detected damage is D4 or even more severe than D4, it should be repaired. There are a few times the damages are more severe than D4. The damage sizes drop down to the pre-defined post-damage state, as shown in Figure 4. There is a time interval between the inspection time and the time the repair is done which is represented by a red cross. An enlarged view is plotted in to give a high-resolution view of the time interval.

The different damage propagation rates reflected in the three realizations are due to the random outcome of sampling of parameters in the simplified crack propagation model.

The crack size can be calculated based upon the following iterative computational scheme. Given the initial defect size, the iterative scheme directly uses the differential format ( $a(t_{i+1}) = a(t_i) + \Delta a$ ) to calculate the crack sizes for all the time steps until the end of lifetime or collapse.

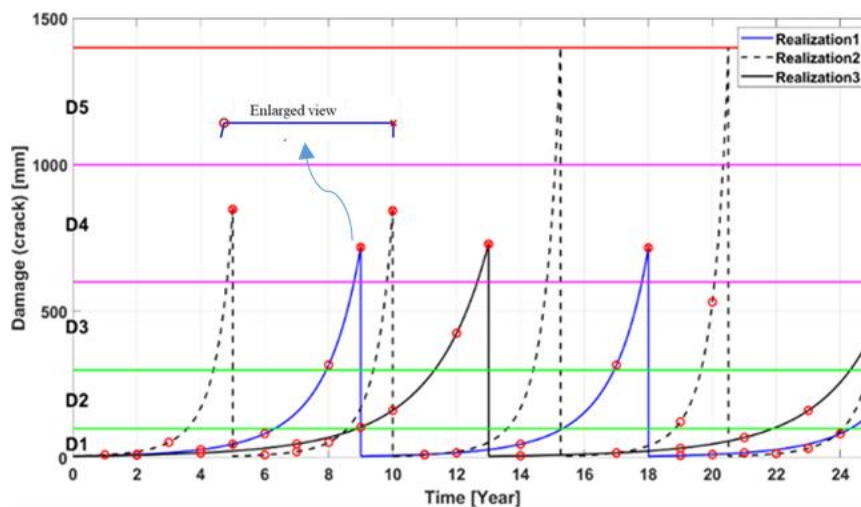


Figure 4 Three Realizations Showing Working Philosophy in the CAR Tool

## Effect of Inspection Plans and Decision Rules

Given an inspection plan and a decision rule, the code decides what to do, based upon the outcome of each inspection. First of all, the code determines whether or not the actual damage is detected, by means of simulating the inspection procedure. Then, there will be the following three scenarios for which the code decides to take reasonable actions.

- No detection.

It should be noted that 'no detection' indicates two possibilities, namely no actual damage and the actual damage is not detected. For the former case, the code moves to the next time step/ load cycle to simulate the damage size. For the latter case, the code will keep all the realizations until the next inspection.

- Detection, but the damage is less severe than the critical damage specified in the corresponding decision rule. No repair is done.
- Detection, and the damage is equal to or more severe than the critical damage specified in the corresponding decision rule. Repair should be done as soon as possible.

## Filtering Damage Propagation

The filtering approach is used when decisions are to be taken at some actual time during the design lifetime (e.g. at year 10 after installation of the blade) where the inspection and repair history is known up to that time.

The idea behind filtering is to remove/ screen out the realizations where the simulated damage states do not fulfil the physical inspection outcomes at the specific inspections already performed before the actual time.

For the operational stage, filtering is to screen out those realizations that do not satisfy the in-history inspection outcomes. The principles of filtering can be interpreted as follows:

- a total of  $N$  realizations are generated at  $t=0$ , given a combination of an inspection plan and a decision rule;
- at a certain time where the history of inspection results and repairs are known  $M_1$  realizations can be kept, if the simulated inspection results and repairs coincide exactly (the other  $N-M_1$  realizations will be removed/ screened out).

## Risk Assessment

### Overview

This section is intended to briefly present the framework of the risk assessment, which includes the decision-tree-based probabilistic analysis and the cost model quantifying the failure consequences. The theoretical basis for this framework has been documented in other separate reports issued for WP2.

## Cost Model

### Overview

In the cost model, the breakdowns of expenses in the total cost, including the inspection expenses, the repair expenses, the logistics-related expenses and the downtime expenses, will be interpreted. The approaches for calculating these expenses will be presented in the following sub-sections.

The inspection, repair and logistics-related expenses are assumed to be fixed terms (i.e. no uncertainties - it is noted that uncertainties of these parameters can easily be included). The inspection expenses may only include the expenses of the inspection activities or may include both the expenses of the inspection activities and the expenses for the technician salary and the vessel & equipment expenses. The repair expenses generally include the prices of the new components replaced for the damaged ones and the associated expenses for testing and recovering the states of the new components. The logistics-related expenses include the technician salary, the vessel expenses, and the equipment/device expenses. Sometime, there is overlapped charge between the inspection and the logistics-related expenses.

Compared with repair and logistics-related expenses, the computation of the downtime expenses is more complicated, because the downtime is a stochastic variable and closely related to the weather windows. In the following subsection, the approaches estimating the weather window will be presented.

### Approaches Estimating Weather Window

The maintenance actions are subject to the weather condition of the concerned wind turbine / farm.

An appropriate weather window is required to finish the maintenance for a specific damage category. The waiting time for an appropriate weather window should be taken into account in the decision-making process. Two typical approaches estimating the weather window will be presented as follows.

Approach 1 - based upon the actual metocean time series

This approach requires the complete metocean data to be available for the wind farms where the WTs are analyzed/ assessed for. For onshore WTs, wind speed is the primary dominating factor to be considered. For offshore WTs, wave height is another dominating factor besides wind speed. A function (`calc_wait_time.py`) can be used to estimate the waiting time according to the pre-defined weather limits (e.g. maximum wind speed and significant wave height for safe on-site operation). Generally, the following scenarios are encountered during offshore maintenance (both inspection and repair):

- Scenario 1: There are a few discontinuous periods during which the weather limits for wind and wave are satisfied, but each of these periods does not last long enough for maintenance;
- Scenario 2: There is at least one period during which the weather limits for wind and wave are satisfied, and which is long enough to perform the maintenance

Approach 2 - empirical estimation of the expected waiting time using a linear regression of the relation between maintenance (or commissioning) time and waiting time

In most cases, it is of difficulty to obtain the actual site-specific metocean data. It is suggested to start with a simplified method to estimate the waiting time based upon a database with metocean data representative for the actual site, e.g. the FINO3 database **Invalid source specified**.. The procedure estimating the waiting time will be detailed in the following paragraphs.

The real time series of metocean data (wind speed and significant wave height) contains the chronological combinations of the three aforementioned scenarios. The basic idea is to use the Monte Carlo method to randomly generate failure events (the start time of failure events) in N simulations. The waiting time is calculated in each simulation. The mean waiting time can be obtained based upon the N simulations. The flowchart in Figure 5 illustrates the simulation procedure.

The time series of significant wave height and wind speed in the FINO3 database (one year) were used as an example to demonstrate the estimated waiting time as a function of maintenance time, as shown in Figure 6. The blue dots refer to the discretized waiting time for the corresponding maintenance time. The red line represents the linear fitting against these blue dots.

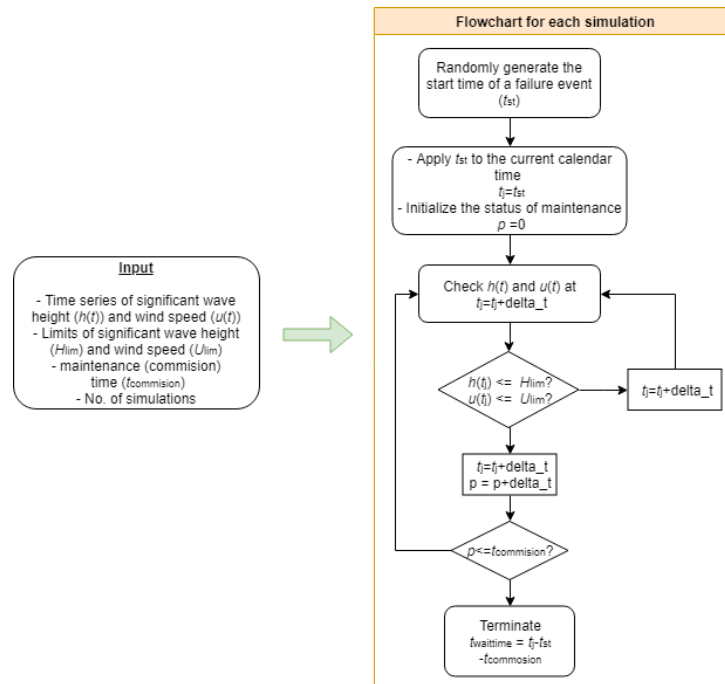


Figure 5 Flow Chart for Estimating Weather Window

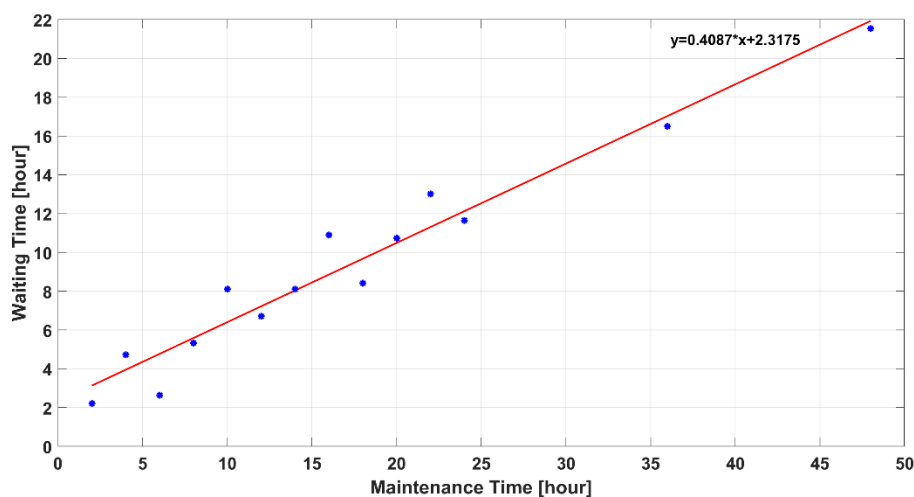


Figure 6 Waiting Time as A Function of Maintenance Time  
(The linear regression line represents the expected waiting time as a function of the required maintenance time)

## Decision Making

### Decision Tree

The classical Bayesian pre-posterior Bayesian decision theory is used as a basis for the decision-making **Invalid source specified**. The theoretical basis can be represented by a decision tree, where some branches are defined to represent decisions made at some specific time, and other branches represent random outcomes, as illustrated in

Figure 7. A decision tree is composed of decision nodes, chance nodes and consequence nodes, all of which are connected by directional links.

The decision maker chooses an inspection plan including an inspection method and an inspection interval (denoted by  $e$  in Figure 7). When the result (denoted by  $S$  in Figure 7) of an inspection is obtained and a damage has been detected, the decision maker needs to decide which type of maintenance (repair or replacement) to be chosen (denoted by the decision rule  $d(S)$  in Figure 7). Realizations of the damage growth process is denoted by  $D$  in Figure 7, and could represent total collapse. The costs (or cost-benefits) associated with each branch are denoted by  $W$  in Figure 7.

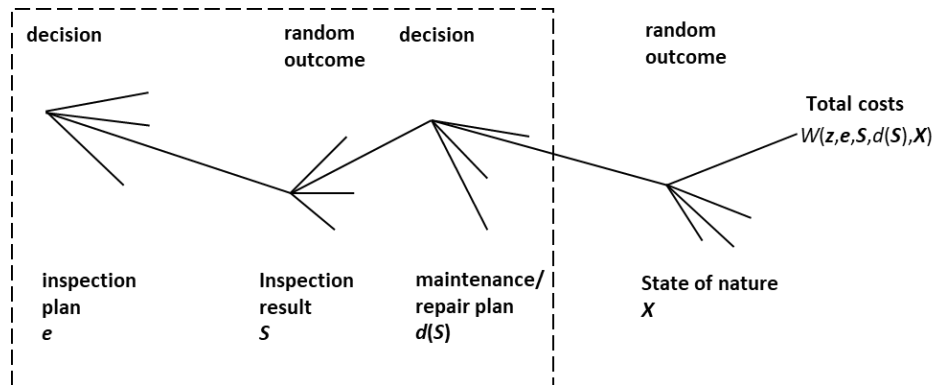


Figure 7 Generic Decision Tree for O&M Decision-making

The notations in Figure 7 can be interpreted as follows:

- $e$  - inspection plan

In the decision-making application for blades, there are the following elements to be considered in an inspection plan:

Inspection method:

Visual inspection (default) by rope access, drones, camera from boat/ ground;

Advance NDT

Inspection intervals:

Half a year, 1 year, ..., 2 year and so on. In the context of decision tress,  $e$  can be expressed as follows:

$e = \{e_1, e_2, e_3, \dots\}$ , where  $e_j$  denotes one combination of an inspection method and an inspection interval.

- $S$  - inspection outcome

Generally, there are two possibilities, i.e.  $I_1$  (undetected) or  $I_2$ (detected). According to the six-level damage categorization scheme, if a damage is detected,  $S$  can be expressed as follows:

$S = \{S_0, S_1, S_2, S_3, S_4, S_5, S_6\}$ , where  $S_0$  denotes the intact state and  $S_6$  denotes the collapse state.

Different notations/ symbols are used to differentiate the inspection outcome from the actual damage states in  $D$ . The probability of detection of  $S_i$ , given an actual damage  $D_i$ , is denoted by  $PoD(S_i | D_i)$ .

- $d(S)$  - decision rules

$d(S) = \{DR_1, DR_2, DR_3, DR_4, DR_5, DR_6\}$ , with  $DR_i$  defined in Table 16. 'R' denotes repair or replace. '-' denotes no action.

Table 16 Summary of Decision rules

Decision Rule	Damage Category					
	$S_1$	$S_2$	$S_3$	$S_4$	$S_5$	$S_6$
$DR_1$	R	R	R	R	R	R
$DR_2$	-	R	R	R	R	R
$DR_3$	-	-	R	R	R	R
$DR_4$	-	-	-	R	R	R
$DR_5$	-	-	-	-	R	R
$DR_6$	-	-	-	-	-	R

- $D$  - damage states

$D$  contains the actual damage states, as follows:

$D = \{D_0, D_1, D_2, D_3, D_4, D_5, D_6\}$ , where  $D_0$  denotes the intact state and  $D_6$  denotes the collapse state.

### Inspection Uncertainty

Nowadays, visual inspection, e.g. by drones or camera on the ground or from a boat for typical inspections, and by rope access for a few special cases, is the most common non-destructive testing (NDT) method used in inspections of WT blades. Due to the uncertainty associated with any NDT, information is needed about the probability of detection (PoD) of a damage with a given size. The PoD is used to quantify the ability of an NDT procedure for detecting a damage with a given size.

### Risk Calculation

Probabilistic analysis includes the PoD of the visual inspection method, the probabilities of being in all states before and just after inspections (prior and posterior probabilities), the transition probabilities from minor damage states to severe damage states. It should be noted that these probabilities are implicitly taken into account in the simulation. For example, the inspection outcome can be simulated by randomly sampling a number and comparing it with the simulated damage size in the realization. If the random number is smaller than the simulated damage size, it indicates the damage can be detected. In this way, PoD is taken into account. The prior and posterior probabilities and the transition probabilities are conditional ones, which depend upon the obtained information ahead of the current inspection, e.g.

when the detected damages have been repaired, whether or not the undetected damages in previous inspections can be detected in the current inspection, etc.. These probabilities should change between different realizations, due to the uncertainties of the parameters in the Paris-Erdogan law. In this way, these probabilities are implicitly considered.

Given an inspection plan and a decision rule, the risk contribution just after each inspection or after a collapse can be estimated. The code sums up all the risk contributions for each simulation and takes the expected risk for the whole lifetime (or remaining lifetime if decisions are made during operation), as given in Eq. (14), after the lifetime simulations are finished.

$$\bar{R} = \sum_{i=1}^{n_{insp}} \left[ \frac{1}{(1+r)^{t_i}} \sum_{j=1}^5 \left( \left( 1 - \sum_{t=1}^{t_i} [1 - P_{f,i,j=6}(t_i)] \right) C_{insp} + P_{repair,i,j} (C_{tech} + C_j + C_{trans}) \right) \right] + \sum_{i=1}^{t_L} \left[ \frac{1}{(1+r)^{t_i}} P_{f,i,j=6}(t_i) (C_{tech} + C_j + C_{trans}) \right] \quad (14)$$

where,  $t_L$  represents the design lifetime.  $C_{tech}$  represents the technician cost.  $C_{trans}$  represents the transportation cost.  $C_{insp}$  represents the inspection cost.  $C_j$  represents the repair cost for the damage category  $j$ .  $r$  is the discount rate.  $t_i$  is the  $i$ -th inspection time.  $P_{f,i,j=6}(t_i)$  denotes the annual collapse (i.e. D6) probability on year  $t_i$  ( $t_i$  also represents the  $i$ -th inspection time).  $P_{repair,i,j}$  denotes the repair probability for the  $j$ -th damage category at the  $i$ -th inspection.

Given the inspection plan  $e_j$  and the decision rule  $DR_k$ , the collapse probability and the repair probability at the  $i$ -th inspection are expressed in Eqs. (15) and (16), respectively.

$$P(D_6|e_j, DR_k, t_i) = \frac{n_6(t_i)}{N} \quad (15)$$

$$P(D_l|e_j, DR_k, t_i) = \frac{n_l(t_i)}{N} \quad (16)$$

where,  $n_6(t_i)$  is the number of realizations, where the blade collapses between the  $(i-1)$ -th and the  $i$ -th inspection.  $N$  is the total number of realizations.  $n_l(t_i)$  is the number of realizations, where the damage propagates to the damage category  $l$  ( $l=1,2,\dots,5$ ) just before the  $i$ -th inspection and the damage should be repaired according to the  $DR_k$ .

The terms in the first block bracket correspond to the risk contributions for the cases/realizations where no collapse occurs. The terms in the second block bracket correspond to the risk contributions for the cases/realizations where collapse occurs. All the costs should be discounted to the time the risk is assessed.

Besides the mean risk, the uncertainty of the risk should be estimated, by giving the 10% and 90% quantiles in order to provide the owner with a clear picture of the risk distribution. Because of the Monte Carlo method used, given a chosen decision rule, the 10% and 90% risk quantiles can be estimated according to all the lifetime simulations.

## Reference

- [1] "Project Report: Root Area Transition Zone - RATZ and Reduction O&M cost of WT blades, Energy Development and Demonstration Program (EUDP) RATZ project, 64015-0062," 2019.
- [2] DNV-GL, "Standard DNVGL-ST-0376: Rotor blades for wind turbines," DNV GL AS, 2015.
- [3] F. M. Jensen, "Ultimate Strength of Large Wind Turbine Blade," Department of Civil Engineering, Technical University of Denmark, Kgs. Lyngby, 2008.
- [4] C. IVS, "Guide2Defects," Guide2Defect, 06 January 2016. [Online]. Available: [www.guide2defect.com](http://www.guide2defect.com). [Accessed 17 December 2018].
- [5] F. Jensen, M. Werk, A. Buliga, T. Pardalakis, C. Berggreen, J. Waldbjoern, J. D. Sørensen, Y. Yang and T. Lindby, "Root Area Transition Zone - RATZ and Reduction O&M cost of WT blades," Energiteknologisk udvikling og demonstration (EUDP), Copenhagen, Denmark, 2019.
- [6] J. P. Waldbjoern, A. Buliga, C. Berggreen and F. M. Jensen, "Out-of-plane deformations of double-curved trailing edge sandwich panels in the root transition zone of a 34m wind turbine blade," *Composite Structures*, p. NaN, NaN.
- [7] P. Brøndsted and R. P. Nijssen, *Advances in wind turbine blade design and materials*, Woodhead Publishing, 2013.
- [8] "Data Report: Full-scale test of a LM58.7m blade with edgewise fatigue loading," Energy Development and Demonstration Program (EUDP) RATZ project, 64015-0062, Roskilde, 2019.

- [9] "Data Report: Full-scale test of a LM58.7m blade with combined static loading," Energy Development and Demonstration Program (EUDP) RATZ project, 64015-0062, Roskilde, 2019.
- [1  
0] "Data report: Full Scale Test SSP 34m blade, Combined static load," Energy Development and Demonstration Program (EUDP) Experimental Research, Phase 2 , Risø, 2010.
- [1  
1] F. M. Jensen, "Ultimate strength of a large wind turbine blade," Risø DTU, PhD Thesis, 2008.
- [1  
2] F. M. Jensen, "Floor™ Patent owned by Bladena Aps". Patent WO 2008.086205, 2008.
- [1  
3] A. B. C. B. F. M. J. Jacob P Waldbjørn, "Multi-axial large-scale testing of a 34 m wind turbine blade section to evaluate out-of-plane deformations of double-curved trailing edge sandwich panels within the transition zone," <https://journals.sagepub.com/eprint/XHMXWCNZAK6WE8WJZ7DG/full>, 2020.
- [1  
4] F.M.Jensen, "Ultimate Strength of Large Wind Turbine Blades".

Simulations

Beam four-point bending

This section describes the Finite Element (FE) model replicating the four point bending configurations on beams tested in section 2.2.

Model Description

The fatigue model consists of two FE models that are run sequentially within a fatigue loop. The workflow is depicted in Figure where the different stages have been numbered for future referencing.

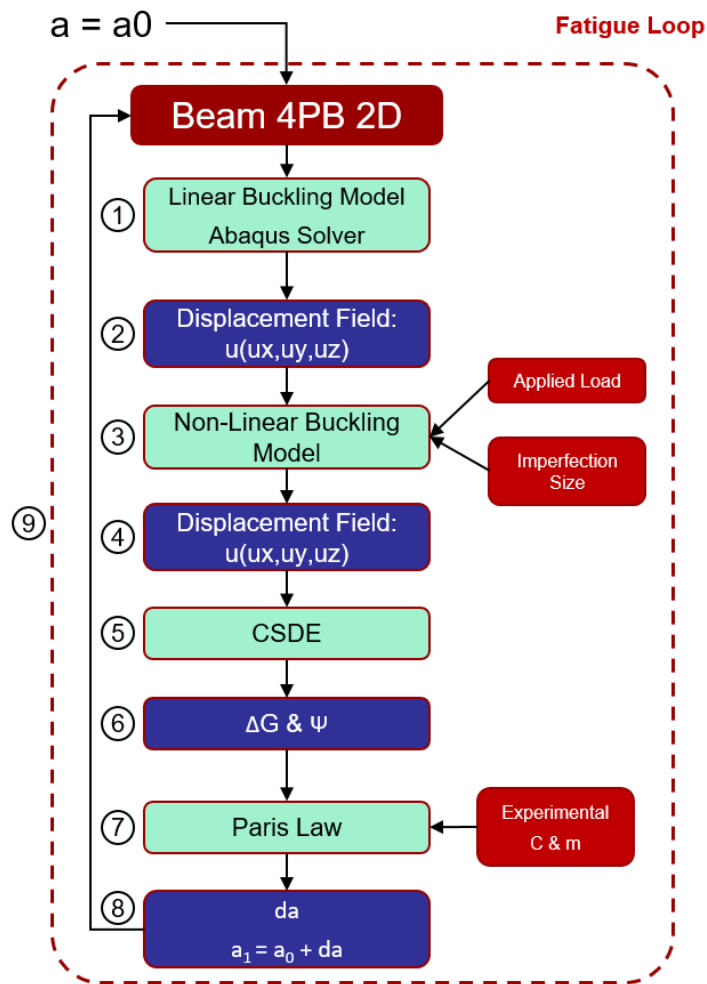


Figure 1: Beam four-point bending model workflow and fatigue loop.

## Linear Buckling Model (stages 1-2)

The first model is a 2D Linear Buckling (LB) model, which is used to obtain the linear buckling load and the deformed shape of the buckling mode of interest. The 2D model is shown in Figure 2 with a detailed view of the crack tip mesh. Such fine mesh is needed in order to apply the Crack Surface Displacement Extrapolation (CSDE) method, which is used to extract the mode I /II energy release rate  $G_{I/II}$ , and the associated mode mixity  $\psi$ .

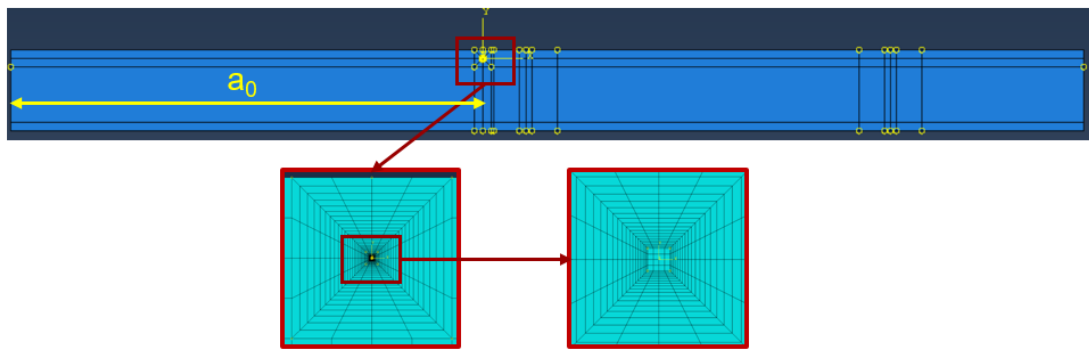


Figure 2: Beam geometry and crack tip mesh detailed view.

By definition, the linear buckling model cannot include any non-linearities. Therefore, the loading and support rollers are replaced by their linear counterparts, as shown in Figure 3.

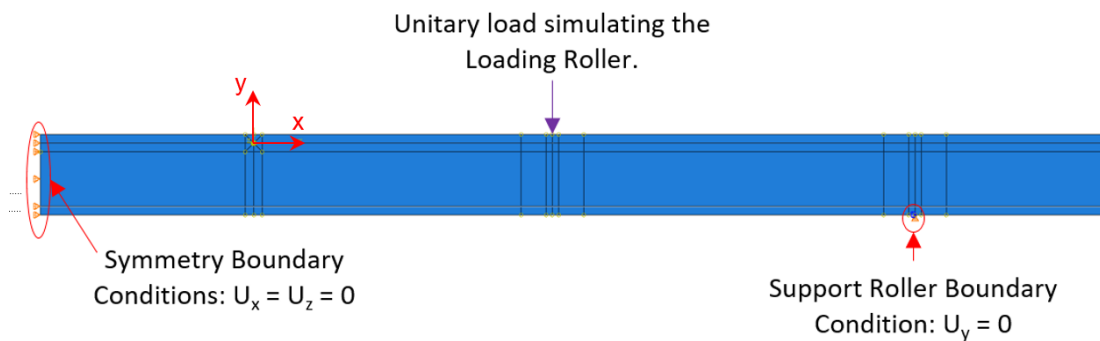


Figure 3: Linear Buckling model loading and boundary conditions.

The resulting linear buckling load  $P_{cr}$  and its associated deformed shape are shown in Figure 4 for two different damage sizes  $a_0$ , (visual scaling factor x20).

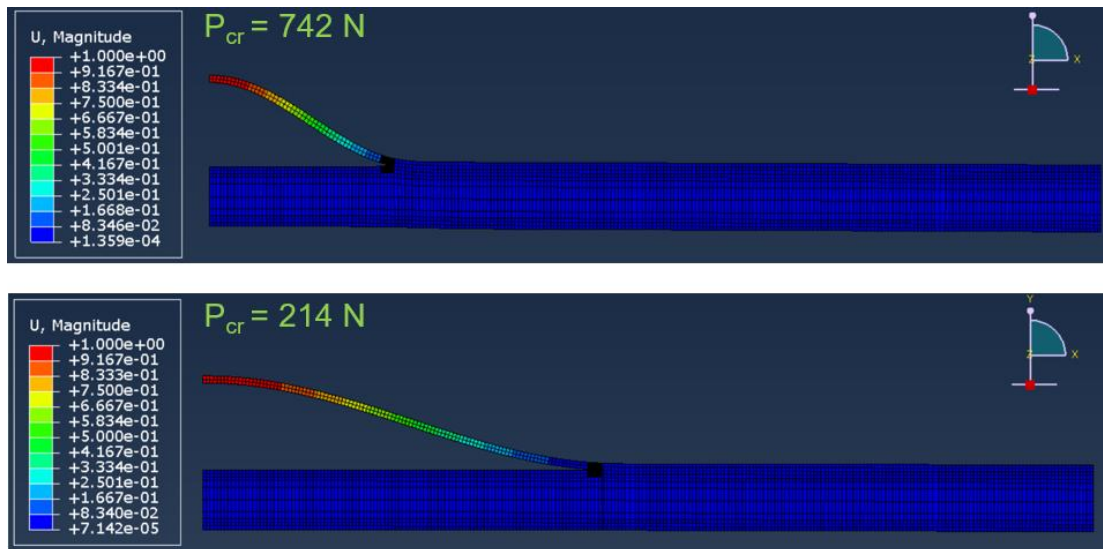


Figure 4: Linear Buckling deformed shape ; top)  $a_0 = 100$  mm ; bottom)  $a_0 = 200$  mm ; viewing scaling factor x20.

This LB model yields a displacement field normalized to a maximum value of one. The deformed shape is automatically extracted and passed on to the Non-Linear Buckling (NLB) model along.

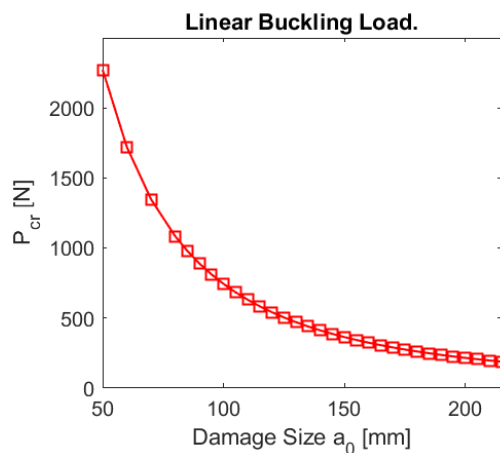


Figure 5: Linear buckling load  $P_{cr}$  vs damage size  $a_0$ .

Figure 5 shows the evolution of the buckling load against the damage size. As expected, the buckling load decreases as the damage size increases. This is explained by the fact that as  $a_0$  tends to zero the system is closer to an intact beam with no damage and therefore higher buckling load. As the damage size increases, the buckling load approaches the buckling load of the isolated facesheet, which in this case is significantly low given the high slenderness (length to thickness ratio) of the isolated facesheet.

## Non-Linear Buckling Model (stages 3-4)

The NLB model incorporates the non-linearities that were absent from the first model. The loading and support rollers are added as well as contact between them and the adjacent surfaces of the facesheets. Contact between the disbanded interfaces is also added to the system.

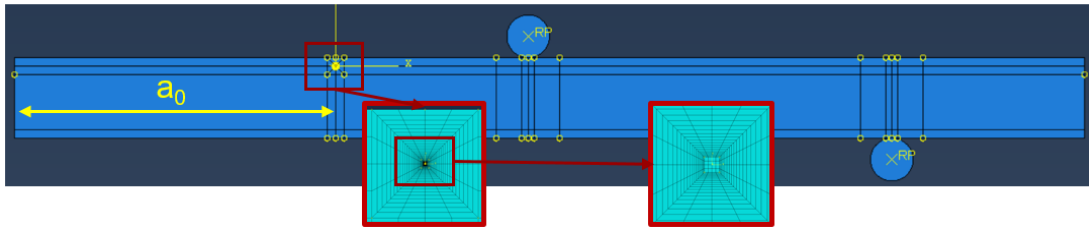


Figure 6: Non-linear buckling geometry and crack tip detailed mesh view.

The NLB model feeds from the LB model by adding the buckled deformed shape to the initial intact geometry.

The user can now select which load level to apply to the loading roller based on the application case. For instance, the experimental loads will be applied during the validation phase of the model while blade loads will be applied when using this model for design or analysis purposes.

Figure 7 shows the resultant deformed shape of a model subjected to a 30 N.m bending moment. In this case, the resulting displacements are representative of the actual load case and can be used for comparison with the experimental data. The crack flank displacements near the crack tip can then be extracted and used to derive the fracture mechanics magnitudes of interest, i.e.  $G_{III}$  and  $\psi$ .

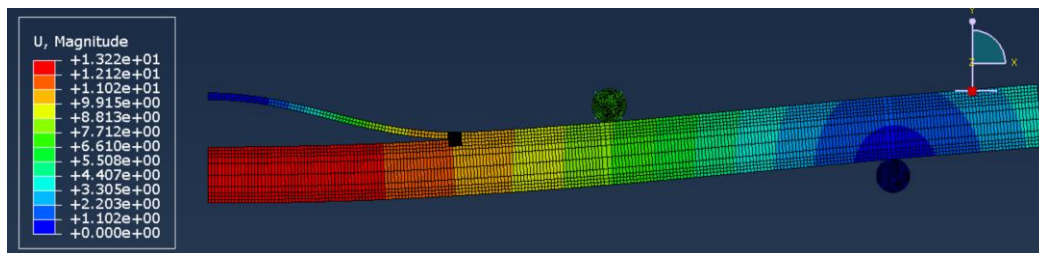


Figure 7: Non-linear buckling deformed shape.  $a_0 = 150$  mm.

## Applied Load, Applied Bending Moment and resulting Bending Stress

The propagation phenomena is largely dominated by the load level acting on the specimen. One can refer interchangeably to every design case or tested specimen by

load level applied to the rig, by applied bending moment to the beam or by resulting stress level.

### Applied Load

The four-point bending test rig consists of two loading rollers, two support rollers, a loading fixture and a slender specimen, see Figure 8. The experiment is controlled via the load  $P$  applied to the loading fixture. It is useful to refer to the specimens by applied load level within an experimental setting.

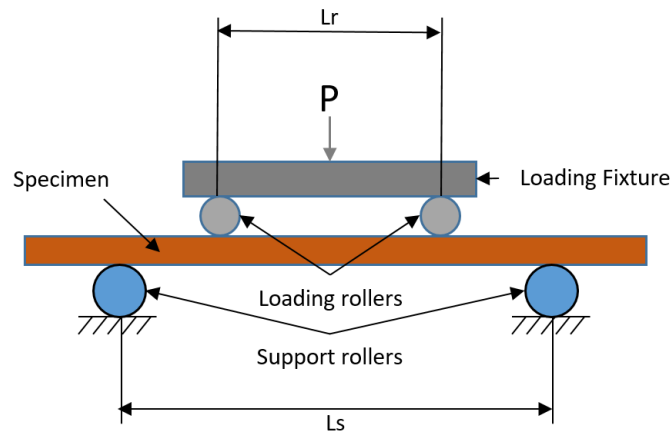


Figure 8: Four-point bending experimental setup.

### Applied Bending Moment

The geometry, loading and boundary conditions of the four point bending tests generate a constant bending moment  $M_b$  in the specimen section between the loading rollers, see Figure 9.

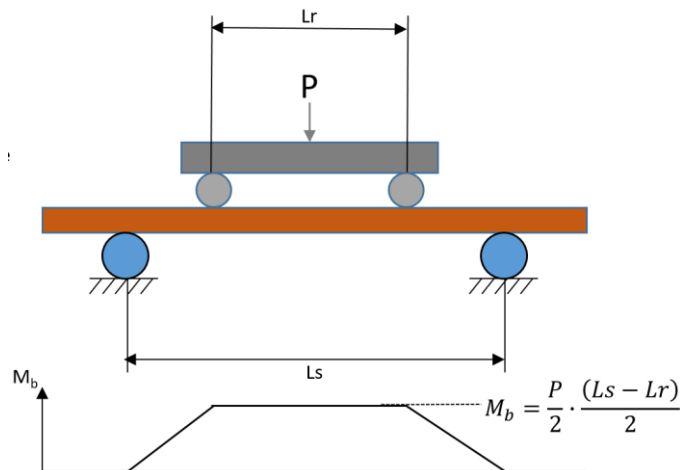


Figure 9: Four-point bending moment diagram.

## Resulting Bending Stress

This approach is more suitable for engineering applications. The associated bending stresses can be derived using basic beam theory:

$$\sigma_b = \pm E_f \cdot \left( \varepsilon_0 + \kappa_b \cdot \frac{H}{2} \right)$$

Assuming pure bending, i.e.  $\varepsilon_0 = 0$ ,

$$\sigma_b = \pm E_f \cdot \left( \kappa_b \cdot \frac{H}{2} \right)$$

Where,

$$H = t_f + t_c + t_f \quad ; \quad \kappa_b = \frac{M_b}{D \cdot b}$$

$$D = \frac{1}{3} \cdot \sum_{i=1}^3 E_i \cdot (y_i^3 - y_{i-1}^3)$$

And,

$t_f$ : Facesheet thickness;                       $t_c$ : Core thickness;                       $b$ : Specimen's width

$E_f = E_1 = E_3$ : Facesheet longitudinal Young's modulus

$E_c = E_2$ : Core longitudinal Young's modulus

$y_i$ : Interface through thickness coordinate with respect to the neutral axis.

For this particular case, the following values are taken:

Parameter	Value	Unit
$\{t_f ; t_c ; b\}$	{ 2 ; 14.72 ; 60 }	[mm]
$\{E_f ; E_c\}$	{ 14014 ; 71 }	[MPa]
$\{y_0 ; y_1 ; y_2 ; y_3\}$	{ -9.36 ; -7.36 ; 7.36 ; 9.36 }	[MPa]
D	$3.955 \cdot 10^6$	[N.mm]

Table 17: Geometry and material properties used along the report.

## Fracture Mechanics analysis (stages 5-6)

Once the LB model and the NLB model are implemented, models with increasing damage size  $a_0$  are run in order to understand the crack-tip state and its evolution as the crack propagates.

Figure 10 shows the evolution of  $G_{III}$  and  $\psi$  with increasing damage size under constant loading. It can be seen that the mixed mode energy release rate increases with the damage size. This can be explained by the fact the critical buckling load decreases with damage size as shown in Figure 5. Therefore, since the load applied to the system is kept constant, as the buckling load decreases, a higher portion of the applied load is directed to the post-buckling regime of the system, generating higher crack flank openings and therefore higher energy release rates at the crack tip.

It can also be seen that the mode mixity evolves from a mode I dominated to a mode II dominated state.

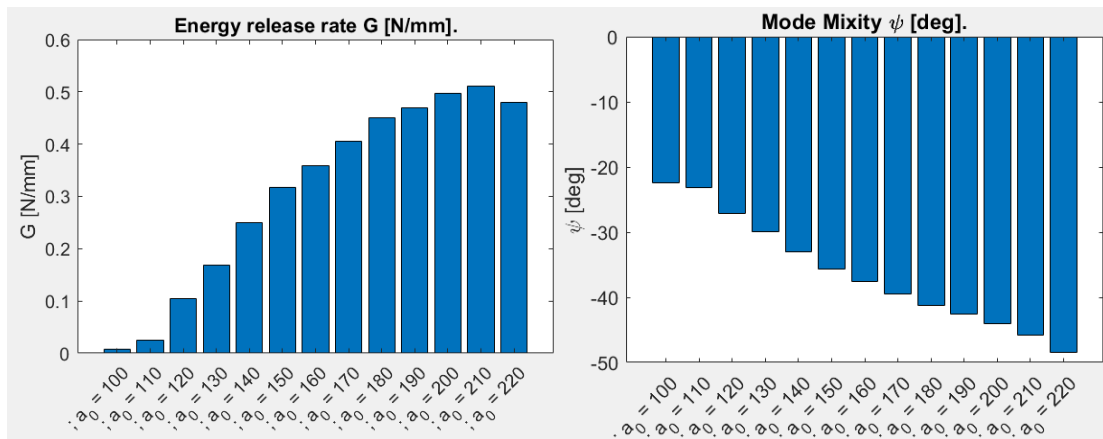


Figure 10: Left) Mixed mode energy release rate  $G_{III}$  ; Right) Mode mixity  $\psi$ ; for increasing damage size  $a_0$ .

The analysis is performed for different levels of applied bending moment; the results in terms of  $G_{III}$  and  $\psi$  are shown in Figure 11.

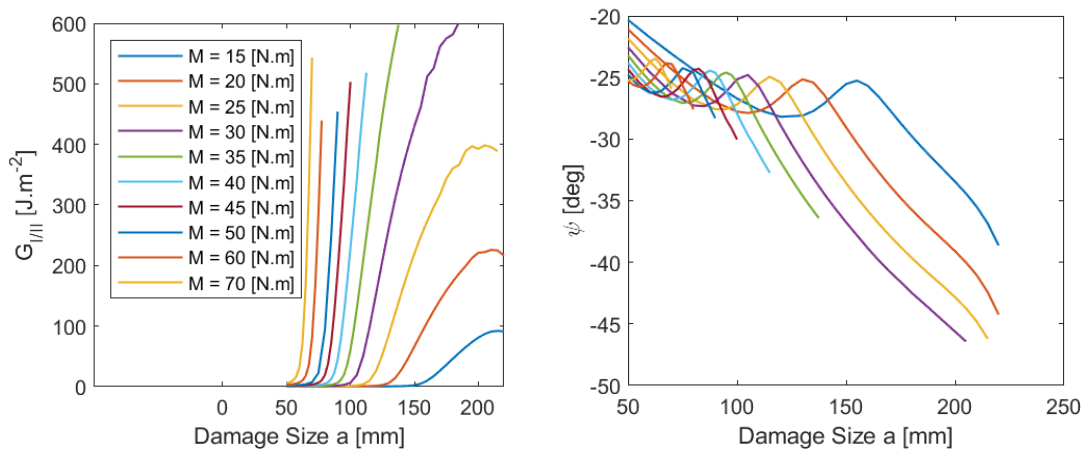


Figure 11: Left) Mixed mode energy release rate  $G_{III}$  ; right) Mode mixity  $\psi$ ; for increasing damage size  $a_0$  and different levels of applied bending moment  $M_b$ .

In terms of mode mixity, it can be seen that the trend for the mode mixity evolution is the same for every applied bending moment; all curves show an evolution from mode I dominated opening to a mode II dominated state.

In terms of energy release rate, lower load levels show a stabilization of the energy release rate at high damage size whereas higher applied load levels show an exponential growth of  $G_{III}$ . This has a significant impact on the Crack Propagation Rate (CPR) as shown in the following section.

## Crack propagation analysis

When analyzing damage propagation, the crack tip energy release rate and mode mixity are compared to reference levels in order to assess the nature of the propagation phenomenon. These levels are measured experimentally and consist of the propagation threshold  $G_{th}$  and the static fracture toughness  $\Gamma$ . There is a dependency of both these levels with the mode mixity.

$$G_{th} = F(\Psi)$$

$$\Gamma = H(\psi)$$

The static fracture toughness  $\Gamma$  is the energy release rate above which the crack propagates statically. The crack will propagate instantaneously until the energy release rate falls below  $\Gamma$ .  $\Gamma(\psi)$  is taken from ref. [1] and is as follows:

$$\Gamma(\psi) = G_{1C} \cdot [1 + \tan^2[(1-\lambda) \cdot \psi]]$$

Where  $G_{1C} = 400 \text{ J.m}^{-2}$  and  $\lambda = 0.05$ .

The propagation threshold  $G_{th}$  is the energy release rate below which propagation occurs so slowly that it can be neglected. This threshold is measured experimentally and is also mode mixity dependent. For the moment, while experimental data is generated,  $G_{th}$  is arbitrary taken as 5% of  $\Gamma$ .

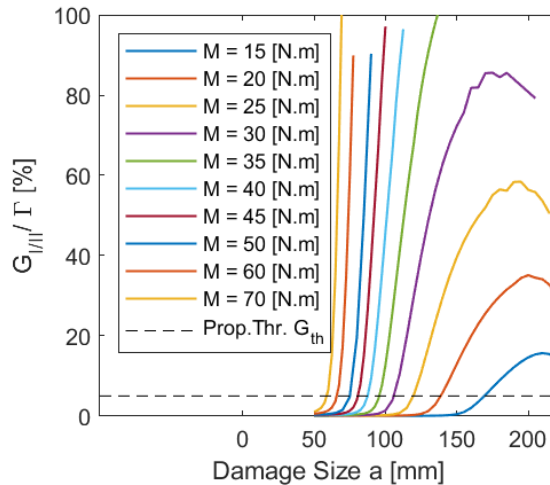


Figure 12: Normalized mixed mode energy release rate  $G_{III}$  for increasing damage size  $a_0$  and different levels of applied bending moment  $M_b$ .

Based on the data shown in Figure 12 and the energy release rate thresholds, the engineer can evaluate whether static, fatigue or no propagation at all will occur depending on the stress state and damage size of point of interest. Therefore, the propagation chart shown in Figure 13 can be generated.

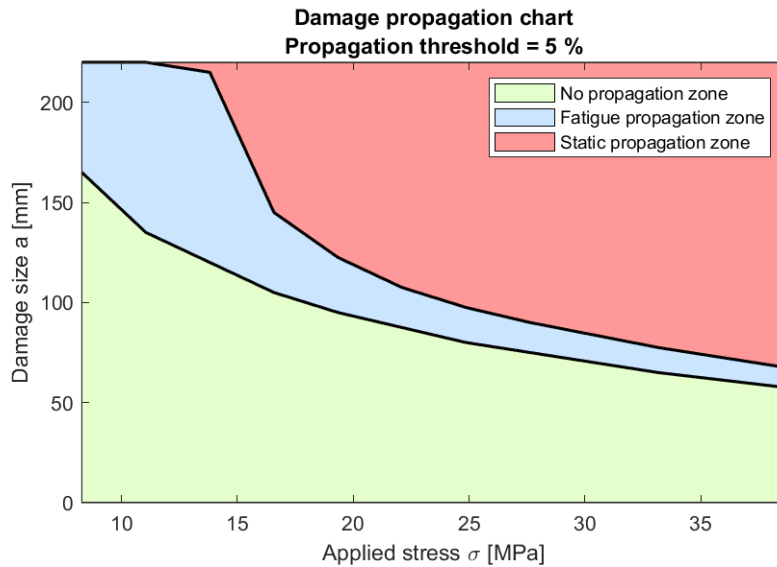


Figure 13: Stress vs damage size crack propagation chart.

The exploitation of the chart above is illustrated by means of four examples. The analysis is based on two assumptions:

- Firstly, it is assumed that the engineer knows the stress state  $\sigma_b$  of the area of interest; this can be done either via FE modeling or via experimental methods such as DIC or strain gage measurements.
- Secondly, it is also assumed that the damage size is known, this can be done via inspections on the blade or via engineering assumptions.

It is therefore assumed that the couple  $\{\sigma_b ; a_0\}$  is known to the engineer.

**Case 01:**  $\{\sigma_b ; a_0\} = \{25 \text{ MPa}; 50 \text{ mm}\}$

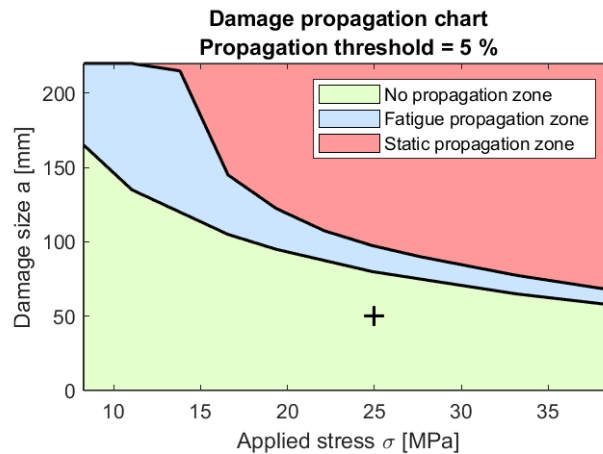


Figure 14: Stress vs damage size crack state diagram ; case 01.

The point of interest is located within the no propagation zone. It can be concluded that, based on the propagation threshold, the damage will not propagate under fatigue loading.

**Case 02:**  $\{\sigma_b ; a_0\} = \{20 \text{ MPa}; 150 \text{ mm}\}$

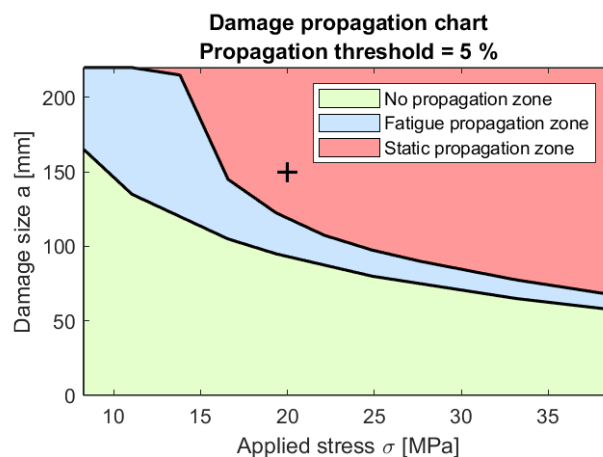


Figure 15: Stress vs damage size crack state diagram ; case 02.

The point of interest is located within the static propagation zone. It can be concluded that the damage will propagate instantly until it meets an edge or junction within the structure. This case can generate a catastrophic failure of the structure.

**Case 03:**  $\{\sigma_b ; a_0\} = \{12 \text{ MPa}; 175 \text{ mm}\}$

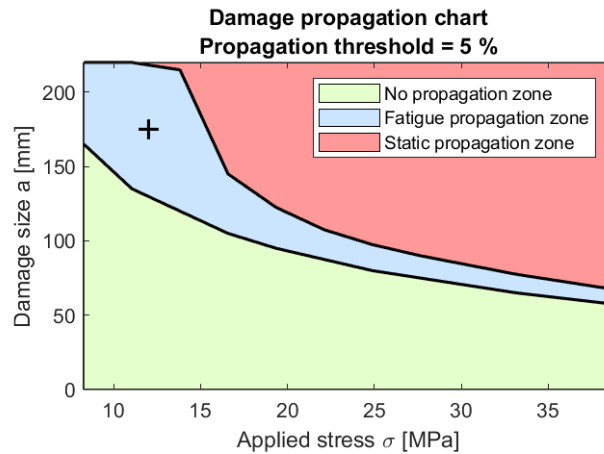


Figure 16: Stress vs damage size crack state diagram ; case 03.

The point of interest is located within the fatigue propagation zone. It can be concluded that the damage will propagate under fatigue loading. The area will need periodical inspections to ensure that the damage does not reach a critical size.

**Case 04:**  $\{\sigma_b ; a_0\} = \{77 \text{ MPa}; 30 \text{ mm}\}$

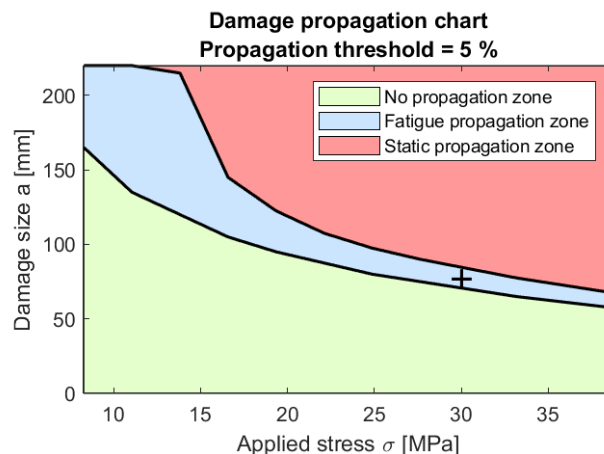


Figure 17: Stress vs damage size crack state diagram ; case 04.

The point of interest is located within the fatigue propagation zone as in case 03. However, the narrow margin between the no propagation and the static propagation

zone indicates that the propagation rate will be much higher for case 04. Therefore, a more conservative maintenance strategy should be considered

### Crack propagation rate, (stages 7-8)

Once the energy release rate has been charted for different load levels and damage sizes, it is now possible to derive the crack propagation rate functions  $da/dN$ .

A relationship between  $da/dN$  and  $G_{I/III}$  needs to be established experimentally and then introduced into the model in order to determine the crack growth during each cycle. While the experimental relation is generated, a Paris Law relation is assumed where both  $C$  and  $m$  are mode mixity dependent.

$$\frac{da}{dN} = C(\Delta G)^m$$

$$\Delta G = G_{max} - G_{min}$$

Where  $G_{max}$  and  $G_{min}$  correspond to the energy release rate at maximum and minimum load respectively within the fatigue cycle. From now on, for the sake of simplicity,  $R = G_{min}/G_{max} = 0$  and therefore  $\Delta G = G_{max} = G_{I/III}$ . The values for  $C$  and  $m$  are taken from ref. [2].

The CPR functions are generated and shown in Figure 18 for different levels of applied bending moment.

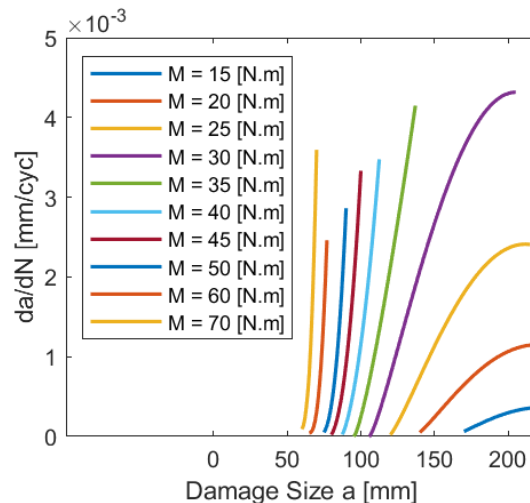


Figure 18: Crack propagation rate functions for increasing damage size  $a_0$  and different levels of applied bending moment  $M_b$ .

## Crack propagation, stage 9

At the end of cycle  $n$ , the accrued crack length  $a_{n+1}$  is calculated based on the crack growth for cycle  $n$   $da_n$  and the crack length at the beginning of the cycle  $a_n$ :

$$a_{n+1} = a_n + da_n$$

The accrued crack length at the end of cycle  $n$ ,  $a_{n+1}$  is transferred via the fatigue loop and becomes the initial crack length  $a_0$  for cycle  $n+1$ . A new FEM will be generated using the accrued crack length and a new cycle will be run according to the workflow depicted in Figure . The process continues until stopped by the user or, in this particular case, when one of the following criteria is met:

1.  $G \geq \Gamma$  → The system has reached the point of static propagation.
2.  $a \geq 220$  mm → The crack has reached the loading roller.

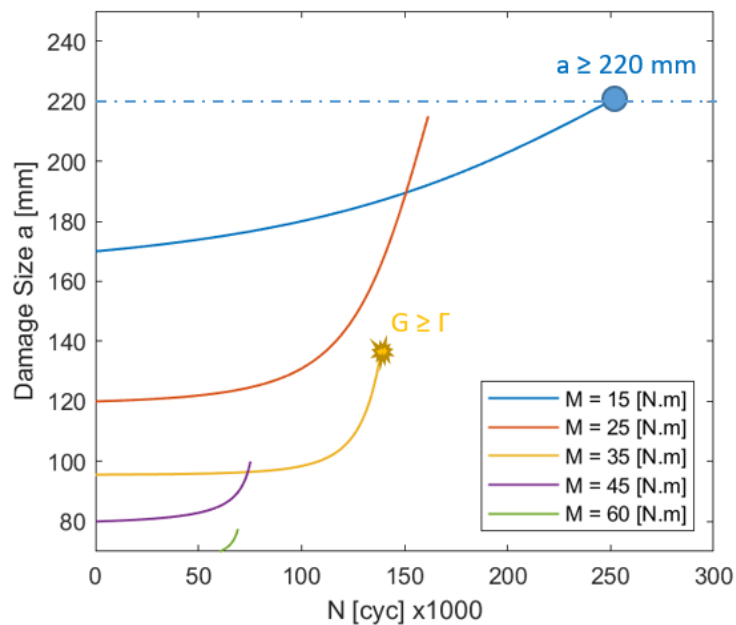


Figure 19: Damage size evolution under fatigue loading for different levels of applied bending moment  $M_b$ .

## Expected run time

The current workflow runs on four cores in DTU's high performance cluster in ca. 35 seconds per cycle. It has been seen that increasing the number of cores no longer reduces the simulation time.

This ca. half minute run time per cycle yields an estimated lead-time of 40 days for 100.000 cycles. In order to reduce the calculation time the cycle jump method described in ref [3] is applied. The cycle jump efficiency ranges between 90% and 98%, bringing lead-time under 24 hours.

## Model Validation

This section will contain a comparison between the experimental data and the numerical data once the experiments are concluded.

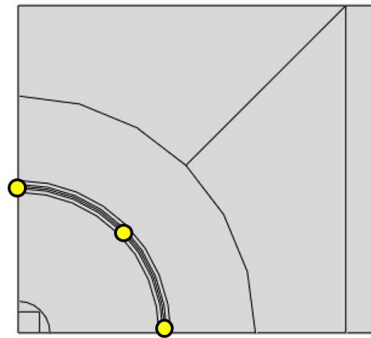
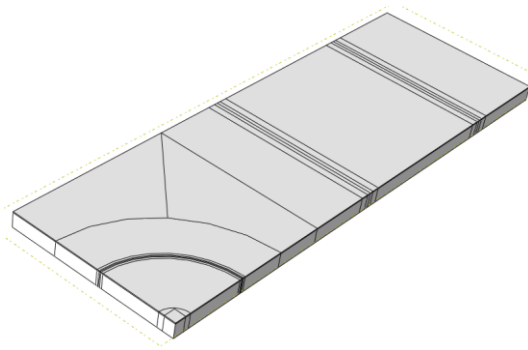
## Panel four-point bending

This section describes the Finite Element (FE) model simulating the four point bending configurations on **panels** tested in section 2.3.

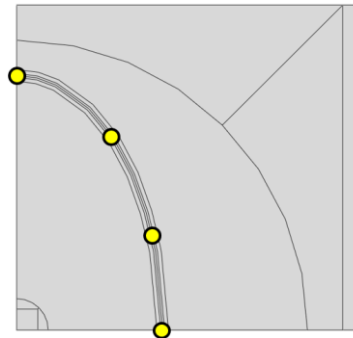
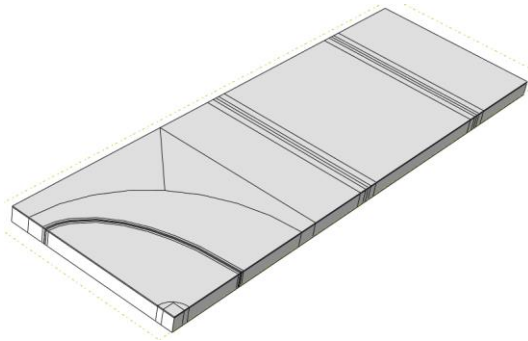
## Model Description

The fatigue model consists of three FE models that are run sequentially within a fatigue loop. The workflow follows a similar structure to the one shown in in Figure with the addition of a disbond front submodel in between the Non-Linear Buckling (NLB) model and the CSDE engine.

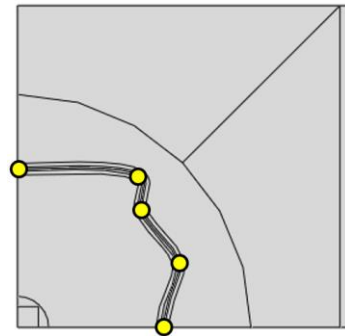
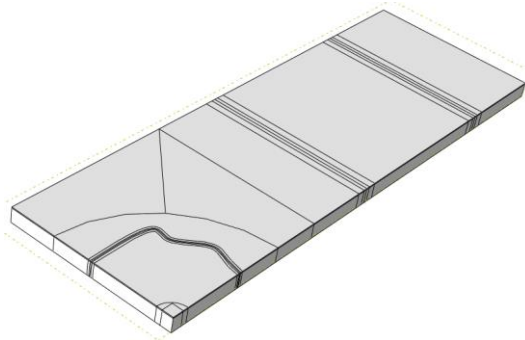
The main difference is in the modelling of the crack. In the panel model, we no longer have a 1D single crack propagating in a 1D space but a 2D disbond propagating in a 2D space. In order to simulate its propagation, the disbond front is discretized in station points. These station points are used to give shape to the disbond as well as evaluation points where the fracture mechanics engine calculates the energy release rate and mode mixity. The user no longer gives the initial crack length  $a_0$  as a single scalar input but as vector containing the coordinates of as many station points as necessary to give the disbond the desired shape. Figure 20 shows three examples on how the station points can be given to define disbonds with different shapes. Figure 21 shows the updated workflow including the submodel in between the NLB model and the CSDE engine.



a) Circular Disbond ; 3 station points ; left) 3D view ; right) top view



b) Elliptical Disbond ; 4 station points; left) 3D view ; right) top view



c) Irregular Disbond ; 5 station points ; left) 3D view ; right) top view

Figure 20: Model geometry views of different disbond shapes.

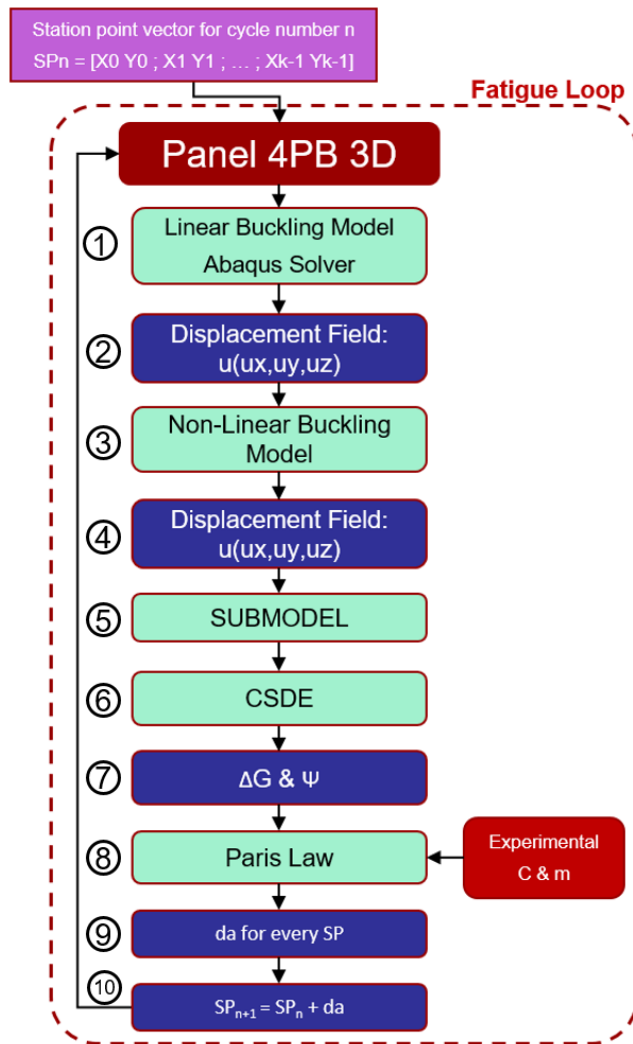


Figure 21: Panel four-point bending fatigue model workflow.

### Linear Buckling Model (stages 1-2)

As for the beam 4PB models, the first model is a Linear Buckling (LB) model, which is used to obtain the buckling load and the deformed shape of the buckling mode of interest. The 3D model is a quarter model of the panel and is shown in Figure 22. As opposed to the beam models, the LB and NLB models do not include the detailed crack tip mesh as doing so would result in a substantial increase in computational time.

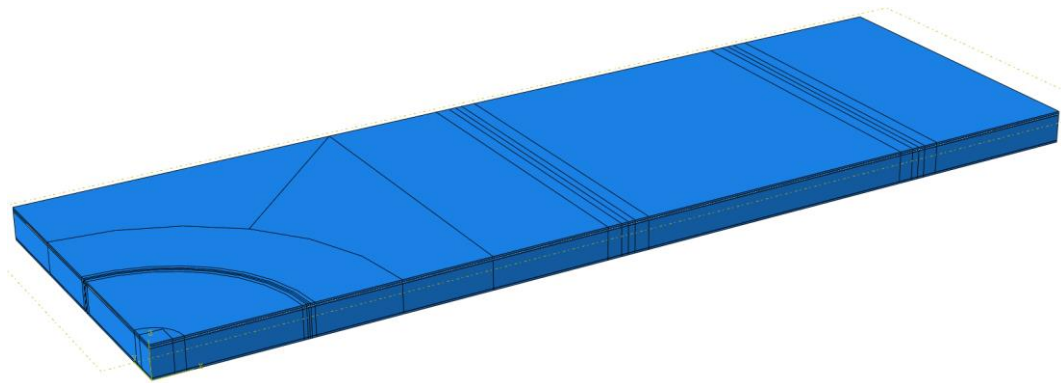


Figure 22: Linear Buckling model geometry.

By definition, the linear buckling model cannot include any non-linearities. Therefore, the loading and support rollers are replaced by linear simplifications, as shown in Figure 23 Figure 3.

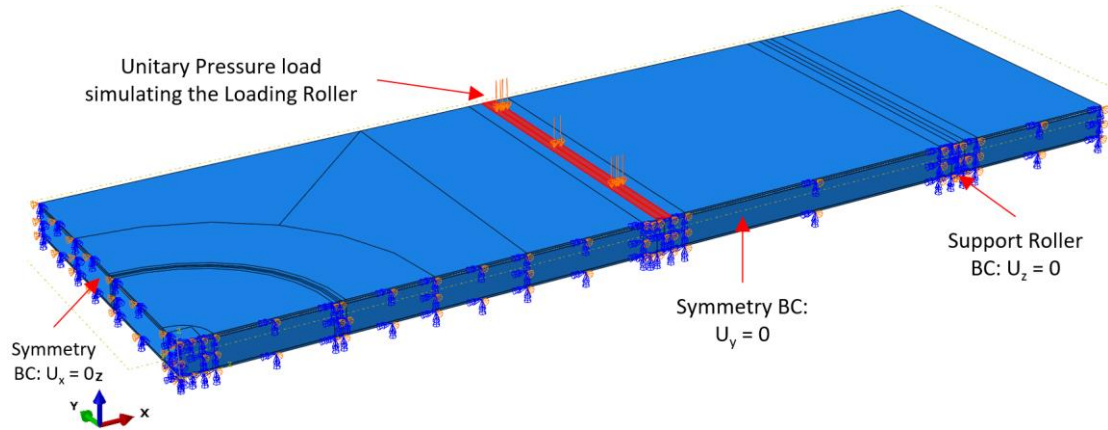
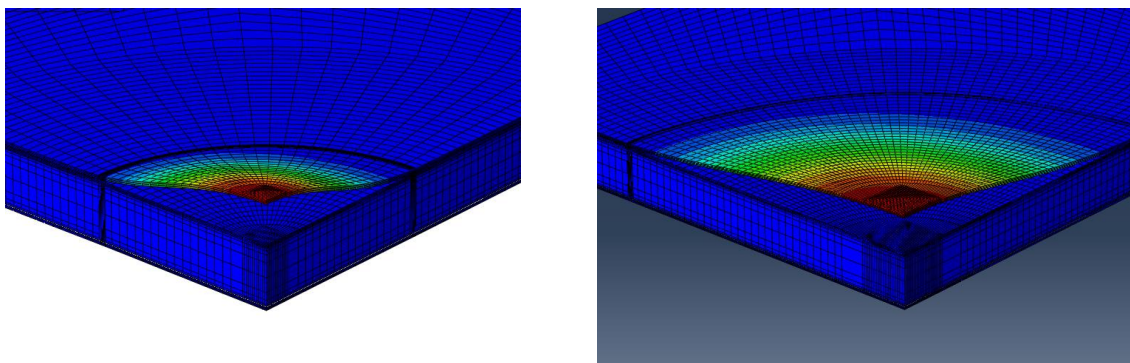


Figure 23: Linear Buckling model loading and boundary conditions.

The resulting linear buckling load  $P_{cr}$  and its associated deformed shape are shown in Figure 24 for two different disbond diameters  $D_d$ , (visual scaling factor x10).



a)  $D_d = 200$  mm

b)  $D_d = 400$  mm

Figure 24: Linear Buckling deformed shape; viewing scaling factor x10.

This LB model yields a displacement field normalized to a maximum value of one. The deformed shape is automatically extracted and passed on to the Non-Linear Buckling (NLB) model.

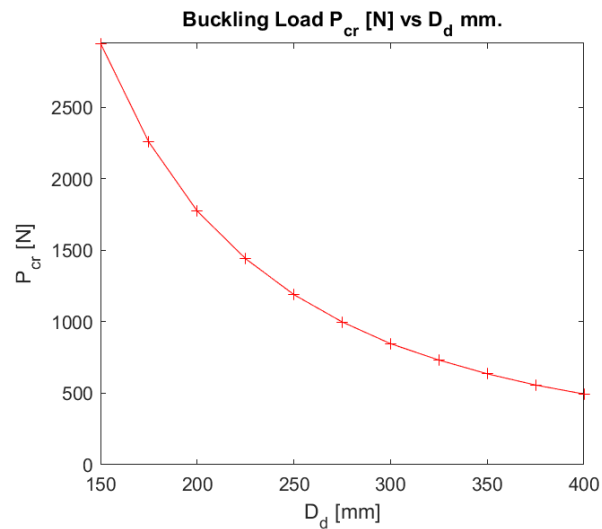


Figure 25: Linear buckling load  $P_{cr}$  vs disbond diameter.

Figure XX shows the evolution of the buckling load against the disbond diameter. As expected, the buckling load decreases as the disbond size increases. This is explained by the fact that as  $D_d$  tends to zero the system is closer to an intact panel with no damage and therefore higher buckling load. As the disbond size increases, the buckling load approaches the buckling load of the isolated facesheet, which in this case is significantly low given the high slenderness (length to thickness ratio) of the isolated facesheet.

### Non-Linear Buckling Model (stages 3-4)

The NLB model incorporates the non-linearities that were absent from the LB model. The loading and support rollers are added as well as contact between them and the adjacent surfaces of the facesheets. Contact between the disbonded interfaces is also added to the system to prevent interpenetration.

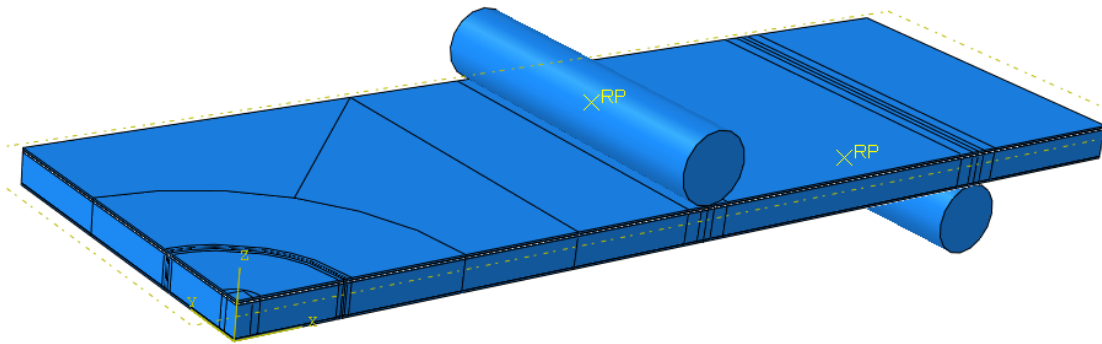


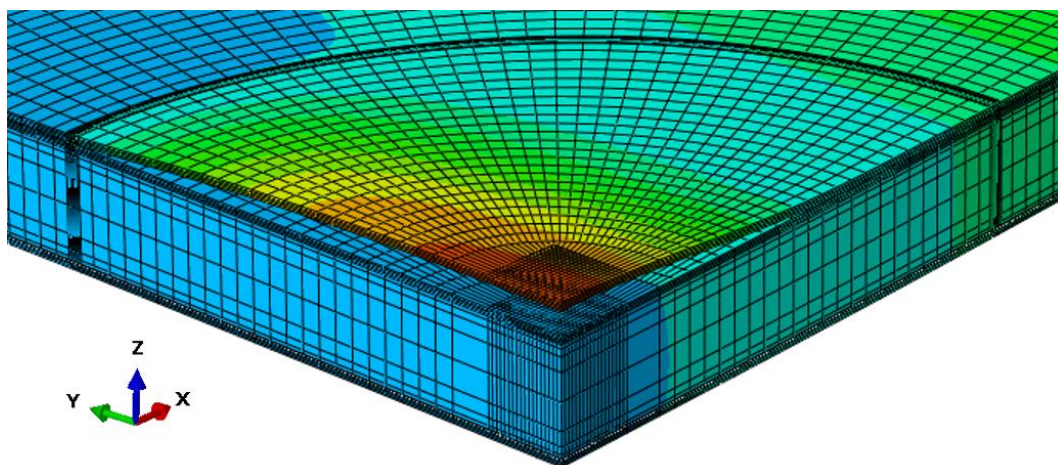
Figure 26: Non-linear buckling model geometry.

The NLB model feeds from the LB model by adding the buckled deformed shape to the initial intact geometry.

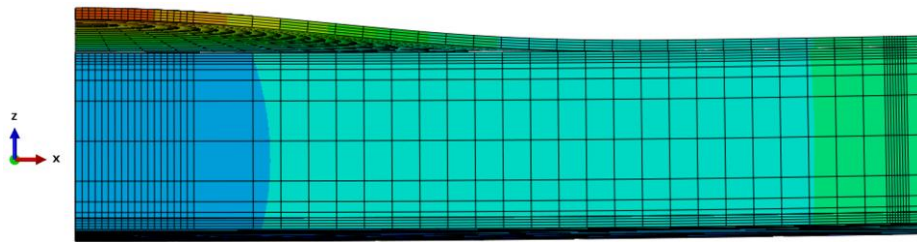
The user can now select which load level to apply to the loading roller based on the application case. For instance, the experimental loads will be applied during the validation phase of the model while blade loads will be applied when using this model for design or analysis purposes.

Figure 27 shows the resultant deformed shape of a model subjected to a 25 mm downward displacement of the loading roller. In this case, the resulting displacements are representative of the load case and can be used for comparison with the experimental data.

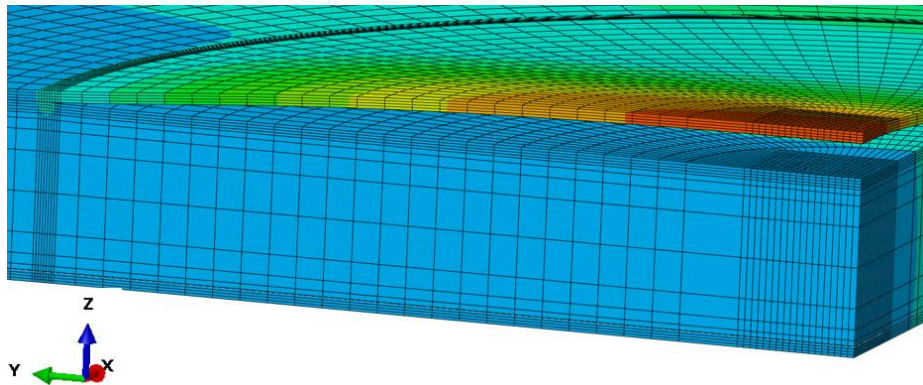
Figure 27 b) and c) show detailed views of the opening of the disbond at the crack front for the 3 and 12 o'clock positions. It can be seen that the disbond does not open uniformly. The disbond opening reaches all the way up to the crack front at the 12 o'clock position whereas at the 3 o'clock position it reaches merely 50% of the disbond diameter. This hints to a tendency of the disbond to propagate mainly along the 12 o'clock direction.



a) Global view of the disbond deformed shape



b) Detailed view of the 3 o'clock position of the disbond



c) Detailed view of the 12 o'clock position of the disbond

Figure 27: Non-linear buckling deformed shape ;  $D_d = 300$  mm.

## Applied Load vs Applied Displacement

During the testing of the beam 4PB specimens, it was quickly noticed that performing the tests under constant load/bending moment will result in a static propagation of the crack after a certain number of cycles. This is because, as the crack propagates, the buckling load decreases, and since the applied load is constant, a higher and higher portion of the injected load/energy feeds into the post-buckling regime. Consequently, the disbond opening increases as the buckling load decreases until, for a critical crack length, the fracture toughness of the interface is reached and the crack propagates statically. In order to avoid this phenomenon, the tests switched to displacement control and so did the simulations. By switching to displacement control, the applied load will decrease as the crack propagates and therefore ensuring a fatigue propagation of the crack through the entirety of the test. Once a certain level of applied displacement yields no more crack propagation, the displacement level is increased and the test continues.

### Applied Displacement

The four-point bending test rig is equivalent to the one depicted in Figure XX. The only difference is that the test is controlled via the applied displacement  $U_z$  at the actuator instead of the load  $P$ .

The FE model is implemented so that the user can select whether to drive the simulation by using applied load, applied bending moment or applied displacement.

### Submodel (stage 5)

In order to run the fracture mechanics analysis, a very fine mesh of the crack tip is needed. If this mesh were to be incorporated to the global model, the need for smooth transition elements from the crack front area to the rest of the model will yield an astronomically heavy model. This would result in a dramatically increased computational cost as well as difficulties when manipulating the different files associated with the calculation. In order to avoid this, a detailed submodel of the crack front area is automatically created based on the station points provided by the user. Figure 28 shows a view of the submodel within the context of the global model.

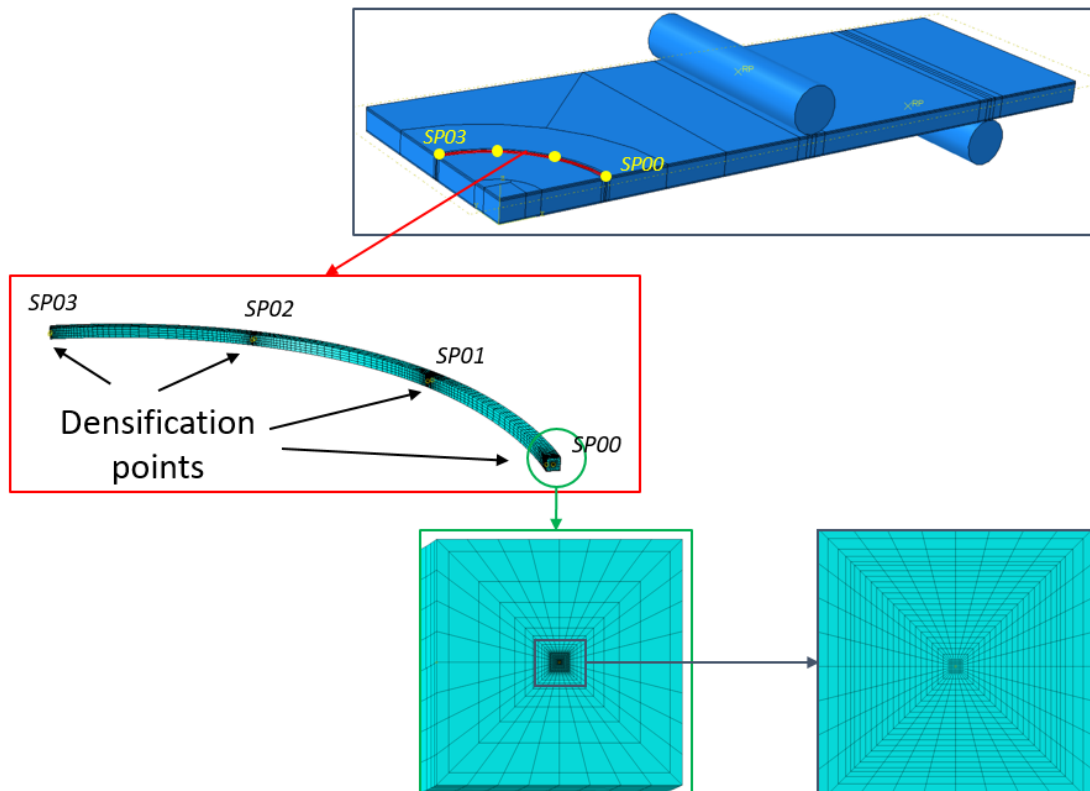


Figure 28: Top) Global model ; middle) Submodel ; bottom) Zoom on disbond front mesh.

The Submodel uses the station points as the driving points for the geometry generation as well as densification points. The mesh is locally densified along the circumferential direction ( $\theta$ ) at the station points in the circumferential direction in

order to ensure a smooth transition with respect to the very fine crack tip elements. The station points become the points where the fracture mechanic properties are evaluated via de CSDE. Therefore, from this stage of the calculation, they will be referred to as evaluation points.

Once the submodel is generated, the algorithm will automatically apply as boundary conditions to the submodel the displacements extracted from the global model at the surfaces defined as the border of the submodel. This border region must be topologically coincident between the global and the submodel. The boundary conditions can then also be seen as loads since the global model is driving the displacement of the submodel borders. No other load is applied to the submodel.

Figure 29 shows two detailed views of the disbond opening at the 12'oclock and 3 o'clock positions.

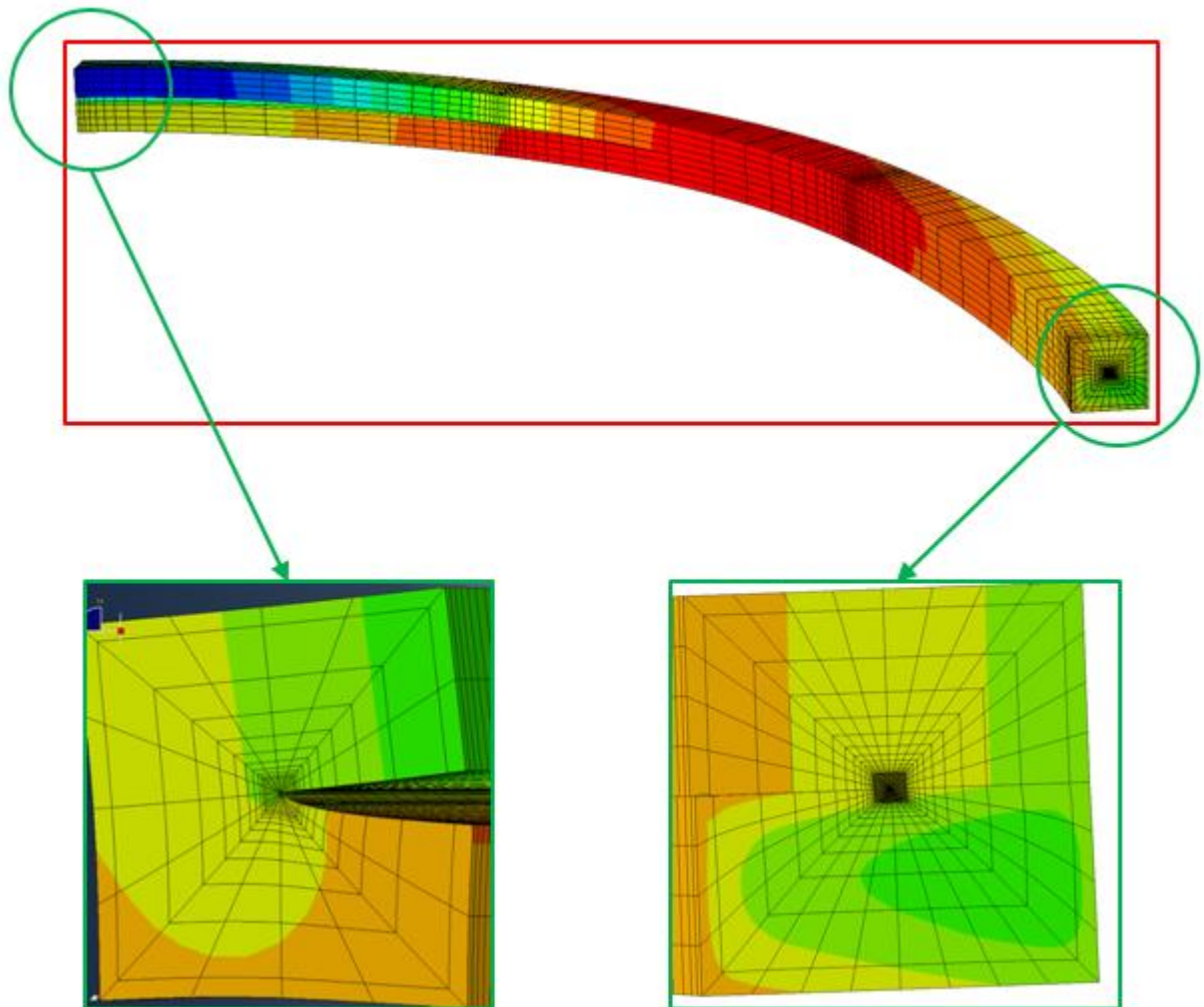


Figure 29: Top) Disbond front deformed view ; bottom) Detail views on the 12 and 3 o'clock disbond front openings.

## Fracture Mechanics analysis (stages 6-7)

Once the submodel run has concluded, the flank displacement profile at every station point is extracted and run through the CSDE engine. Studies similar to those performed in section 3.1 can be conducted. Figures similar to Figure 10 can be created with the difference that now the fracture mechanic properties are evaluated for every Station Point (SP) instead.

For instance, Figure 30 and Figure 31 show the influence of the disbond diameter in the mixed mode energy release rate  $G_{III}$  and the mode mixity  $\psi$ .

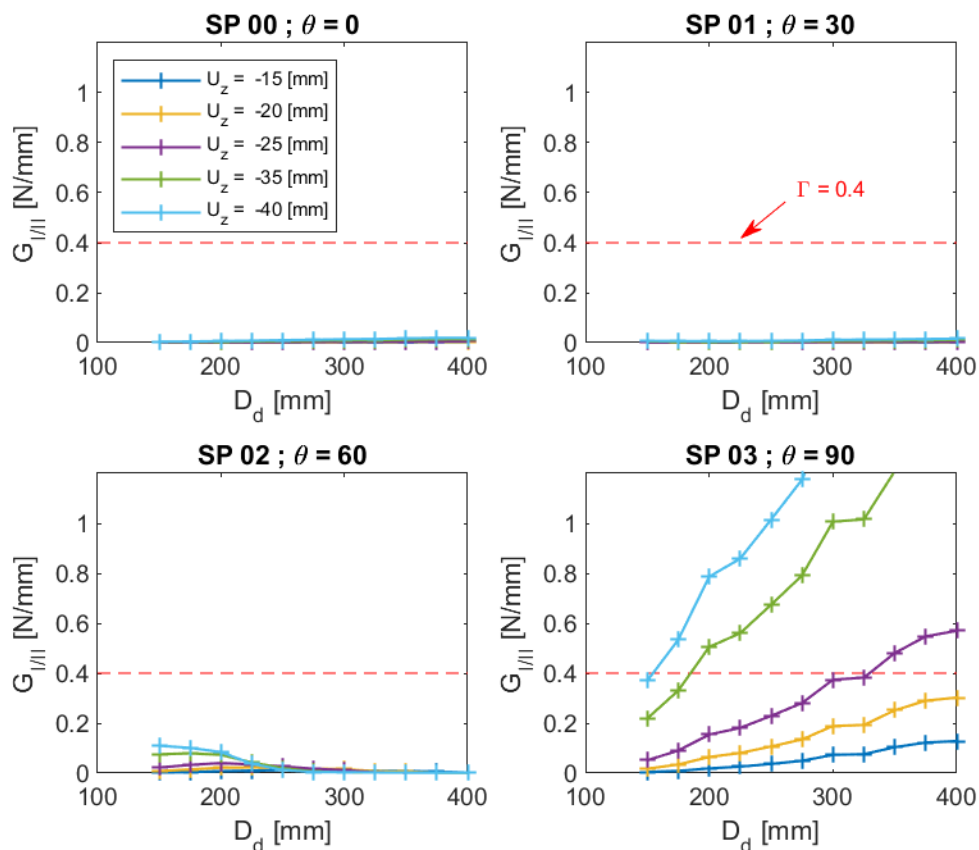


Figure 30: Mixed mode energy release rate  $G_{III}$  for different disbond diameter at 4 station points, i.e. at 4 circumferential locations.

It can be seen that most of the energy release rate is concentrated at the 12 o'clock position of the disbond front ( $\theta = 90$ ). It can then be predicted that the damage will propagate along the 12 o'clock direction first, gradually transitioning to an elliptical shape until it reaches the edge of the panel, see figure XX. The expected fracture toughness  $\Gamma_I$  for pure mode I is overlaid in the graphs (- -). Under the assumption that  $\Gamma_I = 400 \text{ J.m}^{-2}$ , for an initial diameter  $D_d = 300$  mm, the applied displacement should

be under 25 mm in order to avoid static propagation of the disbond at the 12 o'clock position.

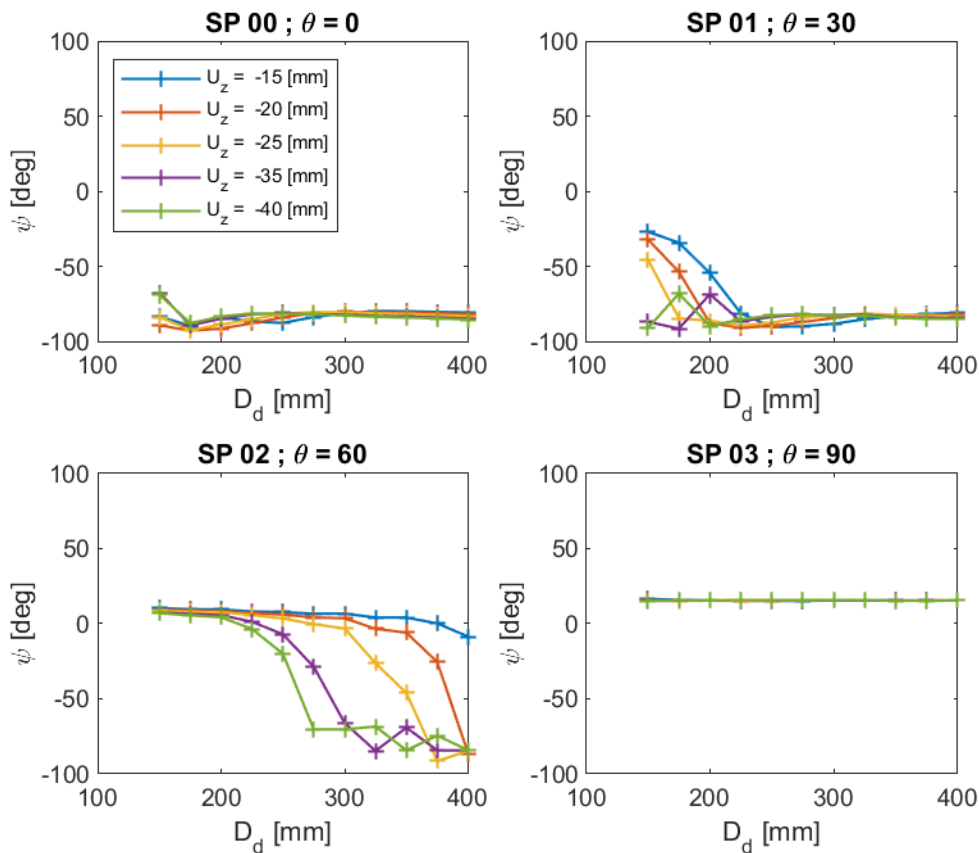


Figure 31 Mode mixity  $\psi$  for different disbond diameter at 4 station points, i.e. at 4 circumferential locations.

Regarding the mode mixity, it can be seen that, for  $D_d \geq 300$  mm, the mode mixity tends to  $\psi = -90$  deg, i.e. pure mode II, for all station points with  $\theta \leq 60$ . The mixed mode energy release rate at those station points is significantly low so the mode mixity is not expected to play a role in this station points. Finally, it can be seen that the mode mixity stays constant for  $\theta = 90$  at ca.  $\psi = +20$ . This value can be used in order to define the moment ratios at which the DCB-UBM tests need to be performed.

Since this a 3D calculation, the mode III energy release rate  $G_{III}$  can also be evaluated and is shown in Figure 32.

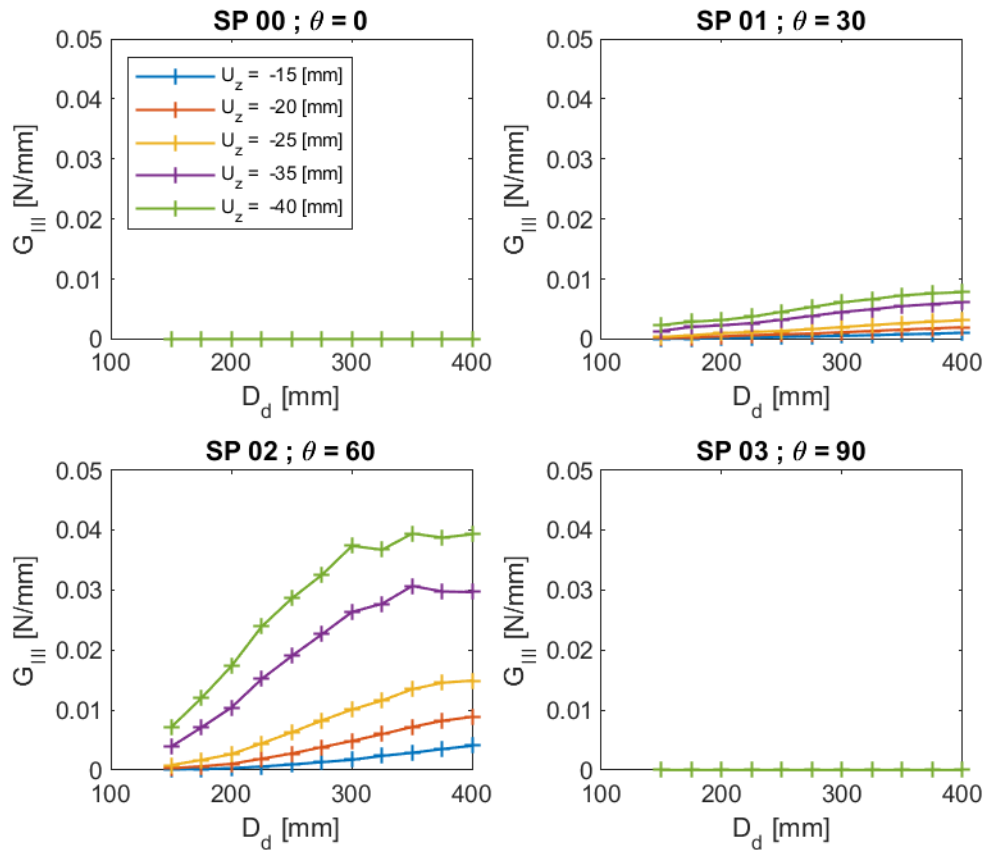


Figure 32: Mode III energy release rate  $G_{III}$  for different disbond diameter at 4 station points, i.e. at 4 circumferential locations.

It can be seen that  $G_{III}$  is mostly concentrated at the 1 o'clock position ( $\theta = 60$ ). Even though there is very few literature available for mode III fracture toughness (if any), it can be seen that the  $G_{III}$  is about 10 times higher and therefore propagation will occur mainly under mixed mode I/II. It can also be noted that  $G_{III} = 0$  at the 3 and 12 o'clock position, this is due to the symmetry boundary conditions imposed by the quarter model hypothesis.

### Crack propagation analysis

The crack propagation method for the panels under four point bending is the same as for the beam cases, refer to section 3.1.

### Crack propagation rate, (stages 8-9-10)

The disbond propagation rate is obtained following the same methodology as for the beam cases; refer to section **Error! Reference source not found.** stages 7-8 for more details.

Since the energy release rate plots show that propagation will only occur in the 90-degree station point (SP #4), the post processing focus is set on the 90-degree position going forward. Figure 0-33 shows the disbond propagation rate functions for 4 circumferential station points for the target stress levels.

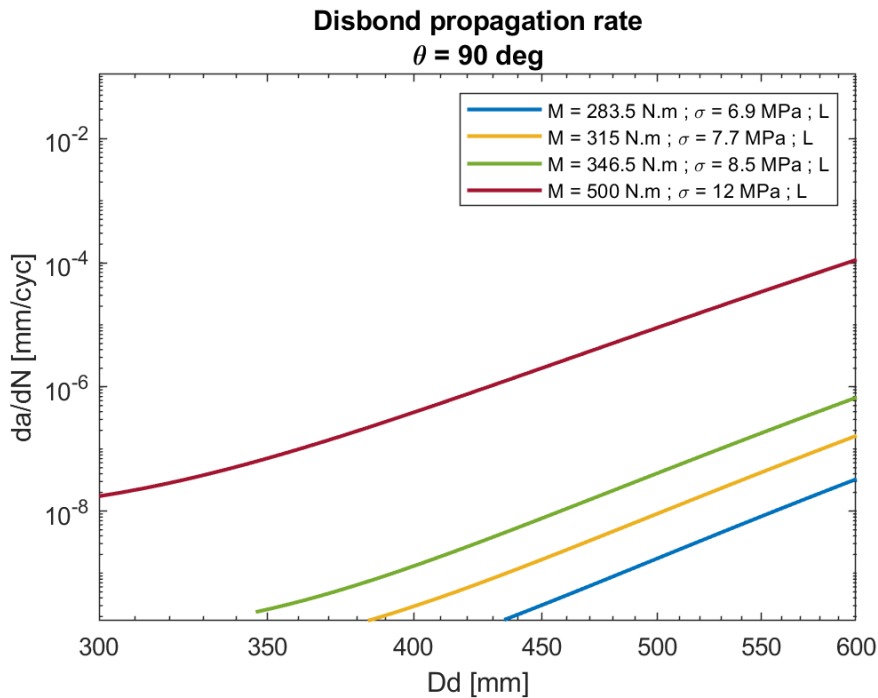


Figure 0-33: Disbond propagation rate functions for the 90 deg station point under different bending stress levels.

It can be noted that the expected propagation rate for the panel models are significantly lower than the beam models.

### Crack propagation, (stages 9-10)

The disbond propagation rate is obtained following the same methodology as for the beam cases; refer to section **Error! Reference source not found.** stage 9 for more details.

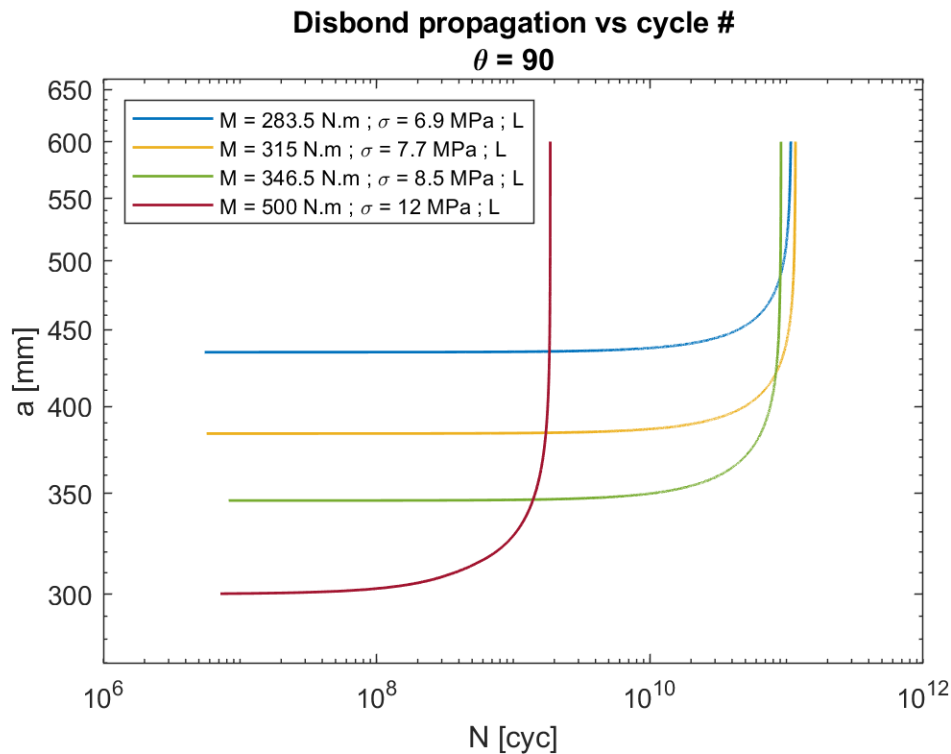


Figure 0-34: Disbond propagation rate functions for different levels of applied bending stress.

The following table displays the number of cycles it takes the disbond to reach a diameter  $D_d = 600$  mm for different initial damage sizes and stress levels. The data is extracted from Figure 0-34 and displayed in table format for convenience sake.

Table 18: Number of cycles needed to reach  $D_d = 600$  mm for different initial damage sizes  $D_d^0$ ;  $\sigma_0 = 7.7$  MPa.

$D_d^0$ [mm]	Applied Bending Stress			
	$\sigma_0 - 10\%$	$\sigma_0$	$\sigma_0 + 10\%$	$\sigma_0 = 12$ MPa
400	$\infty$	6.7e10	1.5e10	7.9e7
450	6.3e10	1.2e10	3.1e9	1.7e7
500	1.2e10	2.7e9	7.8e9	3.9e6
550	2.36e9	6.4e8	1.5e8	8.5e5

### Project Output: Damage Propagation Functions

The crack propagation functions are provided for the stress levels and laminate directions summarized in **Error! Reference source not found.** section **Error! Reference source not found.**. The disbond propagation functions are shown in Figure 0-35

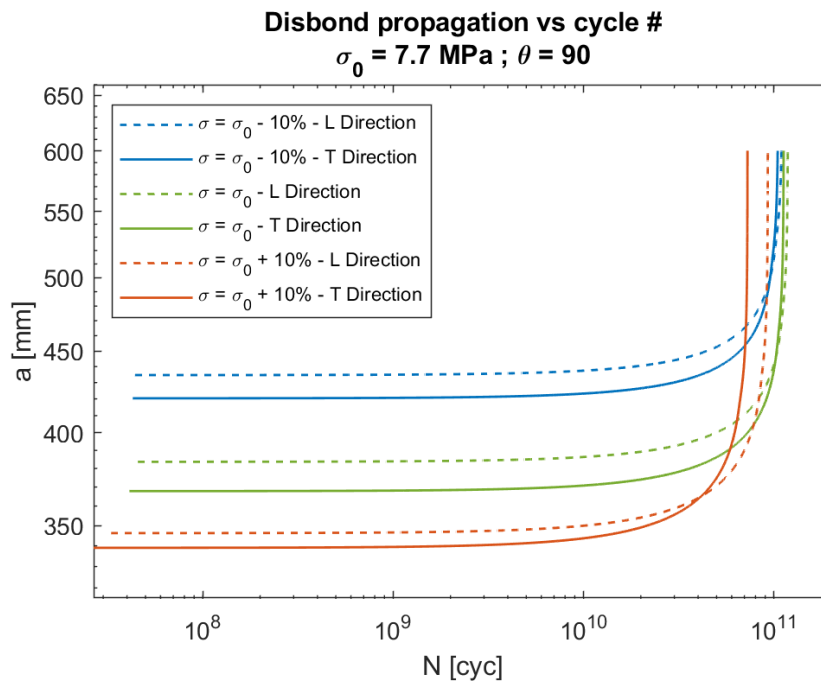


Figure 0-35: Final crack propagation functions.

The crack propagation functions have been delivered to BLADENA in six csv files.

### Model Validation

This section will contain a comparison between the experimental data and the numerical data once the experimental data becomes available.

## Appendix E Sub-Structural Fatigue Testing

### Substructural fatigue testing of a debond damaged wind turbine section

#### introduction

Transverse cracks within the transition zone and max chord region are a frequent problem of varying severity regardless of blade make and model [3]. This hypothesis is from an operational perspective, supported by the wind turbine owners (WTOs) who are reporting a gradually increasing amount of transverse cracks [4]. Believed to be the root cause of these transverse cracks, the out-of-plane deformation of the double curved trailing edge sandwich panels located at the pressure side - referred to as the gauge zone - is evaluated on the inner 15m root section of the SSP34m wind turbine blade - referred to as root section.

Utilizing the fatigue rated multi-axial test rig further described in [5], the breathing/pumping behavior of the gauge zone is evaluated with an implemented artificial debond initiated between the outer face sheet and core material. The shape of the debond is round with an initial diameter of 500mm. The longitudinal distance from the debond center to the root is 4250mm while the debond is centered between the trailing edge shear web and trailing edge in the transverse direction. This defect generates a weak zone where load concentrations are present, which in turns are responsible for the propagation of the damage. By replicating the load occurring during operation provided by wp6 within the CORTIR project, the same damages can be reproduced and a full understanding of the origin of transverse cracks in the panels is for that reason expected.

#### Artificial debond design

The artificial debond induced at the double curved trailing edge sandwich panels is round with a diameter of 500mm. It is fabricated by applying a release film between the core and outer face sheet. To accelerate damage propagation throughout the fatigue test campaign, a modification of the outer face sheet layup have been induced compared to the original. Here an initial design was introduced with a layup of 2 x biax 450g/m<sup>2</sup> - referred to here as design 1. Due to lack of bending stiffness in the outer face sheet for design 1 a new layup consisting of 1 x triax 900 g/m<sup>2</sup> along with 2 x biax 450g/m<sup>2</sup> was induced - referred to here as design 2.

#### DIC measurements

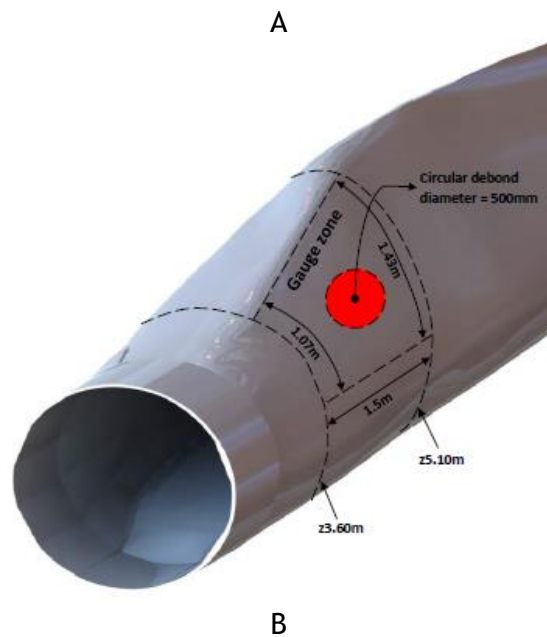
The out-of-plane deformations within the gauge zone is evaluated on the pressure side of the root section through a full-field 3D DIC system of the type: ARAMIS 12M by Gesellschaft für Optische Messtechnik mbh (GOM GmbH). The white light camera setup and performance are presented in table 1.

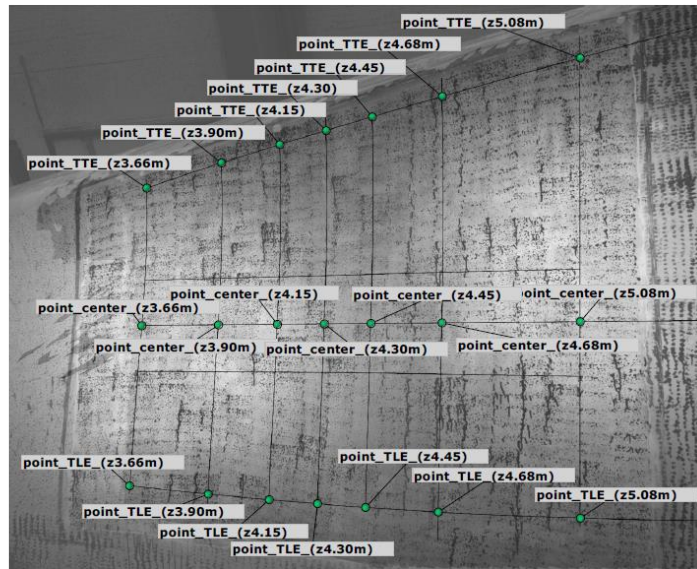
Tabel 1: Setup and performance of the 3D-DIC system

DIC zone	Gauge zone
----------	------------

Technique used	3D DIC system
Subset	40x40px
Shift	6px (85% overlap)
Camera	Dalsa Falcon2 FA-80-12M1H with an 12-bit, 4096x3072pixel CMOS (6.00µm pitch) censored and 24mm lens
Field of View	2250x1764mm (4050x2882px)
Measurement points	9531
<b>Displacement</b>	
Spatial resolution	22.23mm, 40px
<i>Resolution</i>	
In plane	0.045mm, 0.081px
Out of plane	0.090mm, 0.16px

The gauge zone along with the initiated debond between the outer skin and core material is presented in figure 1a. The out-of-plane deformation is monitored through a number of discrete measurement points located along a transverse and longitudinal path according to figure 1b and 1c respectively.





C

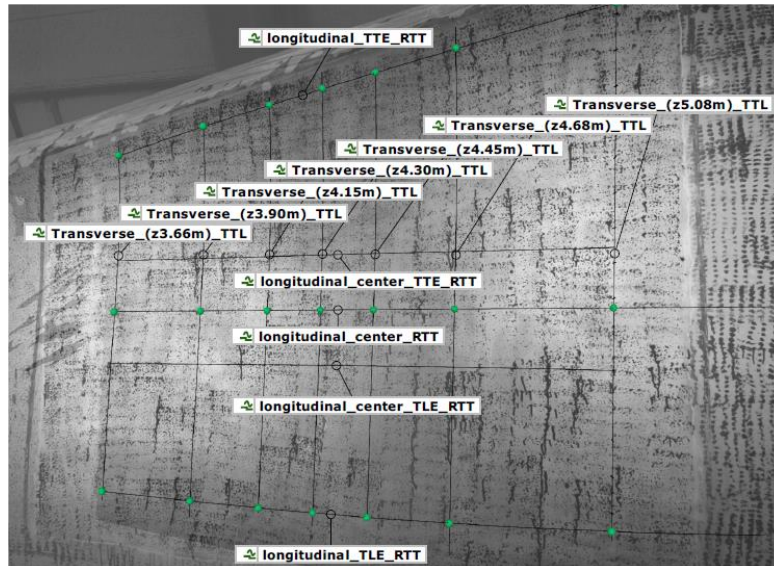


Figure 1: Location, dimensioning and labelling of gauge zone

Considering  $A(z)$  and  $C(z)$  as rigid points, the relative out-of-plane deformation of point  $B(z)$  is derived with the longitudinal distance from the root  $z$  using the rigid body removal method illustrated in Figure 2. The  $z$  - axis is running along the longitudinal axis of the blade with its origin at the root pointing towards the tip.

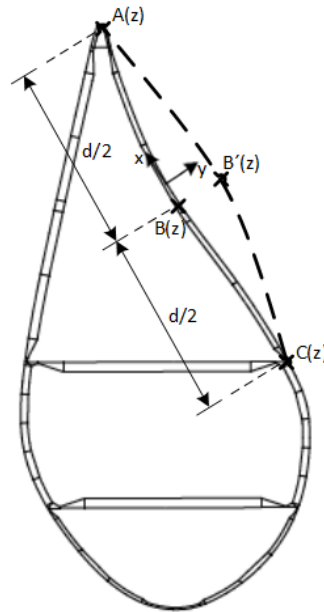


Figure 2: Principle of the rigid body removal method

Knowing the absolute measured deformation normal to the surface (along the y-axis according to the local coordinate system in Figure 2) for each of the three points named A(z), B(z) and C(z), the out-of-plane deformation  $B'(z)$  is derived according to eq. (1).

$$B'(z) = B(z) - \frac{A(z)+C(z)}{2} \quad (1)$$

The longitudinal path A, B and C in Figure 1c is discretized in a finite number of points, which are aligned in the transverse direction with the longitudinal distance to the root z. Each group of aligned points represents a cross section in which the out-of-plane deformation  $B'(z)$  is derived according to eq. (1). The transverse path is likewise discretized in a finite number of points, where point A(z) and C(z) is defined as the two outer points located at TE and after the shear web respectively. The out-of-plane deformation  $B'(z)$  along the chord width x of each of the intermediate points are derived according to eq. 1 in the trailing towards leading edge (TTL) direction.

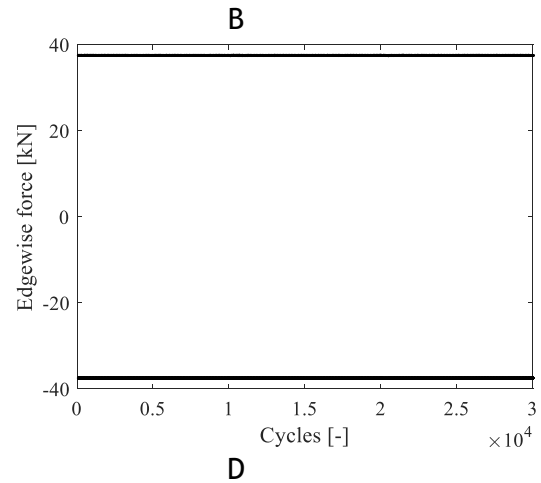
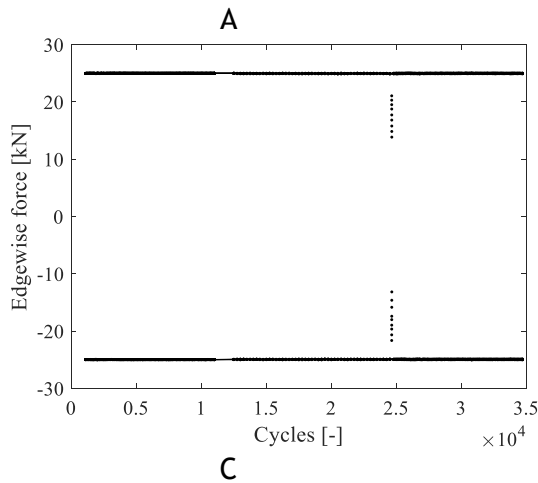
### Results

The out-of-plane deformation within the gauge zone of the root section is evaluated with a combined load configuration comprising two dofs including: edgewise loading ( $F_y$ ) and torsional moment ( $M_z$ ). Flap wise loading named  $F_x$  will remain zero throughout the entire test campaign. With a sinusoidal waveform and phase shift of 90 degrees  $F_y$  and  $M_z$  is applied with a max load of 50kN and 75kNm respectively - referred to here as a 100% load magnitude. This load configuration is according to [6] found to generate the highest magnitude of out-of-plane deformation within the gauge zone. In the fatigue test program the following fatigue test sequences are executed according to table 2 with the DIC results given in appendixes.

Table 2: Key results related to fatigue test sequence

Fatigue test sequence [-]	Number of cycles [-]	Load magnitude [%]	Frequency [Hz]	R [-]	Appendixes [-]
1	1000 (done)	50	0.1	-1	-
2	10.000 (done)	50	0.1	-1	-
3	1252 (terminated)	50	0.2	0	-
4	12.450 (terminated)	50	0.2	-1	-
5	10.000 (done)	50	0.2	-1	-
6	10.000 (done)	75	0.1	-1	-
7	10.000 (done)	75	0.1	-1	-
8	10.000 (done)	75	0.1	-1	-
9	10.000 (done)	100	0.1	-1	-
10	10.000 (done)	100	0.1	-1	-
11	10.000 (done)	100	0.1	-1	-
12	9333 (terminated)	100	0.1	-1	-
13	19.389 (terminated)	100	0.1	-1	-
14	48.207 (terminated)	100	0.1	-1	-
15	17.762 (terminated)	100	0.1	-1	-
16	5439 (terminated)	100	0.1	-1	-
17	489 (terminated)	100	0.1	-1	-
Total	195.321	-	-	-	-

From table 2 the root section is loaded with a magnitude of 50, 75 and 100% referred to here as load sequence 1, 2 and 3 respectively. Furthermore, a redesign of the artificial debond has been initiated within load sequence 3 referred to here as load sequence 3a and 3b for design 1 and design 2 respectively. The dashed line outlined in table 3 separates load sequence 3a and 3b. System performance of the hydraulics including peak and valley force achieved as a function of cycles is presented in figure 3 and 4.



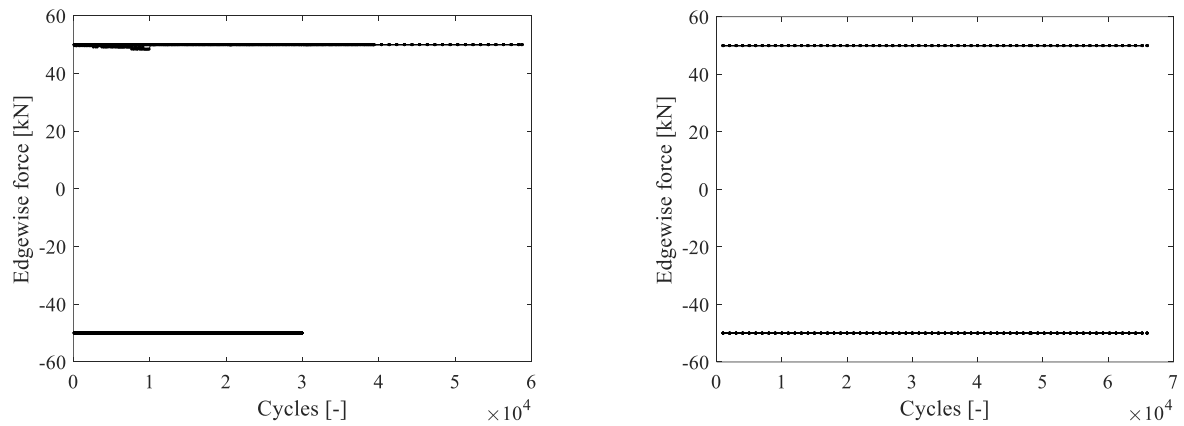


Figure 3: peak and valley edgewise force including a) load sequence 1, b) load sequence 2, c) load sequence 3a and d) load sequence 3b

From figure 3 and 4 a constant force amplitude is identified in the  $F_y$  and  $M_z$  direction throughout all fatigue test sequences. For the last cycles of fatigue test sequence 4 (see figure 3A and 4A) a sudden drop of the achieved  $F_y$  and  $M_z$  is identified due to a sudden drop of global stiffness caused by failure of the load introduction rig.

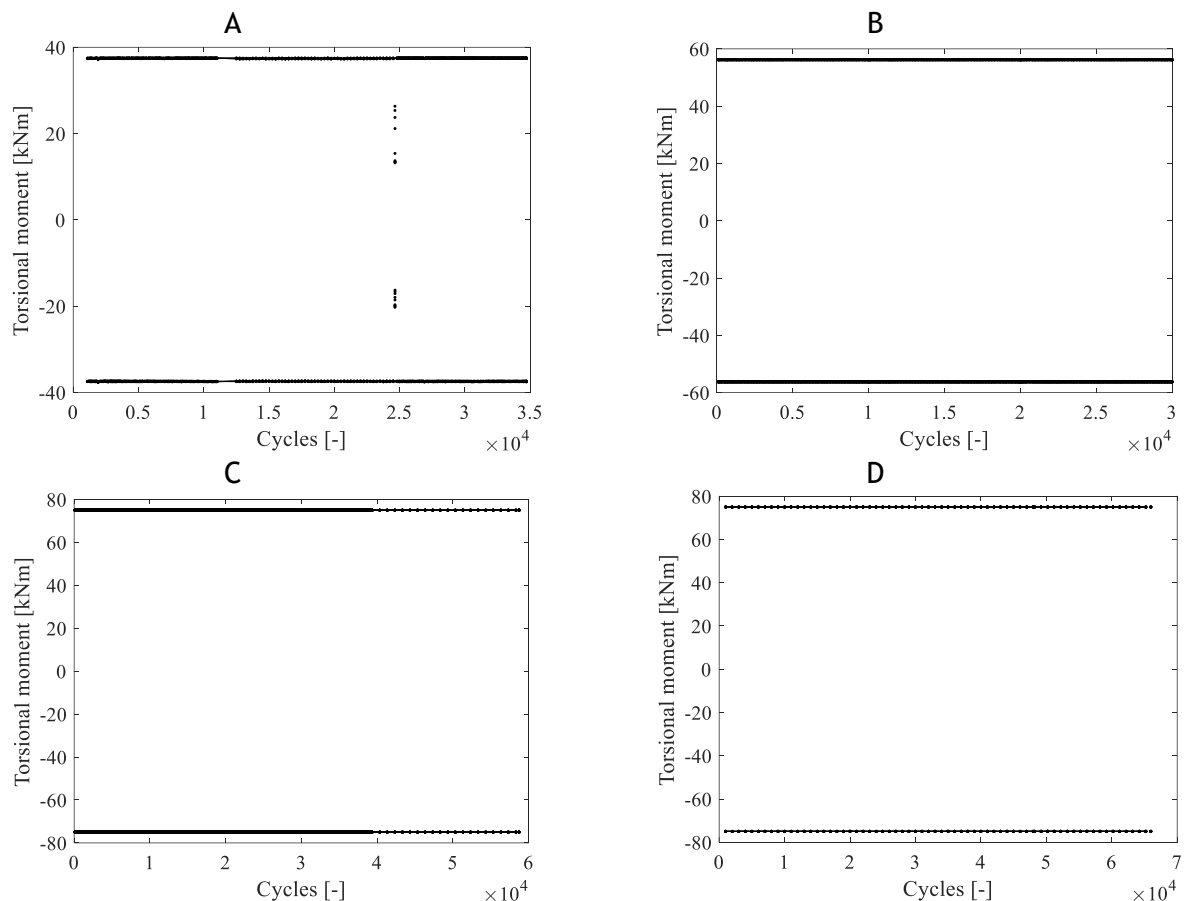


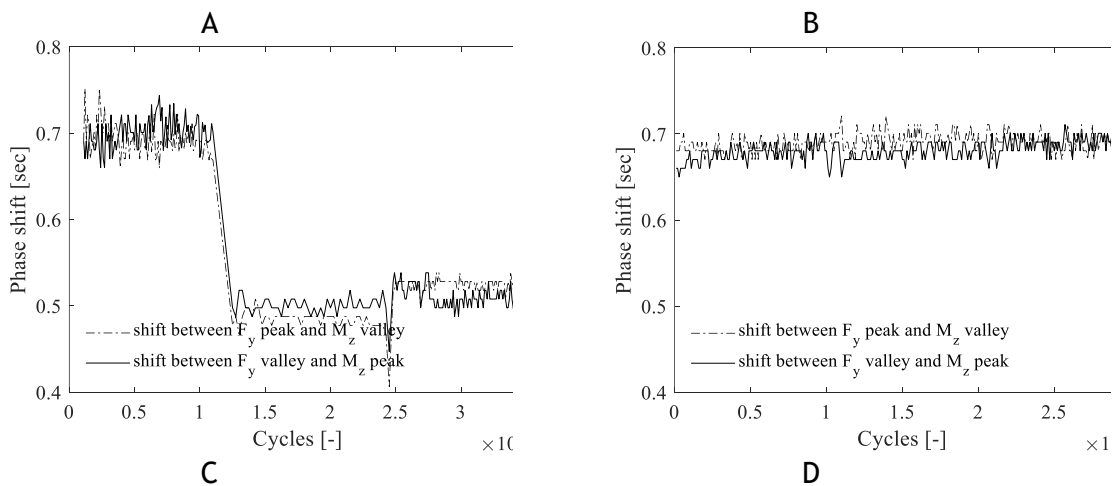
Figure 4: peak and valley torsional moment including a) load sequence 1, b) load sequence 2, c) load sequence 3a and d) load sequence 3b

The mean and standard deviation of the peak and valley load achieved for each of the three dofs including  $F_x$ ,  $F_y$  and  $M_z$  is given in table 3.

Table 3: key results related to fatigue test sequence

Test Sequence [-]	$F_x$ [kN]				$F_y$ [kN]				$M_z$ [kNm]			
	Peak		Valley		Peak		Valley		Peak		Valley	
	Mean	Std	Mean	Std	Mean	Std	Mean	Std	Mean	Std	Mean	Std
2	1.49	0.02	-1.54	0.02	24.9	0.01	-24.9	0.01	37.4	0.03	-37.5	0.03
4	2.44	0.02	-2.29	0.02	24.9	0.02	-24.9	0.02	37.4	0.05	-37.4	0.04
5	2.75	0.02	-2.62	0.01	24.9	0.02	-24.9	0.02	37.5	0.03	-37.5	0.03
6	2.59	0.01	-2.66	0.01	37.5	0.01	-37.5	0.01	56.2	0.02	-56.2	0.03
7	2.75	0.02	-2.64	0.35	37.5	0.01	-37.5	0.01	56.2	0.01	-56.2	0.03
8	2.66	0.02	-2.54	0.47	37.5	0.01	-37.5	0.01	56.2	0.01	-56.2	0.03
9	3.56	0.03	-3.48	0.72	49.9	0.27	-49.9	0.01	74.9	0.02	-74.9	0.03
10	3.65	0.04	-3.76	0.03	49.9	0.01	-49.9	0.01	74.9	0.02	-74.9	0.04
11	3.71	0.03	-3.84	0.03	49.9	0.01	-49.9	0.01	74.9	0.02	-74.9	0.04
12	3.74	0.03	-3.89	0.08	49.9	0.01	-49.9	0.01	74.9	0.02	-74.9	0.04
13	3.86	0.05	-4.04	0.06	49.9	0.01	-49.9	0.01	74.9	0.02	-74.9	0.03
14	3.58	0.03	-3.70	0.03	49.9	0.01	-49.9	0.01	74.9	0.02	-74.9	0.02
15	3.77	0.02	-3.87	0.03	49.9	0.01	-49.9	0.01	74.9	0.02	-74.9	0.03
16	3.79	0.06	-3.93	0.07	49.9	0.35	-49.9	0.01	74.9	0.02	-74.9	0.03
17	3.82	0.09	-4.01	0.08	49.9	0.02	-49.9	0.01	74.9	0.05	-74.9	0.15

$F_y$  and  $M_z$  are operated with a phase shift of 90 degrees to achieve the highest magnitude of out-of-plane deformation according to [6]. To quantify the synchronization of  $F_y$  and  $M_z$  the phase shift relative to each other is represented in figure 5.



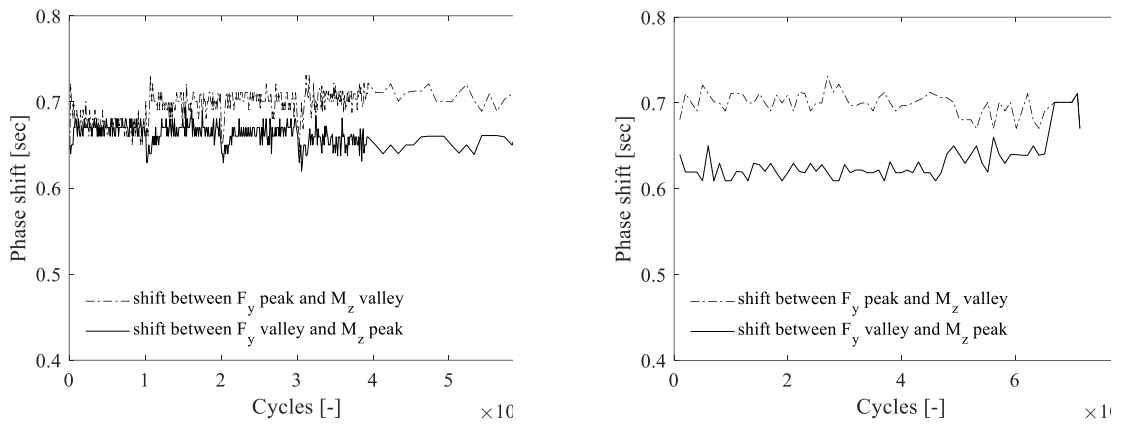
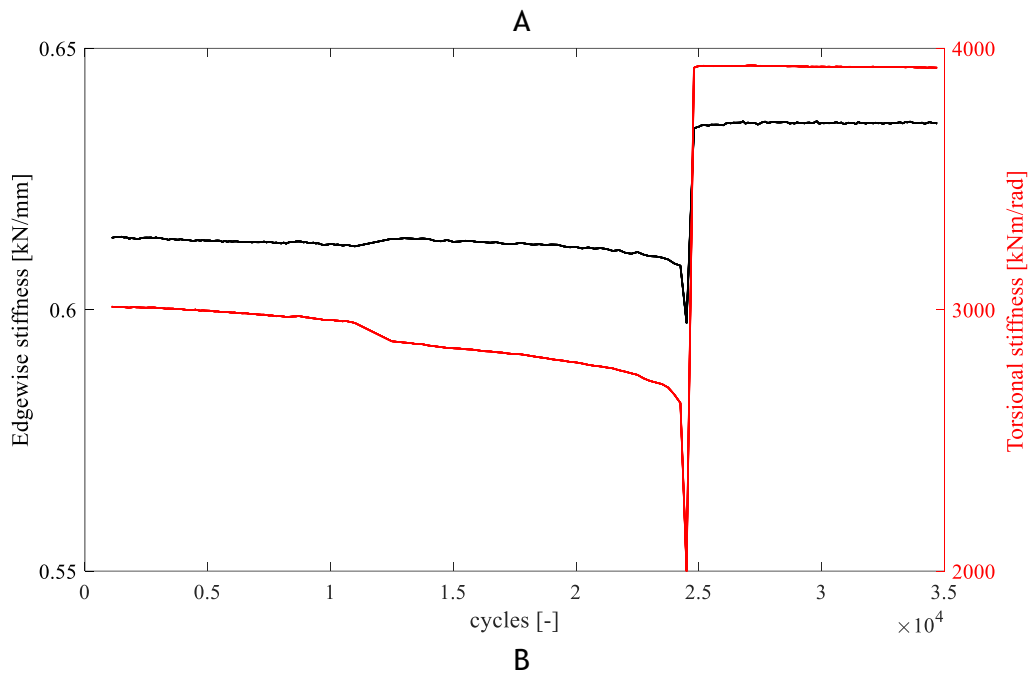
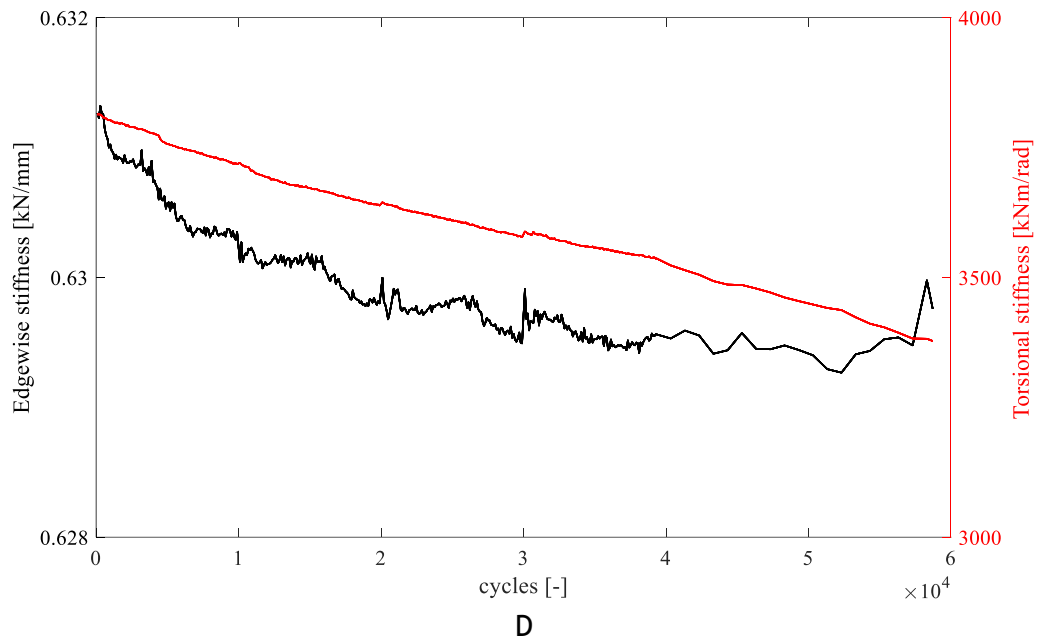
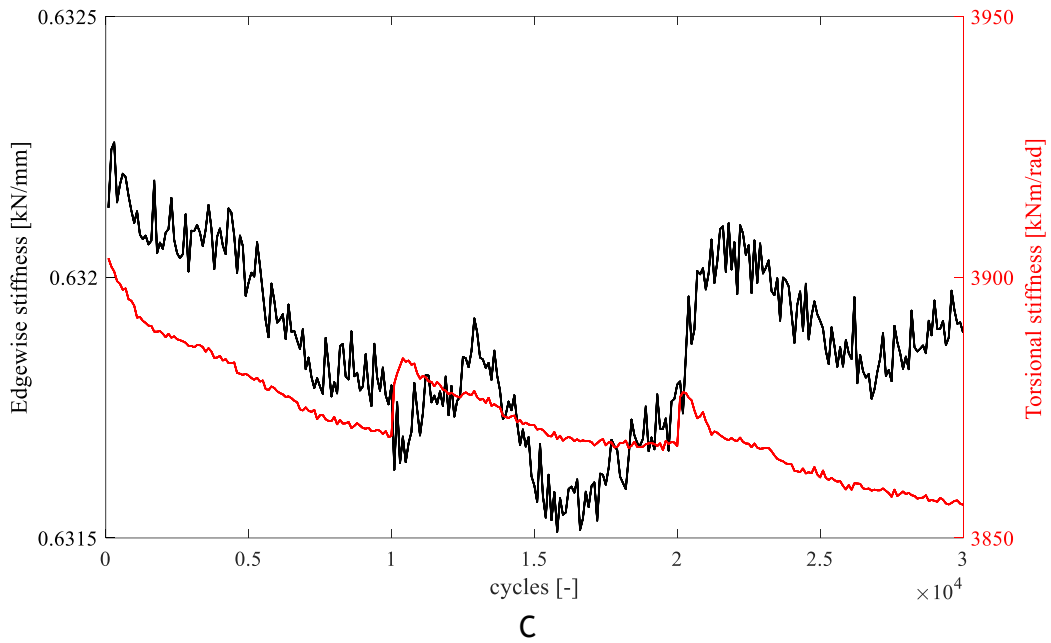


Figure 5: phase shift between dof<sub>y</sub> and rot<sub>z</sub> including a) load sequence 1, b) load sequence 2, c) load sequence 3a and d) load sequence 3b

According to figure 5  $F_y$  is in lead of  $M_z$  with a magnitude of approximately 0.7 sec (0.44rad) and 0.5 sec (0.62rad) at an execution frequency of 0.1 and 0.2Hz respectively. Improved synchronization has been attempted through 1) PID tuning of the hydraulics and 2) the use of appropriate compensators.





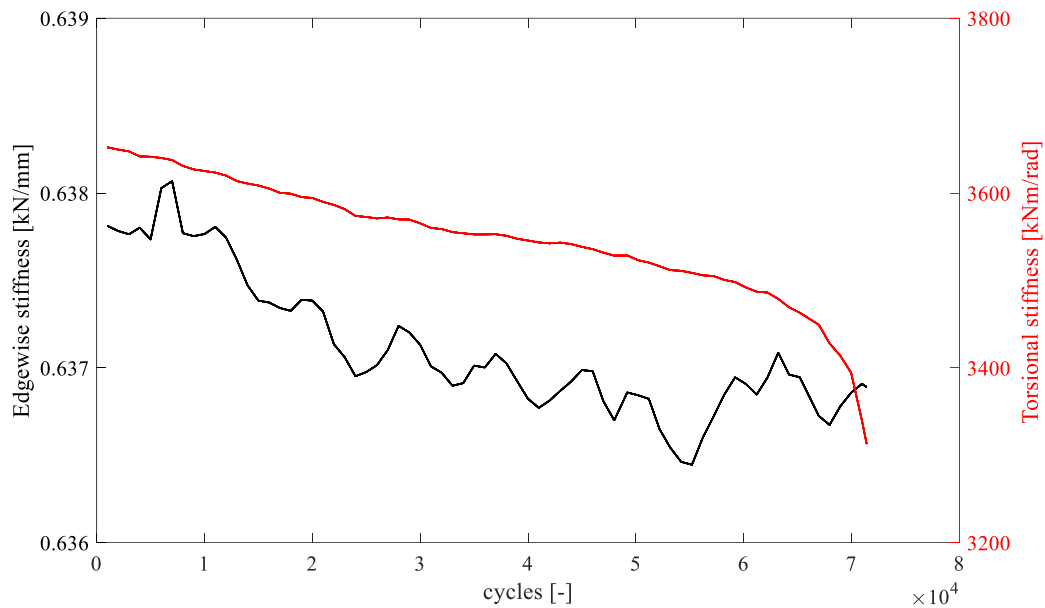


Figure 6: global stiffness (force vs disp) of dofy and rotz including a) load sequence 1, b) load sequence 2, c) load sequence 3a and d) load sequence 3b

From figure 6a a gradually decrease of global stiffness in both the  $F_y$  and  $M_z$  direction is observed within fatigue test sequences 1 through 4. At the end of fatigue test sequence 4, a sudden drop in the global stiffness is observed which aligns with the sudden failure of the load introduction zone. After a major repair of the load introduction rig along with further reinforcement of the tip end of the blade the fatigue test campaign were reinitiated. From fatigue test sequence 5 through 13 (see figure 6b and 6c) a small but graduate degradation of the global stiffness is identified - especially concerning the  $M_z$  direction. Fatigue test sequence 13 have been terminated due to sudden emerging noises from the load introduction zone. From visual inspection, some crack propagation is identified in the leading edge region meaning that no further testing will be initiated before further structural reinforcement is achieved. After minor reinforcement of the load introduction zone the test have been reinitiated - stiffness response is outlined in figure 6d running from fatigue test sequence 14 through 17. Major damages are now observed in the load introduction zone is identified which needs repair before the test can be restarted. This is furthermore identified from figure 6d where a sudden drop in the rotational stiffness is identified. To investigate whether the stiffness degradation of the specimen is related to structural degradation of the blade, the stiffness in terms of force vs strain output of strain measurement on the outer skins surface is evaluated in figure 7

A

B

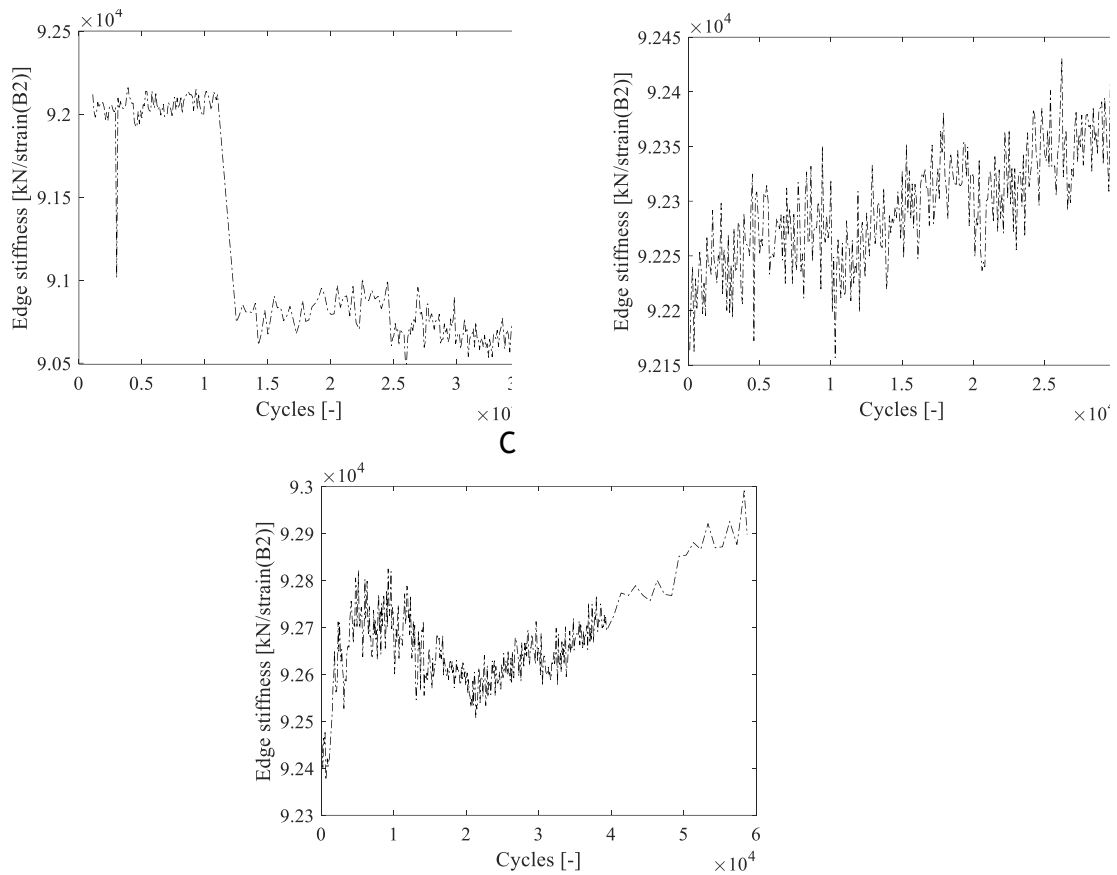


Figure 7: global stiffness (force vs disp) of dofy and rotz including a) load sequence 1, b) load sequence 2 and c) load sequence 3a

From figure 7 a rather constant stiffness is identified meaning that no structural degradation of the test specimen itself is evident. The sudden drop in stiffness seen from fatigue test sequence 3 through 5 is governed by the increase of execution frequency. From load sequence 14 through 17, no data have been acquired due to a faulty strain gauge. An extract of the force feedback as a function of time is given in figure 8 including flap- and edgewise bending along with torsional moment.

A

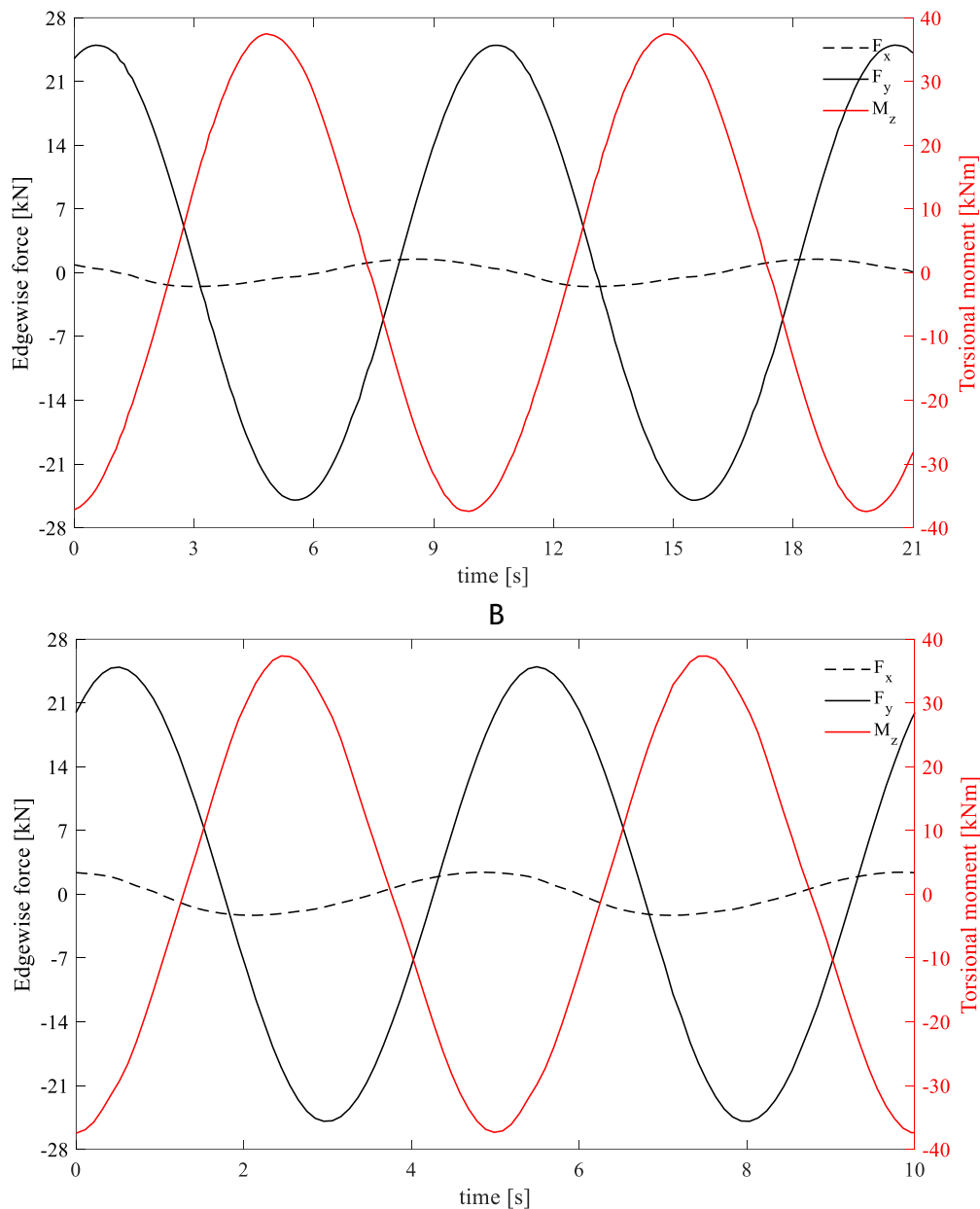
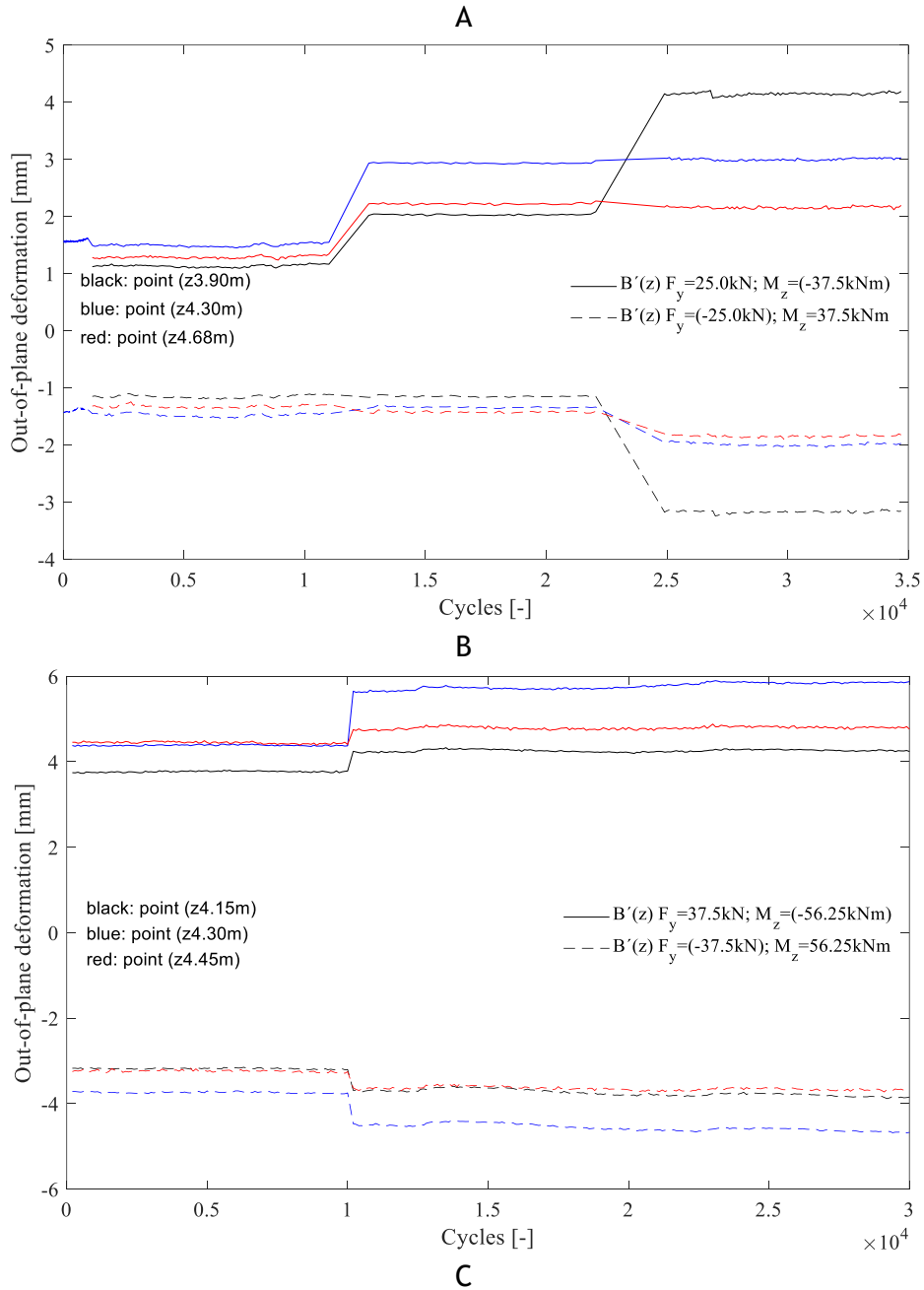


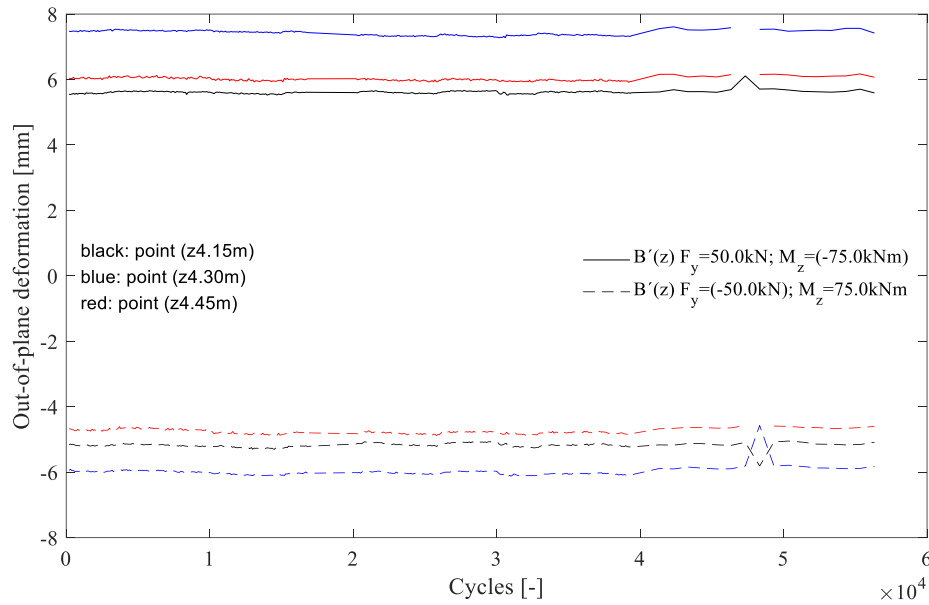
Figure 8: global stiffness of dofy and rotz including A) execution frequency of 0.1Hz and B) execution frequency of 0.2Hz

Here the phase shift between dofy and rotz is clear and becomes more pronounced when the frequency increases. Furthermore, a minor reaction force in the flap wise direction is introduced due to actuator dynamics. Improvement have been sought through tuning of the hydraulics and compensators. Probably a RT compensator is needed for further improvements.

Fatigue test sequence 1, 3 and 17 are not included in the above figures given the low number of cycles achieved - see table 2. Furthermore, no DIC measurements for fatigue test sequence 15 and 16 is available due to availability issues with the DIC system.

From figure 9, key results are presented covering the out-of-plane deformation at the selected measurement points (see figure 1B).





D

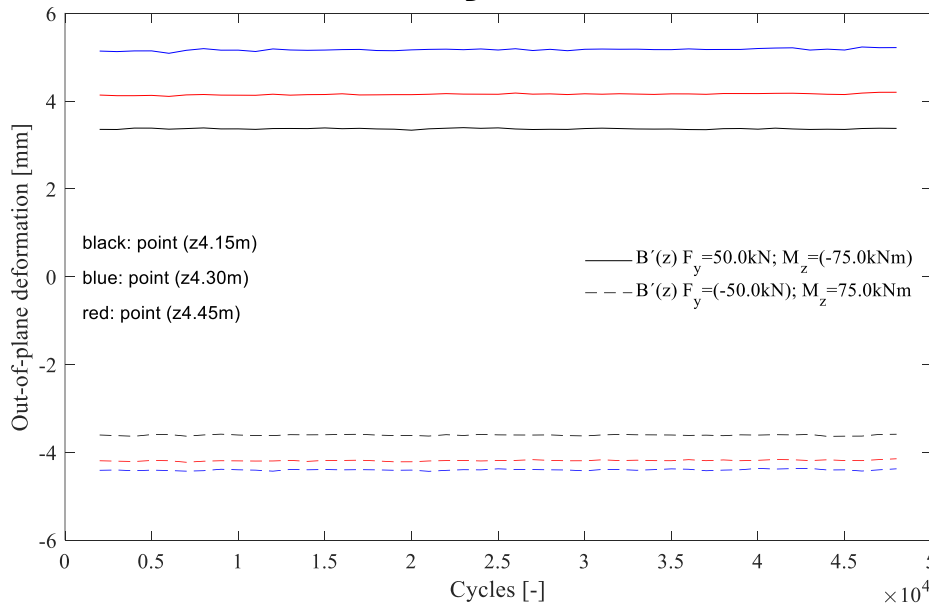
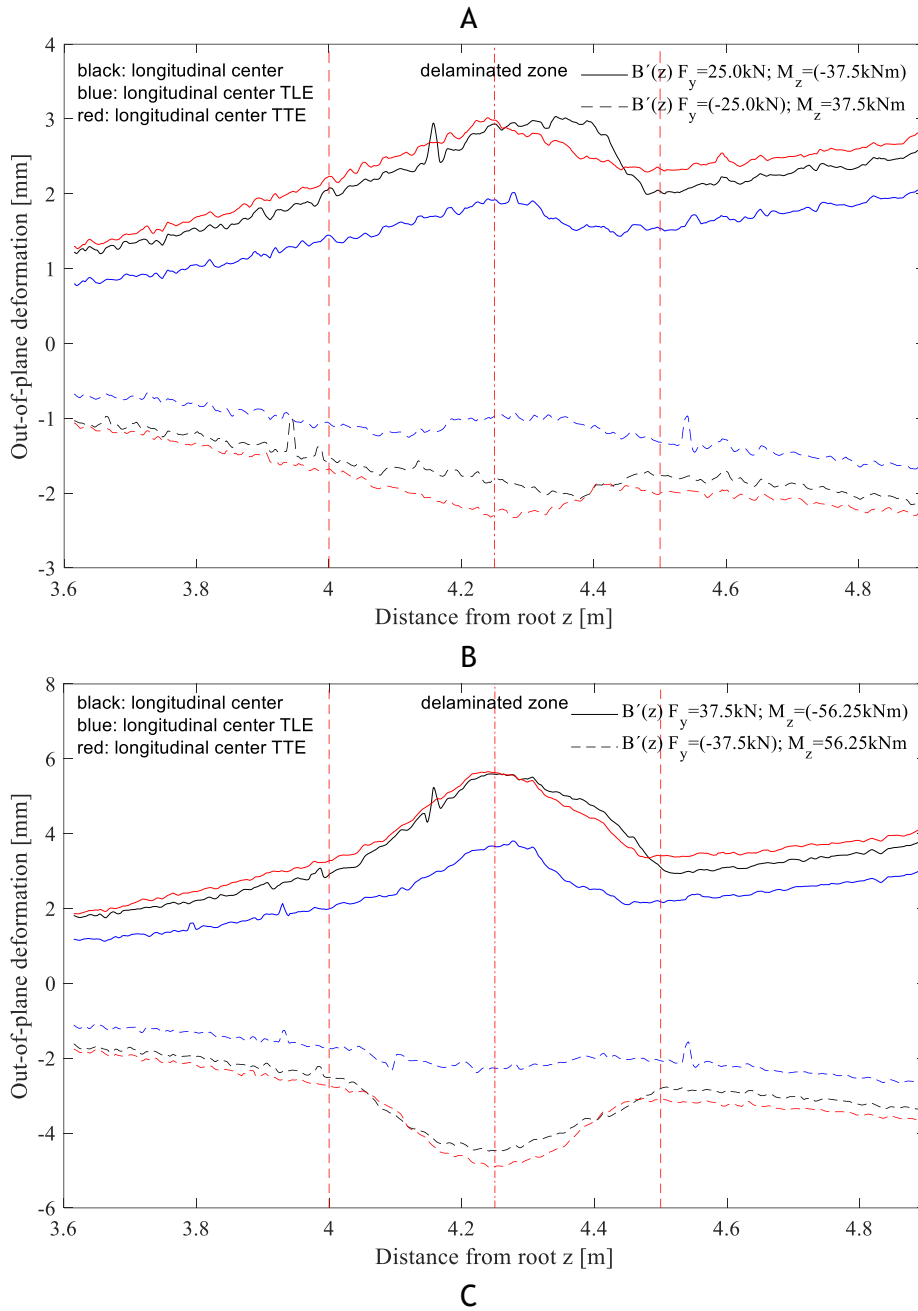
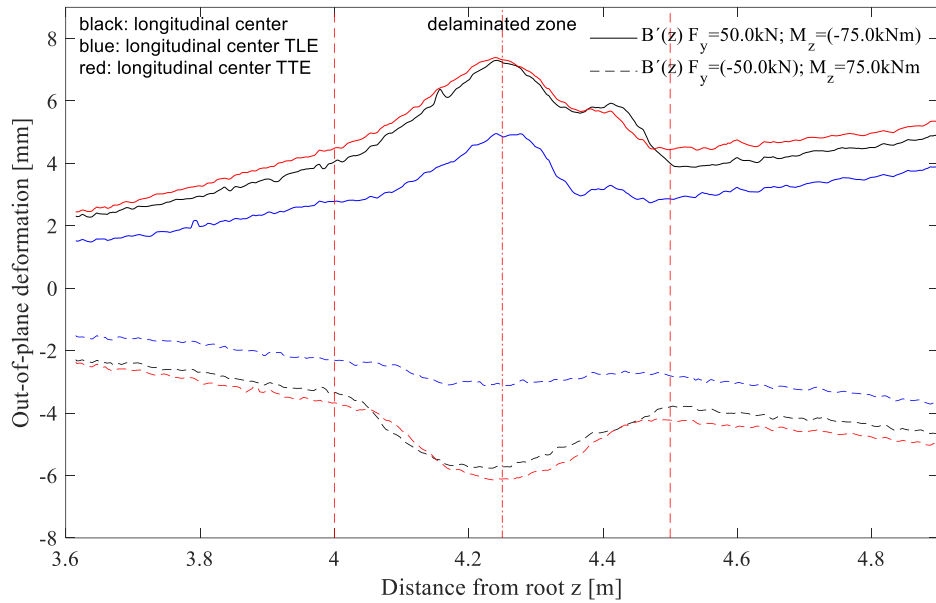


Figure 9: out-of-plane deformation at selected points including a) load sequence 1, b) load sequence 2, c) load sequence 3a and d) load sequence 3b

From figure 9a a sudden increase of the out-of-plane deformation is detected between fatigue test sequence 4 and 5. This is probably due to the release of the debond between the core and outer skin governed by the sudden failure of the load introduction rig. Repeated In figure 9b a sudden increase of the out-of-plane deformation is detected between fatigue test sequence 6 and 7. This is due to the establishment of a ventilation channel to the debond zone through a pneumatic pressure applied from the inside (see appendix 15). From fatigue test sequence 7 to 8 a gradually increase of the out-of-plane deformation is detected as a function of cycles. Last an expected drop of the out-of-plane deformation is seen between fatigue test sequence 13 and 14 given the added thickness (hence bending stiffness) to the out face sheet of the gauge zone.

The out-of-plane deformation along the longitudinal path is given in figure 10 for fatigue test sequence 5, 8, 9 and 14 respectively.





D

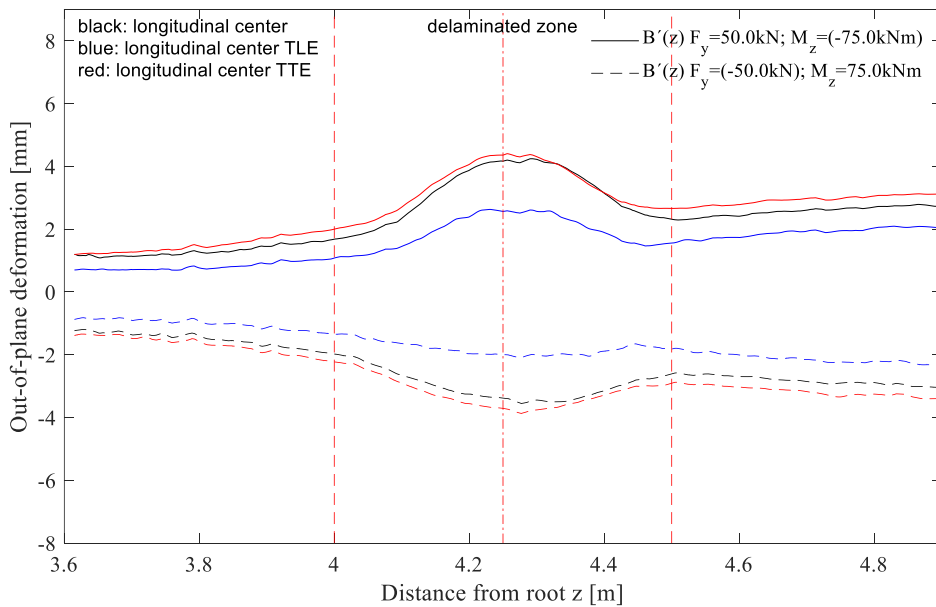


Figure 10: out-of-plane deformation along a longitudinal path including a) load sequence 1, b) load sequence 2, c) load sequence 3a and d) load sequence 3b

From figure 10 a clear and graduate increase of the out-of-plane deformation is identified as a function of the load magnitude. At a 75% load magnitude a clear debond front is visible in the measurements. When increasing the load magnitude further up to 100% the outer skin starts to wrinkle - properly due to the significant reduced thickness of the outer skin. Given the fact that the bending stiffness of the outer skin is nearly zero, the appearance of transverse cracks throughout the fatigue test campaign is by the author considered unlikely. A updated design of the gauge zone (design 2) was initiated with the aim to increase bending stiffness. The out-of-plane deformation acquired for design 2 is outlined in figure 10d. As expected, the out-of-plane deformation is reduced and the wrinkling of the outer face sheet

eliminated. No propagation of debond front nor crack propagation is detected as this point.

A quasi-static test have been initiated to evaluate the out-of-plane deformation as a function of load magnitude. Here a 100% load magnitude is applied over 49 equally distributed load steps forming a triangular waveform comprising 3 periods, both dofs including dof<sub>y</sub> and rot<sub>z</sub> are operated with a phase shift of 90 degrees according to figure 7. DIC results for half a loading period (load index 21 through 29) are given in appendix 1 through 3. The test has been executed prior to fatigue test sequence 1, 3 and 5 respectively to evaluate structural integrity.

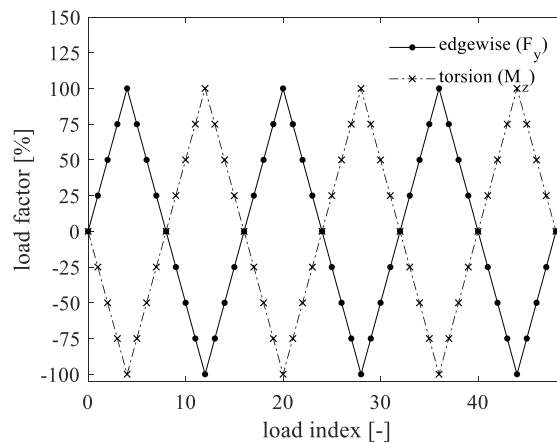


Figure 11: load index in quasi-static test

Global stiffness in the  $F_y$  and  $M_z$  direction is evaluated within each quasi-static (QS) test sequence through linear regression. All available results are given in table 4.

Table 4: key results related to quasi-static test sequence

QS test sequence [-]	Prior to fatigue test sequence [-]	$F_y$ [kN]		$M_z$ [kNm]		Appendixes [-]
		Stiffness [kN/mm]	$R^2$ [-]	Stiffness [kNm/rad]	$R^2$ [-]	
1	1	0.6030	0.999	2878.6	0.992	-
2	5	0.6011	0.999	2808.3	0.991	-
3	10	0.6245	0.999	3750.4	0.996	-
4	14	0.6030	-	2878.6	-	-
5	17	0.6028	-	2875.2	-	-

The debond front is monitored through DIC by evaluating the out-of-plane deformation of the center path according to eq. 1. However, a discontinuity of the displacement pattern in the longitudinal and transvers direction can be difficult to identify in the current setup - especially when the outer face sheet is subjected to tension (out-of-plane deformation in the positive direction following the active coordinate system I figure 2). For that reason, the boundary of the debonded zone is identified through “coin tapping”. The distance from edge to edge through the center

of origin in the transverse, longitudinal and 45 degree angle named  $d_y$ ,  $d_x$  and  $d_{xy}$  respectively (see figure 4) is identified for each fatigue test sequence according to table 5.

Table 5: boundary of delaminated zone

Test sequence [-]	$d_x$ [mm]	$d_y$ [mm]	$d_{xy}$ [mm]
1	-	-	-
2	-	-	-
3	508	502	497
...	...	...	...

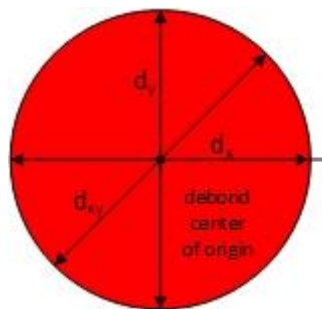


Figure 12: principle sketch of debonded zone and corresponding principle axis

A better approach on identifying the debond front will be investigated. Preferable using DIC - alternatively using "coin tapping" or alternative approach.

The majority of DIC results are presented in appendix (see appendix 1 through 14). Furthermore a pneumatic loading of the debond zone has been conducted, all relevant results are presented in appendix 15.

## References

- [1] "Project Report: Root Area Transition Zone - RATZ and Reduction O&M cost of WT blades, Energy Development and Demonstration Program (EUDP) RATZ project, 64015-0062," 2019.
- [2] DNV-GL, "Standard DNVGL-ST-0376: Rotor blades for wind turbines," DNV GL AS, 2015.

- [3] F. M. Jensen, "Ultimate Strength of Large Wind Turbine Blade," Department of Civil Engineering, Technical University of Denmark, Kgs. Lyngby, 2008.
- [4] C. IVS, "Guide2Defects," Guide2Defect, 06 January 2016. [Online]. Available: [www.guide2defect.com](http://www.guide2defect.com). [Accessed 17 December 2018].
- [5] F. Jensen, M. Werk, A. Buliga, T. Pardalakis, C. Berggreen, J. Waldbjoern, J. D. Sørensen, Y. Yang and T. Lindby, "Root Area Transition Zone - RATZ and Reduction O&M cost of WT blades," Energiteknologisk udvikling og demonstration (EUDP), Copenhagen, Denmark, 2019.
- [6] J. P. Waldbjoern, A. Buliga, C. Berggreen and F. M. Jensen, "Out-of-plane deformations of double-curved trailing edge sandwich panels in the root transition zone of a 34m wind turbine blade," *Composite Structures*".
- [7] P. Brøndsted and R. P. Nijssen, *Advances in wind turbine blade design and materials*, Woodhead Publishing, 2013.
- [8] "Data Report: Full-scale test of a LM58.7m blade with edgewise fatigue loading," Energy Development and Demonstration Program (EUDP) RATZ project, 64015-0062, Roskilde, 2019.
- [9] "Data Report: Full-scale test of a LM58.7m blade with combined static loading," Energy Development and Demonstration Program (EUDP) RATZ project, 64015-0062, Roskilde, 2019.
- [10] "Data report: Full Scale Test SSP 34m blade, Combined static load," Energy Development and Demonstration Program (EUDP) Experimental Research, Phase 2 , Risø, 2010.
- [11] F. M. Jensen, "Ultimate strength of a large wind turbine blade," Risø DTU, PhD Thesis, 2008.
- [12] F. M. Jensen, "Floor™ Patent owned by Bladena Aps". Patent WO 2008.086205, 2008.

[1  
3] A. B. C. B. F. M. J. Jacob P Waldbjørn, "Multi-axial large-scale testing of a 34 m wind turbine blade section to evaluate out-of-plane deformations of double-curved trailing edge sandwich panels within the transition zone,"  
<https://journals.sagepub.com/eprint/XHMXWCNZAK6WE8WJZ7DG/full>, 2020.

[1  
4] F.M.Jensen, "Ultimate Strength of Large Wind Turbine Blades".

# Appendix F      Tip Solution

## Lightning Damages Assessment

ENERGITEKNOLOGISK UDVIKLINGS-  
OG DEMONSTRATIONSPROGRAM



---

# CORTIR

---

Task 8.1 - Lightning damage assessment and incident pressure

Christian Løjtved, Stuart Clyens, Jesper Boelt

EUDP

J.nr. 64018-0507

MAY, 2019

ECC  
Næstved

## Contents

1. Introduction.....	3
1.1. Failure due to lightning.....	3
2. Lightning types .....	4
2.1. Lightning orientation .....	4
2.2. Lightning polarity.....	5
2.3. Basis for protection .....	6
3. Lightning protection .....	7
4. Probability.....	8
4.1. Current.....	8
4.2. Strike distance .....	9
4.3. Blade length.....	10
4.4. Location .....	10
4.5. Wind farms and local position.....	11
5. Temperature.....	11
5.1. For Pin-hole .....	12
6. Pressure .....	13
6.1. Published pressure citation .....	13
6.2. GER Approach.....	14
6.3. Incident Overpressure .....	14
6.4. Shape of spar gap channel.....	17
7. Conclusion and Further Work.....	18
8. Bibliography.....	19

## 1. Introduction

The aim of this work package has been to establish a deeper understanding of the blade damage caused by lightning strikes, in order to gain a better estimate of the pressures generated. The result of this work has been the establishment of a model for the incident pressures within the blade tip, when the aerodynamic blade profile is exposed to an unintended lightning strike. The incident pressure acts as the input for WP8.2 in the evaluation of reflected pressure within the blade.

This work in this work package has been supported by WP9 (Product development) who has established the lightning workshop and supported with blade design and dimensions.

**Deliverable 8.1:** Evaluation of free expansion incident pressure at lightning strike.

### 1.1. Failure due to lightning

The following observations are based on a dialog with Søren Find Madsen from Polytech<sup>1</sup> during the Lightning workshop held at Bladena ApS. The observations are the result of field inspections of wind turbine blades exposed to lightning strikes.

- Pressure effect due to unintended lightning strikes, causes failure at the trailing edge (TE).
- Pinholes are a result in unintended lightning impact. The pinholes have diameters of approximately 2cm.
- Lightning strike trends to enter through other parts than the TE, which is rarely exposed to a direct impact.
- The presence of water has a larger influence than salt.
- The drain hole(s) and the likelihood of the presence of water have a tendency to attract lightning strikes.
- Some design have built-in drain-holes in the tip receptor to prevent unintended damaged in the fibre reinforced polymer (FRP).
- The presence of water in the blade tip is a common observation and can be up to 20 litres.

---

<sup>1</sup> Lightning Workshop, Bladena, Trekroner, 5/4-2019

## 2. Lightning types

There are four types of lightning, cloud to cloud (CC), cloud to air (CA), cloud to ground (CG) and ground to cloud (GC) lightning, where the last two are the ones that have to be taken into account when designing wind turbine blades.

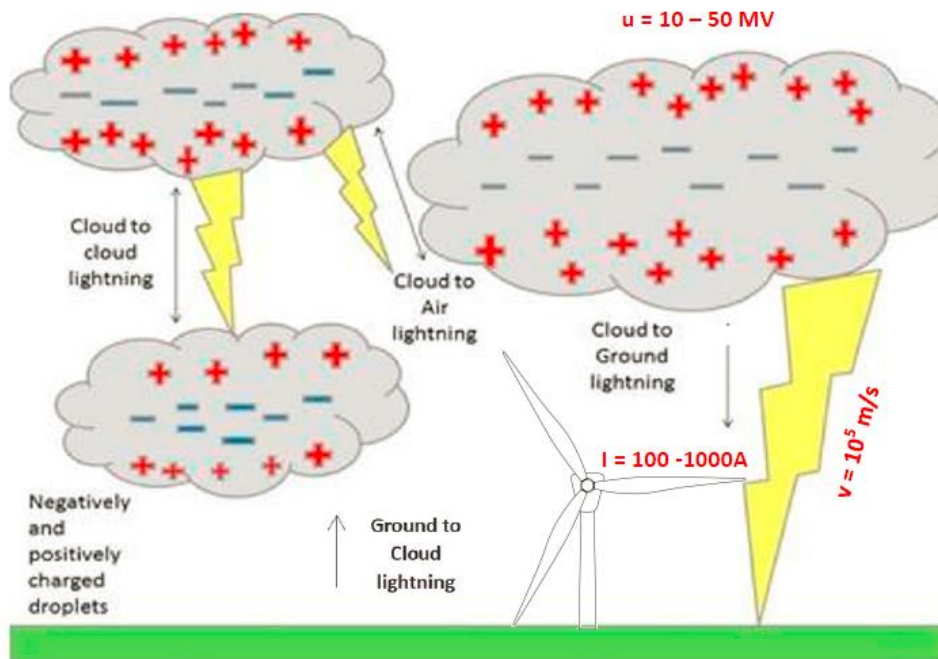


Figure 2.1 – Lightning types

### 2.1. Lightning orientation

The GC type is also known as upwards lightning whereas CG is known as downwards lightning, where each has their characteristics.

Lightning Direction		
Upwards (GC)	Vs.	Downwards (CG)
Slow		Quick
Leaves the tip		Important for all structures
Predominant for tall structures (>60m [1])		
Often negative polarity		

Table 2-1 – Upwards (GC) vs Downwards (CG)

## 2.2. Lightning polarity

In addition to direction, lightning is divided into two further categories, positive and negative which refer to the polarity of the lightning strike.

The polarity can, like a battery, have both a + (positive) or – (negative) sign and this represents the charge at the end. For negative lightning strikes which are the most common type (90-95%) there is a transfer of a negative charge from the cloud to the ground. The typical negative charged bolt is about 300,000,000 volts and 30,000 amps of power [2].

Positive lightning only makes-up about 5-10% of all lightning strikes and originates from the top of the thunderstorm. The ground is normally shielded from this positive charge by the negative charges in the central part of the storm. But in the case of a positive strike with large travel distance can such a strike be up to 10 times stronger and 10 times longer than a negative strike. Reaching 1 billion volts and 300,000 amps in combination with long duration is the reason these types of strikes cause a lot of damage.

Strikes		
Positive	Vs.	Negative
5-10%		90-95%
1,000,000,000 Volts		300,000,000 Volts
300,000 Amps		30.000 Amps
50.000 °C		50.000 °C
Duration = 10 x Negative		Less energy and magnitude => less damage
High energy and magnitude = > high damage		

Table 2-2 – Polarity

### 2.3. Basis for protection

Growing turbine size increases the focus on lightning protection and the IEC 61400-24 standard applies to lightning protection of wind turbine generators and wind power systems and defines the lightning environment for wind turbines and application of the environment for risk assessment.

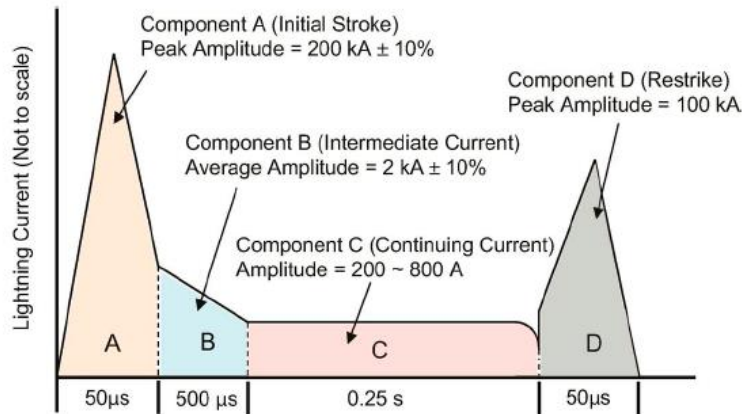


Figure 2.2 - Lightning Analysis of Wind Turbines [3]

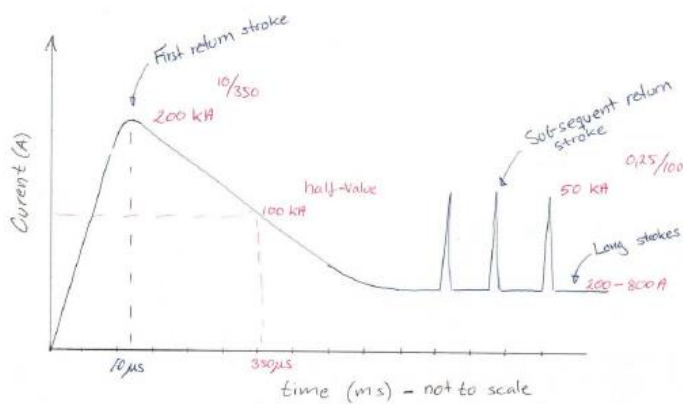


Figure 2.3 – Illustration of risetime to peak and decay time (half current)

### 3. Lightning protection

There are two main types of lightning protection system. The “older” button receptor type which comprise a number of point receptors connected to a “down” conductor (high voltage cable), which again is connected to the trailing web along the blade length.

The newer designs often tends to combine the button receptors with a tip receptor to increase potential near the tip and at the same time isolate the lightning strike from the FRP blade material.

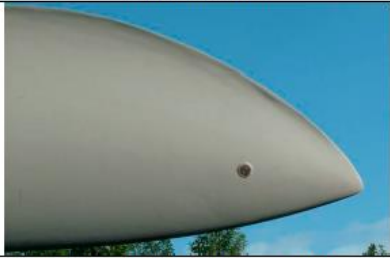
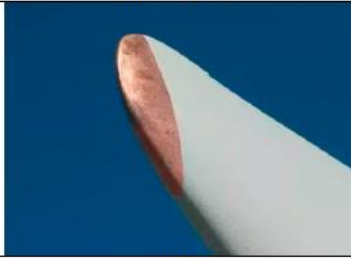
Button receptor	Vs.	Tip receptor
		
Ref. Lightning receptor, Te Uku Wind Farm turbine blade		Ref.: [4]

Table 3-1 – Receptor design

A lightning strike that hits the turbine blade at its top position will, for a 0.5s duration, move along the trailing edge (TE) for as long as a blade rotation of 45 degrees, causing most damage along the TE, assuming a tip speed of 100m/s and a rotor radius of 60m.

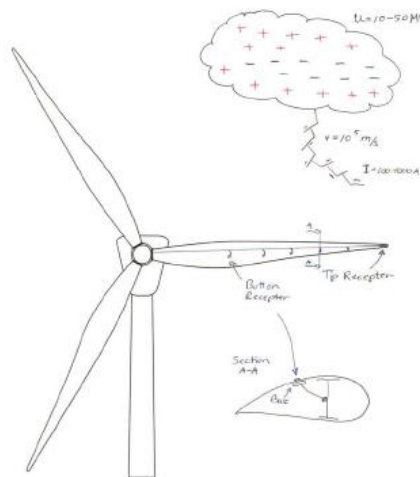


Figure 3.1 – Illustration of lightning receptors

## 4. Probability

The risk assessment which acts as the basis for the lightning protection of wind turbines is dominated by the probability functions, which again are divided into several categories such as current distribution, receptor design, geographic location and local position within a wind turbine farm.

### 4.1. Current

Four lightning protection levels (LPL) have been defined, each having a fixed maximum and minimum lightning current parameter. A wind turbine has to withstand LPL 1 which is the highest level with a minimum current of 3kA and a maximum of 200kA<sup>2</sup>.

LPL	I	II	III	IV
Maximum current (kA)	200	150	100	100
Minimum current (kA)	3	5	10	16

Figure 4.1 - Lightning current for each LPL based on 10/350µs waveform.

The upper and lower limit for LPL 1 corresponds to 98% of lightning strikes where most of the lightning strikes are expected to have amplitudes of 30kA.

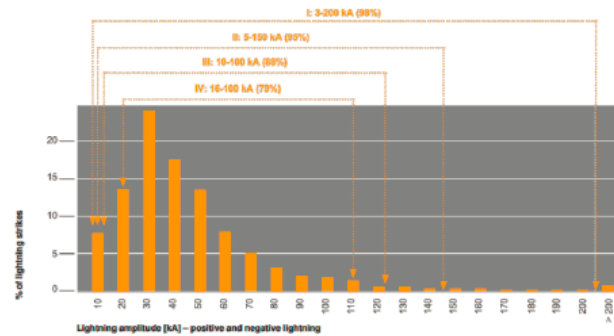


Figure 4.2 - Probability distribution of lightning amplitudes [5]

<sup>2</sup> IEC 61400-24 / EN 61400-24

## 4.2. Strike distance

Capture surfaces and strike distance are two values that affect whether the lightning strike sees the blade and its capture surfaces (receptors).

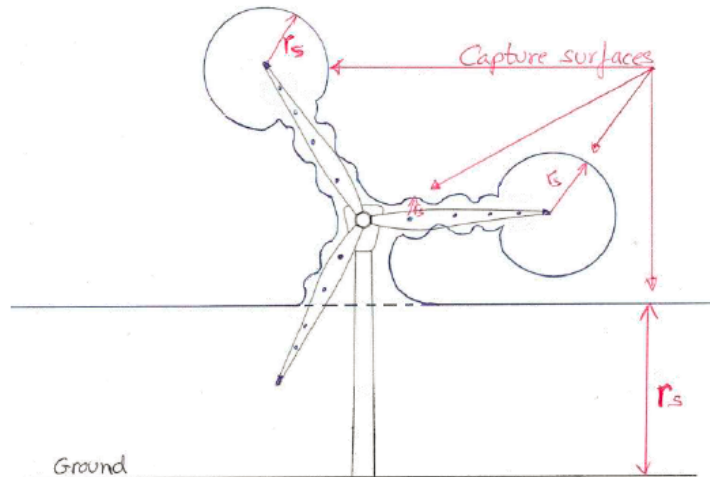


Figure 4.3 – Illustration of Capture surfaces

The strike distance is a function of the return-stroke peak current and is defined as the distance from the descending leader to the object to be struck when an upward connecting leader is initiated from an object.

The probability to capture the lightning strike by the blade receptors increases for falling current in the return-stroke.

Strike distance [m]	
I, kA	rs, m
2	16
5	28
10	45
30	91
50	127
100	200
150	260
200	313

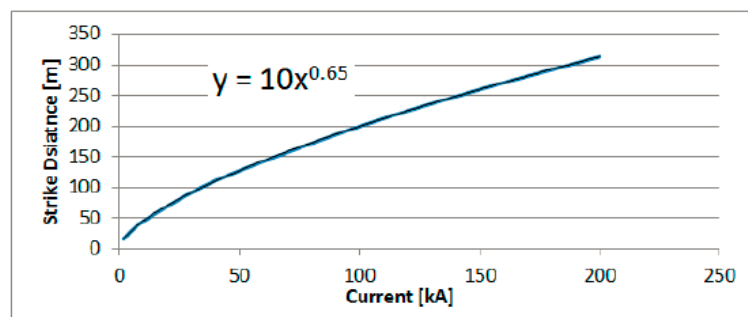


Figure 4.4 – Strike Distance as function of Current<sup>3</sup>

A return-stroke peak current of 200kA result in a strike distance of 313m which drastically reduces the probability of capturing the lightning strike by the receptors.

<sup>3</sup> Love (1987; 1993)

### 4.3. Blade length

Lightning damage along blades with mixed fiberglass and carbon fibre structure [1] has been measured and there is a clear trend that the tip of the blade attracts the largest percentage of lightning striking.

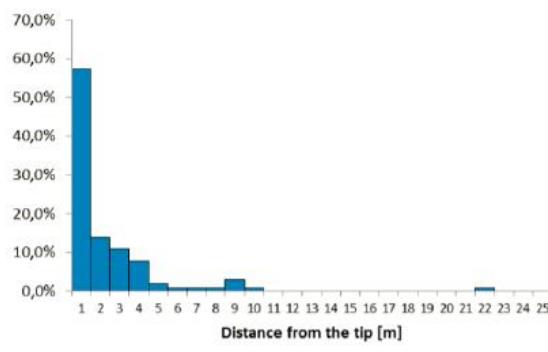


Figure 4.5 – Lightning strike location relative to tip distance

This observation correlated with the position of the lightning receptors and with the fact that the capture surface is at its highest position at the blade tip.

### 4.4. Location

Ground flash density or CG-density is a measure of number of lightning strikes over a given area and differ from region to region.

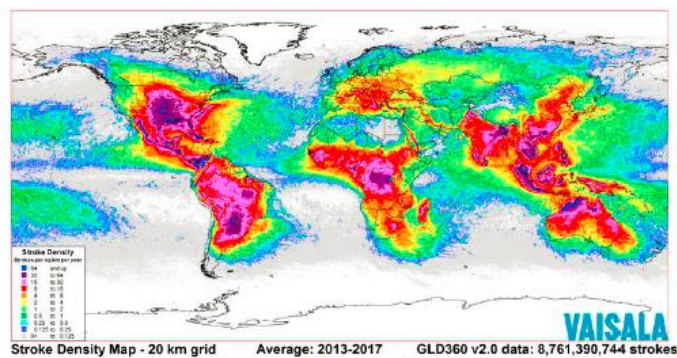


Figure 4.6 – Global flash density [6]

The colourful flash density map indicates the number of strokes per sq. km per year. It can be seen that Egypt and Antarctica are “lightning-free” zones whereas northern parts of Australia and southern India are hot spots for lightning strikes.

#### 4.5. Wind farms and local position

The individual location of the actual wind turbine also impacts the probability of lightning strike.

It has been documented that turbines in wind farms positioned upwind have a much greater probability of getting hit by lightning. The probability reduces for the turbines located deeper into the park.

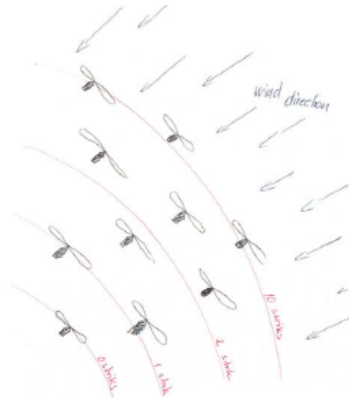


Figure 4.7 – Lightning strike probability in wind farms

#### 5. Temperature

A lightning strike is followed by a temperature increase. For a perfect strike where the lightning goes through either a button or tip receptor the corresponding change in temperature is only around +20°C.

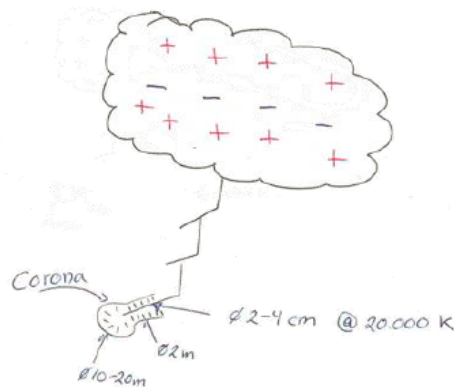


Figure 5.1 – Temperature within lightning ball

This is not the case in the air, where the resistance causes the temperature to increase to approximately 20,000K to 30,000K within the middle of the lightning channel which has a diameter of approximately 2-4cm. The same effect is observed at pinholes strikes, where the high resistance in both blade material and air causes the temperature to increase above the melting point of the blade material.

### 5.1. For Pin-hole

A pin-hole is a result of lightning strikes that misses the receptors and thereby strikes the blade causing local damage to the blade. Such pin-hole now acts as an upward streamer which increases the probability for further unintended lightning strikes at locations away from the receptors.


Table 5-1 – Pin-holes observation on blades after unintended lightning strike

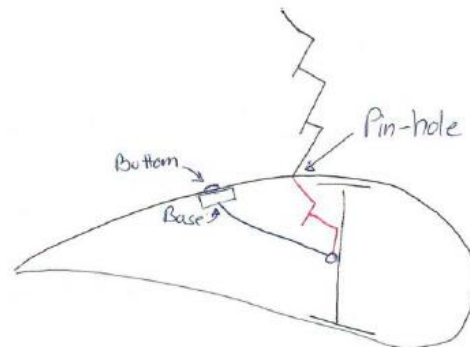


Figure 5.2 – Illustration of unintended lightning strike through a pin-hole

## 6. Pressure

It's a known fact that the lightning strike is followed by an overpressure, but of what magnitude?

Most attempts to predict the pressure is by the rapid temperature rise, which is predicted to be in the range of 10,000K to 30,000K, in the return stroke channel.

### 6.1. Published pressure citation

There is a common consensus that the stroke channel can be simplified to a cylinder, from where the shock wave is propagating from, but the pressure is more uncovered.

Citation from published literature	Ref.
Lightning is an event which heats air to 30,000 K in less than 10 u-seconds (Uman, 1987). A sudden increase in pressure and temperature causes surrounding air to expand at a rate faster than the speed of sound.  Thunder contains a roughly cylindrical initial pressure shock wave at the lightning channel in excess of 10 atmospheres. The shock wave decays to a sound wave rapidly, within meters.	[10]
It is probable in light of the available shock wave data, that the initial pressure in the lightning channel is considerable in excess of 10 atm.	[11]
As discussed in subsections 4.65 and 12.2.2, the return stroke heats the channel created by the preceding stepped or dart leader from near 10,000K to near 30,000K or more in several microseconds or less. The return-stroke channel pressure must increase in response to this rapid temperature rise since there is insufficient time for the channel particle density to decrease appreciably. The spectroscopic data (Orville 1968c) indicate an average channel pressure of about 10 atm ( $10^6 \text{ N m}^{-2}$ ) during the first 5 $\mu\text{s}$ . Such a channel overpressure will result in an expansion of the luminous channel and the formation of a shock wave that propagates outward and eventually beyond the luminous channel, which attains pressure equilibrium with the surrounding atmosphere within tens of microseconds (Orville 1968c).	[12]
The details of the energy input to short channel sections and resultant formation of an outward-moving shock wave have been modelled by Hill, Plooster, Jones et al. Troutman, and Colgate and McKee. Overpressure of the order of 4 or 5 atmospheres are predicted at about 5 cm from the channel and about 1 or 2 atmospheres at 10 cm.	[13]
During a lightning strike, the temperature of the lightning bolt channel is raised to about 24,700°C, in a few microseconds. This causes the temperature around the channel to rise suddenly, meaning that the pressure in the channel suddenly increases to several atmospheres, as does the volume of space it occupies.  This sudden rise in volume causes a sudden cylindrical pressure shock wave, which may reach pressures of more than 10 to 20 atmospheres (1013,25 kPa to 2026,5 kPa) in the vicinity of the lightning bolt channel.	[14]

Table 6-1 – Citation on lightning channel pressure

Published literature seems to assume/predict an overpressure in the order of 5 to 20atm but the pressure are indications and often without documentation about at which distance.

The overall problem is that the pressure within the stroke channel can't be measure and second it will vary as function of time and radius.

## 6.2. GER Approach

The author of this report has developed a different approach called Gap-Energy-Release (GER), which refers to the energy released in the lightning spark gap from the point of impact to the high voltage cable within the blade.

Calculations using time domain has shown, that the release of energy within the spark gap (power loss) varies over time but by fixing some of the variables is it possible to evaluate the GER as function of the spark gap length.

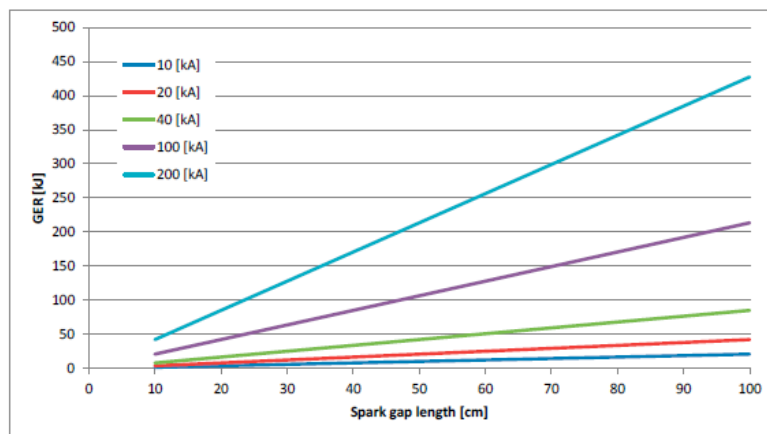


Figure 6.1 – GER as function of spark gap length

The GER values in Figure 6.1 are based fixed constants for lightning profile and atmosphere.

The GER is linear depending on the spark gap length and peak current whereas greater length or increased strength respectively results in greater GER value.

## 6.3. Incident Overpressure

By establishing a correspondence between the lightning strike energy release and the amount of explosive material required to release the same amount of energy it is possible to estimate over-pressure based on the over-pressure equation developed by Charles Kingery and Gerald Bulmash. This is an equation widely recognised for giving accurate engineering predictions of free-field pressures and is based on data from explosive tests in the range of 1kg to 400,000kg.

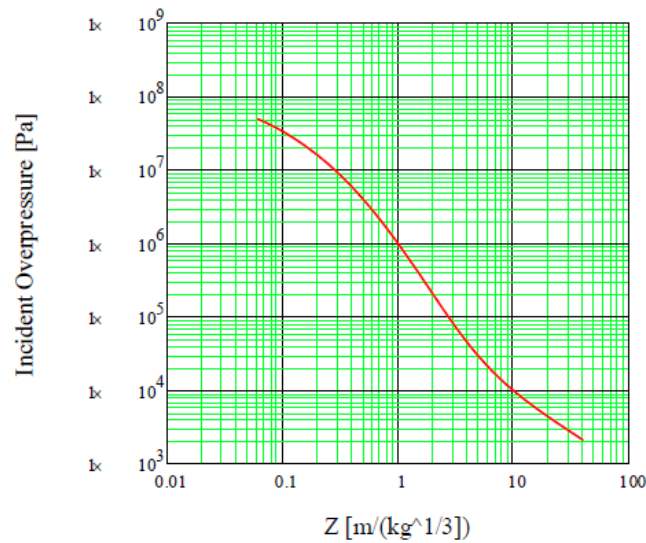


Figure 6.2 – Incident Overpressure as function of scaled distance.

Bursts close to a surface result in a phenomenon known as surface burst (SB), which for wind turbine blades could be relevant if the lightning strike (energy release) takes place near the centre web or the aerodynamic profile. The surface burst is somewhat different from the free air burst. In a surface burst the initial shock is instantly amplified at the point of detonation due to surface reflections.

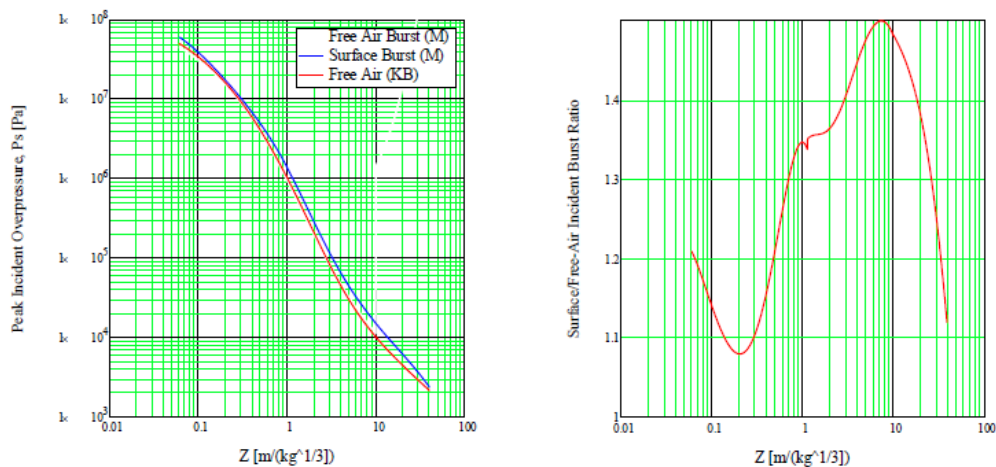


Figure 6.3 – Peak Incident Overpressure: (left) Free-Air vs. Surface Burst; (right) Ratio between Free-Air and Surface Burst.

The graph to the right shows the ratio between the Free-Air incident pressure and the Surface incident pressure as function of the scaled distance. The pressure from a surface burst is always larger than the

Free-Air but the ratio varies as function of the scaled distance from a minimum of 1.1 to 1.5 at its maximum.

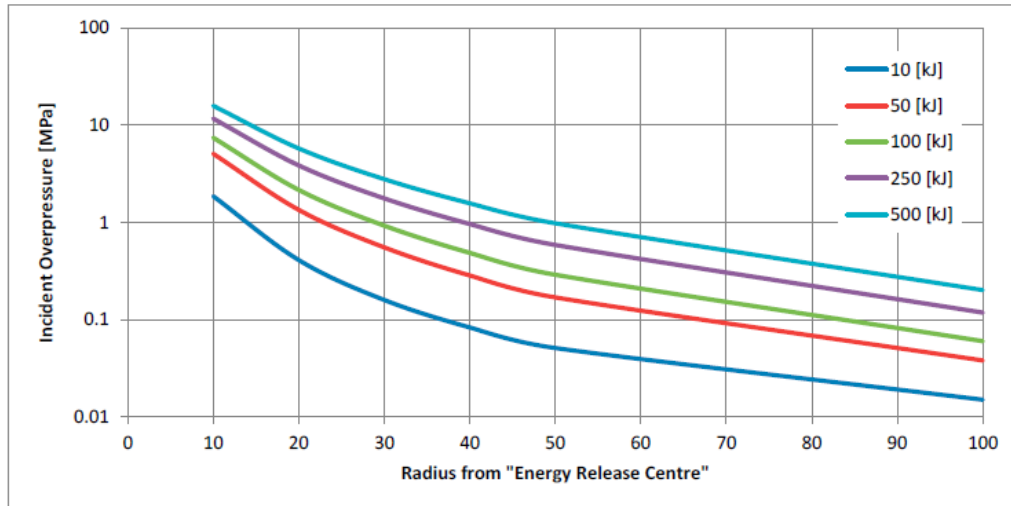


Figure 6.4 – Free-Air Incident Overpressure based on GER values in the range of 10 to 500 kJ.

The incident pressure curves in Figure 6.4 with log values along the y-axis indicates how rapidly the pressure drops with increasing distance from the “energy release centre”, being the centre of the cylindrical lightning spar channel.

The published pressures values from section 6.1 give estimates in the range of approximately 5 to 20atm which correspond to the 10kJ curves in Figure 6.4 which in combination with a 30kA lightning strike (highest probability) would correspond to a 15-17cm lightning spark gap (see Figure 6.1).

Figure 6.4 show how the pressure change as function of radius based on the GER approach and that the incident overpressure can exceed 10 MPa (100atm) which is a factor of 5-20 times the published indication from section 6.1.

### 6.4. Shape of spar gap channel

The pressure curves in the previous sections are based on the assumption that the pressure evolves from a spherical centre. The lightning channel is more like thin rod or a cylinder depending on the scale, from comparing the diameter of the lightning channel relative to the total length of the lightning strike or down to the length of the spark gap within the blade.

The U.S. Army Corps of Engineers [15] have studied the effect of explosive shapes and type of explosive. The results show that the incident (surface) pressure varies within only few percent between a spherical shape and a rod with a ratio of  $H/D=20/1$  in the scaled distance range of  $Z=4$  to 40.

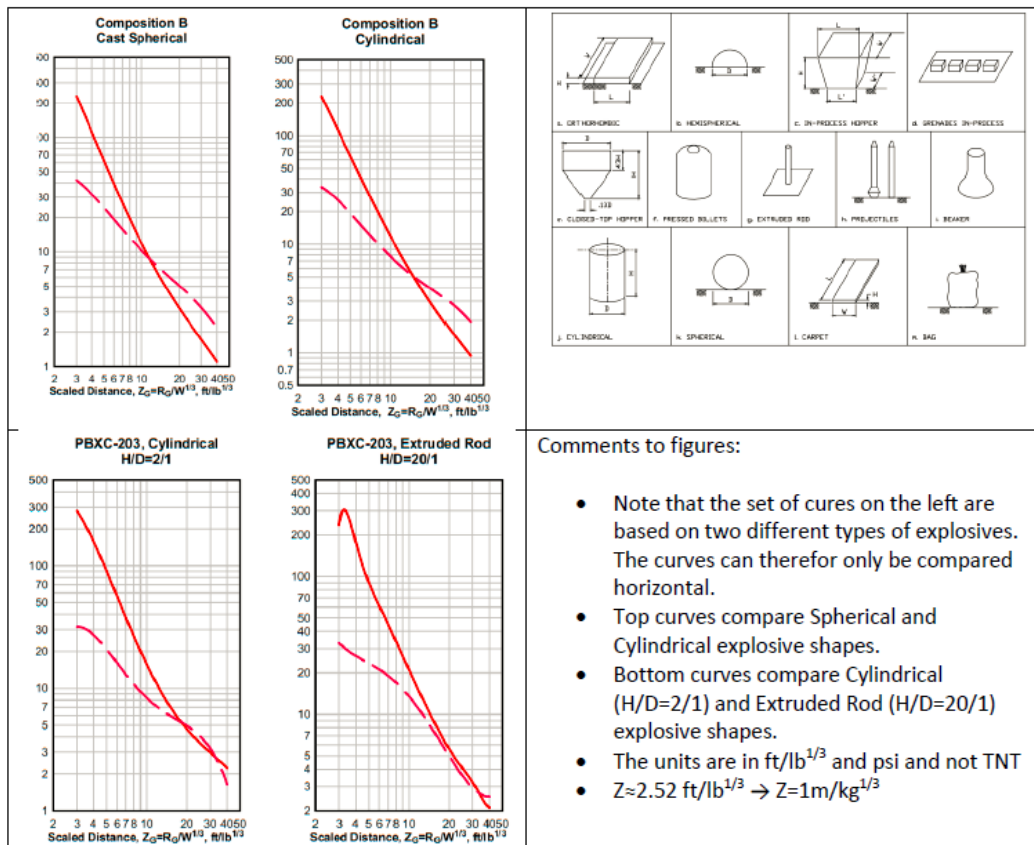


Table 6-2 – Shape of explosive [15]

The two lower curves in Table 6-2 indicates that very slender explosive a near distance ( $Z$  values below 4 ft/lb<sup>1/3</sup> equal to 1.6 m/kg<sup>1/3</sup>) are affected by the shape of the explosive. This corresponds to a spark gap of 60cm assuming an average lightning channel of 3cm.

The Chord length of a 60meter blade 2m from the tip is approximately 45cm limiting the H/D ratio to something between 15/1 down to 1/5 depending on the a centralisation of the high voltage cable and the point of impact.

## 7. Conclusion and Further Work

The work carried out in WP8.1 has involved assessing the initial overpressure due to unintended lightning strike in the tip of the turbine blade. This work has led to the following:

- A broad understanding of lightning strikes and the probability for unintended damages on wind turbine blades has been established.
- A new Gap-Energy-Release (GER) approach has been derived, based on the lightning strike current distribution and spark gap resistance within the blade. The method can be used to calculate the energy release for a given spark gap length and current distribution over time.
- The incident overpressure as function of the GER magnitude has been established. The overpressure distribution can together with blade profile and "energy release centre" estimate the incident pressure at any given position within the blade profile.
- It has been documented that the overpressure caused by the lightning strike channel with sufficient accuracy can be simplified to a spherical burst. The magnitude of the burst as function of the distance (radius) is calculated using Charles Kingery and Gerald Bulmash overpressure equation.
- The initial expression for the peak overpressure must not be confused with the pressure acting on the panels within the blade profile. The acting pressure is magnified by 2-20 times by reflection effect such as surface burst and wall reflected pressure effects. WP8.2 will continue the work done in this work package to establish an estimate for the peak reflected pressure, using the newly established GER approach.

## 8. Bibliography

- [1] S. F. Madsen, "Lightning protection zoning and risk exposure assessment of wind turbines," EWEA Offshore 2015 – Copenhagen, 2015.
- [2] D. R. Poelman, "On the Science of Lightning," Royal Meteorological Institute of Belgium, Belgium, 2010.
- [3] Y. Wang, "Advanced Wind Turbine Technology," 2018, pp. 143-173.
- [4] R. Wiseman, "How often does lightning strike wind turbines?," Quora, 4 May 2017. [Online]. Available: <https://www.quora.com/How-often-does-lightning-strike-wind-turbines>. [Accessed 9 April 2019].
- [5] OBO, "Lightning protection guide," obo.de, 2015.
- [6] Vaisala, "GLD360 Stroke Density Map," Vaisala, [Online]. Available: <https://www.vaisala.com/en/media/29131>. [Accessed 10 April 2019].
- [7] WXGuard, "Kansas Wind Turbine Blade Punctured by Lightning," WXGuard, 25 May 2013. [Online]. Available: <https://wxguardwind.com/lightning-news/kansas-wind-turbine-blade-punctured-by-lightning/>. [Accessed 9 April 2019].
- [8] Y. Blades, YEC Blades, [Online]. Available: <http://www.yceblades.it/en/solution-lab/>. [Accessed 9 April 2019].
- [9] S. Times, "Turbine blade repaired after lightning strike," 2013.
- [10] R. Kithil, "The Thunder Mechanism," National Lightning Safety Institute, 2019.
- [11] M. A. Uman, Lightning, Dover Publications , 2012.
- [12] V. A. Rakov and M. A. Uman, Lightning : physics and effects, New York: Cambridge University Press, 2002.
- [13] C. J. Andrews, M. A. Cooper, M. Darveniza, D. M. J. Andrews, M. A. Cooper, M. Darveniza and D. Mackerras, Lightning Injuries: Electrical, Medical, and Legal Aspects, CRC Press, 1991.
- [14] R. Blumenthal, "Is lightning's 'blast' as bad as its strike?," Mail&Guardian, 2014.
- [15] P. JAMES C. DALTON, "UNIFIED FACILITIES CRITERIA (UFC)," U.S. Army Corps of Engineers, 2008.

# Reflected Pressure Effect and Panel Pressure

ENERGITEKNOLOGISK UDVIKLINGS-  
OG DEMONSTRATIONSPROGRAM



---

## CORTIR

---

Task 8.2 - Reflected pressure effects and panel pressure

Christian Løjtved, Stuart Clyens, Jesper Boelt

EUDP

J.nr. 64018-0507

AUGUST, 2019

ECC  
Næstved

## Contents

1. Introduction.....	3
2. Wave Propagation .....	3
3. Reflected Pressure.....	4
4. Geometry.....	8
5. Reported Observation .....	9
6. Test Setup .....	10
7. Test Results.....	11
7.1. Air-Burst.....	12
7.2. Surface-Burst .....	13
8. Pressure Calculation .....	14
9. Pressure Variation Schema.....	15
10. Conclusion and Further Work.....	16
11. Bibliography.....	16
Appendix - Blade Tip Lightning Defects.....	17

## 1. Introduction

The aim of this work package has been to establish a deeper understanding of the pressure wave reflection within the blade. The result is a model for the wall reflected pressures, generated within the blade tip, when the aerodynamic blade profile is exposed to unintended lightning strike phenomena. The reflected pressure acts as the input to Product Development work package (WP9) and as input for the construction and modification of a test rig for high strain rate material testing (WP8.3).

This work in this work package has been supported by WP9 (Product development) who has provided physical cross section samples for wave reflection testing.

**Deliverable 8.2:** Evaluation of reflected pressure within the blade

## 2. Wave Propagation

The pressure wave resulting from unintended lightning strikes can be divided into three basic types, which depend on the energy release centre (origin) relative to its surroundings. Free-Air burst (a) and Surface burst (c) has already been described in deliverable 8.1 [1], however there is a third type that is likely to play a role and it's the Air-Burst (b).

- (a) Free-Air Bursts: The energy is released in air and the pressure waves propagate spherically outwards and interact with a given structure without prior interaction with other obstacles.
- (b) Air-Bursts: The energy is release in air, the pressure waves propagate spherically outwards and interacts with an initial structure/component before impacting the structure/component of interest. The initial impact creates a Mach wave front which influences the pressure wave impinge the secondary structure/component.
- (c) Surface-Bursts: The energy is released near a surface where the pressure waves immediately interact locally with the surface and propagate hemi-spherically outwards.

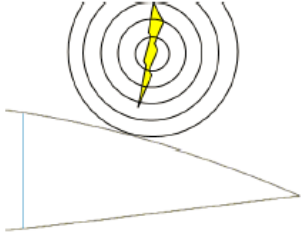
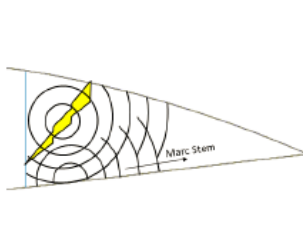
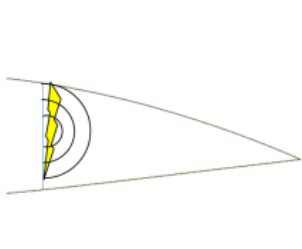
		
Free-Air burst	Air burst	Surface burst

Table 2-1 – Wave Propagation

The origin and structure defines wave-propagation, type, path, wave-intensity and the final pressure acting on the structure.

### 3. Reflected Pressure

Reflected pressures are generated as pressure waves come in contact with a surface and are of bigger magnitude than the incident pressure wave. The reflected overpressure arises from the change of momentum when the moving air changes direction as a result of striking the surface [2].

Pressure reflection can be split into two categories i.e. weak and strong pressure waves, where the first type are often referred to as pressure-waves (a) and second as shock-waves (b) [3].

- (a) The weak-wave travels as it moves along air particles that collide with a surface, which in an ideal linear elastic case bounces back and thereby result in a reflected pressure equal to the incident pressure and the surface is thereby exposed to a doubling of the acting pressure.
- (b) The strong-wave is a non-linear phenomenon, where reflected particles is obstructed by newly incoming particles. The surface is thereby exposed to a much higher pressure than the incident.

In addition to distinguishing between pressure and shock waves, the reflected pressure also depends on surface geometry, material and the size, weight, distance and interference of other obstacles between the wave propagation origin and the structure of interest.

Furthermore, the angle between the initial pressure wave propagation direction and the reflecting surface influences the reflection type; split into four ranges underneath, see Figure 3.1 and Figure 3.2 for further illustration:

- (a) Perpendicular; to the direction of the pressure wave, in which normal reflection occurs and is the most severe case.
- (b) Acute; causes an oblique reflection.
- (c) 40-60°; which causes Mach stem formation a high incident pressures
- (d) 40-80°; which causes Mach stem formation a low incident pressures

The point at which the air wave and the reflected wave merge is also known as the triple point.

The equation for the peak reflected overpressure ( $P_r$ ) in case of a perpendicular reflection, zero angle, is given by [4]:

$$P_r = 2P_{inc} \frac{4P_{inc} + 7P_{atm}}{P_{inc} + 7P_{atm}}$$

Where the  $P_{inc}$  is the incident peak overpressure and  $P_{atm}$  the ambient pressure. From this equation is it possible to obtain the minimum and maximum reflection values which stretching from 2 to 8 times the incident pressure.

The equation is based on the assumption that the pressure wave has its origin as standard sea level condition and that the ratio of specific heats of atmospheric gases is constant and equal to 1.4.

The reflected pressure for a non-perpendicular angle between the wave propagation direction and the affected surface can be expressed in terms of the reflection coefficient  $c_{ra}$ , which is defined as:

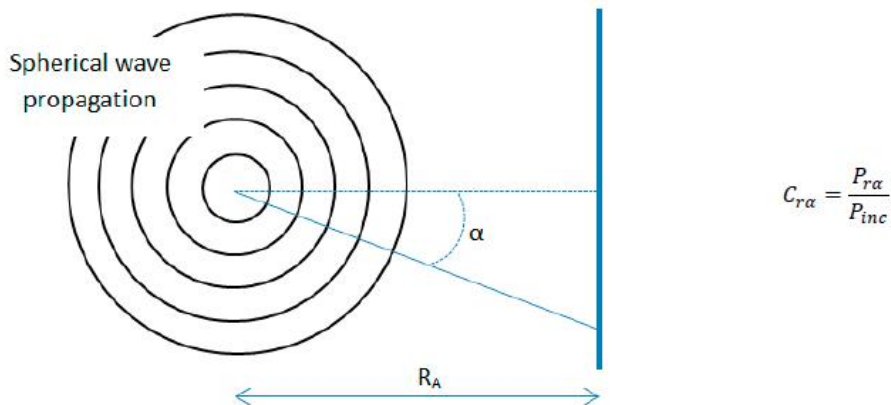


Figure 3.1 - Reflected pressures non-perpendicular angles

The peak incident overpressure versus, the angle of incident pressure, is presented in Figure 3.2, with larger overpressure to the left and smaller incident overpressures to the right [5].

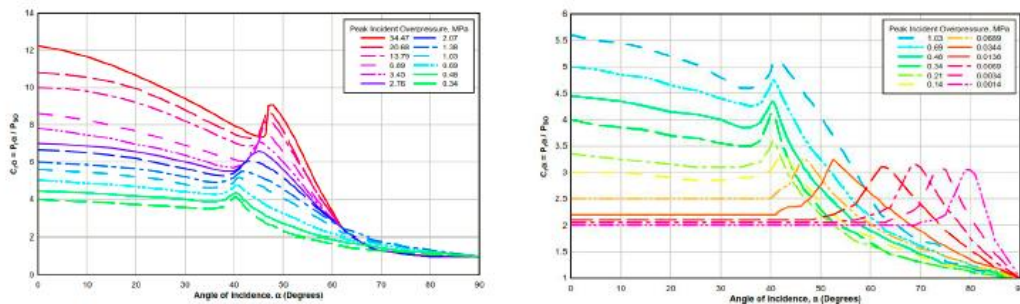


Figure 3.2 - Reflected pressure coefficient at various angle of incidence pressure [5].

Experimental investigations have shown that the reflected pressure can be several times higher than the incident pressure. The maximum reflected pressure is given by the above equation, and is the result of pressure waves (under severe conditions) making air behave in a non-ideal manner [6], which is a fundamental assumption in the equation.

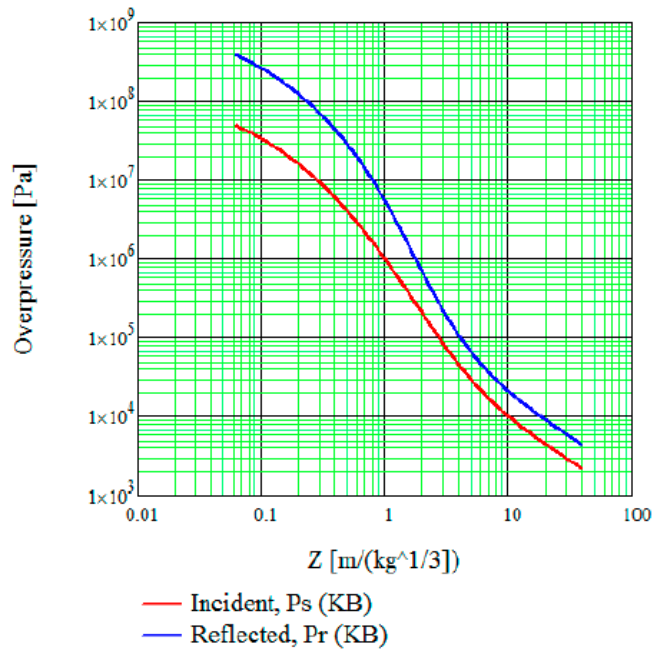


Figure 3.3 - Incident and Reflected overpressure as function of scaled distance.

The relationship between both incident and reflected pressure (perpendicular) relative to the scaled distance is presented in Figure 3.3. The theory behind the reflected pressure is an extension of that has already been presented in Task 8.1 figure 6.5 [1].

Figure 3.4 shows how the respective incident and reflected pressure curves vary as function of distance. The log values along the y-axis indicates how fast the pressure drops with increasing distance from the “energy release centre”, being the centre of the cylindrical lightning spar channel.

The ratio between the reflected (lower graph) and the incident pressure (upper graph) in Figure 3.4 is presented in Table 3-1

Energy Release [kJ]	Radius [cm]					
	10	20	30	40	50	100
10	6.34	4.19	3.10	2.63	2.43	2.13
50	7.26	5.93	4.62	3.72	3.15	2.29
100	7.48	6.51	5.40	4.44	3.74	2.47
250	7.65	7.06	6.28	5.45	4.71	2.85
500	7.74	7.34	6.78	6.13	5.47	3.32

Table 3-1 – Reflected/Incident ratio (R/I ratio)

Increasing energy and reducing radius results in a larger R/l ratio, because of increasing the non-linear effect, described previously in this section. Vice versa will reduce release energy and larger radius result in an R/l ratio of approximately 2, where the double pressure comes from the linear elastic bounce effect.

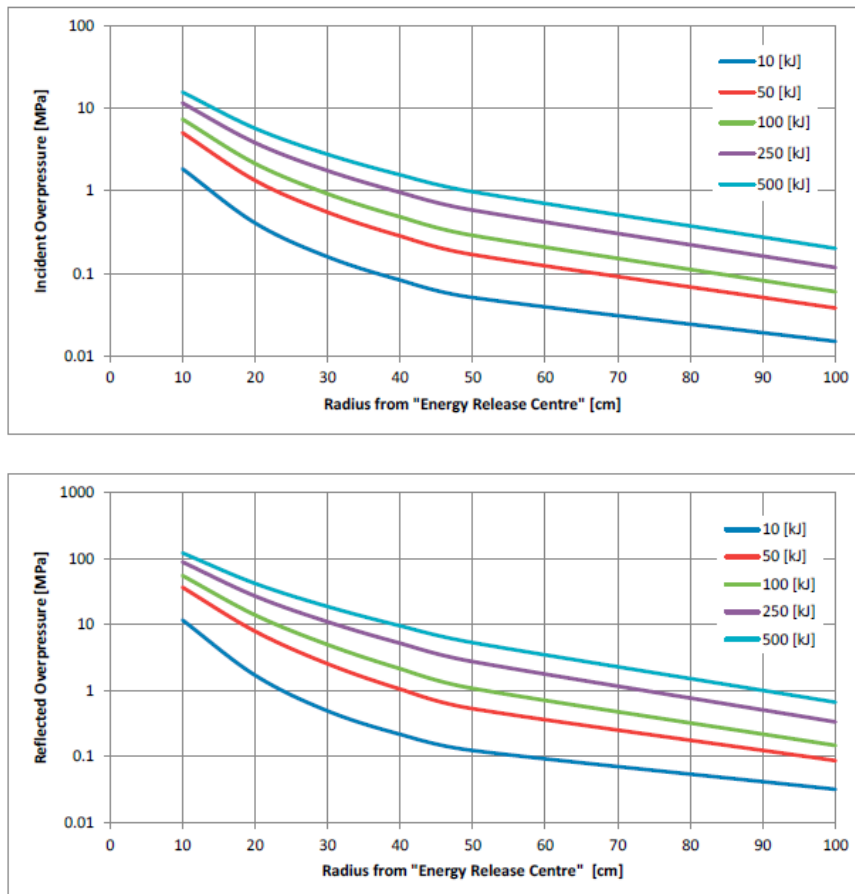


Figure 3.4 - Free-Air Incident and Reflected Overpressure based on GER values in the range of 10 to 500 kJ

#### 4. Geometry

The slenderness ratio of a wind turbine blade is increasing towards the blade tip. The cross section shown below is a cut-out approximately 1 meter from the tip. The total width is approximately 800mm and the height 130mm corresponding to a slenderness ratio of approximately 6.15. This specific blade design has a down conductor positioned in the leading edge and has a main spar box that reaches within 1 meter near the blade tip.



Figure 4.1 - Blade cross section 1 meter from tip

This particular section, at 1 meter from the tip, has a trailing edge (TE) angle of approx.  $10^\circ$  with an inner height of 80mm and an adhesive build-up of approx. 140mm

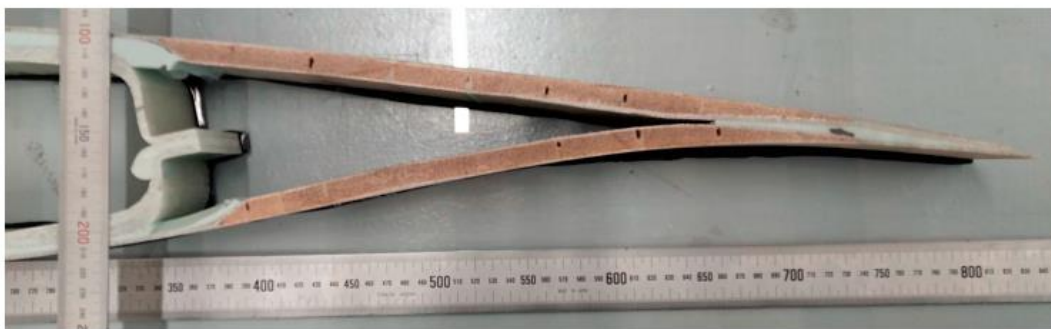


Figure 4.2 – Trailing edge 1 meter from tip

Other designs, such as those mentioned in the appendix, are often with a single shear web or hollow. In the case of a hollow design is the down conductor attached to the skin of the blade.

## 5. Reported Observation

Pronto Solutions has contributed with observations done during repair of three blade types. The complete report is listed in the appendix and the major details are listed in Table 5-1, together with an illustration of the expected path for the lightning arc.

	Tecsis/TPI/MFG 48.7C	Siemens B45 & B53	Mitsubishi 29.5R
Tip observation/repairs	+75	12	2
Blade Materials	Glass/Carbon/Core	Glass/Foam	Glass/Core/Balsa
Web type	I-type	Box-Type	2x C-Channel
Webs (last meter)	YES	NO	NO
Downconductor (type)	Insulated 19 strand #8 alumoclad	Tinned copper braid	Tinned copper braid
Downconductor (pos)	Sidewall of the shearweb	Centrally suction shell	Centrally attached to the TE side of the LE web or centrally to the pressure shell
Receptor	Block (275mm from tip)		
TE angle	15°	Slender	<10°
Adhesive Material	Epoxy		Melted plastic
TE adhesive length	125-150mm		140mm
Impact occurred	N/A	Receptor	Receptor
Exit wound	1 meter from tip near spar cap drop off (3 to 2 layer)		
Arc blast		Off the block through the core material toward the TE	Weakened spot of the conductor and through the shell
TE failure origin (from tip)	0.7-1m	0.4m	
Longitudinal propagation	2.5m	0.7m	2.2-17.5m
TE adhesive failure	Adhesive (through centre)	Cohesive (separation from skin)	Cohesive (separation from skin)
Adhesive condition		Largely left intact—some cracking	Minor stress cracking
Illustration (web, conductor, arc)			

Table 5-1 – Reported observation from unintended lightning strike repairs

Common for all three cross sections is that, the path from the down conductor to the trailing edge, is uninterrupted and all have been repaired for open TE either, in the form of adhesive or cohesive failure in the TE adhesive joint.

Another observation which is notable is that the return-stroke does not always follow the path of the initial stroke, so, even for an ideal impact through the receptor, an unintended situation can arise resulting in an internal arc blast within the blade profile.

## 6. Test Setup

The wave propagation within the blade profile, provided by Bladena, has been tested for the TE reflecting effect. The test setup consists of a power supply, a solenoid impactor, switching relay and an Arduino microcontroller programmed to control the impactor.

The profile was glued to a transparent plate, then filled with water and illuminated from above in a perpendicular angle. A canvas was fixed underneath the transparent plate.

The illuminated wave propagation on the canvas was recorded by a high speed camera from the opposite side of the profile.

The illumination was carried out using a central light source but could have been improved by the use of a collimated beam source; somewhat achievable by using a Fresnel lens and a strong light source placed at the lens focal distance.

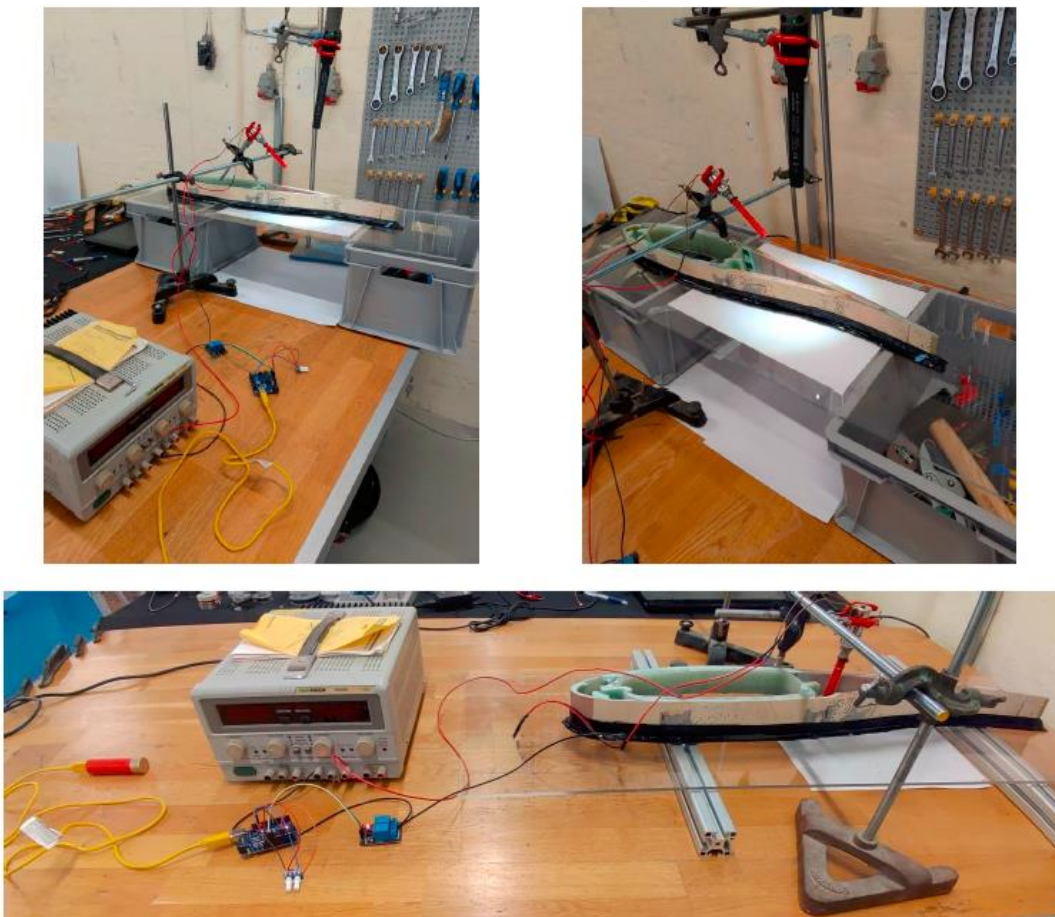


Figure 6.1 – Wave propagation test setup

## 7. Test Results

Two wave propagation tests for the TE blade tip has been investigated, Air-Burst (Figure 7.1.a) where the wave origin is centralised within the TE section and second a Surface-Burst (Figure 7.1.b) where the wave origin is located near the suction shell.

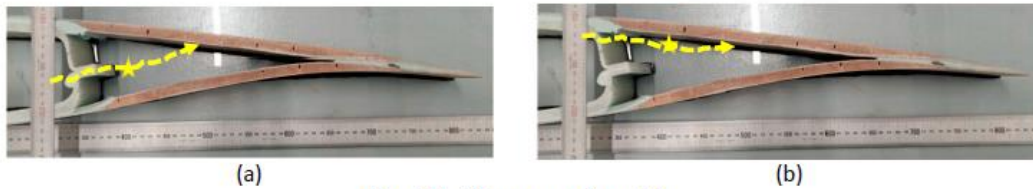


Figure 7.1 – Wave propagation origin

The liquid within the profile cause the waves to damp out more rapidly than in air, making it a somewhat more difficult to see the effects all the way to the TE but the test and recordings clearly illustrates the wave reflection effects, which is the purpose of this test.

### 7.1. Air-Burst

An air burst is simulated by mounting the wave generator at a position central within the TE as shown in Figure 7.2. This simulates a lightning arc from the profile centre to the skin of the TE illustrated by the yellow dotted line.

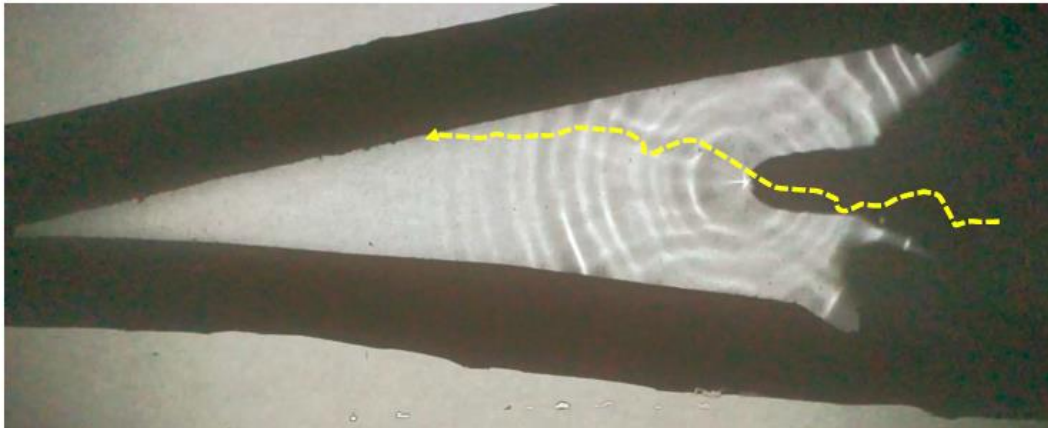


Figure 7.2 – Air-Burst Wave propagation recorded with camera

The waves propagate outwards from the origin and reflect from the skins after which both incident and the two reflected pressure waves propagate towards the TE. The wave pattern is highlighted on the following picture, with red curve for the incident curve and orange dotted lines for the reflected wave.

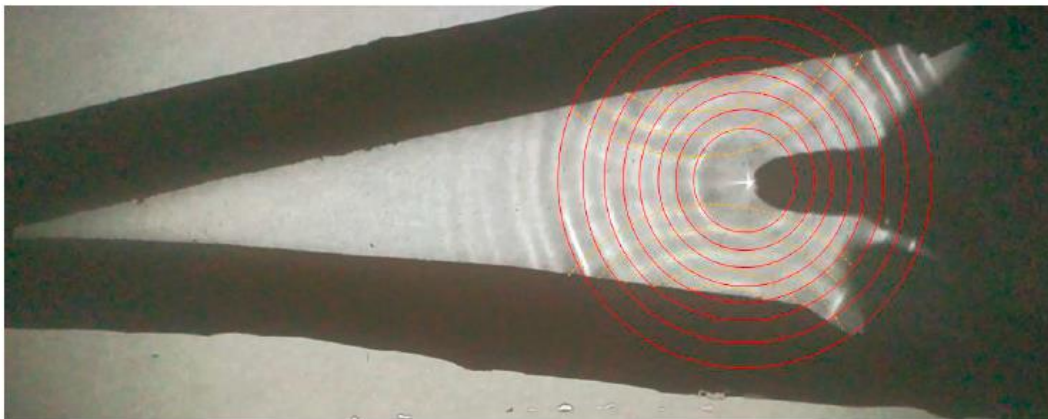


Figure 7.3 – Air-Burst wave reflection

## 7.2. Surface-Burst

Surface burst are simulated by mount the wave generator near the suction shell as shown in Figure 7.4. This simulates a lightning arc running along the shell and exiting through the skin of the TE, illustrated by the yellow dotted line.

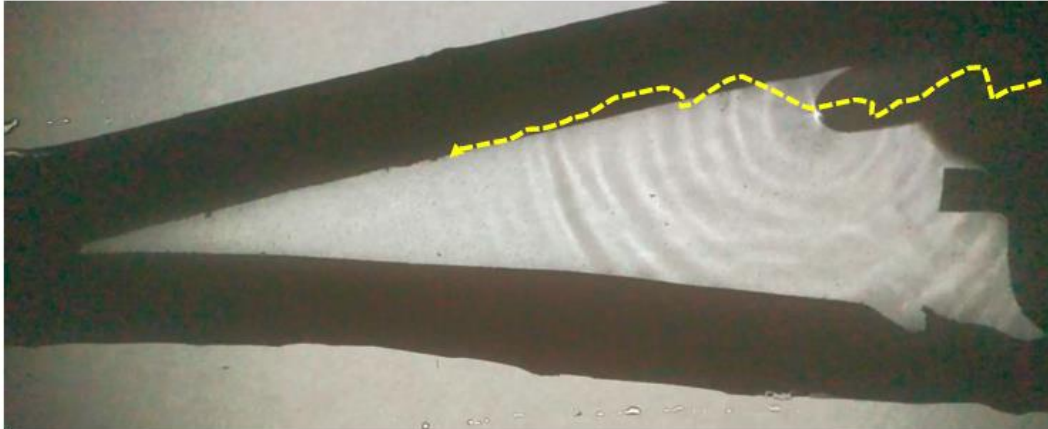


Figure 7.4 - Surface-Burst Wave propagation recorded with camera

The waves propagate outwards from the origin and reflect on the skins in a nearly perpendicular angle. The two wave fronts, incident and reflected, propagate together towards the TE. The wave pattern is highlighted on the following picture, with red curve for the incident curve and orange dotted lines for the reflected wave.

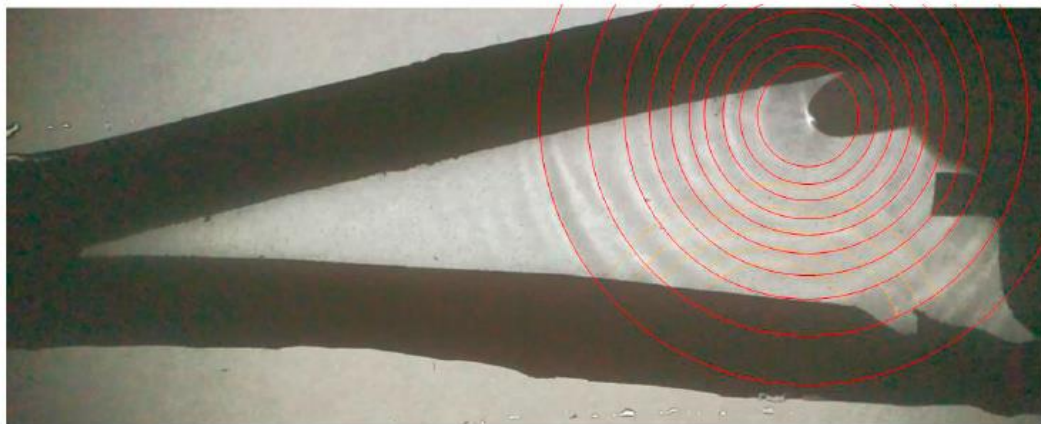


Figure 7.5 – Surface-Burst wave reflection

## 8. Pressure Calculation

The blade cross section used for the wave reflection has a cord length of approximately 800mm at 1meter from the tip and the TE angle is approximately  $10^\circ$ , corresponding to observations from other profiles.

The following assessment is based on the following assumptions:

- A slender hollow profile with TE angle of  $10^\circ$  and aspects ratios according to the profile on Figure 8.1 [1].
- The down conductor is position on the pressure shell, centralised in respect to the UD reinforcement.
- The lightning strike is received through a tip receptor and the return stroke arc, blast off a weakened spot in the down conductor and through a pin-hole in the suction shell as the blade rotates.
- The return stroke has a current of 100kA and based on the following constants: Risetime ( $\tau_1$ ) =  $10\mu\text{s}$ , Decay time ( $\tau_2$ ) =  $350\mu\text{s}$ , Correction factor ( $n$ ) = 7, Ambient pressure ( $p$ ) = 1atm and Correction coefficient ( $a$ ) = 0.8. For further details see Task 8.1 [1].

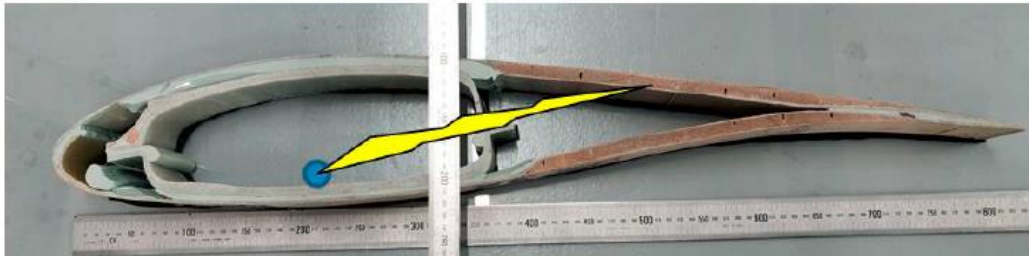


Figure 8.1 – Illustration of an unintended lightning arc within the blade profile.

Figure 8.1 illustrates the assumptions for an unintended surface-burst within the blade. Using the GER approached presented in Task 8.1 would such an arc in a high current lightning strike (100kA) correspond to a GER value of 64.1 kJ.

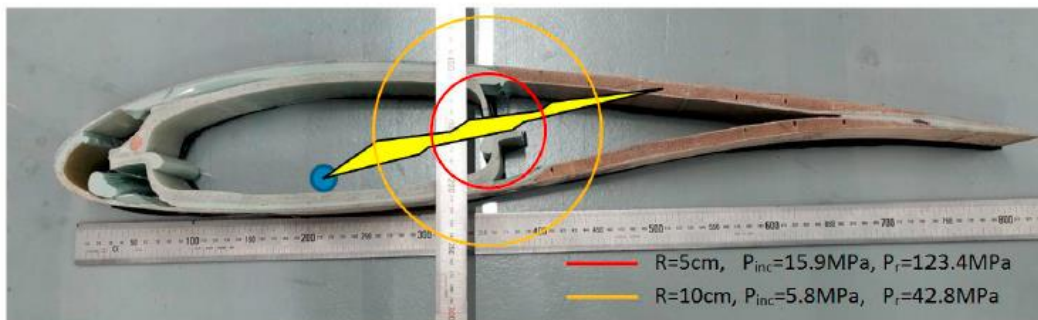


Figure 8.2 – Incident pressure values

The incident pressure propagation outwards from the arc centre is expected to have a pressure of 15.9MPa as it reaches the profile shell. The reflected pressure can be expected to achieve a pressure up to 7.7 times the incident pressure, equivalent to 123.4MPa, assuming perpendicular and rigid surface reflection.

## 9. Pressure Variation Schema

A recommended procedure to calculate of the pressure variation within the blade profile due to lightning is shown schematically in Figure 9.1.

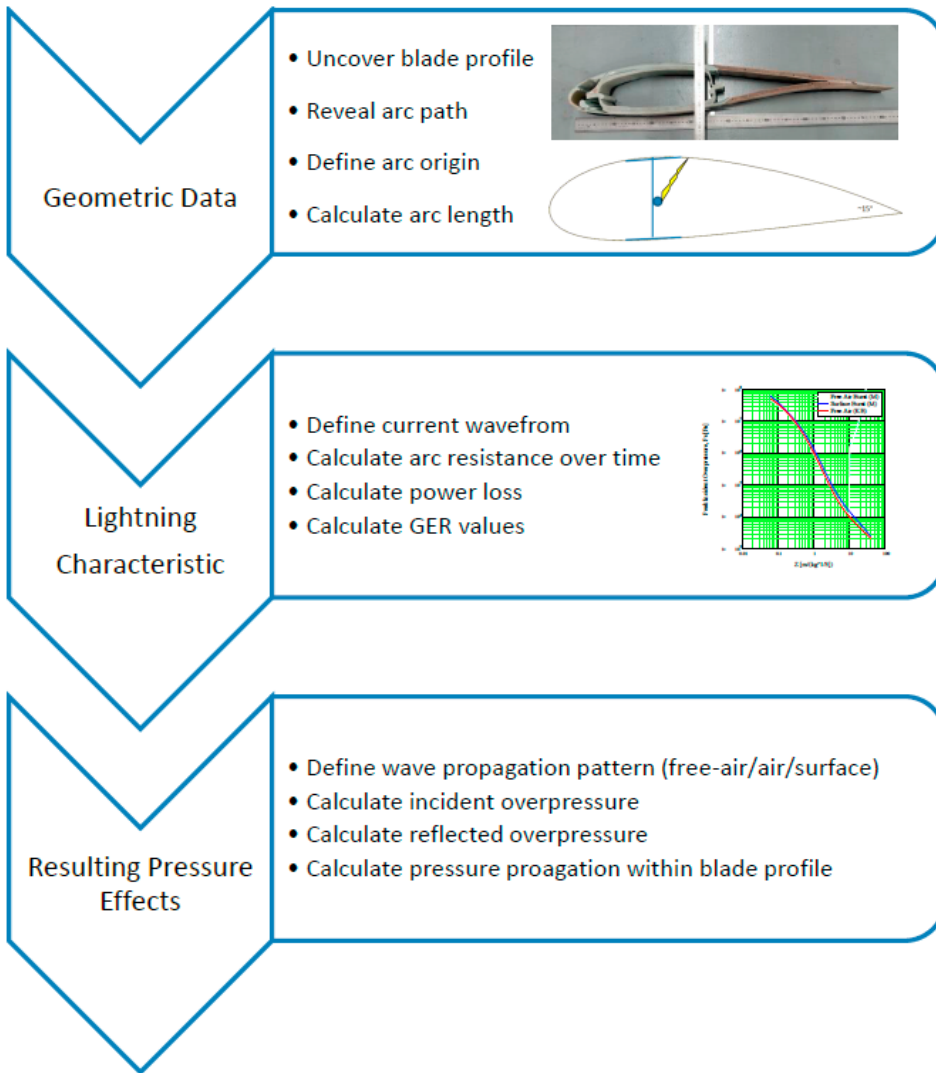


Figure 9.1 - Diagram of pressure variation calculation for the TE structure of the turbine blade

## 10. Conclusion and Further Work

The work carried out in WP8.2 has involved assessing the reflected overpressure due to an unintended lightning strike in the tip of the turbine blade. This work has led to the following conclusions:

- Observation indicates that the down conductor and its position dominate when a return stroke results in an unintended lightning arc within the blade profile.
- Hollow profiles have fewer possibilities in respect to fixing the down conductor and are often fastened to the shell of the profile.
- For webbed profiles all the way to the tip, it is possible to fix the down conductor to the web.
- An ideal lightning impact through the receptor can be followed by an internal arc during return stroke.
- The experimental test setup has been used to show how pressure waves propagate towards the TE.
- Calculation has shown that peak pressures up to 123MPa are to be expected for high current lightning strikes, where the arc is traveling 30cm within the blade profile.
- A schematic approach, to identify the resulting pressure effects within the blade has been suggested.
- Stress levels and strain rates will form a basis for inputs to WP8.3 and WP8.4

## 11. Bibliography

- [1] C. Løjtved, S. Clyens and J. Boelt, "Lightning damage assessment and incident pressure," ECC, Næstved, 2019.
- [2] S. Glasstone and P. J. Dolan, "The Effects of Nuclear Weapons," United States Department of Defense and the Energy Research and Development Administration, 1977.
- [3] M. N. P. P. V. G. Khurd, "Effects of different reinforcement schemes and column shapes on the response of reinforced concrete columns subjected to blast loading," IRJET, 2018.
- [4] B. W.E., Explosions in Air, Austin TX USA: Univ. of Texas Press, 1973.
- [5] N. F. E. U.S. Army Corps of Engineers, Structures to Resist the Effects of Accidental Explosions Command, Air Force Civil Engineer Support Agency, 2008.
- [6] E. C. - I. f. t. P. a. S. o. t. Citizen, "Calculation of Blast Loads for Application to Structural Components (Report EUR 26456 EN)," European Commission, 2013.

## Appendix - Blade Tip Lightning Defects

**E-mail:** Re: Lightning strike data causing trailing edge opening, **Sendt:** 3. maj 2019 21:08

Reece Yeadon  
Operations Manager  
Pronto Solutions  
6530 S US Hwy 377 Unit 1  
Stephenville, TX, 76401  
C: 605.299.6447  
E: [ryeadon@prontowind.com](mailto:ryeadon@prontowind.com)



There are 4 blade models that come to mind when asked about this topic: Trailing Edge Splits caused by Lightning Strikes.

1. Tecsis/TPI/MFG 48.7C
2. Siemens B45 & B53
3. Mitsubishi 29.5R

**48.7C** : Used by GE on the 1.6XLE. It features an I-Type shearweb with carbon fiber sparcaps. The downconductor (to the best of my memory) is an insulated 19 strand #8 alumoclad conductor that is fixed to the sidewall of the shearweb and attached by an integrated lug to an aluminum receptor tip. This blade also features two copper mesh faraday cages—one between the gelcoat and outermost laminate which covers the entire blade, and a second faraday cage between the innermost carbon fiber layer on the sparcap and the glass fiber chopped strand matting.

The two shells are joined at the TE at an angle of approx. 15° with (I believe) an epoxy adhesive that ranges from 125mm to 150mm chordwise. With this specific blade, I have never been able to locate (75+ tip repairs) where the lightning impact occurred—only the exit wound, which was almost always approx. 1m from the tip directly off the carbon fiber where the sparcap laminate orientation drops from 3 layers to 2 layers. The trailing edge split occurs at Z=48m – Z=47.5m and grows longitudinally rootwise. I've seen as much as 2.5m of longitudinal propagation. The adhesive generally gets cracked through the center of the adhesive buildup instead of it separating/delaminating from the inner skin. It was always my opinion that the arc blast was so severe on this blade tip due to the excessive number of conductible surfaces.

**B45/B53** : Used by Siemens as options for the 2.3MW on-shore platform, it features Siemens' signature Box-Type shearweb, but the TE Split almost always occurs directly at the tip through approx. 400mm rootwise of the tip (I've seen as much as 700mm of longitudinal propagation) where there is no shearweb yet. The downconductor is a tinned copper braid which is centrally laminated inside the suction shell and attached via integrated lug to a receptor block approx. 275mm from the tip. The block has two threaded areas (one on SS, one on PS) for the receptors to thread in to the block.

The laminate orientation of the tip is primarily biaxial glass fiber (between 8-12 layers depending on location) with a closed-cell foam core that is very dense. What I have observed (12 repairs) is that the receptor receives the strike and the arc blast occurs off the block through the core material toward the TE. Most times the adhesive along the TE is largely left intact—some cracking—and is separated/delaminated from one of the shells. This blade does have a very slender profile at the tip, so the temperature spike causing the air expansion always separates the core material and usually exits the TE of the blade tip where the laminate buildup is the thinnest.

**29.5R** : Used by Mitsubishi on the 1000A, it features two independent C-Channel Type shearwebs with Unidirectional glass fiber sparcaps. The downconductor is tinned copper braid and is centrally attached to the TE side of the LE Shearweb. These Shearwebs stop at approx. Z=27.9m, at which point the blade is hollow and the downconductor is attached centrally to the pressure side inner skin. This location is also that last place that a core material is used. Rootwise from 27.9m, a 130mm strip of balsa is found approx. 50mm from the aft shearweb and approx. 350mm from the TE. In the outboard-most 1.6m of blade, the laminate orientation is biaxial glass fiber with chopped strand backing.

The adhesive along the TE is more of a melted plastic than a chemical, and the tack characteristic of this adhesive is very poor. The TE of this blade is quite narrow, probably less than 10°, with an adhesive buildup of approx. 140mm chordwise.

I've only been able to get my hands on two of these repairs, but in both cases the pressure shell was entirely separated/delaminated from the plastic adhesive, with only minor stress cracking (presumably from flap loading) to the adhesive. In case one, the TE had severely propagated (17.5m rootwise), and in case two, 2.2m rootwise from the tip. In both cases, the TE Split was the secondary damage. The strike was received through the receptor, the arc blast was off a weakened spot of the conductor and through the shell, and the trailing edge was opened (in my opinion) from the expansion of air coupled with the poor quality adhesive and propagated due to cross-sectional distortion.

## Planning Construction and Modification of test rig

ENERGITEKNOLOGISK UDVIKLINGS-  
OG DEMONSTRATIONSPROGRAM



---

# CORTIR

---

Task 8.3 – Planning, construction and modification of test rig

Christian Løjtved, Stuart Clyens, Jesper Boelt

EUDP

J.nr. 64018-0507

FEBRUAR, 2019

ECC  
Næstved

## Contents

Summary.....	3
1. Introduction.....	3
2. Wave Propagation.....	4
3. Methods of high strain rate testing.....	5
3.1. Development of the Hopkinson Bar Impulsively loaded iron wire .....	5
3.2. The Hopkinson pressure bar.....	5
3.3. The split Hopkinson Bar.....	7
3.4. The torsional slit Hopkinson bar.....	7
3.5. Summary of Hopkinson Bar Developments.....	8
4. Design and implementation of modification for GFRC testing .....	9
4.1. General .....	9
4.2. Test equipment.....	9
4.2.1. General .....	9
4.2.2. Torque head and clamp.....	10
4.2.3. Modifications to the clamp design .....	11
4.2.4. Strain gauges .....	12
4.2.5. Strain gauge amplifier and oscilloscope .....	12
4.3. Modifications to test sample mounting to allow high throughput testing .....	13
4.3.1. Test sample geometry .....	13
4.3.2. Test sample mounting modifications .....	13
5. Theory of the torsional Hopkinson bar.....	15
5.1. One dimensional torsional wave propagation theory.....	15
5.2. Shear wave propagation in the torsional split Hopkinson bar .....	16
6. Modifications to the torsional split Hopkinson bar to allow low strain rate testing .....	17
6.1. General .....	17
6.2. Low strain rate testing.....	18
7. Conclusions.....	18
8. Bibliography.....	19
Appendix 1.....	20

## Summary

The Danish company Bladena have developed a strut concept with the potential to be useful if mounted internally in the tip area of wind turbine blades. These struts are designed to counteract the impulsive loads generated in the tip area when the blade tip is struck by lightning. When a blade tip is subject to a lightning strike the strut can undergo strain rates which far exceed the strain rates that material suppliers normally test their materials. Presently there is no data available related to the high strain rate behaviour of the strut material. This report describes the design and construction of a torsional split Hopkinson bar modified specifically to allow both low and high strain rate testing of samples manufactured from the materials used to manufacture struts. The report includes a short review of the testing materials at high strain rates and a description of the theory of the torsional split Hopkinson bar.

## 1. Introduction

During the lifetime of a wind turbine the entire structure may be expected to be struck by lightning several times. When lightning strikes the blades of a wind turbine, which are relatively thin and weak compared to the wind turbine tower, significant damage can occur. Such damage can be so extensive that the turbine can no longer operate and the turbine must be taken out of service so that the damaged blade can be repaired or replaced.

All modern wind turbine blades are now fitted with lightning conductors, which have reduced the number of blades suffering damage from lightning strikes. However it has been established that certain lightning strikes, which do not pass down the lightning conductor, can result in large electrical discharges within turbine blades. These discharges generate correspondingly large over-pressure pulses within the air contained inside the turbine blade cavity and, when these over-pressure pulses propagate into the relatively weak, trailing edge area of the blade, they have a tendency to cause the trailing edge of the blade to split and burst open.

The damage caused by the impulsive loads resulting from electrical discharge is presently so serious that engineers have begun to explore methods to mitigate their effects. One such method, developed by the Danish company Bladena, involves the use of a reinforcing strut mounted in the trailing edge region of turbine blade cavities.

The reinforcing strut developed by Bladena is presently manufactured from a glass fibre reinforced polymer Durostone EPR-S1 supplied by the German company Rochling. This polymer combines a low electrical conductivity with high mechanical strength. However, to date, the mechanical strength properties of this material have only been investigated under quasi-static loading conditions i.e. at strain rates of  $10^{-4}$ - $10^{-2}$ /s. Clearly, because struts are subjected to a large dynamic load during a lightning strike discharge, the response of the strut material to dynamic loads is of great interest.

This report describes modifications to a torsional Hopkinson to allow testing the response of Durostone EPR-S1 to dynamic mechanical loads.

**Deliverable 8.3:** Planning and construction/modification of test rig

## 2. Wave Propagation

When a mechanical load is applied to a material it results in a strain rate within the material. If the load is applied slowly the resulting strain rate is also low ( $10^{-4} - 10/s$ ). The characterisation of the mechanical properties of materials at low strain rates is well understood. This type of testing is usually carried out using some form of mechanical screw or hydraulic testing machines the design and use of which are well understood.

In contrast to low strain rate testing, when a material is subjected to rapid loading resulting in high strain rates ( $10^2 - 10^6/s$ ) inertial forces must be taken into account and this requires specialised equipment described below.

The various methods used to measure the mechanical response of materials over different ranges of strain rates are shown in Table 2.1

Table 2.1			
Strain rates [s <sup>-1</sup> ]	State	Test Machines / Techniques	Typical physical scenario
$10^{-4} - 10$	Static / Quasi-static	Mechanical testing machines e.g. Instron	Stretch forming, extrusion
$10 - 10^2$	Quasi-static	Hydraulic testing machines	Sheet metal forming operations, superplastic forming operations,
$10^2 - 10^4$	High Strain Rates	Hopkinson bar techniques (Compressive, Tensile, Shear)	Forging, hammer/baton blows, severe car crashes, bullet impacts, explosions
$10^4 - 10^6$	Very High Strain Rates	Flyer-/Taylor impact-/Pressure shear impact- plate	Plastic explosives, rocket weapons, antitank missiles

### 3. Methods of high strain rate testing

The development of methods used to measure the high strain rate behaviour of materials is briefly discussed in the following part of the report. These methods focus on establishing techniques to control and measure stress waves within test equipment and avoid stress wave reflections which can influence test results.

#### 3.1. Development of the Hopkinson Bar Impulsively loaded iron wire

In 1872 J Hopkinson [1], [2] published two papers in “the Proceedings of the Manchester Literary and Philosophical Society” describing work he had carried out to investigate the rupture of iron wire by a blow. These papers describe a theory of how stress waves propagate through an iron wire fixed at one end whilst the other end is suddenly loaded under tension by an impulse generated by a moving mass impacting a stop attached to the end of the wire. The papers also present experimental results obtained under different loading conditions which were varied by using different impacting masses and impact velocities. By varying these parameters it was possible to investigate whether the rupture of the iron wire occurred near the impulse end or near the fixed end of the wire. It was shown that “half the velocity of impact needed to break the wire near the mass is sufficient to break it at the fixed point”.

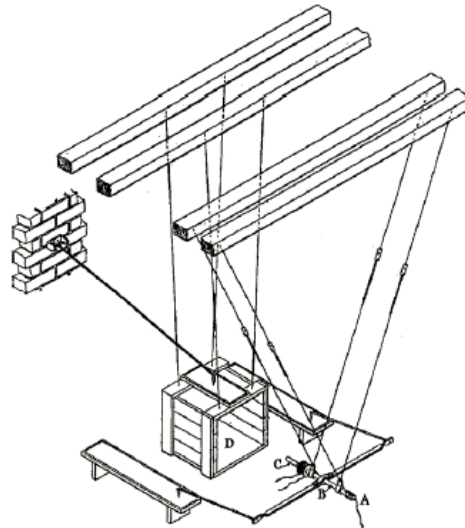
Thirty three years later B.Hopkinson, the son of J Hopkinson, built on his father’s pioneering work and formulated analytical expressions for the total increase in the length of an impulsively loaded wire, which is fixed at one end [3]. He carried out an experiment in which the momentary extension of the wire was measured using a contact device and a ballistic galvanometer. Basically the contact device was placed at different distances from the loaded end of the wire and contact or no-contact was identified by the response of the ballistic galvanometer.

Multiple experiments were needed to determine the wire extension however the work is probably the first to measure dynamic extension with state of the art technology.

#### 3.2. The Hopkinson pressure bar

In 1914 B Hopkinson developed an experimental technique to measure the pressure produced by the impact of a bullet or by the detonation of gun cotton. This technique, which is shown in Figure 3.1, became known as the Hopkinson Pressure Bar and is one of the most famous methods for determining the dynamic mechanical properties of materials. In his paper describing the technique [4] Hopkinson reported that “if a rifle bullet be fired against the end of a cylindrical steel rod there is a definite pressure applied on the end of the rod at each instant of time during the period of impact”. In other words the bullet generates a pressure pulse. In Hopkinson’s experiments a compressive impact pulse generated by a bullet or gun cotton detonation at A was allowed to propagate down a long rod, marked as B in Figure 3.1. This compressive pulse was reflected from the free end of the long rod as a tensile pulse. Hopkinson described how a short rod (C) of the same material as the long rod was mounted coaxially and in contact with the long rod. A compressive pulse propagated down the long rod and into the shorter rod and reflected as a tensile wave from the free end of the shorter rod would result in the shorter rod “flying off” the longer rod. The momentum of this short rod (C) was measured by a ballistic pendulum, shown as (D) in Figure 3.1. By measuring the maximum displacement and period, and knowing the mass of the ballistic pendulum, the momentum of the flying piece (C) can be determined. Hopkinson showed that by varying the length of (C),

the maximum amplitude of the pressure and the total duration could be measured, however the pressure pulse shape cannot be obtained.



Apparatus developed by Bertram Hopkinson for the measurement of the pressure produced by the detonation of gun cotton [4]

Figure 3.1

In his paper [4] Hopkinson cited the theory of dispersion in rods described by Love [5] and Hopkinson conducted experiments with smaller bar lengths to study the effect of wave dispersion. In addition the work of Pochhammer [6] and Chree [7] on 3D longitudinal wave propagation in infinite bars had also been published when Hopkinson was carrying out his experiments on the pressure bar in 1914.

The unique method developed by Hopkinson using the pressure bar allowed a wide ranging parametric study of the effects of bar length and diameter, bullet types, gun cotton type, and explosion method to be carried out.

The pressure bar technique had its limitations, however, and in 1948, RM Davies published a critical review of it, stating that it was impossible to "measure dynamic pressures that change in times of the order of  $1 \mu\text{s}$ " and that the change from no pressure in the rod to a pressure wave caused by a striking bullet is not instantaneous but has a rise-time in the order of a few  $\mu\text{second}$  [8].

### 3.3. The split Hopkinson Bar

In 1949, Kolsky published the first paper on the compressional split Hopkinson bar. He further developed the idea behind the pressure bar by attaching mounting a piece of test material between two cylindrical steel bars. By firing a detonator at the end of one of the bars he created a pressure wave that moved down the steel bar attached to the detonator, through the test material and into the second steel bar. By using a parallel plate microphone he could measure the displacement of the free end of the second steel bar [9]. This made it possible to accurately detect the pressure in the bars on both sides of the samples and from this it was possible to calculate the displacements of the faces of the bars and thus how much strain the sample experienced over time. The stress over time is given by the gradient of the displacement of these faces and when both the strain and the stress are known, stress-strain curves can be plotted.

Using this new machine, Kolsky tested five different materials and showed that they responded very differently to dynamic deformation and that this kind of deformation resulted in very different stress-strain properties compared to static or quasi-static deformation [9].

It soon became apparent that this method, although accurate and convenient, also had some built in problems related to it that could not be eliminated. The two most important problems were; (a) the dispersion of longitudinal waves with a wavelength comparable to the bar diameter - this means that as the wave moves down the bar, it disperses and does not remain as a square pulse. (b) the kind of deformation caused by the compression bar results in inertial body forces within the test sample. The test sample does not maintain the same geometry as the test progresses and this change in shape causes an error in the stress measurement that increases with the strain rate [10]. This creates an upper limit for the strain rates at which it is possible to get precise measurements.

### 3.4. The torsional slit Hopkinson bar

It was realised that these problems were not present in a system that produced a torsional strain and several methods for producing such strains were developed, such as dropping weights onto an arm attached to the sample, but this approach causes large bending waves. [11] In 1964 Pope, Vreeland and Wood invented the first torsional SHB. The idea was to store energy as torque until the desired load was obtained and then release it in an instant, creating a large, almost square torsional shear wave that would propagate through the bars and the sample. They held the torque in place by using a glass disc with a metal foil embedded in it. When a large electrical charge was passed through this foil, the glass would break and release the torque. The problem with this method was that the glass could only hold a relatively small torque and only waves of small amplitudes could be produced, making tests of high strength materials almost impossible [10].

In 1969, Lewis and Campbell built a machine to meet the need to achieve higher strain rates. Instead of the glass disc, they used cement to hold the bars in place that broke when the input bar was twisted enough. Although this technique allowed much larger strain rates to be obtained, it had several grave problems; the cement would not break at exactly the same load from one experiment to the other, a new connection had to be cast each time an experiment was performed, the cement took an excessive amount of time to set and if the cement broke asymmetrically, bending waves could be produced, invalidating the measurements of the torsional wave [10].

The first researchers to use clamps to hold the bars in place were Baker and Yew in 1964, preceding Lewis and Campbell's cement coupling. They used a hydraulic system to hold the clamps in place, ejecting a part of the system with an air gun to release the grip on the bar. This, however, created additional axial and transverse stresses that mixed with the torsional stress, muddling the measurements.

In an attempt to prevent these extra stresses, Dowling created a system in 1968 where the clamps were held in place by a piece of metal wire [10]. The release mechanism was then simply cutting this wire, allowing the bar to turn. Although this almost completely removed the non-torsional stresses, the amount of torque that could be stored this way turned out to be rather limited, only making it possible to create stress waves of low amplitudes. This meant that high strength materials like steel and other strong metals could not be properly investigated as with the glass disc.

In 1969 Lewis and Campbell suggesting using a weakened bolt, a snap bolt, to store the torque. The idea is simply to cut a V-shaped groove in a normal high tensile steel bolt and tighten the clamps with it. If the groove has an appropriate cross section, the bolt is strong enough to hold the bar in place when loaded with torque, and weak enough to be breakable simply by further tightening. This method causes almost no additional stresses, is strong enough to hold large torques in place and very quick to prepare, removing the clamping as a time-limiting factor.

### 3.5. Summary of Hopkinson Bar Developments

It has taken around a century from John Hopkinson's first experiments until the development of a fully functional, reliable torsional split Hopkinson bar. During this time, many different approaches have been tried. The particular experimental setup chosen for the work described in this report is a torsional system employing titanium input and output bars and a friction clamp held in place by a notched high tension steel bolt. This system was selected as it has proved to be one of the most reliable methods available for the high strain rate testing of materials.

The split Hopkinson bar is also a versatile instrument. It has been used to characterise the dynamic mechanical behaviour not only of metals but a wide range of other materials including viscous fluids [10] [12], polymers melts [13], foams [14], ceramics [15] composites [16]. Split Hopkinson bars have also been developed that can perform tests at extreme temperatures, both low and high. In 1974 Stevenson and Campbell [17] devised a Hopkinson bar set up that was used to measure the high strain rate behaviour of low carbon steels up to 500°C and in 2009 Li [18] performed tests using a Hopkinson bar operating at 800°C.

## 4. Design and implementation of modification for GFRP testing

The design and construction of a torsional split Hopkinson bar modified to allow high strain rate testing of glass fibre reinforced composites

### 4.1. General

The aim of the work described in this report was to modify an existing torsional Hopkinson bar so that it could be employed for high strain rate testing the glass fibre reinforced composite material used by Bladena to manufacture reinforcing struts for wind turbine blades. The material used by Bladena for strut manufacture is Durostone EPR-S1 supplied by the German company Rochling. The properties of this polymer are described in more detail in Appendix 1.

### 4.2. Test equipment

#### 4.2.1. General

The torsional split Hopkinson bar equipment, used to carry out the high strain rate tests is shown in schematically in Figure 4.1. The equipment comprises two 3 metre long, 18mm diameter bars manufactured from a high strength titanium alloy Ti6Al4V (E). These bars, referred to the input bar I and the output bar O, are supported by a series of plain bearings (B1, B2, B3, B4) which allows the bars to be axially aligned. A tubular test sample T mounted between the ends of the titanium bar using a high strength epoxy adhesive.

In order to subject test samples to a high strain rate a large amplitude, elastic shear wave is generated within and propagated down the input bar I, through a test sample and into the output bar O. This generates high strain rate loading conditions within the test sample. The stress, strain and strain rate within the test sample are determined from the signals generated by strain gauges S1, S0, mounted at the mid-points of the input and out bars, and through the application of one dimensional torsional elastic wave theory.

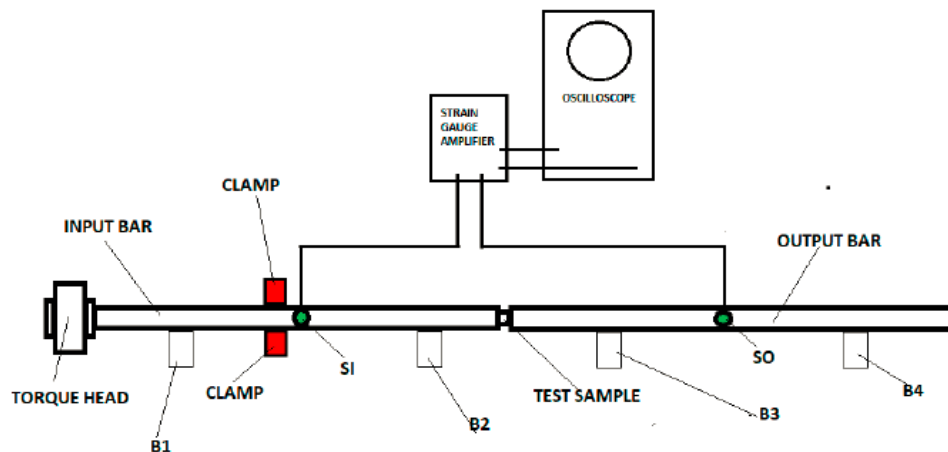


Figure 4.1 - Schematic drawing of a torsional split Hopkinson bar

#### 4.2.2. Torque head and clamp

In order to generate the large amplitude elastic shear wave within the input bar a clamp, positioned just before the mid-point of the input bar, is used to prevent the input bar from rotating. The clamped section of the bar is then rotated using a torque head driven by a hand driven gear box. The torque head is shown in Figure 4.2



Figure 4.2 - Torque head used to twist the clamped section of the input bar

A typical clamp design employed to clamp the input bars of torsional split Hopkinson bars is shown in Figure 4.3

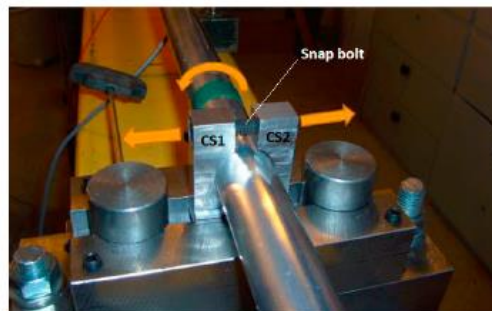


Figure 4.3 - Typical clamp used to lock the input bar of a torsional split Hopkinson bar

The clamp comprises two hinged clamp shoes CS1 and CS2, machined to conform to the input bar, surface. These shoes grip the bar when a snap bolt, passing through the top of the clamps, is tightened. The central section of the snap bolt is machined with a 45 degree "V shaped" notch. In order to rapidly release the clamp, thereby generating an impulsive shear wave in the input bar, the bolt holding the clamp shoes is simply tightened further until it fractures. Snap bolts both before and after fracture are shown in Figure 4.4



Figure 4.4 - Snap bolts used to tighten the clamp shoes

In the typical clamp described above, the input bar is prevented from turning by frictional forces between the clamp shoes CS1, CS2 and the bar. This form of clamp works well when relatively low torques (up to 10Nm) are applied to the input bar by the torque head. However, when larger torques are applied the input bar tends to slip.

#### 4.2.3. Modifications to the clamp design

In order to overcome the problem of the input bar slipping the clamp was redesigned and the clamp shoes shown in Figure 4.3 were replaced by flat shoes shown in Figure 4.5. The input bar was also modified by machining small, diametrically opposed, flat sections on the input bar. In order to clamp the input bar the bar was oriented so that the faces of the flat clamp shoes and the flat sections on the bars were parallel. When a snap bolt was mounted in the clamp shoes and tightened the flat surfaces on the input bar and clamp shoes came into contact and the input bar locked in place. This new clamp system has been found to work well with torques of up to 350Nm.

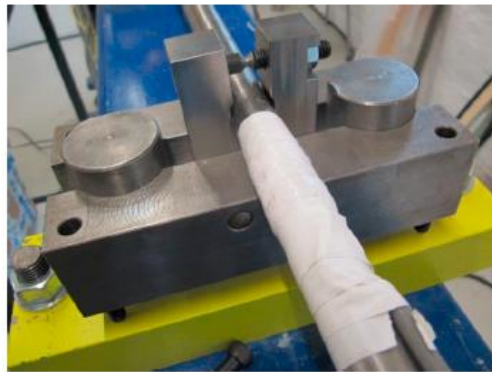


Figure 4.5 - Modified clamp to allow the retention of large torques by the input bar

#### 4.2.4. Strain gauges

Following the release of the clamp, the amplitude of the of the shear wave propagating through the input and out bars was measured using strain gauges mounted on the input and output bars. The strain gauges were mounted on the bars so as to create a Wheatstone bridge at the mid-point of each bar. The particular strain gauge distribution employed was capable of measuring shear strain whilst cancelling out any signals generated as the result of bending stresses. A close up of one of the eight strain gauges used to create the two Wheatstone bridges is shown in Figure 4.6

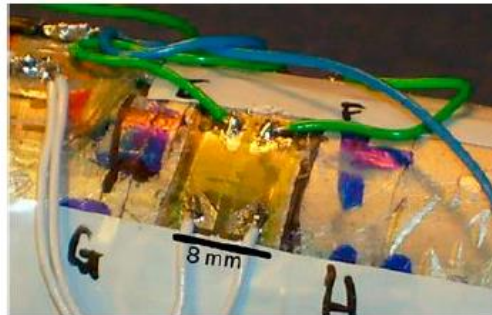


Figure 4.6 - Close-up view of one of the 45o strain gauges used to measure shear strain

#### 4.2.5. Strain gauge amplifier and oscilloscope

The signals from the strain gauges were first fed to a Fylde H379TA wide band amplifier. The amplified strain gauge signals were then fed to a Tektronix DPO 2024 digital storage oscilloscope and finally stored on a computer for further processing. The Fylde wide band amplifier and the Tektronix oscilloscope used to record the strain gauge signals are shown in Figure 4.7

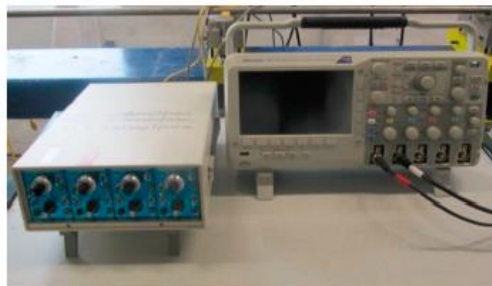


Figure 4.7 - Equipment used to record the strain gauge signals

### 4.3. Modifications to test sample mounting to allow high throughput testing

#### 4.3.1. Test sample geometry

Tubular test samples, usually machined from a solid bar, are used for torsional Hopkinson bar tests. The geometry of the test samples normally employed is shown in Figure 4.8

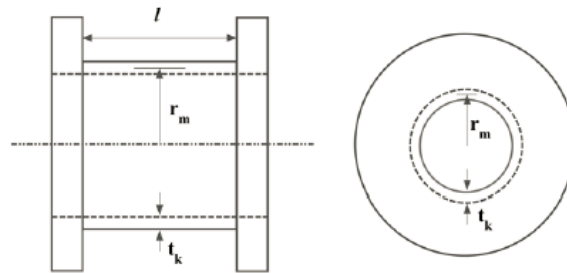


Figure 4.8 - Side and end views of the test samples

As can be seen the test samples are machined so as to create a circular flange at each end of a central tubular test section. The flanges provided a large surface area which allows the test samples to be bonded to the input and output bars of the Hopkinson bar using a high strength epoxy adhesive.

Previously all specimens for testing have been mounted between the input and output bars of the torsional Hopkinson bar using an epoxy adhesive to bond the specimens directly to the ends of the bars. Although this approach works it is time consuming as a minimum of 24 hours must be allowed for the epoxy to cure. This limits testing to one specimen per day.

#### 4.3.2. Test sample mounting modifications

In order to increase the number of samples that could be tested test per day it was decided to develop a new specimen mounting system which involved producing a large set of titanium end caps of the type shown in Figure 4.9. Each test sample was bonded to a pair of end caps as shown in Figure 4.10



Figure 4.9 - Titanium end caps



Figure 4.10 - Typical tests sample bonded to titanium end caps

The recesses machined into the end caps match the geometry of spigots machined on the ends of the inputs and output bars shown in Figure 4.11

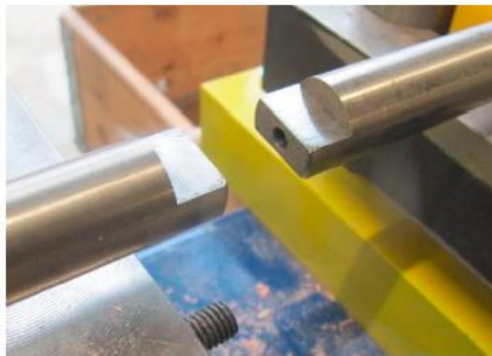


Figure 4.11 - Flat spigots machined on the end of the titanium input and output bars

The spigots allow samples, bonded to a set of end caps, to be quickly mounted between the input and output bars as shown in Figure 4.12. Similarly, after testing, samples can be quickly removed and replaced by a new test sample.



Figure 4.12 - Test sample bonded to end caps and mounted on the input and output bar spigots

## 5. Theory of the torsional Hopkinson bar

### 5.1. One dimensional torsional wave propagation theory

When calculating the stress and the strain experienced by a sample, one dimensional torsional wave propagation theory is employed. When a unidirectional shear wave, similar to that generated by release of the clamp in the setup, is sent through a material, the relationship between the torque and the resulting angular velocity of the bar is given by

$$\omega = \frac{T}{J\rho c} \quad \text{Eq. 5.1}$$

Where (T) is the torque (J) is the polar moment of inertia of the input and output bar material, ( $\rho$ ) is the density of the bar, (c) is the shear wave speed in the bar and  $\omega$  is the angular velocity of the bar. The factor Jpc is also known as the torsional impedance of the bar.

J,  $\rho$  and c are all constants of the bars that remain the same throughout all tests. ( $\rho$ ) was calculated for the particular kind of titanium used in the setup. A sample section was cut off, weighed and measured and the density determined. This was 4.43 grams/cm<sup>3</sup>.

(J) was determined using the expression for the polar moment of inertia for a solid bar which is given by equation below.

$$J = \frac{\pi r^4}{2} \quad \text{Eq. 5.2}$$

For the 18mm diameter titanium bar used for the tests described in this report the equation below gives a value for the polar moment inertia of  $1.03 \times 10^{-8} \text{ m}^4$ .

The speed of propagation of torsional waves through the titanium alloy bars was determined by mounting a short cylinder of the same titanium alloy between the bars and then sending a shear wave down the combined bars. These both served to calculate the shear wave speed as well as determining whether or not gluing samples onto the input/output bars allows propagation of the shear waves through the glued joints.

To determine the shear wave speed, the time between the wave reaching the first and the second strain gauge bridge, ( $t_{bc}$ ), is measured. As the distance between the two bridges was known to an accuracy of around 1mm, finding the wave speed was just a matter of simple division. The measurement of the time was done by measuring the difference in arrival times at the bridges of the same torsional shear pulse. This was done using the oscilloscope and as the input and the transmitted waveforms are very well defined and the beginning of each wave can be read off with an uncertainty of around 10 $\mu$ s at most, which is small compared to the duration of the wave of approximately 1,000  $\mu$ s. Five measurements of ( $t_{bc}$ ) were done, giving an average of 940 $\mu$ s. The distance between the strain gauges,  $x_{\text{gauges}}$ , is 3.00m, so the torsional shear wave speed through the titanium is 3152m/s.

The torsional wave speed c can also be calculated using the relationship between shear modulus (G) and density ( $\rho$ ) as follows.

$$c = \left(\frac{G}{\rho}\right)^{1/2} \quad \text{Eq. 5.3}$$

The manufacturer's value for (G) is 44MPa and density is 4,43grams/cm<sup>3</sup> which when fed into Eq. 5.7 gives a value for (c) of 3151m/s.

## 5.2. Shear wave propagation in the torsional split Hopkinson bar

When a torsional shear wave propagates down the input bar and reaches the input bar-test sample interface part of the input wave is reflected back into the input bar and a part of it is transmitted through the sample to the output bar.

In terms of torque, which is what is determined from the strain gauge bridge signals, the input torque measured by input bar strain gauge bridge is denoted by ( $T_1$ ) and the transmitted torque is denoted by ( $T_2$ ). The reflected torque,  $T_R$  can then be calculated simply by subtracting ( $T_1$ ) from ( $T_2$ ):

$$T_R = T_2 - T_1 \quad \text{Eq. 5.4}$$

This value is always negative because the interface acts almost as a free end, reflecting most of the incoming wave. The angular velocity at the input bar-test sample interface  $\omega_{it}$  can then be calculated by subtracting the reflected torque from the incoming torque and dividing by the torsional impedance as follows

$$\omega_{it} = \frac{T_1 - T_R}{J\rho c} \quad \text{Eq. 5.5}$$

Using Eq. 5.8 to substitute for  $T_R$  in Eq. 5.9 the expression for  $\omega_{it}$  becomes

$$\omega_{it} = \frac{T_1 - (T_2 - T_1)}{J\rho c} = \frac{2T_1 - T_2}{J\rho c} \quad \text{Eq. 5.6}$$

The angular velocity of the output bar-test sample interface is given by

$$\omega_{ot} = \frac{T_2}{J\rho c} \quad \text{Eq. 5.7}$$

since the only torque acting on this interface is ( $T_2$ ). The total difference in angular velocity across the test sample is therefore

$$\Delta\omega = \omega_{it} - \omega_{ot} = 2\left(\frac{T_1 - T_2}{J\rho c}\right) \quad \text{Eq. 5.8}$$

The average shear strain rate ( $\dot{\gamma}$ ) in the test sample is given by

$$\dot{\gamma} = \Delta\omega \cdot \frac{r_m}{l} \quad \text{Eq. 5.9}$$

where ( $r_m$ ) is the average radius of the sample and ( $l$ ) is its length. In a tube-like sample similar to those used, the average radius is the inner radius of the sample plus half its wall thickness.

The shear strain ( $\gamma$ ) at any instant ( $t$ ) is found by simply integrating the shear strain rate expression between the start of the test and ( $t$ ).

$$\gamma = \int_0^t \dot{\gamma} dt = \int_0^t \Delta\omega \frac{r_m}{l} dt \quad \text{Eq. 5.10}$$

The shear stress ( $\tau$ ) in the test sample is given by

$$\tau = \frac{T_2}{2\pi r_m^2 t_m} \quad \text{Eq. 5.11}$$

Where ( $r_m$ ) is the mean radius of the tubular test specimen and ( $t_{m\text{is}}$ ) the mean wall thickness.

## 6. Modifications to the torsional split Hopkinson bar to allow low strain rate testing

### 6.1. General

In order to be able to compare the high strain rate behaviour of test materials with their behaviour under quasi static loading it was necessary to construct a low strain rate testing device.

Figure 6.1 shows a general view of the torsional Hopkinson bar modified to carry out low strain rate testing. As can be seen the long input and output bars used for high strain rate testing are replaced by a short bar (A), mounted in the torque head (T), and a short bar (B) mounted in an adjustable clamp (c). The ends of both of these bars are machined with spigots to allow samples to be mounted for testing in the same way as the sample are mounted for high strain rate testing.



Figure 6.1 - The torsional split Hopkinson bar set up to carry out low strain rate testing

## 6.2. Low strain rate testing

Low strain rate testing is carried out by mounting a test sample, bonded to end caps, between bars (A) and (B) and then using the torque head to apply a shear load to the test specimen. The shear load applied to the test specimen is measured using strain gauges attached to bar (B) and the shear strain at a given shear load is measured via the large rotary dial, shown in Figure 6.2, which is attached to the torque head.

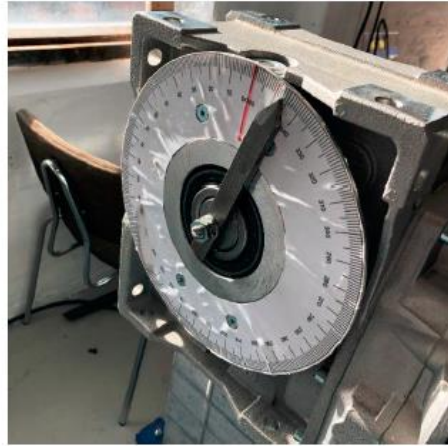


Figure 6.2 - Rotary dial use to determine shear strain at low strain rates.

## 7. Conclusions

- a) The modifications to the torsional Hopkinson bar described above allow the mechanical behaviour of tubular test samples to be measured at both low and high strain rates essentially using the same test equipment.
- b) The modifications made to the torsional Hopkinson bar allow large input torques to be supported by the input bar, thereby enabling high strain rates to be achieved when the torsional Hopkinson bar is used in the high strain rate mode.
- c) The machining of flat spigots on the ends of the input and out bars, combined with the use of test samples bonded to end caps, allows test samples to be quickly mounted between the input and output bars and tested. Similarly samples can be quickly removed and replaced.

## 8. Bibliography

- [1] o. J, "On the rupture of iron wire by a blow," *Original Papers-by the late John Hopkinson*, vol. Article 38, no. Vol II, pp. 316-320, 1872.
- [2] H. J, "Further experiments on the rupture of iron wire," *Original Papers-by the late John Hopkinson*, vol. Article 39, no. Vol II, pp. 316-320, 1872.
- [3] H. B, "The Effects of Momentary Stresses in Metals.," *Proc. R. Soc. London*, vol. A 74, p. 498–506, 1905.
- [4] H. B, "A method of measuring the pressure produced in the detonation of high explosives or by the impact of bullets," *Philos. Trans. R. Soc. London, Ser* , vol. A 213, p. 437–456, 1914.
- [5] L. AEH, *Mathematical Theory of Elasticity*, 2nd edition, ambridge Univ Press, 1934.
- [6] P. L, "Über Fortplanzungsgeschwindigkeiten kleiner Schwingungen in einem unbergrenzten isotropen Kreiszyylinder," *J. Reine Angew. ,* vol. Math. 81, p. 324 , 1876.
- [7] C. C, "The equations of an isotropic elastic solid in polar and cylindrical coordinates, their solution and applications," *Trans. Cambridge Philos. Soc.*, no. 14, p. 251–369., 1889.
- [8] a. RM, "A critical study of the Hopkinson pressure bar," *Philos. Trans. R. Soc. London, Ser*, vol. A 240, p. 375–457, 1948.
- [9] K. H, "An investigation of the mechanical properties of materials at very high rates of loading," *Proc. Phys. Soc. London, Sect.*, Vols. B 62(II-B), p. 676–700, 1949.
- [10] L. Shen, I. Y. Phang, T. Liu and K. Zeng, "Nanoindentation and morphological studies on nylon 66/organoclay nanocomposites," *II. Effect of strain rate.*, vol. 45, p. 8221–8229, 2004.
- [11] D. P. Pope, T. Vreeland and D. S. Wood, "Rev. Sci. Instrum," vol. 1351 , no. 35, 1964.
- [12] M. G. Stevenson and J. D. Campbell, "High Strain Rate Testing of a Low Carbon Steel to High Strains over a Range of Temperatures, Using a Torsional Hopkinson-bar Apparatus," University of Oxford, Oxford, 1974.
- [13] M. C. Tsao, "Plastic properties of metals and alloys at high strain rates," Oxford University, Oxford , 1973.
- [14] P. R. Mantena, A. Al-Ostaz and A. H. D. Cheng, "Dynamic response and simulations of nanoparticle-enhanced composites.," *Composites Science and Technology*, vol. 69, p. 772–779, 2008.
- [15] R. Feng and K. T. Ramesh, "The Rheology of Lubricants at High Shear Rates. Transactions of the ASME," *ASME*, vol. 115, p. 640–649, 1993.
- [16] R. M. Davies, "A critical study of the Hopkinson pressure bar. Philosophical transactions of the Royal Society of London," Royal Society of London, 1948.
- [17] S. C. Chou, K. D. Robertson and J. H. Rainey., "The Effect of Strain Rate and Heat Developed During Deformation on the Stress-Strain Curve of Plastics."
- [18] S. S. Sarva, S. Deschanel, M. C. Boyce and W. Chen, "Stress-strain behavior of a polyurea and a polyurethane from low to high strain rates," *Polymer*, vol. 48, p. 2208–2213, 2007.

## Appendix 1

<b>Technische Daten</b> <b>Durostone® Plattenmaterial</b> <b>Technical data</b> <b>Durostone® sheet material</b>		Prüfmethode Test method	Einheit Unit	EPR S1	EPR S5	EPM S7	EPR S6	UPR S19
Standardfarbe Standard colour		–	–	rot red	natur natural	natur natural	natur natural	natur natural
Harzart Type of resin		–	–	Epoxid		Epoxid	Epoxid	Polyester
Dichte Specific gravity		ca.	ISO 1183 meth 1	g/cm <sup>3</sup>	1,90	1,90	2,00	1,95
Brandverhalten Flammability			UL 94	–	–	–	VO	–
Biegezugfestigkeit Bending strength	Biegezugfestigkeit senkrecht zur Schichtichtung Bending strength	⊥	ISO 178	MPa	500	300	600	350
	Dehnmodul senkrecht zur Schichtichtung Modulus of elasticity	⊥	ISO 178	GPa	20	15	30	20
	Druckfestigkeit senkrecht zur Schichtichtung Compressive strength	⊥	ISO 604	MPa	300	550	400	450
	Schlagzähigkeit Impact strength (Charpy)		ISO 179	kJ/m <sup>2</sup>	100	200	300	200
	Zugfestigkeit Tensile strength		ISO 527	MPa	400	250	500	400
	Spaltlast Deformation load		DIN 53463	N	4000	4000	4000	4000
Elektrische Eigenschaften Electrical properties	Spez. Durchgangswiderstand Volume resistivity		IEC 60093	Ω X cm	10 <sup>14</sup>	10 <sup>14</sup>	10 <sup>14</sup>	10 <sup>14</sup>
	Oberflächenwiderstand Surface resistivity		IEC 60093	Ω	10 <sup>12</sup>	10 <sup>12</sup>	10 <sup>12</sup>	10 <sup>12</sup>
	Durchschlagfestigkeit bei 60 °C Electric strength at 60 °C	⊥	IEC 60243-1	kV/mm	10	10	15	15
	Relative Permittivität bei 40 – 62 Hz Relative permittivity at 40 – 62 Hz	ca.	IEC 60250	ε <sub>r</sub>	5	5	5	5
	Vergleichswert der Kriechbegleitung Comparative tracking index		IEC 60112	CTI	225	225	600	600
Thermische Eigenschaften Thermal properties	Linearer Ausdehnungskoeffizient Coefficient of linear expansion		–	10 <sup>-6</sup> /K	10–20	10–20	10–20	10–20
	Wärmeleitfähigkeit Thermal conductivity		ISO 8302	W/m K	0,3	0,3	0,3	0,3
	Thermisches Langzeitverfahren *) Thermal Endurance *)		IEC 60216	T.L	180	180	180	155
	Wärmealterungsstufe Heat-aging class		IEC 60085	–	H	H	H	F

# Strain rate testing and material screen

ENERGITEKNOLOGISK UDVIKLINGS-  
OG DEMONSTRATIONSPROGRAM



---

## CORTIR

---

Task 8.4 - Strain rate testing and material screening

Christian Løjtved, Stuart Clyens, Jesper Boelt

EUDP

J.nr. 64018-0507

SEPTEMBER, 2020

ECC  
Næstved

## Contents

Summary.....	3
1. Introduction.....	4
2. Low strain rate tests of GFRP - Durostone EPR-S.....	5
2.1. Tensile testing.....	5
2.2. Torsional testing.....	8
2.3. Stress criteria – Tensile/Torsional fracture stress relation.....	9
3. High strain rate tests of GFRC - Durostone EPR-S1.....	11
3.1. Using test samples representative of the bulk test material.....	11
3.2. Test sample geometry.....	12
3.3. Scaling tests.....	12
3.4. Torsional test results.....	13
3.5. Application of the experimentally determined stress criterion to the torsional shear results.....	14
4. Conclusions.....	15
Low strain rate tensile tests.....	15
Low strain rate torsional tests.....	15
Stress criteria for Durostone EPR-S1.....	15
High strain rate tests.....	15
Appendix – Data sheet - Durostone EPR-S1.....	16

## Summary

The Danish company Bladena have developed a strut which is mounted internally in the tip area of wind turbine blades. The strut is employed to counteract the impulsive loads generated when a blade tip is subject to a lightning strike. This report describes the first series of material characterisation tests, carried out at both low and high strain rates, on the glass fibre reinforced polymer composite used to manufacture the struts. The low strain rate tests were carried out using standard, mechanical low strain rate testing methods, the high strain rate tests were carried out using a split Hopkinson torsion bar.

Scaling tests were also performed to establish the sensitivity of the mechanical test results to test sample geometry. The overall results show that scaling tests are critical in establishing the minimum thickness of the tubular test samples used for the torsional split Hopkinson bar tests. The low strain rate tests, carried out in both tension and torsion indicated that the manufacturing process used to produce the EPR-S1 composite rods had resulted in an alignment of the composite fibres within the rods. This was found to be the case when the internal structure of the rods was examined. The low strain rate tests also provided data which allowed a fracture stress criteria to be formulated which allows tensile fracture stress data to be extracted from shear fracture stress data (and vice versa). The high strain rate tests have shown that the polymer composite tested exhibits a low strain rate sensitivity with no indication of the onset of adiabatic shearing. This indicates that the Durostone EPR-S1 material is well suited for use in the manufacture of struts to counteract impulsive loads.

## 1. Introduction

During the lifetime of a wind turbine the entire structure may be expected to be struck by lightning several times. When lightning strikes the blades of a wind turbine, which are relatively thin and weak compared to the wind turbine tower, significant damage can occur. Such damage can be so extensive that the turbine can no longer operate and the turbine must be taken out of service so that the damaged blade can be repaired or replaced.

Modern wind turbine blades are typically fitted with lightning conductors, which have reduced the number of blades suffering damage from lightning strikes. However the study done in WP 8.1 and 8.2 estimates that certain lightning strikes, which do not pass down the lightning conductor, may result in large electrical discharges within turbine blades. Such discharges can generate correspondingly large compression pulses within the air contained inside the turbine blade cavity and, when these compression pulses propagate into the relatively weak, trailing edge area of the blade, they have a probability to cause the trailing edge of the blade to split and burst open.

The damage caused by the impulsive loads resulting from electrical discharge is presently so serious that engineers have begun to explore methods to mitigate their effects. One such method, developed by the Danish company Bladena, involves the use of a reinforcing strut mounted in the trailing edge region of turbine blade cavities.

The reinforcing strut developed by Bladena is presently manufactured from a glass fibre reinforced polymer Durostone EPR-S1 supplied by the German company Rochling. This polymer combines a low electrical conductivity with high mechanical strength. However, to date, the mechanical strength properties of this material have only been investigated under quasi-static loading conditions i.e. at strain rates of  $10^{-4}$ - $10^{-2}$ /s. Clearly, because struts are subjected to a large dynamic load during a lightning strike discharge, the response of the strut material to dynamic loads is of great interest.

This report describes mechanical tests carried out to determine fracture stress of specimens manufactured from Durostone EPR-S1, a glass fibre reinforced polymer. Low strain rate tensile tests carried out using a hydraulic mechanical tester are described as well as low strain rate torsional tests carried out using the low strain rate modification of the torsional Hopkinson bar described in Report 8.3. Finally the results high strain rate tests, carried out using the torsional Hopkinson bar also described in Report 8.3 are reported.

This work in this work package has been supported by WP9 (Product development) who has provided physical material samples for the material testing.

**Deliverable 8.4:** Strain rate testing and material screening

## 2. Low strain rate tests of GFRP - Durostone EPR-S

### 2.1. Tensile testing

#### Test equipment

The low strain rate tensile tests were carried out by mounting the tensile test specimens, shown in Figure 2-1, in a test sample holder shown in Figure 2-2. The test sample holder comprises two parts; an outer frame F and a platen P which can move freely within the frame. When the test sample holder, fitted with a test sample, is mounted in a hydraulic press, as shown in Figure 2-3, the test sample holder allows the compressive loads, generated by a hydraulic press, to be converted into tensile loads which are applied to the test samples.



Figure 2-1 – Tensile test specimens

The test samples were machined on a lathe from a solid bar of Durostone EPR-S1 material. The central test section was machined with a diameter of 8mm and a gauge length of 20mm. In order to avoid stress concentrations and ensure that the tests specimen fractured cleanly in the central section, the shoulders leading into the central test section were machined so as to have a radius of approximately 50mm.

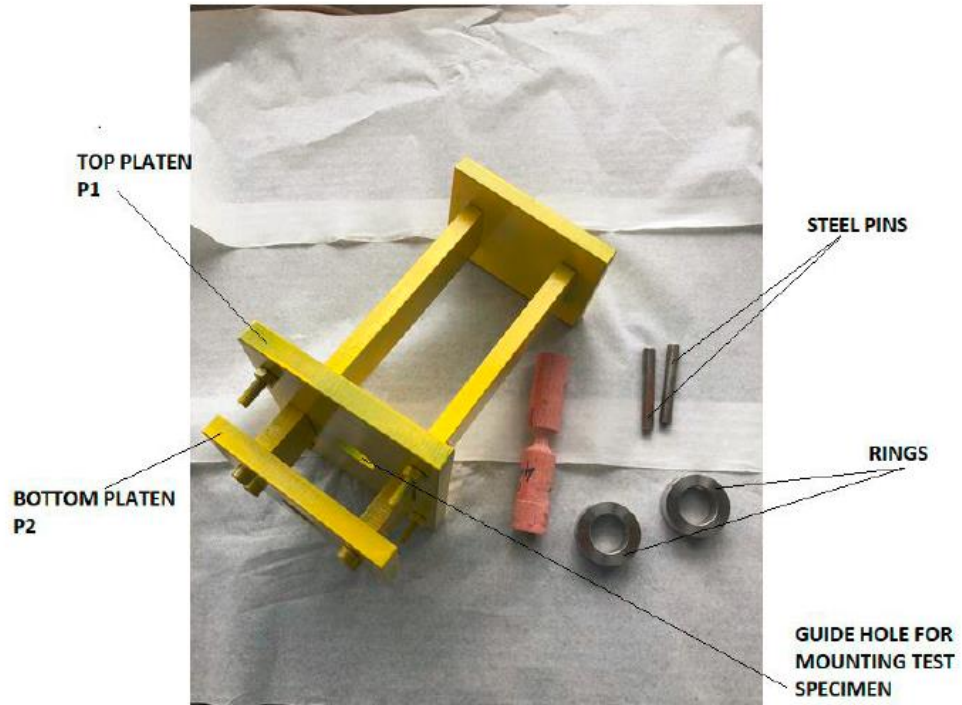


Figure 2-2 – Testing frame

Figure 2-2 shows the testing frame in which the test specimens were mounted for testing.

The test specimens were aligned in central guide holes drilled in the top and bottom platens and held in place using locking rings and steel pins which passed both through the rings and the end sections of the test specimens.

Having set up a test specimen in the testing frame the frame was mounted in a hydraulic press, as shown in Figure 2-3 and a load applied to the specimen. The maximum fracture stress was then recorded via a pressure sensor connected to the piston of the press.



Figure 2-3 – Test sample mounted in hydraulic press



Figure 2-4 – Fractured test sample

#### Low strain rate tensile test results

The hydraulic press and test sample holder were used to determine the fracture stress of a series of 5 test samples at a strain rate of approximately  $10^{-3}/s$ . A typical test sample after testing is shown in Figure 2-4.

The results of these tests are listed in Table 2-1

Table 2-1	
Sample	Tensile fracture stress (+/- 5%) [MPa]
1	350
2	358
3	386
4	388
5	365
<b>Mean</b>	<b>369</b>
<b>Standard Deviation</b>	<b>13.8</b>

As can be seen from the table the mean tensile fracture stress is 369MPa which closely corresponds to the value of 400MPa for the tensile fracture stress published by the supplier, see Appendix 1.

## 2.2. Torsional testing

### Equipment

The low strain rate torsional tests were carried out using a low strain rate test unit fitted to the split torsional Hopkinson bar described in the report 8.3. The low strain rate unit is shown in Figure 2-5



Figure 2-5 – Low strain rate torsional test unit

### Low strain rate torsional test results

The results of the low strain rate torsional tests are shown Table 2-2

Sample	Torsional fracture stress +/-5% (MPa)
1	123
2	120
3	123
4	121
5	122
Mean	122
Standard deviation	1.22

### 2.3. Stress criteria - Tensile/Torsional fracture stress relation

This section evaluates the relationship between the tensile and torsional fracture stress and establish a stress criteria ratio for Durostone EPR-S1 based on experimental test results.

There are a lot of criteria which describe the relationship between the tensile strength and the shear strength of materials. Two of the most widely used for metals are the Tresca and von Mises criteria, where the von Mises criterion is more conservative.

The two criteria are as follows:

$$\tau_{Tresca} = \frac{\sigma}{2} = 0.5 \cdot \sigma \quad \rightarrow \quad \sigma_{Tresca} = 2 \cdot \tau$$
$$\tau_{von\ Mises} = \frac{\sigma}{\sqrt{3}} \approx 0.577 \cdot \sigma \quad \rightarrow \quad \sigma_{von\ Mises} = \sqrt{3} \cdot \tau$$

Both Tresca and von Mises criteria apply to isotropic materials and are not recommended for orthotropic materials such as glass fibre reinforced polymer (GFRP). For orthotropic materials criteria such as max stress, Tasi-Wu, Puck, and others, are often used. These criteria evaluate the stresses in the individual material directions relative to the limit values and, depending on the criteria, distinguish between tensile and compressive behaviour.

One of the tensile test samples tested in the present project failed in an unintended way, due to shear in the end cap region, as shown in Figure 2-6 below. This figure reveals a clear view of the fibres within the rod of the EPR S1 material. As can be seen the proportion of horizontally oriented fibres is relatively low, which is most probably a result of the method used to manufacture the EPR-S1 material. The structure shown in the figure indicates that the rod material has been extruded and the fibres are therefore primarily oriented in an angle between 0 and 45 degrees relative to the direction of extrusion.



Figure 2-6 - EPR S1 30mm rod cross section, the white lines are the chopped glass fibres within the material.

Such orientation is also known as a triax laminate for a woven fabric.

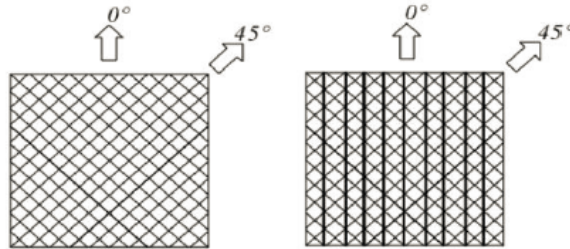


Figure 2-7 - Woven laminate fabric, Left biax and right triax

The shear/tensile strength ratio for biax and triax laminates depend on the “biax angle” and the UD/Biax ratio. The following two figures plots the shear/tensile strength ratio for a biax and a triax laminate using respectively max stress and Tsai-Wu failure criteria.

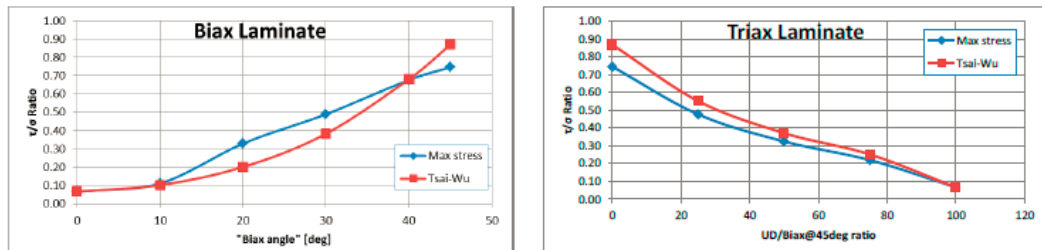


Figure 2-8 - Shear/tensile strength ratio for different laminates

The quasi-static shear/tensile ratio for the EPR S1 material, using average test values, is 1/3. This is approximately half the ratio of an isotropic material and a result of the orthotropic fibre orientation. The ratio correspond to a triax laminate with 50% UD fibre, assuming that the biax angle is 45deg.

Figure 2-6 could indicate that such ratio of fibre is a plausible explanation for relative low shear/tension strength ratio and it is therefore concluded that it is an acceptable value which furthermore, can be used to calculate the tensile strength as a function of shear stress at any given strain rate.

Expressed as an equation, the relationship between tensile and shear stress for the EPR-S1 material, which has been established experimentally, is as follows

$$\tau_{EPR-S1} = \frac{1}{3} \cdot \sigma_{EPR-S1} \quad \rightarrow \quad \sigma_{EPR-S1} = \tau_{EPR-S1} \cdot 3$$

Where  $\tau_{EPR-S1}$  denotes the shear fracture stress of the EPR-S1 material and  $\sigma_{EPR-S1}$  denotes the tensile fracture stress of the EPR\_S1 material.

### 3. High strain rate tests of GFRC - Durostone EPR-S1

#### 3.1. Using test samples representative of the bulk test material

The high strain rate tests described in this section of the report were carried out using the torsional split Hopkinson bar shown in Figure 3-1. The design, construction and use of this equipment have been described in detail in Report 8.3.



**Figure 3-1 - Torsional split Hopkinson bar for high strain rate shear testing**

The high strain rate tests carried out required the use of tubular test samples with a relatively thin wall, see section 3.2. However, when carrying out any tests to determine the mechanical properties of a material, it is essential to use a test specimen that has the same properties of the corresponding bulk material. In the particular case of the test samples used for high strain rate testing described in this section of the report, it was essential to know that wall thickness of the test specimens was thick enough to contain enough material to be representative of the bulk test material. Therefore, an initial series of tests were carried out to measure fracture stress using test specimens with a range of wall thicknesses. If the specimens tested were truly representative of the bulk test material there should be no dependency on wall thickness. The aim of this initial test series was therefore to find the critical wall thickness of the test specimen above which the fracture stress did not change.

### 3.2. Test sample geometry

Tubular test samples were employed for both scaling and high strain rate testing. The test samples were machined on a lathe from a solid, 30mm diameter rod of Durostone EPR-S1 glass fibre reinforced polymer. The geometry of the machined test samples is shown in Figure 3-2

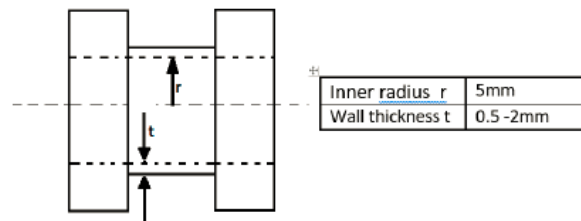


Figure 3-2 – Cross section of the test samples used for the scaling and high strain rate tests

As can be seen the tubular test samples were machined so as to create a circular flange at each end of a central tubular test section. The flanges provided a large surface area which allowed the test samples to be bonded to the input and output bars of the Hopkinson bar using a high strength epoxy adhesive.

### 3.3. Scaling tests

The fracture stresses measured using test specimens with wall thicknesses ranging from approximately 0.5 to 2 mm are shown in Figure 3-3. The figure indicates that, for wall thicknesses below approximately 1.1mm, the fracture stress decreases linearly with decreasing wall thickness. This is because, below a critical wall thickness, the material in the wall does not contain enough fibers and fibers of sufficient length to be representative of the bulk material. From these results was concluded that, in order to be certain that the tests specimens are representative of the bulk test material, the critical wall thickness was 1.5 mm and that the wall thickness of test specimens must be at least this critical wall thickness.

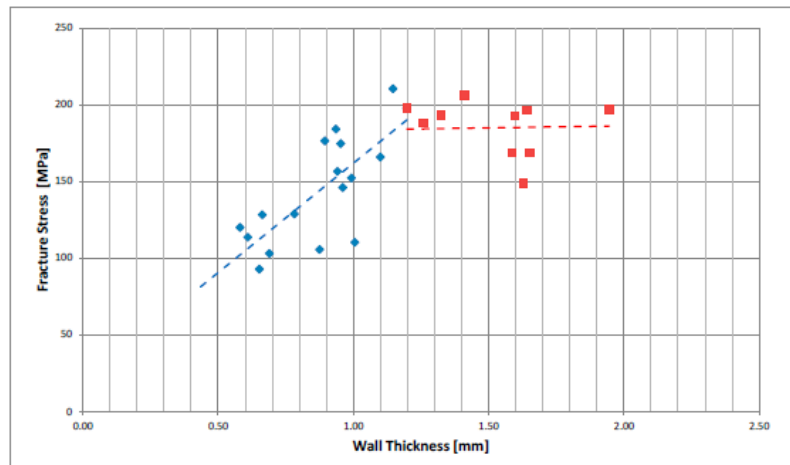


Figure 3-3 - Plot showing the dependence of fracture stress on wall thickness

### 3.4. Torsional test results

The high strain rate torsional tests of the Durostone EPR-S1 samples involved measuring the fracture stress of over 30 test samples at strain rates ranging from approximately 750/s to 5,000/s. The results of these tests, plotted with the fracture stresses measured at low strain rates, are shown in Figure 4.4.1 below. As can be seen the slope of the fracture stress-strain rate curve is approximately 0.014 indicating only a slight increase of shear stress with strain rate i.e. the fracture stress of the Durostone EPR-S1 test material exhibits a low strain rate sensitivity.

In contrast to the Durostone EPR-S1 glass fibre reinforced polymer, the fracture stress of most non-reinforced polymers tends to increase significantly at strain rates between approximately 100-2,500/s and then sharply decreases above 2,500/s due to adiabatic shear. This is a process in which is heat generated by the rapid deformation of the test material and, if the heat cannot flow from the deformation zone quickly enough, results in an overall loss of strength. This phenomena is known as adiabatic shearing and the strain rate at which it occurs indicates the upper limit of strain rate a particular material can withstand before catastrophic failure. As can be seen from Figure 3.3.2, the Durostone EPR-S1 material does not show indications of adiabatic shear even at shear strain rates of 5,000/s , which correspond to a severe impact load.

Shear strain rates of approximately 5,000/s correspond to the upper limit of the shear strain rates that can be achieved using the torsional split Hopkinson bar used for the tests described in this report. In view of the high amplitude impact loads resulting from a lightning strike determining the strain rate at which adiabatic shearing occurs in the Durostone EPR-S1 would be of great interest and should be determined in the future, possibly by developing methods to extend the strain rate range of torsional Hopkinson bars.

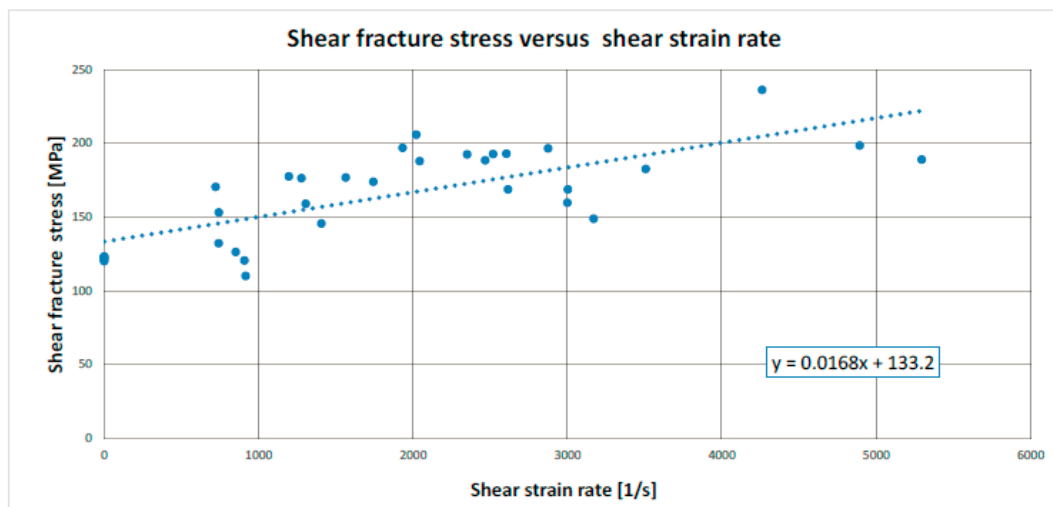


Figure 4.4.1 - Plot showing the dependence of fracture stress on strain rate

### 3.5. Application of the experimentally determined stress criterion to the torsional shear results

The experimentally determined a tensile/shear stress criterion of 3, which related tensile fracture stress to torsional fracture stress, was applied to the torsional fracture stress data to convert them into tensile fracture stress data. The results of this conversion are shown in Figure 3-4

The tensile strain rate equivalent to the shear strain rate is based on the von Mises yield criteria (Kerguignas, 1977) and the hypothesis of volume incompressibility of solid. Therefore, the equivalent tensile strain rate  $\dot{\epsilon}_{eq}$  to shear strain rate becomes<sup>1</sup>:

$$\sigma_{von\ Mises} = \sqrt{3} \cdot \tau \quad \rightarrow \quad \dot{\epsilon}_{eq} = \frac{\dot{\gamma}}{\sqrt{3}}$$

Until proven otherwise, it is assumed that same ratio applies to the Durostone EPR-S1 material, as further investigation is outside the scope of this project.

It should therefore be noted that a factor of  $1/\sqrt{3}$  is used to convert torsional strain rates into tensile strain rates. It can be seen from Figure 4.5.1, that tensile strain rates resulting from this conversion range up to a maximum of approximately 3,000/s.

The results shown in Figure 3-4 indicate that the Durostone EPR-S1 material can withstand tensile loads applied at strain rates up to at least 3,000/s.

For comparison, the in-plane strain rate, of a simply supported 400x400x4mm biaxial GFRP plate, is approximately 100/s when exposed to an energy pressure wave of 430kJ released 10cm above its face. It is therefore concluded that the range of strain rate, tested in this work covers the range relevant for the given application.

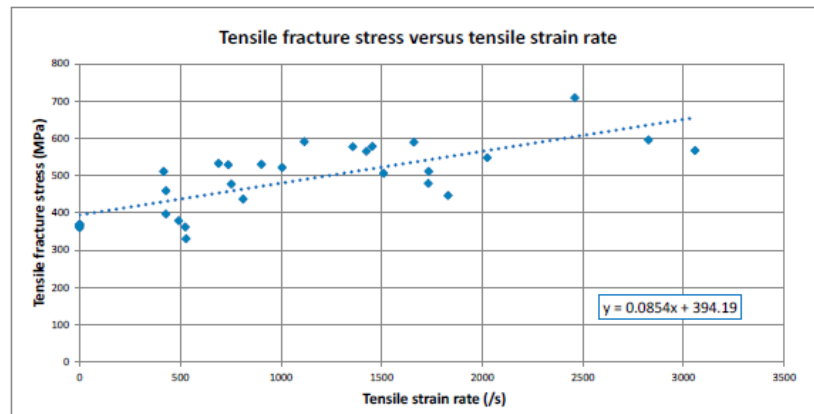


Figure 3-4 – Tensile fracture stress versus tensile strain rate

<sup>1</sup> Further information is given in: The Relationship Between Tensile Strength and Shear Strength in Composite Materials Subjected to High Strain Rates, by Chi-Yuen Chiem and Zeng-Gang Liu, published in April 1988 in the Journal of Engineering Materials and Technology.

## 4. Conclusions

### Low strain rate tensile tests

The low strain rate tensile tests showed that the tensile fracture strength of the Durostone EPR-S1 test material supplied by Bladena was approximately 369MPa which corresponds reasonably closely with the tensile strength value of 400MPa quoted in the data sheet supplied by the manufacturer.

### Low strain rate torsional tests

The low strain rate shear tests showed that the shear fracture strength of the Durostone EPR-S1 material was approximately 122MPa which is lower than would be expected if all the fibres of the composite material were randomly oriented.

### Stress criteria for Durostone EPR-S1

The stress criteria relating tensile/shear fracture stresses for Durostone EPR-S1 was determined experimentally and found to have a value of 3. This value reflects the fact that the material, which was supplied in bar form, is manufactured using a method which tends to more align fibres preferentially along the axis of bar. As consequence of this alignment the material is significantly stronger in tension than would be expected if the fibres of the composite were aligned randomly.

### High strain rate tests

The Durostone EPR-S1 material only exhibits a relatively small increase in fracture stress with strain rate over the entire range of strain rates tested. This means there is only a small increase in the materials ability to withstand impact loads. However even at shear strain rates of over 5,000/s (corresponding to tensile strain rates of approximately 3,000/s) the Durostone EPR-S1 material shows no signs of the onset of adiabatic shearing making it particularly well suited for the manufacture of wind turbine wing support struts.

## Appendix - Data sheet - Durostone EPR-S1

Technische Daten Durostone® Plattenmaterial		Prüfmethode Test method	Einheit Unit	EPR S1	EPR S5	EPM S7	EPR S6	UPR S19
Technical data Durostone® sheet material								
Standardfarbe Standard colour	–	–	–	rot red	natur natural	natur natural	natur natural	natur natural
Harzart Type of resin	–	–	–	Epoxid		Epoxid	Epoxid	Polyester
Dichte Specific gravity	ca.	ISO 1183 meth 1	g/cm <sup>3</sup>	1,90	1,90	2,00	1,95	
Brandverhalten Flammability		UL 94	–	–	–	–	VO	–
Mechanische Eigenschaften in Hauptfaserrichtung Mechanical properties in main reinforcement sense	Biegespannung beim Bruch senkrecht Bending strength	⊥	ISO 178	MPa	500	300	600	350
	Elastizitätsmodul aus dem Biegeversuch Modules of elasticity	⊥	ISO 178	GPa	20	15	30	20
	Druckfestigkeit senkrecht zur Schichtrichtung Compressive strength	⊥	ISO 604	MPa	300	550	400	450
	Schlagzähigkeit (Charpy)		ISO 179	kJ/m <sup>2</sup>	100	200	300	200
	Zugfestigkeit Tensile strength		ISO 527	MPa	400	250	500	400
	Spaltkraft Delamination load		DIN 53463	N	4000	4000	4000	4000
Elektrische Eigenschaften Electrical properties	Spez. Durchgangswiderstand Volume resistivity		IEC 60093	Ω X cm	10 <sup>14</sup>	10 <sup>14</sup>	10 <sup>14</sup>	10 <sup>14</sup>
	Oberflächenwiderstand Surface resistivity		IEC 60093	Ω	10 <sup>12</sup>	10 <sup>12</sup>	10 <sup>14</sup>	10 <sup>12</sup>
	Durchschlagfestigkeit bei 90 °C Electric strength at 90 °C	⊥	IEC 60243-1	kV/mm	10	10	15	15
	Relative Permittivität bei 48 – 62 Hz Relative permittivity at 48 – 62 Hz	ca.	IEC 60250	ε <sub>r</sub>	5	5	5	5
	Vergleichszahl der Kriechwegbildung Comparative tracking index		IEC 60112	CTI	225	225	600	600
Thermische Eigenschaften Thermal properties	Linearer Ausdehnungskoeffizient Coefficient of linear expansion		–	10 <sup>-6</sup> K <sup>-1</sup>	10–20	10–20	10–20	10–20
	Wärmeleitfähigkeit Thermal conductivity		ISO 6302	W/m K	0,3	0,3	0,3	0,3
	Thermisches Langzeitverfahren <sup>1)</sup> Thermal endurance <sup>1)</sup>		IEC 60216	T.L.	180	180	180	155
	Wärmeklasse Insulating class		IEC 60085	–	H	H	H	F

### Anmerkungen

<sup>1)</sup> Die Grenztemperatur und Wärmeklasse wurden nach IEC 60216 anhand der Veränderung der Biegefestigkeit (50%) nach 20.000 h festgelegt.

⊥ = senkrecht zur Schichtung  
|| = parallel zur Schichtung

Bei den angegebenen Werten in dieser Broschüre handelt es sich um Mittelwerte, die durch laufende statistische Prüfungen und Kontrollen abgesichert sind. Diese Daten sind reine Beschaffenheitsangaben und führen nur bei ausdrücklicher Vereinbarung zu kaufverträglichen Zusicherungen.

### Remarks

<sup>1)</sup> The temperature limit and insulating class have been specified in accordance with IEC 60216 on the basis of the change in bending strength (50%) after 20.000 h.

⊥ = perpendicular to the lamination  
|| = parallel to the lamination

The data mentioned in this brochure are average values ascertained by current statistical returns and tests. The above data is provided purely for information and shall not be regarded as binding unless expressly agreed in a contract of sale.

## Appendix G Elastic Instability and Fracture Mechanics (Light Approach)

### Debond Study for Global FEM Blade Model

During the project, Bladena has worked on methods for simulating global FEM blade models where debond of sandwich panels is present. This work included a method for generating an outer face sheet (skin) debond from the core of the sandwich panel during pre-processing, while also developing a new post-processing tool to investigate the ‘gap’ development between the debonded face sheet and remaining sandwich structure. Also, various post-processing of results has been conducted to investigate the effect of debonding and to indicate elastic instability.

### FEM Model

A global FEM model of the SSP34m blade (same blade as used for the large-scale testing in DTU Structural Lab) was used during the debond studies. The global FEM blade model of the SSP34m is shown in Figure .

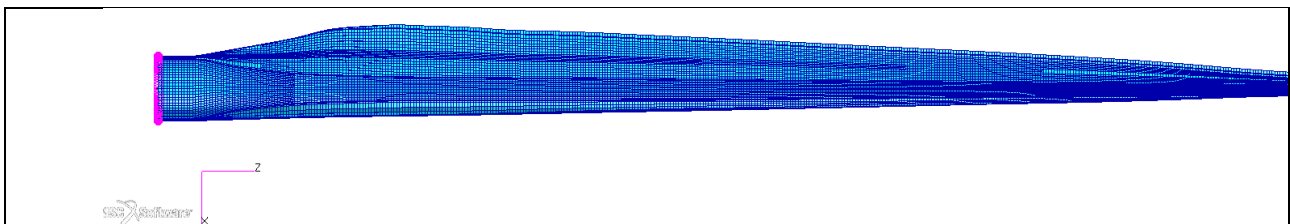


Figure 1: Global FEM blade model of SSP34m

The SSP34m FEM blade model is built/created using Bladena in-house pre-processing tool - BMT (Blade Modelling Tool). The blade generated from BMT is *intact*; no structural damages/defect present. Implementing structural damages (e.g. debonding) shall be done by the user through the FEM software (MSC. Patran).

### Boundary Conditions and Loads

The root fixture is simulated through an RBE2 (Rigid Body Element) with MPC (Multi-Point Constraint) by locking all three translational degrees of freedom of the nodes located at the root.

Combined load cases are investigated. The edgewise load (x-direction) contribution is done using the gravitational load and the flapwise loads (y-direction) are taken as a realistic loading. The gravitational load uses the volume and user-specified densities for each material at each element. The flapwise loads are applied in the aerodynamic center (approx.) in 3 positions along the blade. The flapwise loads are listed in Table 19 and the used load cases are shown in Table 20.

Table 19: Flapwise Load Overview

Load Name	Total Load	Position
Flap 1	40.6 kN	14 m
Flap 2	37.7 kN	18 m
Flap 3	66.8 kN	24 m

Table 20: Load Case Overview

Load Case (LC)	Description
Comb2xFlap_TTL	- All 3 flapwise loads applied - Scaled x 2.0 - Gravity load applied (TTL) - Scaled x 1.0
Comb2xFlap_LTT	- All 3 flapwise loads applied - Scaled x 2.0 - Gravity load applied (LTT) - Scaled x 1.0
3xComb2xFlap_TTL (No Convergence)	- All 3 flapwise loads applied - Scaled x 6.0 - Gravity load applied (TTL) - Scaled x 3.0
Comb2xFlap_8xTTL (Extreme Case)	- All 3 flapwise loads applied - Scaled x 2.0 - Gravity load applied (TTL) - Scaled x 8.0
Comb2xFlap_8xLTT (Extreme Case)	- All 3 flapwise loads applied - Scaled x 2.0 - Gravity load applied (LTT) - Scaled x 8.0

## Applying Debond - Outer face sheet (skin) from core

As Bladena's in-house pre-processing tool, BMT, generates an intact blade, with no structural defects and damages, Bladena has developed an initial method for generating/simulating a debond of outer face sheet (skin) from the sandwich core. The methodology and outcome are shown in Figure 2.

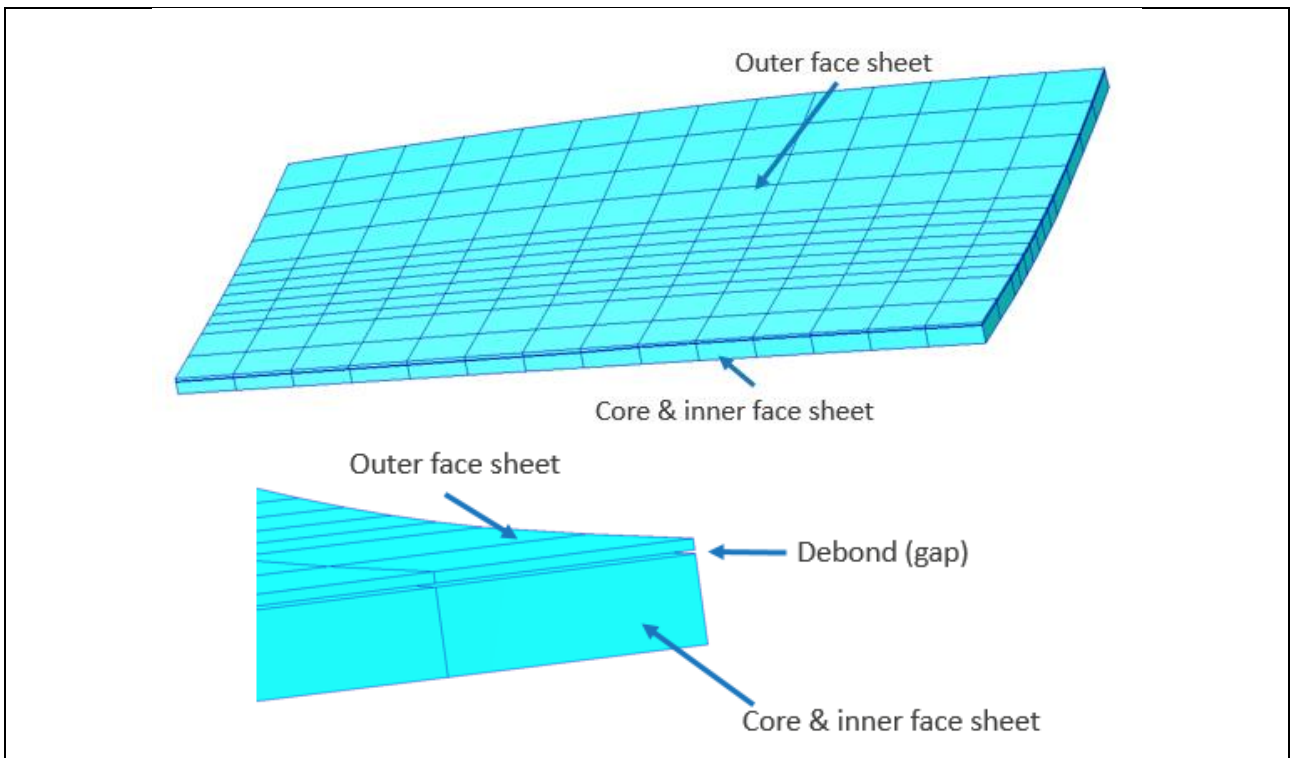


Figure 2: 'Cut-out'-view of debonded area. Outer face sheet is separated from the core and sandwich panel. 1mm gap introduced

The method developed consists of splitting elements at the user-defined debonded location (e.g. pressure side panel in max chord). A small gap (debond) between the splitted element surfaces is created and the material properties for the elements are updated accordingly.

The procedure for creating debond in MSC. Patran (FEM software used) has been explained thoroughly in steps and the methodology has already been used for commercial tasks.

## Debond Sizes/Areas Investigated

3 different debond (*Debond A*, *Debond B* and *Debond C*) areas have been used during this study. These are described in the figures below, where the debonded areas are shown with red contour.

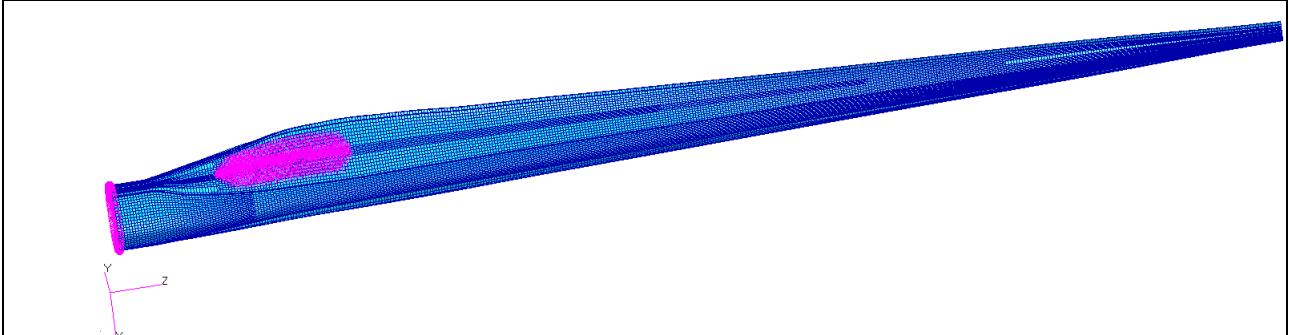


Figure 3: Debond A: Debond introduced on pressure side (PS) panel. Starting at 3m to 7m and includes solid sections 41-45. L = 4m, W = 1.4m

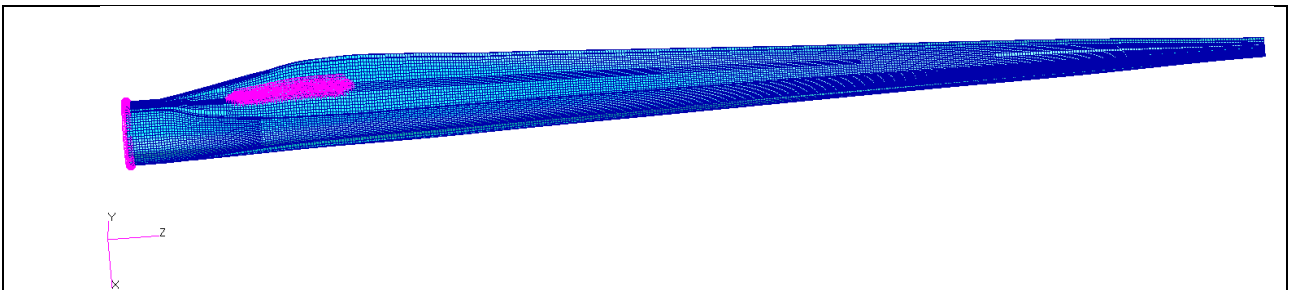


Figure 4: Debond B: Debond introduced on pressure side (PS) panel. Starting at 3m to 7m and includes solid sections 41-45. L = 4m, W = 0.8m

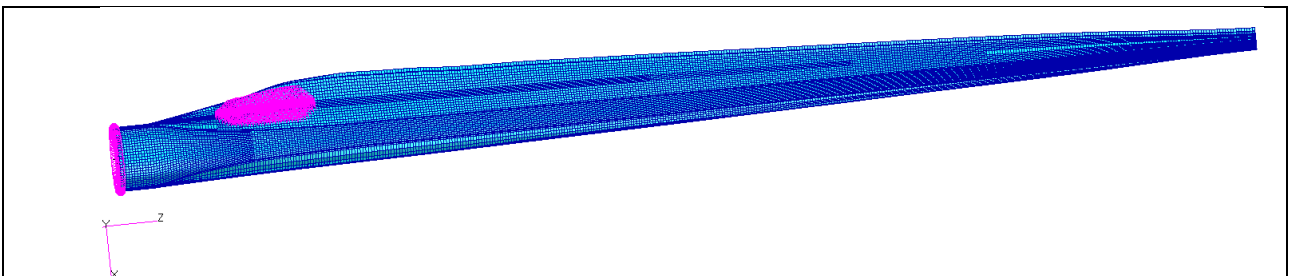


Figure 5: Debond C: Debond introduced on pressure side (PS) panel. Starting at 3m to 7m and includes solid sections 41-45. L = 4m, W = 1.4m

The different debond sizes illustrated above are listed in Table 21.

Table 21: Overview of investigated debond sizes/areas

Debond	Start [m]	Ends [m]	Location	Length [m]	Width [m]	Area [m <sup>2</sup> ]
Debond A	3	7	PS	4	1.4	5.6
Debond B	3	7	PS	4	0.8	3.2
Debond C	3	6	PS	3	1.4	4.2

## Results

### Panel Deformation - Longitudinal Waves

#### 'Contact'-verification

The initial state of the debond methodology in a FEM environment includes *contact* in the simulations between debonded face sheet and core. In Figure 6 and Figure 7 the effect of applying '*contact*' is illustrated. If '*contact*' is not applied the face sheet and core can 'go-through' each other, see Figure 6, which is not representable for reality. In Figure 7 '*contact*' has been applied and now the face sheet and core have the same magnitude of deformation - the two material panels (face sheet and remaining sandwich structure) are not 'going through' each other.

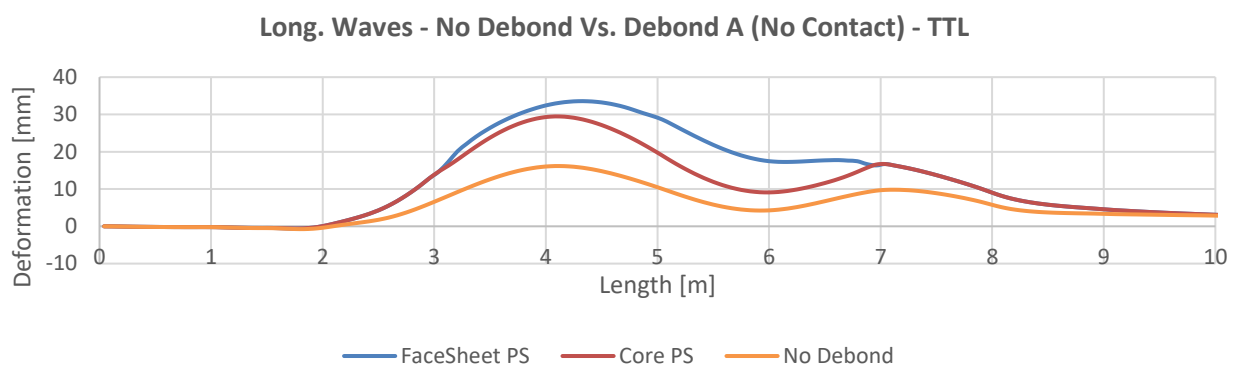


Figure 6: Longitudinal Waves of blade with 'No Debond' and 'Debond A'. No contact is applied between debonded face sheet and core and the two curves do not match - face sheet is 'going through' core. LC = Comb2xFlap\_TTL

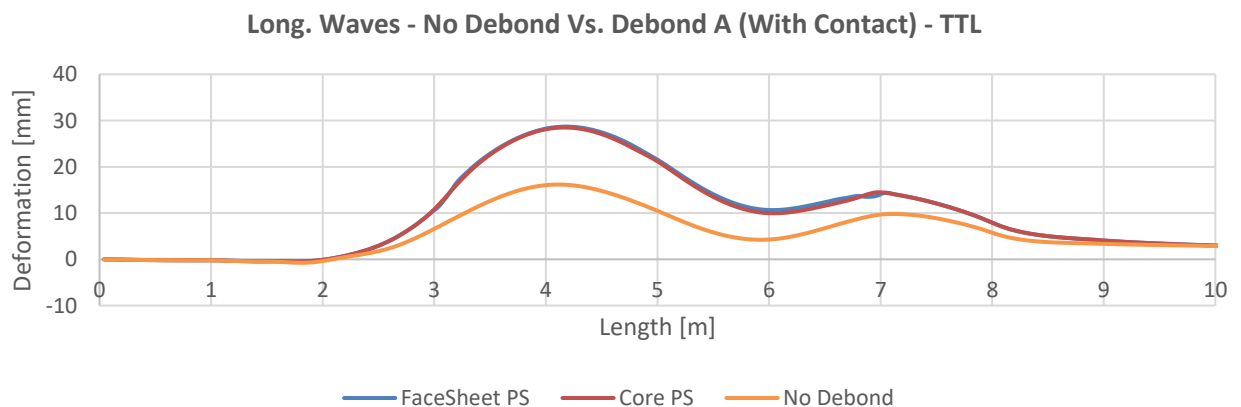


Figure 7: Longitudinal Waves of blade with 'No Debond' and 'Debond A'. Contact is applied (deformable bodies) between debonded face sheet and core and the two curves matches. LC = Comb2xFlap\_TTL

## Deformation Comparison

Below in Figure 8 and Figure 9 the longitudinal panel deformation (middle of PS, S43) is plotted for 'No Debond' and 'Debond A', respectively. The plots show the difference between TTL and LTT combined loading.

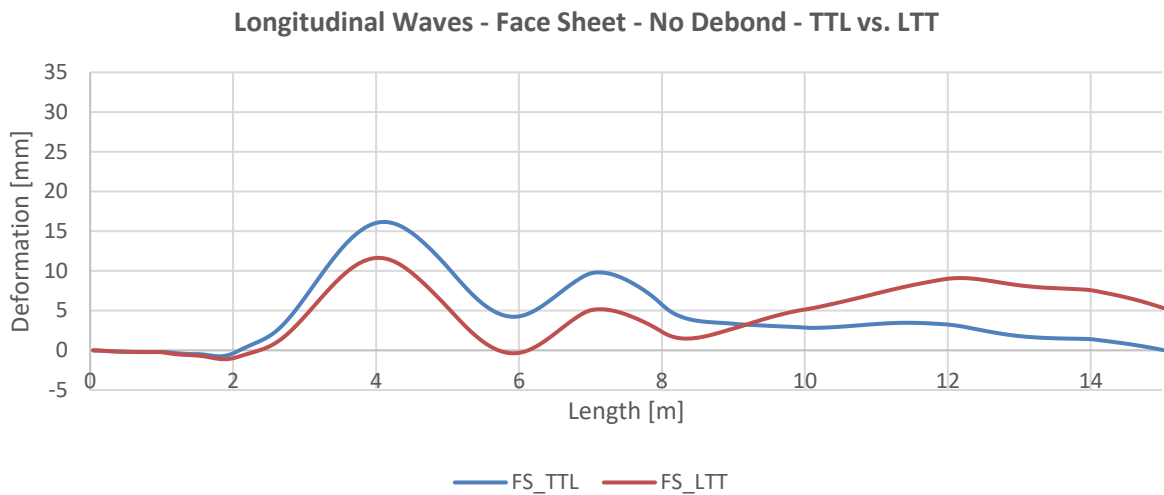


Figure 8: Longitudinal waves (deformation) of middle of PS panel (S43), 0-15m of 'No Debond'. Combined loads with gravitational load giving TTL and LTT are plotted. LC = Comb2xFlap\_TTL (blue) & Comb2xFlap\_LTT (red)

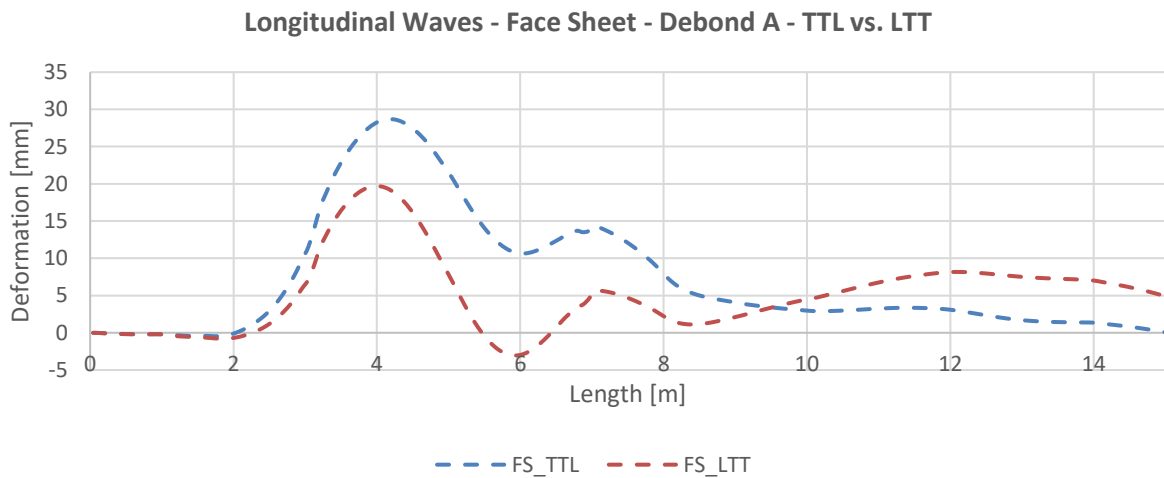


Figure 9: Longitudinal waves (deformation) of middle of PS panel (S43), 0-15m of 'Debond A'. Combined loads with gravitational load giving TTL and LTT are plotted. LC = Comb2xFlap\_TTL (blue) & Comb2xFlap\_LTT (red)

The debond causes a loss in panel stiffness which can be seen by comparing the maximum deformations for 'No Debond' and 'Debond A'. The maximum local deformation for 'Debond A' is approximately 75% larger than 'No Debond'.

In Figure 10 the deformation of PS panel (middle, S43) is plotted for all 3 different debond sizes and the blade with no debond ('Reference Model'). The plots are extracted from the combined loading (TTL).

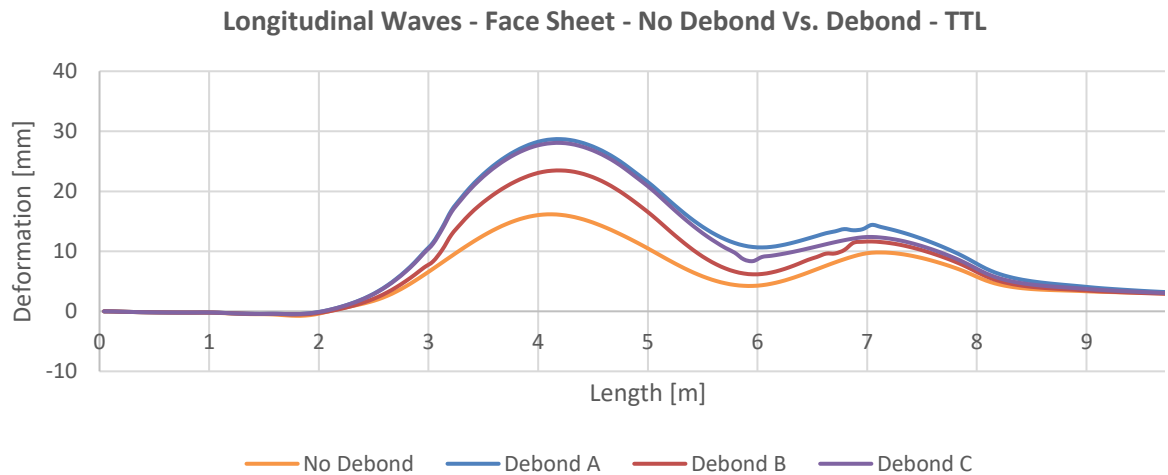


Figure 10: Longitudinal Waves on PS panel from 0-10m of the blade. Comparison between debond sizes. LC = Comb2xFlap\_TLL

‘Debond C’ is shorter, but wider than ‘Debond B’, and has a larger deformation.

‘Debond C’ has approximately the same maximum deformation pattern as ‘Debond A’ while being 1m shorter.

‘Debond B’ has the same length as Debond A, but is slimmer and has the smallest deformation of the three debond sizes.

## Strain - Longitudinal (X) and Transverse (Y) and Gap Development

From the longitudinal wave deformation plot in Figure 10 the maximum deformation occurs at 4.4m (approximately) of the blade length. In Figure 11 the deformed (scaled x4) cross-section at 4.4m of the 'Debond A'-model is shown under combined loading (TTL).

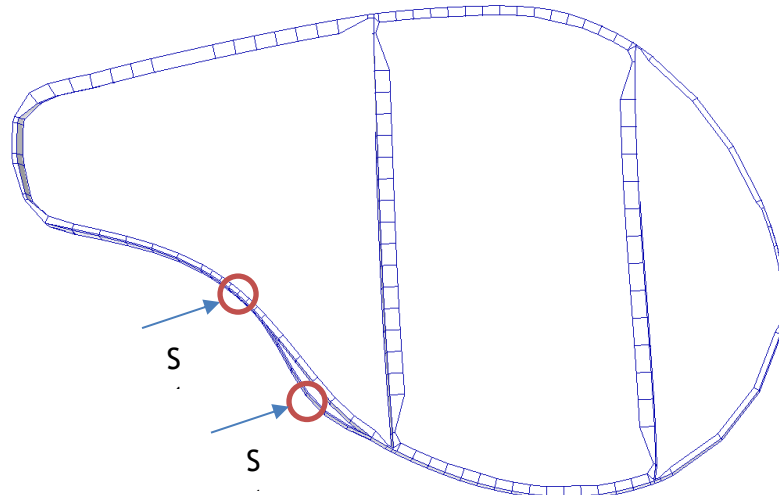


Figure 11: Deformed (scaled x4) cross-section at 4.4m of 'Debond A'-model. Maximum longitudinal wave deformation at centre of panel (S43). Due to debonding of outer face sheet the face sheet (S41) deflects/deforms away from the remaining sandwich material (out-of-plane). LC = Comb2xFlap\_TTL

### S43 (middle of PS panel) Investigation

In Figure 12 the longitudinal and transverse strain development of S43 (middle of PS panel) at 4.4m under combined loading (TTL) is plotted for all 4 FEM models. The strains are extracted from the outer face sheet (Layer 1 = Triax & Layer 3 = Triax).

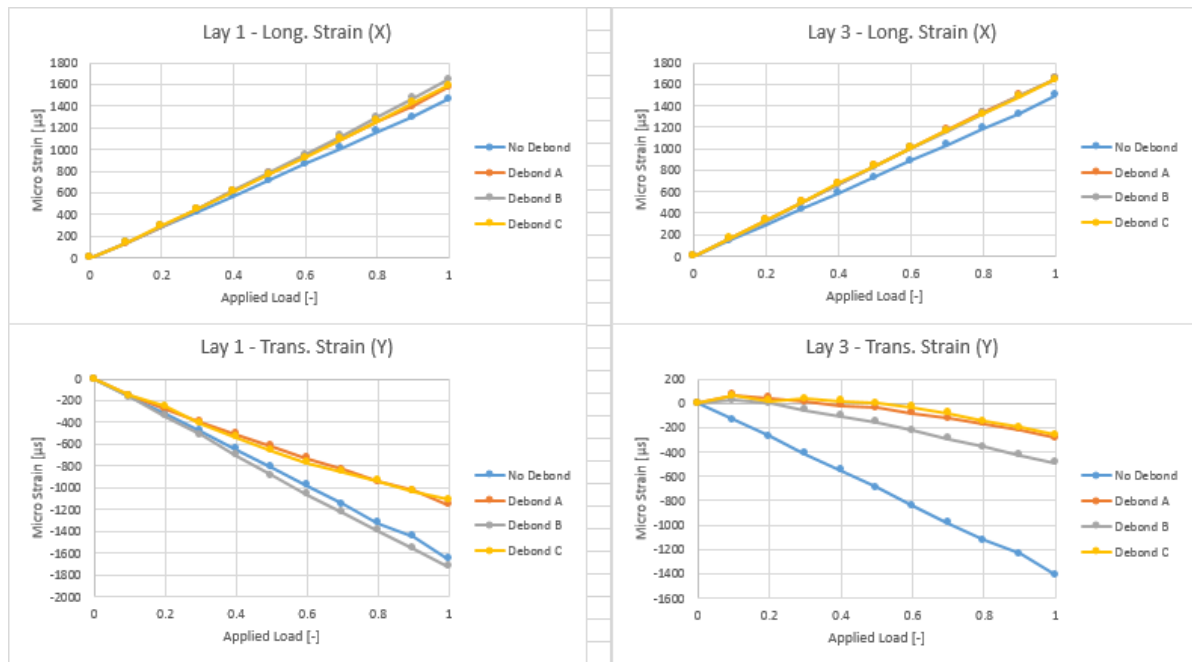


Figure 12: Longitudinal (X) and Transverse (Y) strain of S43 at 4.4m during combined load (TTL) for 'Reference Model' and the different debond sizes. LC = Comb2xFlap\_TTL.

The debond (damages) causes the longitudinal strains (in both Layer 1 and Layer 3) to increase slightly from 1450  $\mu\text{s}$  to 1650  $\mu\text{s}$  (approx. 13%).

The transverse strain (in both Layer 1 and Layer 3) changes significantly for 'Debond A' and 'Debond C' (both wide debonds). Transverse strain in Layer 1 for 'Debond B' (slim & long debond) is almost not affected, while Layer 3 sees a significant reduction (as seen for 'Debond A' and 'Debond B').

In Figure 13 and Figure 14 the Back-To-Back (B-to-B) strain comparison between 'Reference Model' and 'Debond A' are plotted.

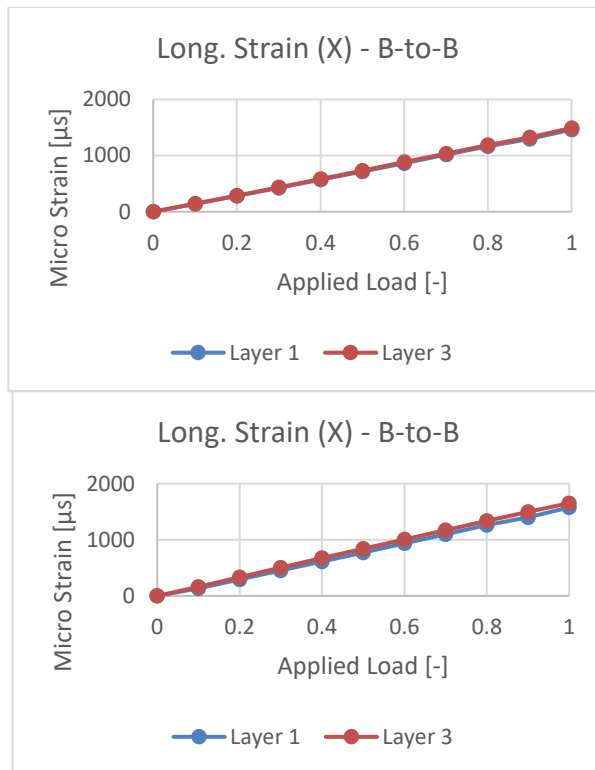


Figure 13: 'Reference Model' (LEFT) & 'Debond A' (RIGHT): Longitudinal (X) strain Back-To-Back of S43 (middle of PS panel) at 4.4m. LC = Comb2xFlap\_TTL

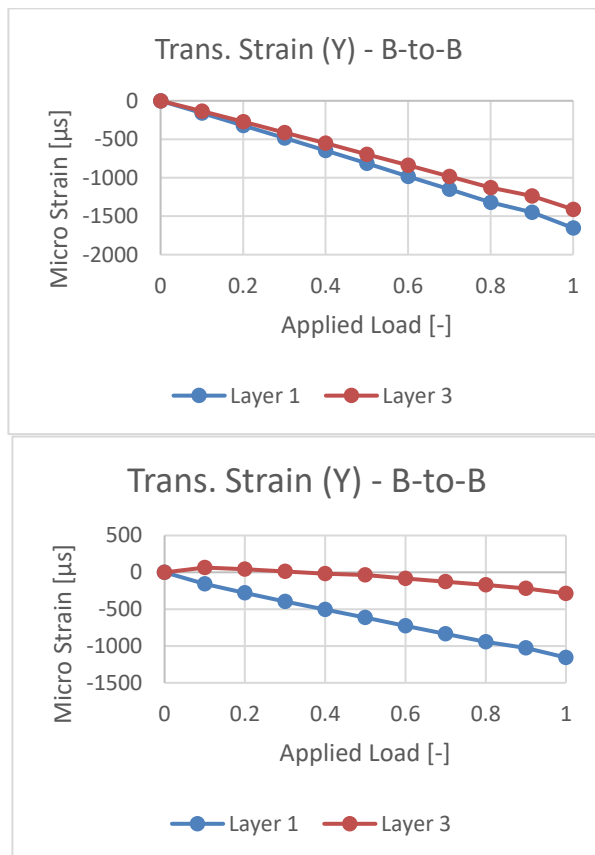


Figure 14: 'Reference Model' (LEFT) & 'Debond A' (RIGHT): Transverse (Y) strain Back-To-Back of S43 (middle of PS panel) at 4.4m. LC = Comb2xFlap\_TTL

For the 'Reference Model' the strain curves for Layer 1 and Layer 3 are almost identical (on top of each other). This indicates that membrane (in-plane) stress is dominant compared to bending stress.

For 'Debond A' the curves become more 'separated meaning *more bending stress becomes present* when the face sheet is debonded. This is shown and further elaborated for the investigation of S41.

### S41 (local deformed face sheet) Investigation

The transverse strain (Y) has been further investigated for S41, which is the location of the outward buckled face sheet, see Figure 11. In Figure 15 the transverse strain is plotted for the 'Reference Model' (intact blade). Here, the strains are linear and the same, meaning that again mainly membrane stress is present.

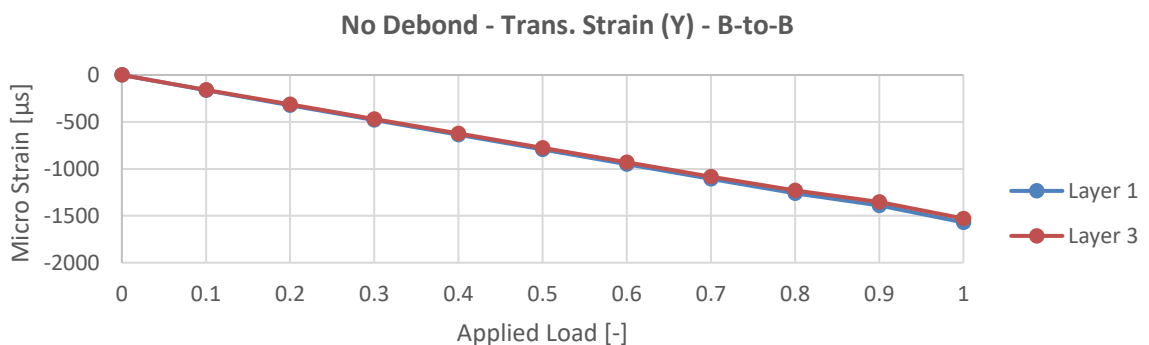


Figure 15: 'Reference Model': Transverse (Y) strain Back-To-Back of S41 (close to SW) at 4.4m. LC = Comb2xFlap\_TTL

The introduction of debond ('Debond A') redistributes the strain. In Figure 16 the strains in Layer 1 and Layer 3 are not the same - 'Normal Strain' is located between the two, indicating the introduction of bending strains. The bending strains are shown in Figure 17.

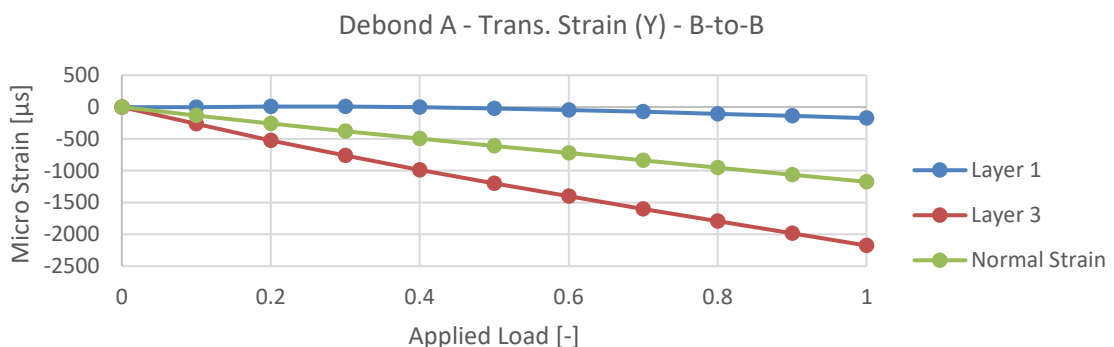


Figure 16: 'Debond A': Transverse (Y) strain Back-To-Back of S41 (close to SW) at 4.4m. LC = Comb2xFlap\_TTL

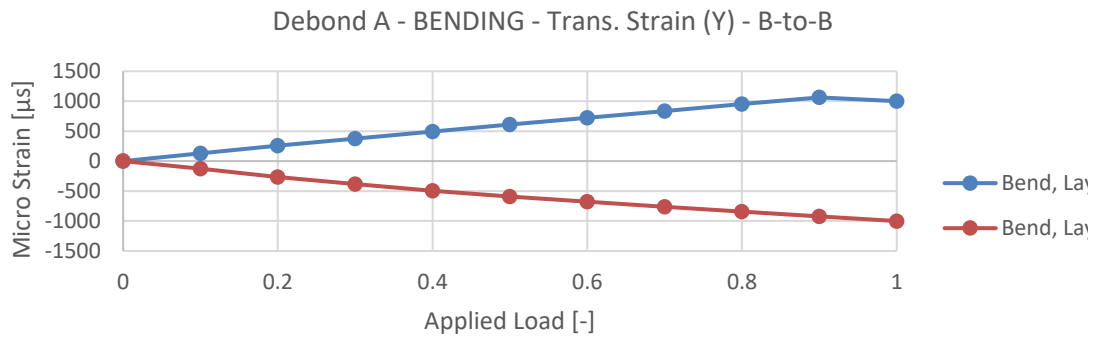
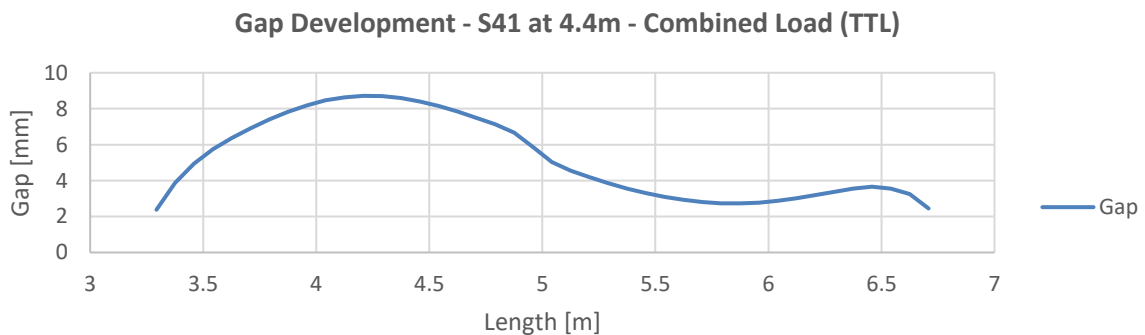


Figure 17: 'Debond A': Transverse BENDING (Y) strain Back-To-Back of S41 (close to SW) at 4.4m. LC = Comb2xFlap\_TTL

The out-of-plane localized deformation of the debonded face sheet, causing an increase in the bending strains indicates that a possible damage (e.g. delamination and/or crack) will occur in the debonded face sheet in that location during operation (cyclic loading).

### S41 (local deformed face sheet) 'Gap' Investigation

As part of these studies, a simple 'gap-analysis'-tool has been created to determine the gap-development along a certain area (solid section) of a debond. In Figure 18 the gap between outer face sheet and core is plotted for S41 (close to SW) at the debonded section (3m-7m).



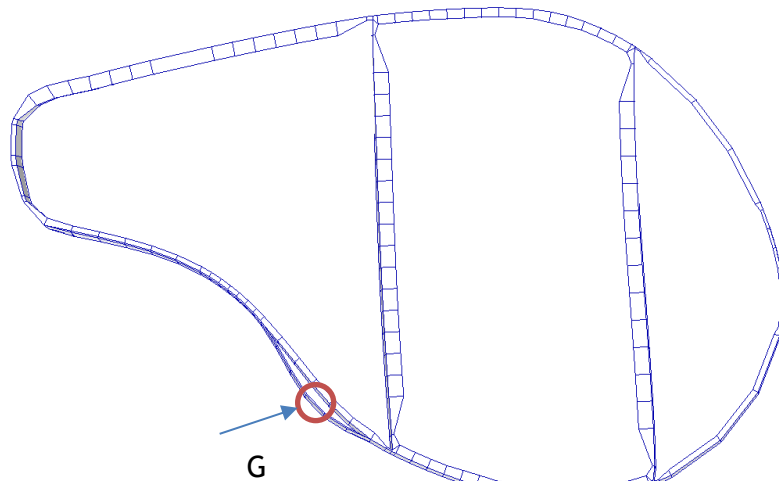


Figure 18: Top: Gap between debonded outer face sheet and core at S41 between 3m to 7m (debonded zone of 'Debond A'). Gap approximately 8.5mm at 4.4m. Bottom: Illustration of gap. LC = Comb2xFlap\_TTL

This 'gap'-tool and investigation can be used to estimate if the blade is subjected to elastic instability under a certain load with a certain debond size e.g. if it seen that the 'gap' becomes unrealistically high. Examples of elastic instabilities are given in the next section.

## Elastic Instability

The SSP34m has been analysed for different extreme loading conditions, to investigate elastic instabilities. The simulation conducted for the extreme load case (3x2xFlapwise + 3xGravity (TTL)) could not converge for the 'Reference Model' i.e. no debond present (intact). The analysis was able to complete approximately 0.47 (47%). The cause for no-converge is due to large local deformation/buckling of suction side (SS) spar cap and panels at the root area transition zone (RATZ). In figures below the global deformation and strain distribution are shown.

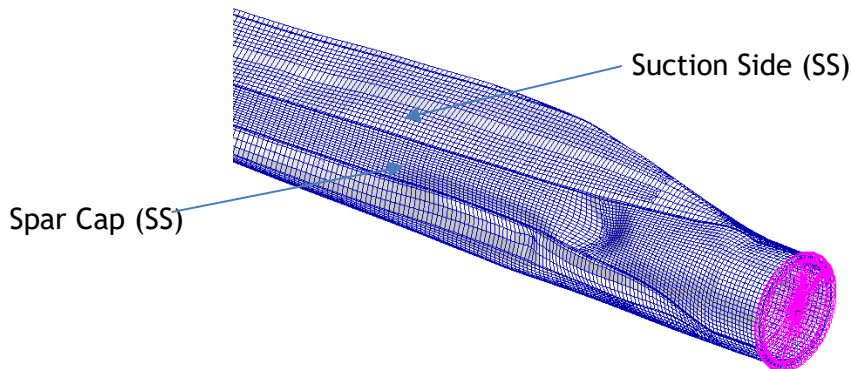


Figure 19: Global deformation (scaled 5x). Large deformation (buckling) of suction side spar cap at RATZ

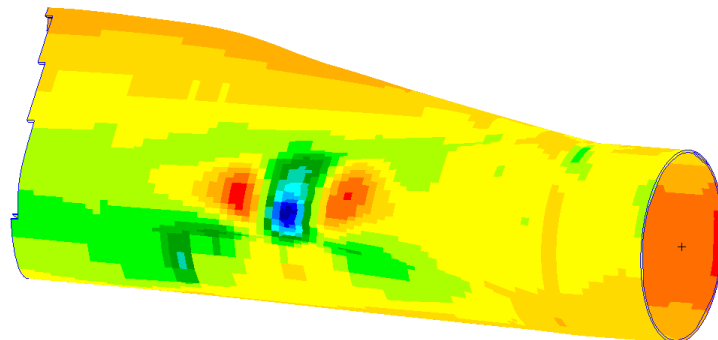


Figure 20: Longitudinal (X) strain (Layer 1) indicates peaks at the buckled spar cap. Layer 1 is in compression (blue), as the spar cap goes inward and in tension (red) on the sides.

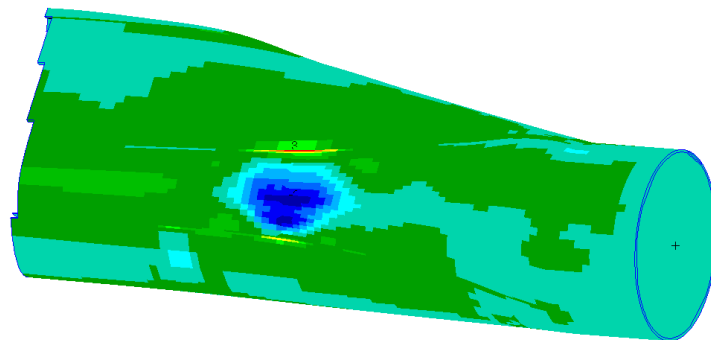


Figure 21: Transverse strain (Y) (Layer 1) indicates peaks at the buckled spar cap. Layer 1 is in compression (blue)

The model and simulation can not converge due to large geometric non-linearities causing instability in the primary load-carrying structure (spar caps). This is a clear example of elastic instability, however, when large deformations, stresses, and/or strains are observed in a model, they can be unrealistically large, meaning damages/collapse in real-life would have occurred.

### Panel Deformation (Secondary Structure)

An example of an elastic instability, where the FEM simulation solution is able to converge, can be if unrealistic large deformations, stresses, and/or strains occur in the secondary structure (e.g. sandwich panels). The SSP34m blade has been investigated for the extreme load case (Comb2xFlap\_8xLTT).

In Figure 22 the longitudinal wave (local deformation in middle of PS panel) is compared between intact blade ('Reference Model') and damaged blade ('Debond A'). The introduction of debond causes minor waves in the debonded zone. Approximately 6 new wave 'tops' can be seen. Also, the debond causes the overall longitudinal wave curve to 'distort/shift/move'.

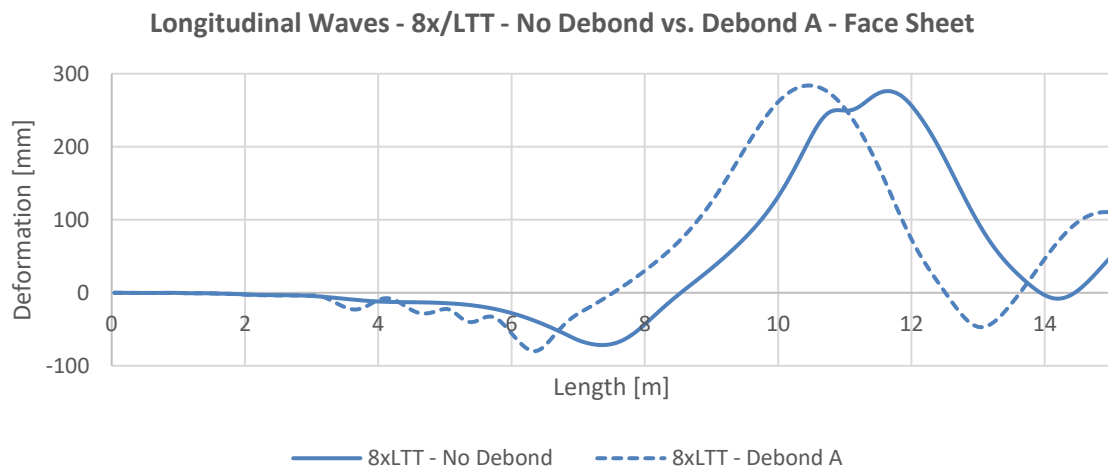


Figure 22: Longitudinal Waves of face sheet on middle of PS panel from 0-10m of the blade. Comparison between intact and damaged blade ('Debond A'). LC = Comb2xFlap\_8xLTT

Very large out-of-plane deformations are seen. Also, a gap is developed at 5.4m, where face sheet and core are separated. This is shown in a 3x scaled deformation plot in Figure 23.

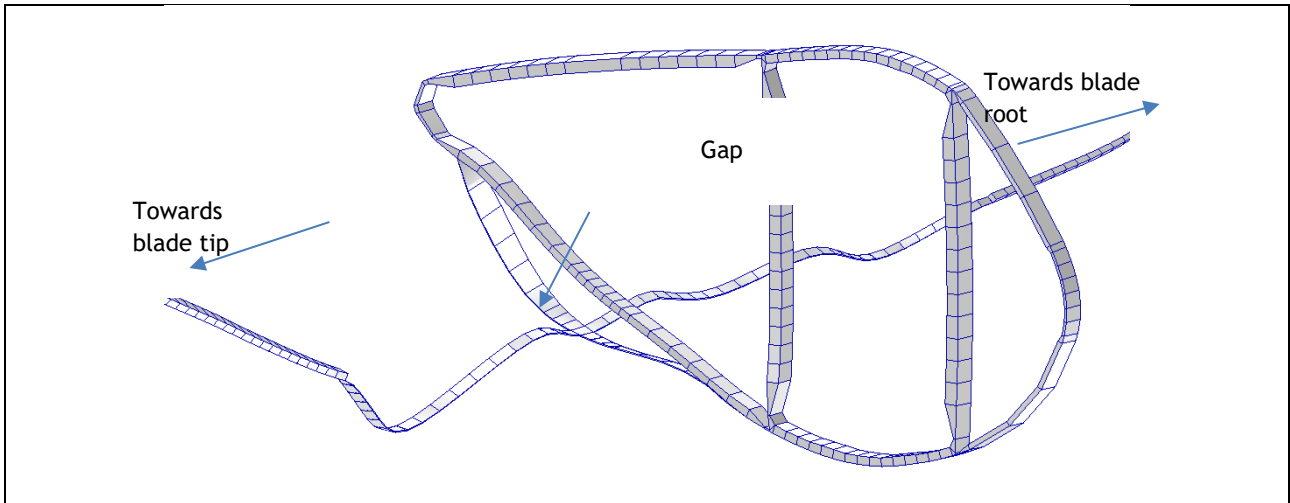


Figure 23: Deformed (3x scaled) cross-section at 5.4m during combined load (8xLTT) and solid section S43. LC = Comb2xFlap\_8xLTT

The developed gap analysis tool is used and in Figure 24 the gap between face sheet and core along the blade in the middle of the PS panel is shown (for 'Debond A')

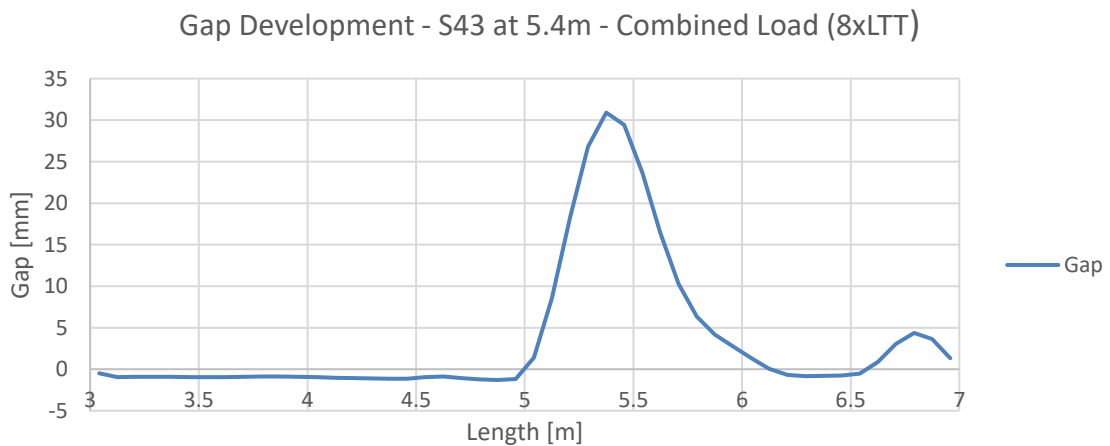


Figure 24: Gap between debonded outer face sheet and core at S43 between 3m to 7m (debonded zone of 'Debond A'). Gap approximately 30mm at 5.4m. LC = Comb2xFlap\_8xLTT

The maximum gap at 5.4m (approx. 30mm) is very large, and some sort of damage would have likely to have occurred. If a real simulation showed this, the recommendation would be to repair the debond causing this behavior. Negative values are present (around -0.8mm). It is assumed this is caused by the simple post-processing method, which does not include rotation between the investigated elements.

The gap development has been investigated as a function of applied load level, and in Figure 25 it can be seen how the localized deformation between pressure side debonded face sheet and core develops as loading increases. Gap between debonded face sheet and core is indicated when the graphs are separated:

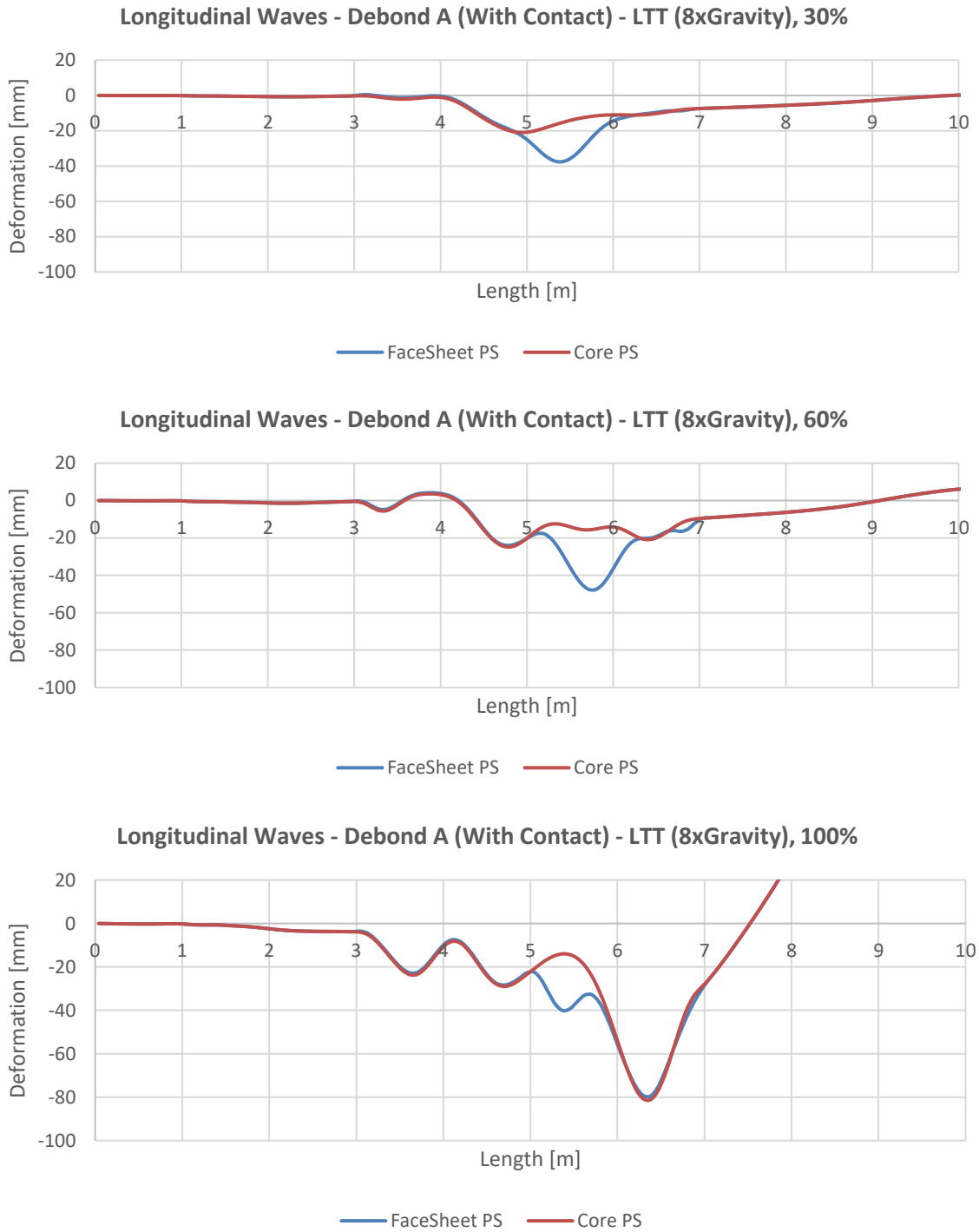


Figure 25: Longitudinal Waves on middle of PS panel from 0-10m of the blade. Comparison between face sheet and core. LC = Comb2xFlap\_8xLTT at 30%, 60% and 100%

In Figure 26 the gap development at 5.4m in middle of PS panel (S43) is seen as function of applied load - combined loading (8xLTT).

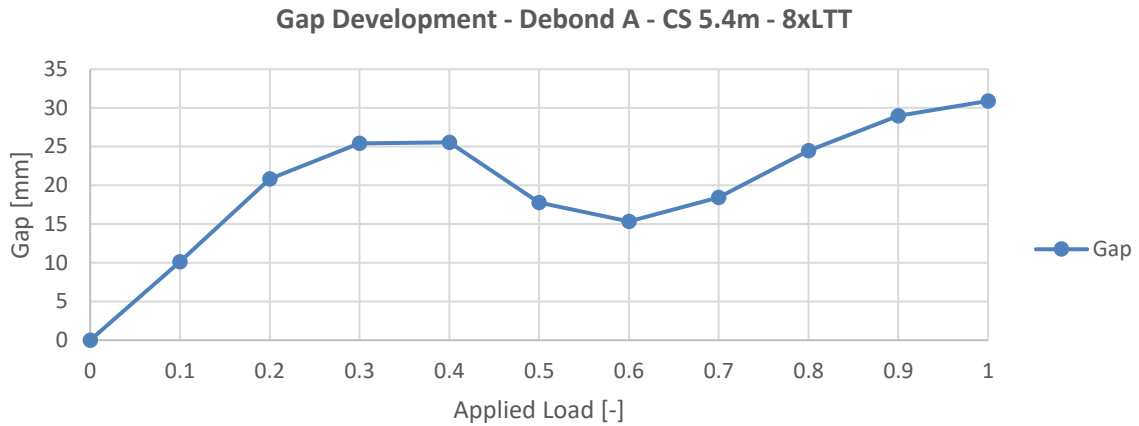


Figure 26: Gap development at 5.4m in the middle of PS panel (S43) of 'Debond A' at combined load (8xLTT) as function of applied load. The gap development is highly non-linear. LC = Comb2xFlap\_8xLTT

## Fracture Mechanics (Light Approach)

During the project, Bladena has worked on and investigated methods to use for understanding debonding in a FEM environment.

The FEM software program used by Bladena is MSC. Patran, which offers the possibility of using the Virtual Crack Closure Technique (VCCT) for analyzing damage front for lower and higher order 2D solids and 3D shells and solids. The following input data must be given for applying a VCCT crack:

Table 22: Input for applying VCCT in Patran

Input Data	Opportunity	Description
Crack Propagation	Direct	Cracks grow when the energy release rate is larger than the user specified crack growth resistance (fracture toughness).
	No Crack	No crack propagation is initially performed.
Crack Growth	Release Glued	Will release MPC definitions (tying) and works with glued contact, RBE2/RRD, and tying type 100. This requires that the crack growth direction be known and is somewhat dictated by the mesh.
Growth Increment	Fixed	With fixed size the crack growth increment is directly given.
Direction	Hoop Stress	This is used for specifying the method for calculating the crack growth direction. <b>Hoop Stress</b> - The individual energy release modes are used for calculating the crack growth direction. This method is also called maximum principal stress criterion. See Marc Volume A, chapter 5,

		section on Fracture Mechanics for details on how this is calculated.
Crack Growth Increment size	'User Value'	This sets the fixed crack growth increment. It specifies the length the crack advances during growth. When re-meshing based growth is specified the given crack growth increment is directly used when extending the crack. For the option of releasing tied interface the crack is grown one element edge at the time, and as many edges as needed to reach the specified growth increment are released.
Mode I Critical SERR, $G_{IC}$	'User Value'	This sets the crack growth resistance (often denoted fracture toughness) for the current crack. This value is used together with the total energy release rate growth criterion and provides the default for the separate modes: Mode I, Mode II, Mode III For each of the crack modes one can specify a separate crack growth resistance. The default is to use the value specified above. These values can be a function of accumulated crack growth (a displacement based non-spatial field), time, or temperature.
Mode II Critical SERR, $G_{IIC}$	'User Value'	
Mode III Critical SERR, $G_{IIIC}$	'User Value'	
Accumulated Crack Growth/Time/Temp Function	'User Value'	It shows list of non-spatial time or temperature dependent fields to select for Crack Growth increment size and resistance. This will write TABLEM1 if selected.

It is possible to investigate crack propagation. Two modes of growth are available:

- *Fatigue*: The user specifies a load sequence time period. During the load sequence, the largest energy release rate and the corresponding estimated crack growth direction are recorded. At the end of the load sequence, the crack is grown using the specified method.
- *Direct*: For direct growth, the crack grows as soon as the calculated energy release rate is larger than the user-specified  $G_c$ . Note that  $G_c$  can be made a function of the accumulated crack growth length to model a crack growth resistance behavior.

Using MSC.Nastran solver the crack opening or propagation must be modeled, so the *uncracked area* is represented by elements:

1. With double nodes and ties.
2. RBE2 or RROD.
3. Glued together via contact definitions.

Bladena has not been exploring the FEM software for crack propagation, however, different static cases (DCB, DCB-UBM and 4PB Panel) have been investigated and benchmarked against analytical solutions and published paper results. The models have been created using 3D solid 8-node hexahedral elements (Hex8) with a *solid shell formulation*.

### DCB-Specimen (Isotropic) FEM simulation:

One end (the end without the initial crack) is fixed in all degrees of freedom. The loading is applied to each beam at the end of the crack. These loads are applied by nodal forces summing up the total load (P) listed in Table 23.

Table 23: DCB specimens investigated (loads, stiffness and width varied)

Specimen	Load, P [N]	Stiffness, $E_x$ [Pa]	Width, W [m]	Length, L [m]	Height, H [m]	Crack length, a [m]
DCB1	5000	2.10E+11	0.050	0.200	0.005	0.050
DCB2	2500	4.13E+10	0.030	0.200	0.005	0.050

The simple DCB FEM model is shown in Figure 27.

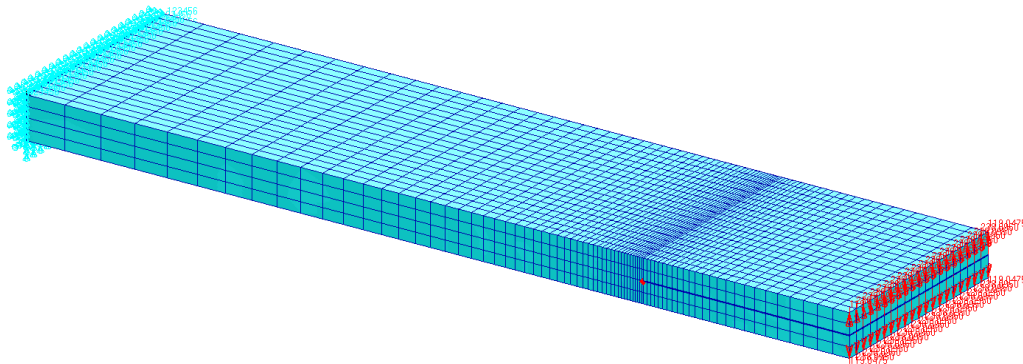


Figure 27: FEM model of DCB specimen

The Mode I strain energy release rate (SERR) referred to as  $G_I$  can be calculated as:

$$G_I = \frac{12 \cdot P^2 \cdot a^2}{W^2 \cdot H^3 \cdot E_x}$$

By extracting the opening ( $\delta$ ) displacement at the end between the two cracked beams, the energy release rate can be determined as:

$$G_I = \frac{3 \cdot P \cdot \delta}{2 \cdot W \cdot a}$$

The deformation plot of DCB1 is shown in Figure 28.

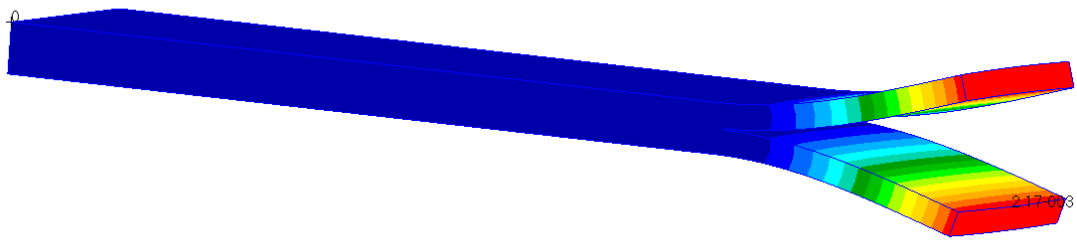


Figure 28: Deformation of DCB1

The total energy release rate,  $G_{tot}$ , is shown in Figure 29 with a 50x scaled deformed DCB1 structure (to be able to see the crack opening). For this analysis with the applied loading, energy release rate is purely Mode I, so  $G_{tot} = G_I$ .

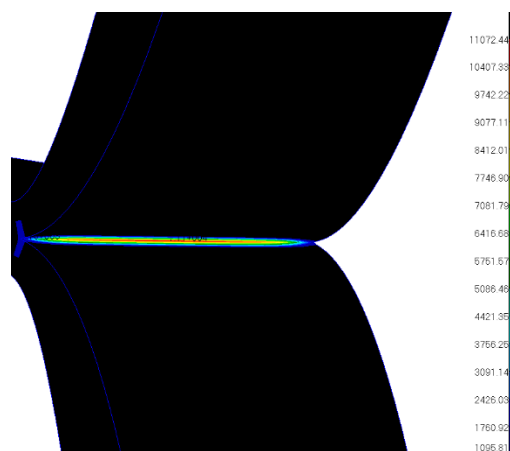


Figure 29: Total energy release rate,  $G_{tot}$ , in the crack front of DCB1

The Mode I energy release rate is extracted at the crack tip nodes for DCB1 and DCB2.

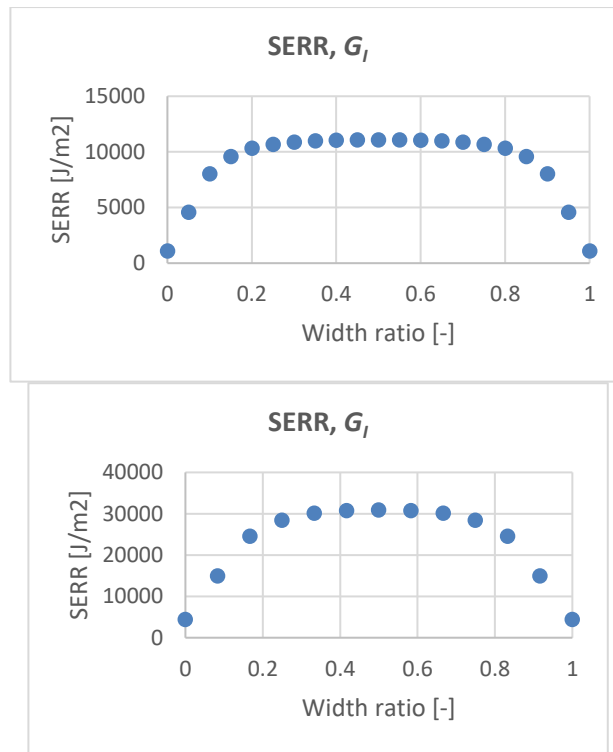


Figure 30: Energy release rate along crack tip nodes (through the width) extracted from Patran for DCB1 (left) and DCB2 (right)

The analyses have been conducted where elements through the thickness have been varied (convergence study). The small convergence study is done for each 'beam' having 1, 2 and 4 elements through the thickness.

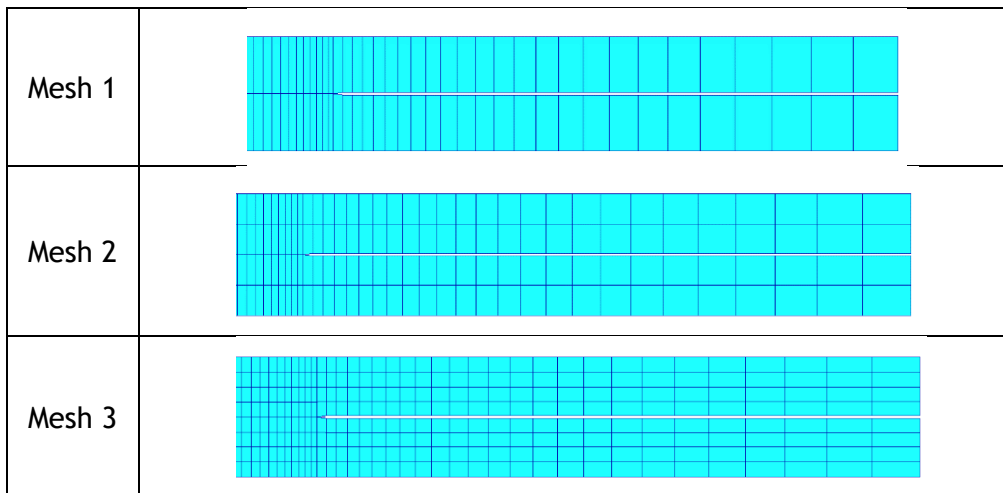


Figure 31: Meshing of DCB specimen

The results from the FEM analysis have been compared to the known analytical solution and presented for the different meshes.

Table 24: Comparison of results for SERR

Specimen	Mesh	$G_I$ Analytical	$G_I$ FEM	Error [%]
----------	------	---------------------	--------------	--------------

		[J/m <sup>2</sup> ]	[J/m <sup>2</sup> ]	
DCB1	1	11428.6	10740.5	6.41
DCB1	2	11428.6	11072.4	3.22
DCB1	3	11428.6	11307.9	1.07
DCB2	2	32687.7	30898.4	5.79

From the DCB study, it is seen that the VCCT-method provides acceptable results for rather coarse mesh densities for the DCB specimen, with isotropic material properties.

#### DCB-UBM-Specimen (Sandwich):

The model is 10mm in width and the nodes are fixed in all translational degrees of freedom in one end in distance of 50mm. Bending moments are applied through a multi-point constraint (MPC, RBE2). The sandwich DCB-UBM specimen cases investigated are:

Table 25: DCB-UBM specimen investigated

Specimen	Load, M <sub>d</sub> [Nm]	Load, M <sub>s</sub> [Nm]	Width, W [m]	Length, L [m]	Height, H <sub>f</sub> [m]	Height, H <sub>c</sub> [m]	Crack length, a [m]
DCB-UBM - Case 1	+0.75 6	-6.048	0.01	0.500	0.002	0.020	0.200
DCB-UBM - Case 4*	+1.18 6	+4.744	0.01	0.500	0.002	0.020	0.200

\*Refers to Case 4 in [1]

In Figure 32 the FEM model of the DCB-UBM (sandwich structure) specimen is shown. The material properties for core and face sheet are taken from [1].

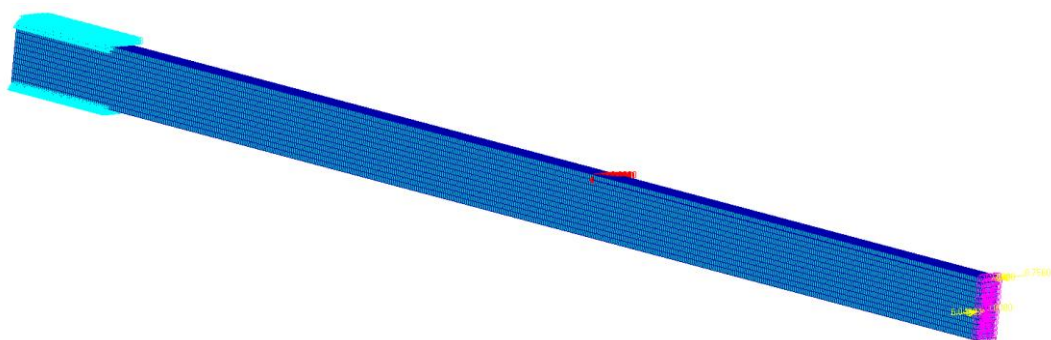


Figure 32: DCB-UBM FEM model with 'fine' mesh

Two different mesh/methodologies have been investigated, see Figure 33. The 'Coarse' mesh is based on the meshing and modeling from BMT, where the blade cross-section is modeled using 1 element through the thickness. The element then

consists of multiple layers. In the 'Finer' mesh model, there are multiple elements through the thickness, so each element has only 1 layer of material.

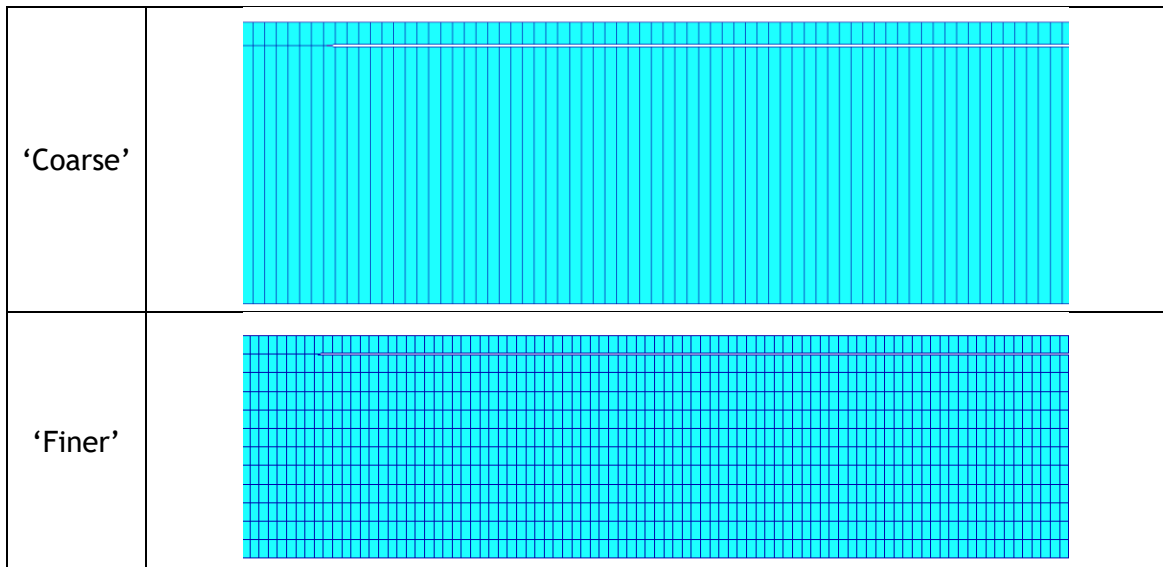


Figure 33: Meshing of DCB-UBM specimen

The 'Coarse' mesh model has been analyzed for Case 1 and Case 4 and the results are compared and benchmarked towards results from [1].

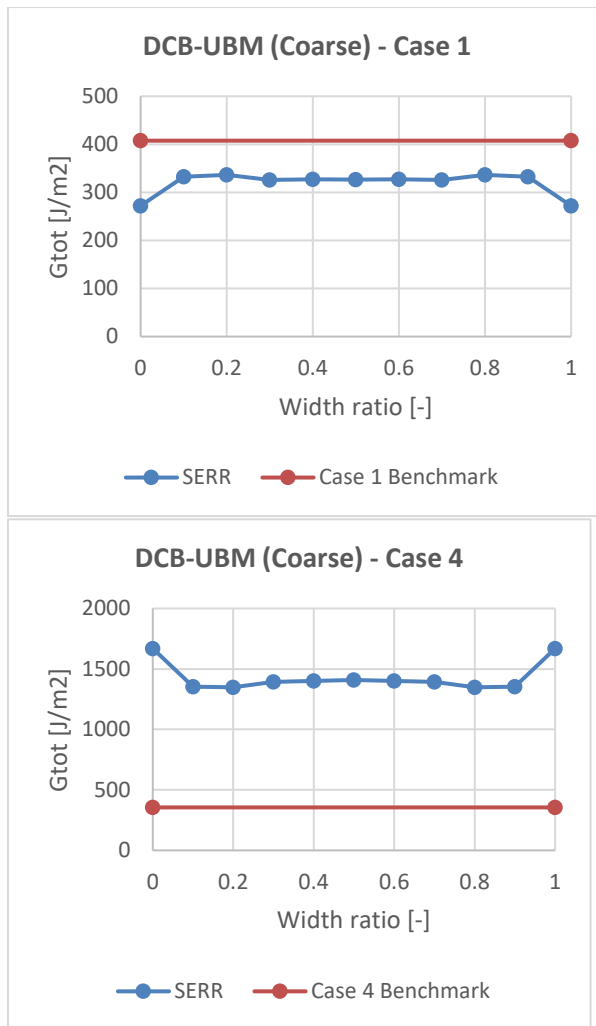


Figure 34: Result comparison of DCB-UBM results - 'Coarse' mesh (BMT methodology).

The result comparison in Figure 34 is not acceptable for Case 4 and the 'Coarse' mesh might not be applicable for evaluating the energy release rate values. The results for the 'Finer' mesh simulation are shown in Figure 35.

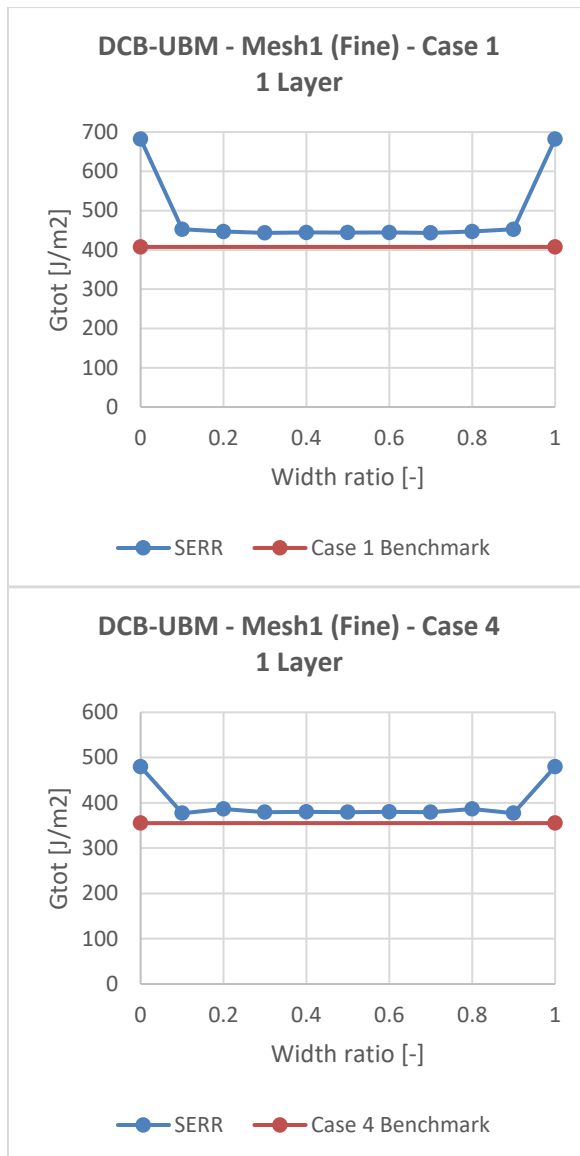


Figure 35: Result comparison of DCB-UBM results - 'Finer' mesh (multiple elements through thickness).

The finer mesh increases the accuracy of the model and for the 'Finer' mesh model both Case 1 and Case 4 provides acceptable results.

The studies and investigations using the VCCT-method in Patran show great potential for Bladerna for further developing better understanding and methods, which can be used as part of services Bladerna can offer for commercial customers, who are asking for this. This will add value to Bladerna.

**4PB-Panel Specimen:**

In Figure 36 the FEM model of the 4PB plate (sandwich structure) specimen is shown.

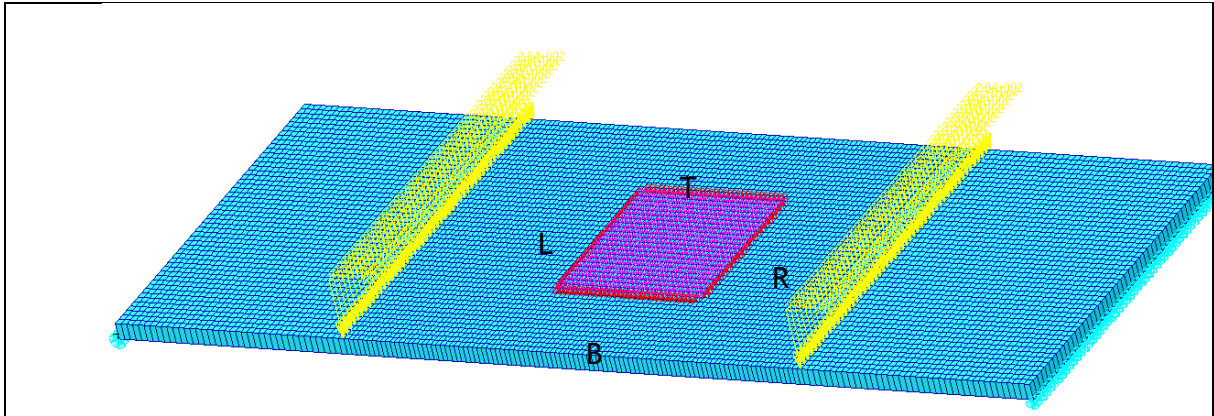
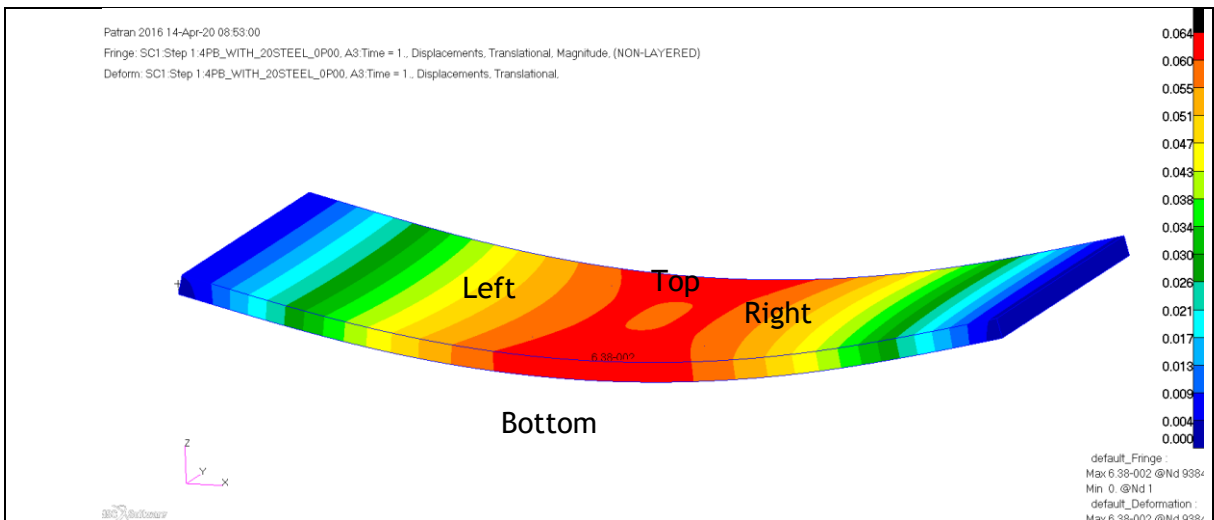
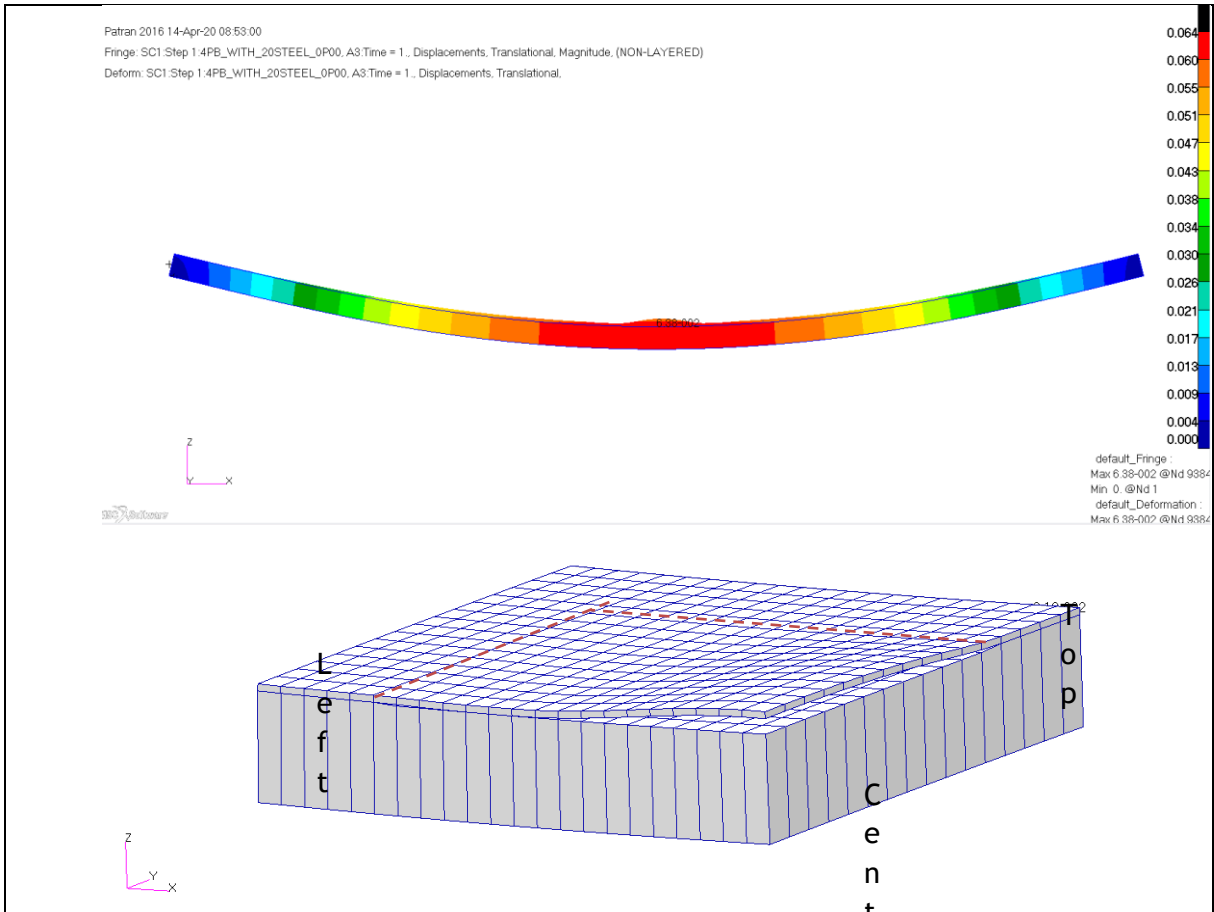


Figure 36: 4PB sandwich plate with rectangular debond zone (300x300mm). 10mm of steel added

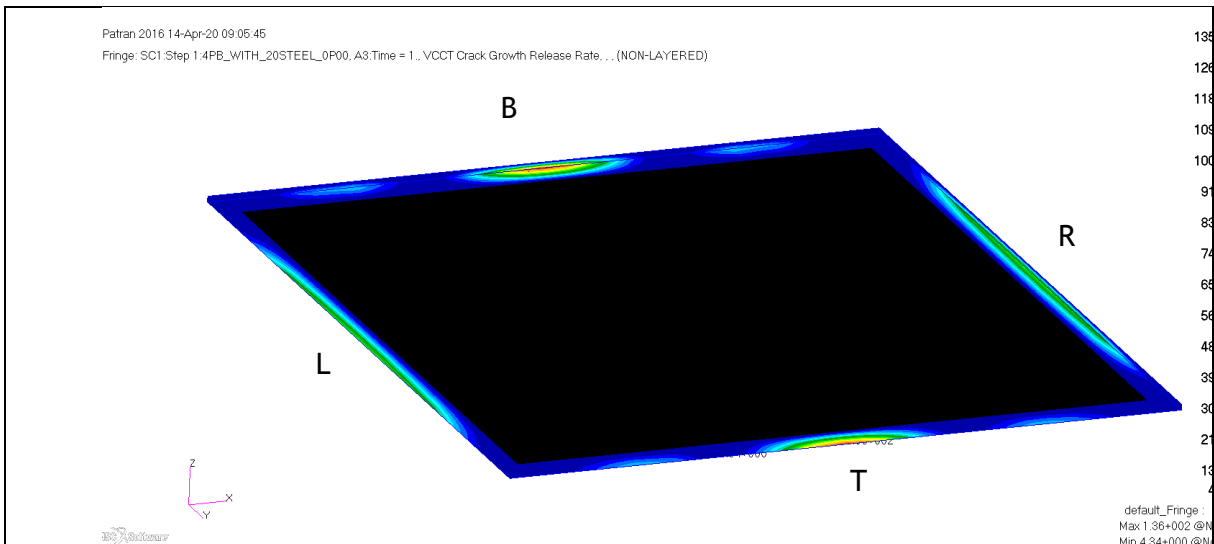
The 4PB FEM simulations are conducted to investigate and verify how the implemented VCCT method works in a 3D case e.g. debonding in multiple directions - longitudinal and transverse. 4 crack fronts have been made at: 'Left', 'Top', 'Right' and 'Bottom'.

In Figure 37 the deformation of the investigated panel can be seen. At the debond zone the face sheet 'pops' out. The debonded interface and model have been simulated with a very coarse mesh, however, the results should be seen as trends.





In the Figure 38 the Total Energy Release Rate ( $G_{tot}$ ) is shown around the crack front of the debonded face sheet.



The maximum value is found at bottom and top of debond zone, which is perpendicular to in-plane compression forces that arise due to the loading configuration. This concludes that the debond will tend to propagate towards 'bottom' and 'top' rather than 'left' and 'right'.

Different plots can be generated to describe the damage and how it is likely to propagate. In Figure 39 the total energy release rate (SERR) is plotted along all 4 edges:

Figure 39: Energy release rate at along the 4 edges of debond

In due to the symmetric geometry and loading condition the maximum values of SERR are located at the middle of each debonded edge. A simplified SERR plot (based on maximum values) around the debond is shown in Figure 40.

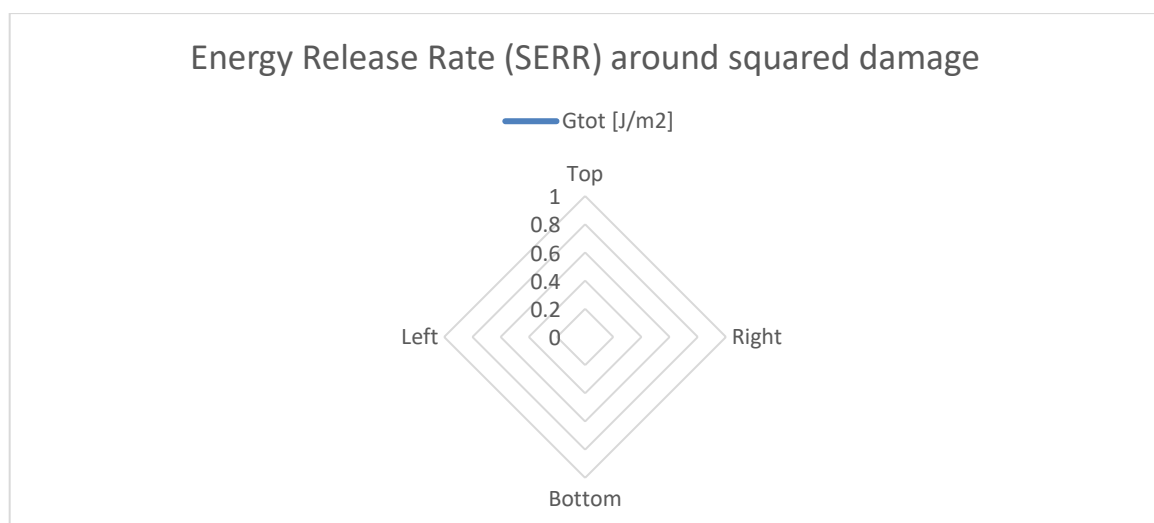


Figure 40: Simplified SERR around edges of debond. Maximum values are used, and these are located in the middle of each edge due to the symmetric geometry and loading.

## References

- [1] *Energy-Release Rate and Mode Mixity of Face/Core Debonds in Sandwich Beams*, Kardomateas, Berggreen, Carlsson, AIAA Journal, April 2013

**Torsion Load Component during Operation**

Wind turbine blades are exposed to flapwise and edgewise loads during operation, which makes the blades deflect - and also twist around their longitudinal axis, see Figure . This is due to a *torsional* load component is being generated.

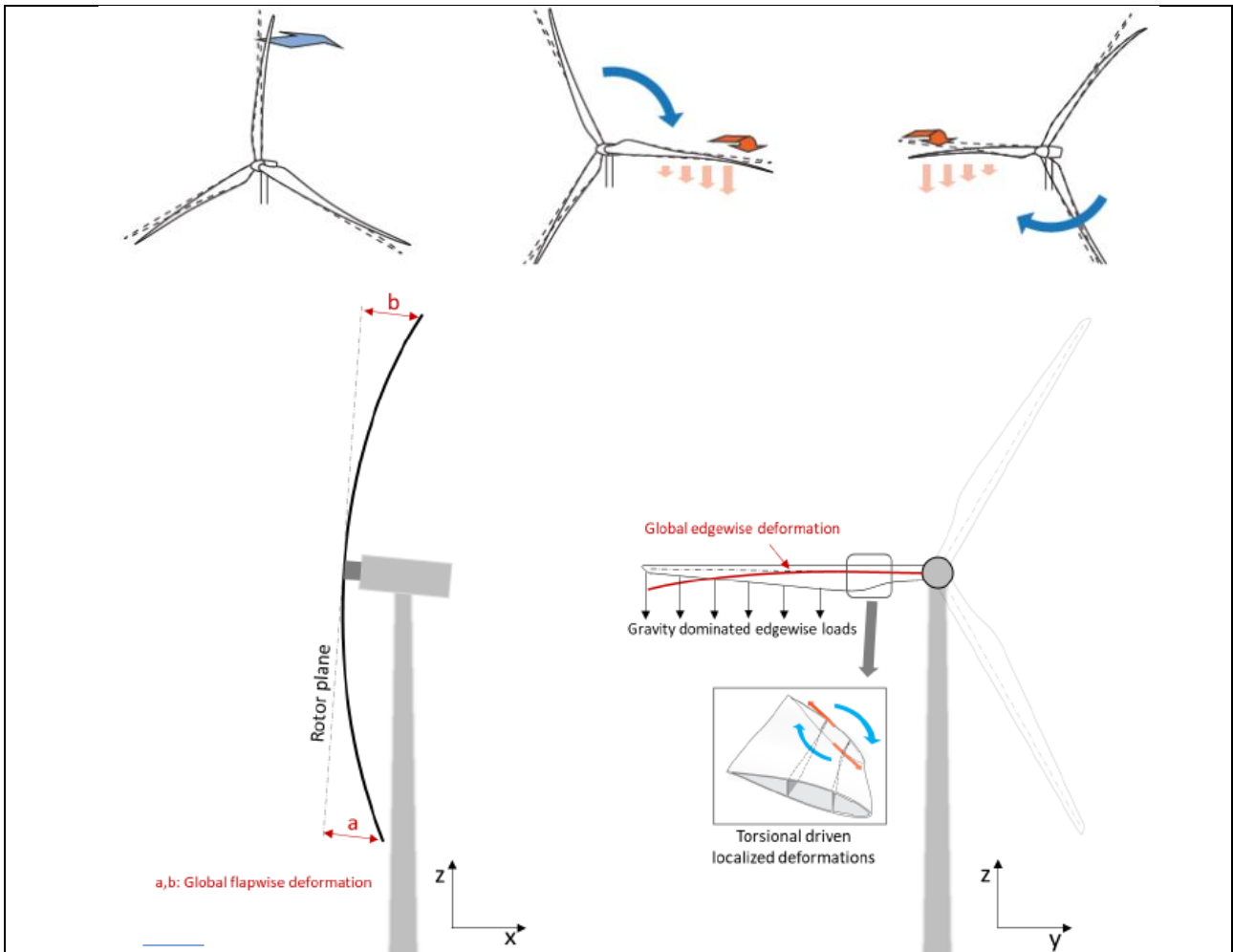


Figure 1: A: Flapwise load marked with blue arrow and deflection. B and C: Illustration of gravitational forces (light orange arrows), which in combination with aerodynamic flapwise loads generates an additional torsional load component (dark orange arrow) - edgewise deflection is TTL (left) and LTT (right). D and E: Torsional load component detail from flapwise and edgewise load contributions during operation and localized effect.

Figure illustrates how the flapwise loading due to incoming wind is deflecting the blade out of the rotor plane, towards the tower. As the blade rotates (due to an edgewise load component generated by the wind crossing the aerodynamic profile along the blade), the gravitational load alternates throughout one full rotation. When the blade azimuth position is horizontal (compared to the vertical tower), the gravitational forces are contributing the most to the edgewise loading, which also generates the torsion in the root and transition zone.

When the blades are in the vertical position (where the gravitational forces are assumed not to contribute to edgewise loading), the blade is still exposed to torsional forces. This is due to the flapwise aerodynamic loads acts in the aerodynamic center of the cross-section at along the blade and *not* in the shear center. The shear center is defined as the point, where transverse loading will *not* generate twisting/torsional rotation. The effect of applying loads in the aerodynamic center can be seen in the next section.

## Effect of Load Application - Torsion

When designing, analyzing and testing wind turbine blades, it is important to take the torsional load component into consideration and therefore be aware of how and where loads should be applied to simulate the blades response in operation. In Figure 2 the today's practice of applying loads to a wind turbine blade during simulations and tests are shown, in comparison with an actual load distribution during operation.

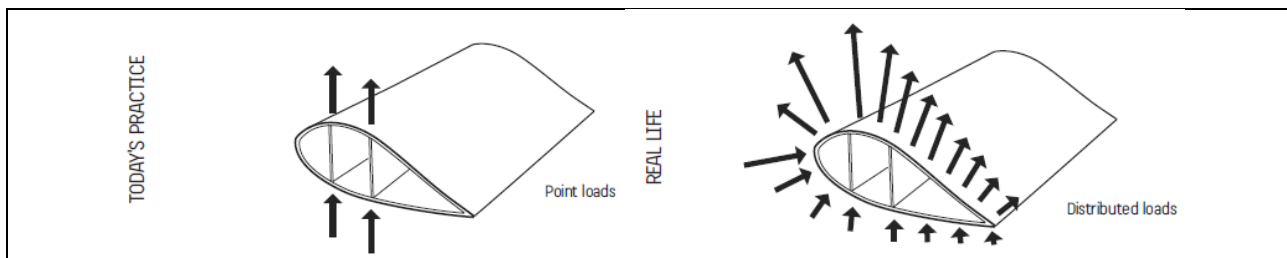


Figure 2: Comparison of loads acting on a wind turbine blade. Left: Today's practice during simulations and testing. Right: Actual load distribution during operation.

Today's practice of applying loads on wind turbine blades during simulations and testing is not conservative and it is Bladena experience that the torsional load component is not captured all the time, which affects the localized behavior, in terms of deformations, strains and stresses, mainly in the transition zone and max chord of the blade. In Figure 3 it is sketched how the torsional load (moment) component is generated, when the realistic distributed loads are simplified to a combined load acting in the aerodynamic center.

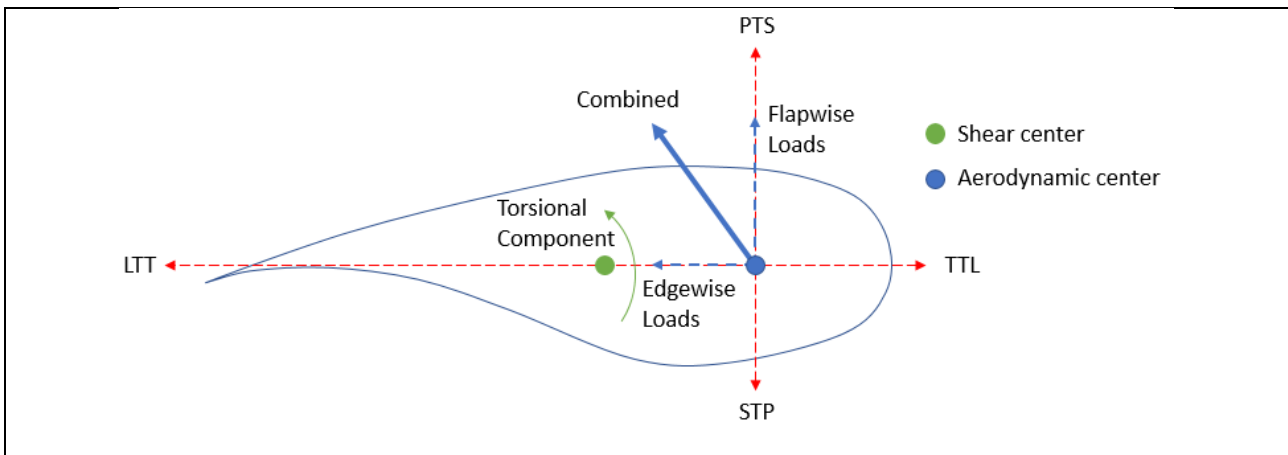


Figure 3: Sketch showing the torsional load component, that occurs as combination of external loading acting in the aerodynamic center.

The effect of location for load application when analyzing a blade using 3D geometric non-linear FEM has been investigated. The root torsional moment of a 70m blade with a large distance between shear webs and load-carrying shell has been investigated. The blade was subjected to combined loading condition with the flapwise loads acting in the pressure-towards-suction (PTS) direction and the edgewise loading was set to the blade's gravitational force in the leading-towards-trailing (LTT) direction. The global FEM-model is shown in Figure 4.

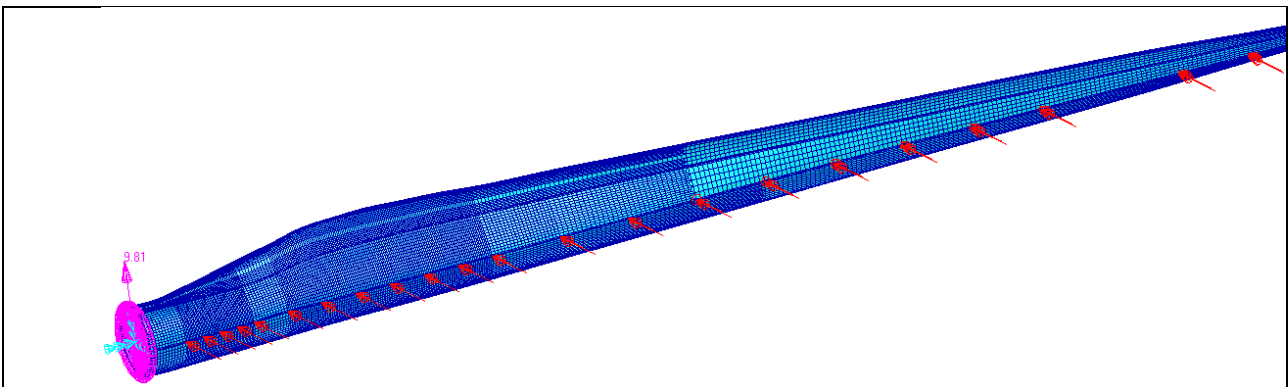


Figure 4: FEM Model of a 70m blade under combined loading - flapwise loads applied along the blade in aerodynamic center and gravity of the blade used to simulate edgewise loading.

The flapwise loads were a realistic load distribution for a blade of 70m. The blade was investigated for two cases:

- The combined loading (PTS+LTT) were applied in the aerodynamic center along the blade
- The combined loading (PTS+LTT) were applied more towards the shear center along the blade

The blade was fixed in the root using a rigid body element (RBE2) multi-point constraint (MPC), so it was possible to extract the root torsional moment. In Figure 5 the development of root torsional moment is shown as a function of applied combined loading for the two above-mentioned cases.

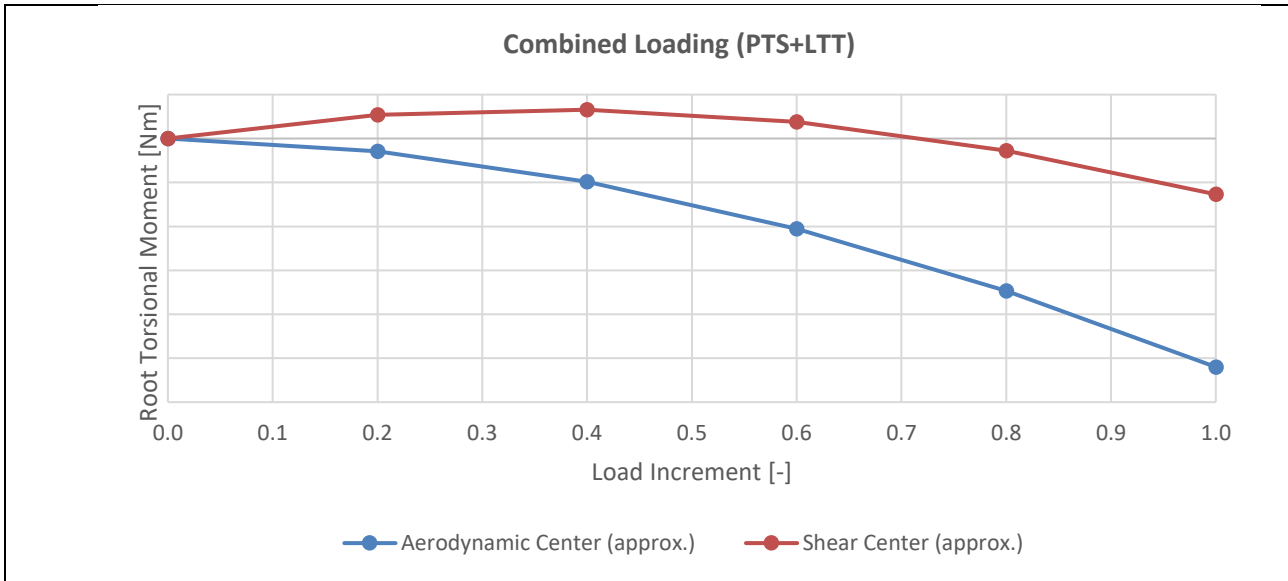


Figure 5: Root Torsional Moment investigated for combined loading. The application of flapwise (PTS) loading has been applied close to aerodynamic center (blue curve) and close to shear center (red curve). Magnitude of flapwise load is the same for the two curves.

From Figure 5 it is shown how much of an impact it has when applying loads to a blade cross-section. In theory the root torsional moment is zero if the loads along the blade is applied exactly in the shear center, however, the absolute value for the case simulating load applied in the shear center is approximately 60 kNm. The absolute value for the case simulating the combined loading acting the aerodynamic center is approximately 260 kNm, which is 4.3 times more (330% increase).

## Torsional Root Moment - Simple Loading vs. Realistic Loading

The torsional load component that arises in a wind turbine blade during operation is a combination of flapwise and edgewise loading (combined loading) acting in the aerodynamic center along the blade (which is offset compared to the shear center). In the previous section, that effect of applying load in the aerodynamic center was compared to applying load in the shear center, which showed to have major impact.

This section describes the investigation conducted of the effect of subjecting a wind turbine blade to a simple loading condition - pure flapwise or pure edgewise in comparison with a more realistic loading condition (flapwise and edgewise loading combined). The focus has been the root torsional moment, to indicate the effect in torsional loading when a blade is subjected to more realistic loading conditions.

The blade used for this investigation was a 70m blade with a flat back design. The blade was fixed in the root using a rigid body element (RBE2) multi-point constraint (MPC), so it was possible to extract the root torsional moment. The blade was subjected to combined loading condition with the flapwise loads acting in the pressure-towards-suction (PTS) direction and the edgewise loading was set to the blade's gravitational force, and varied between the leading-towards-trailing (LTT) and trailing-towards-leading (TTL) direction. The flapwise loads were a realistic load distribution for a blade of 70m. The global FEM-model is shown in Figure 6.

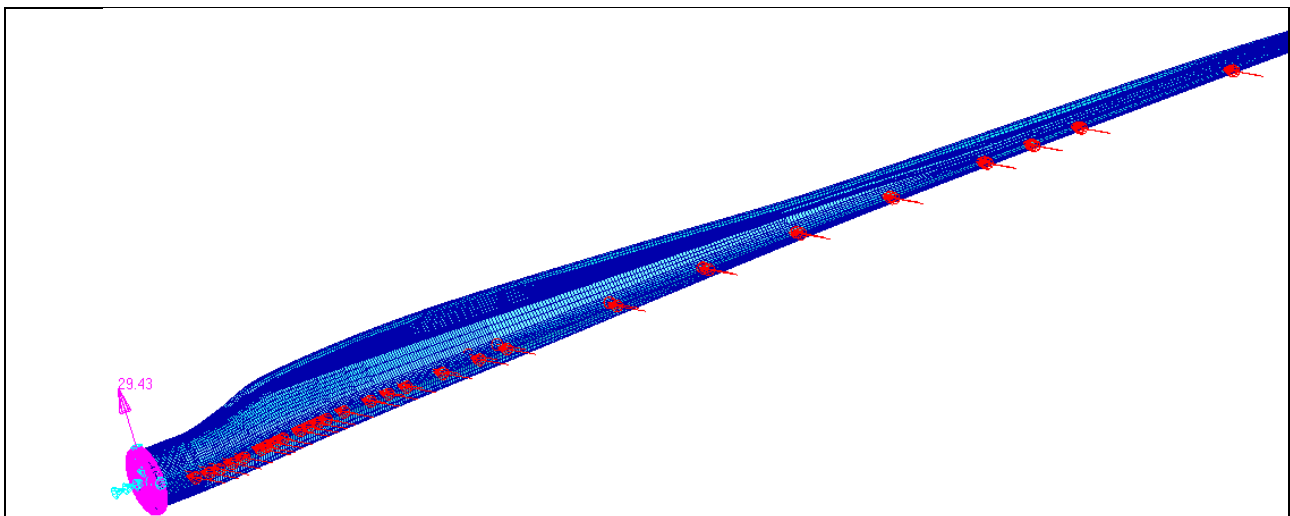


Figure 6: FEM Model of 70m blade with flatback under combined loading - flapwise loads applied along the blade in aerodynamic center and gravity of the blade used to simulate edgewise loading.

The blade was investigated for two cases with combined loading and three load cases with simple one-direction loading:

- The combined loading (PTS+LTT) were applied in the aerodynamic center along the blade
- The combined loading (PTS+TTL) were applied in the aerodynamic center along the blade
- Pure edgewise loading (gravity) in the LTT-direction
- Pure edgewise loading (gravity) in the TTL-direction
- Pure flapwise loading (gravity) in the PTS-direction

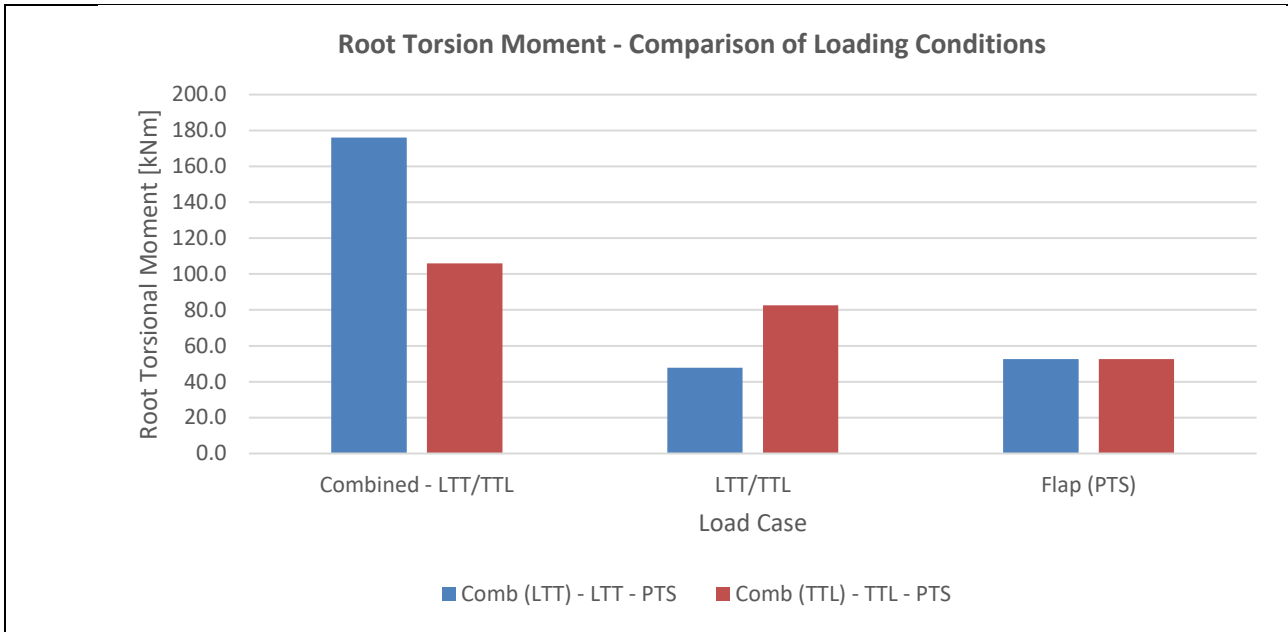


Figure 7: Root Torsional Moment for combined loading condition (PTS+LTT and PTS+TTL), simple edgewise loading (LTT and TTL) and simple flapwise loading (PTS)

In Figure 7, the first two columns shows the extracted root torsional moment for the two combined load cases (PTS+LTT and PTS+TTL), where its shown that for this particular blade the PTS+LTT generates the highest root torsional moment.

The two columns in the center of Figure 7 shows the root torsional moment for the simple edgewise loadings (LTT and TTL), and the last two columns is the blade subjected to a simple flapwise (PTS) loading (the columns are identical).

From Figure 7 it can be seen how the root torsional moment increases, when the blade is subjected to a combined loading condition. The increase in root torsional moment in percentage is illustrated in Figure 8.

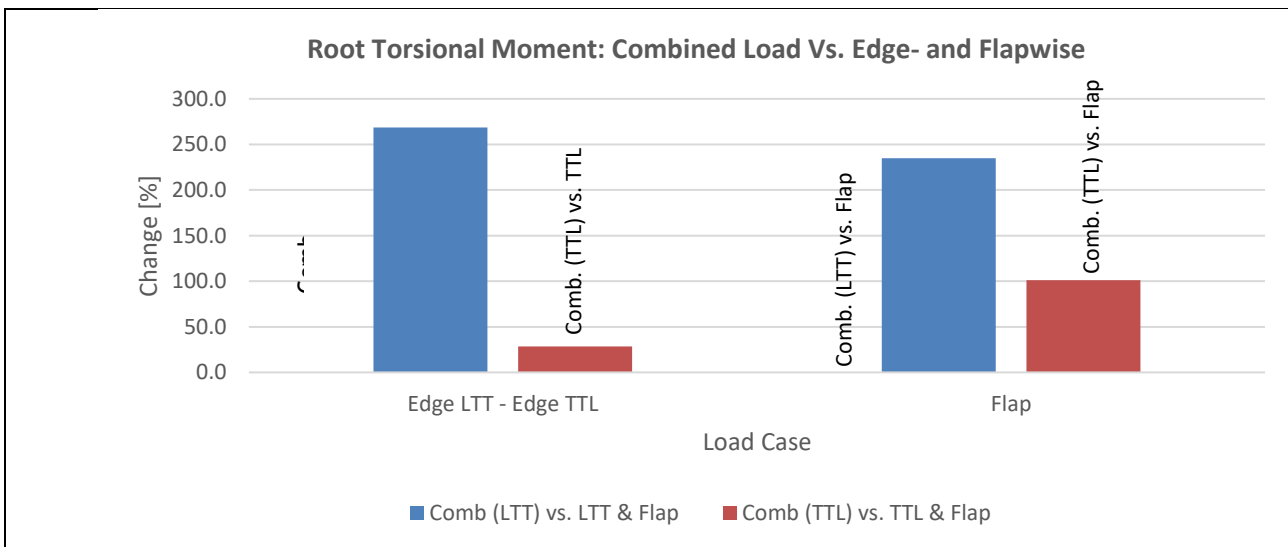


Figure 8: Root Torsional Moment magnitude comparison in percentage between realistic combined loading and simple 1-direction loading condition.

From Figure 8 it is seen that there is a major difference on the torsional load component in the blade depending on applying a combined (more realistic) loading condition than a simple loading condition. The root torsional moment increases for all cases and the summaries for Figure 8 are listed below:

- The root torsional moment for the combined loading condition, flapwise (PTS) + edgewise (LTT) is approx. 270% larger than the blade loaded in pure edgewise loading (LTT)
- The root torsional moment for the combined loading condition, flapwise (PTS) + edgewise (TTL) is approx. 235% larger than the blade loaded in pure flapwise loading (PTS)
- The root torsional moment for the combined loading condition, flapwise (PTS) + edgewise (TTL) is approx. 30% larger than the blade loaded in pure edgewise loading (TTL)
- The root torsional moment for the combined loading condition, flapwise (PTS) + edgewise (TTL) is approx. 100% larger than the blade loaded in pure flapwise loading (PTS)

According to DNV certification standard [1], only static bending test in the simple one-directions (PTS, STP, LTT and TTL) *shall* (is required) be performed. It is then mentioned that a combination of these test directions *may* (not required) also be acceptable, if appropriate. However, based from the studies above, the torsional load component, and structural effect of this, is not fully captured during certification. For the static bending test it is stated in [1], that for torsion, the stiffness distribution should be determined.

The effect of torsion was shown in the previous RATZ EUDP projects led by Bladena, where localized panel bending was used as an evaluation. It was found (by means of testing) that 65% more localized bending is obtained when torsion is applied. From a blade lifetime perspective, this translates directly into less lifetime when torsion is considered, hence the absolute need to consider torsion in the design and test phase of blades.

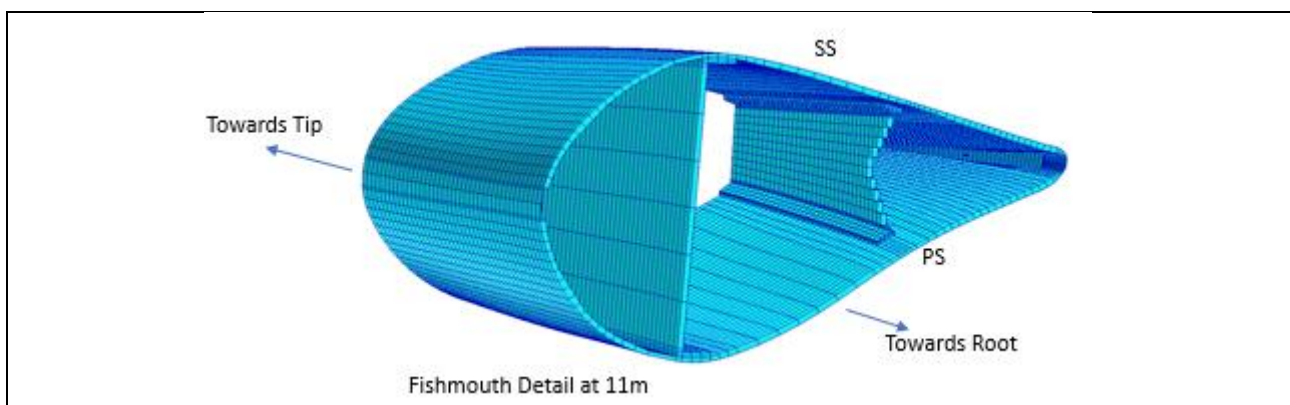
## Effect of Damage (Elastic Instability) - Torsion and Structural Response

During the project, Bladena has worked on and developed an early state methodology of simulating structural damages within wind turbine blades. This methodology is referred to as *Elastic Instability* and is a method that is meant for analyzing the effect of various damages in wind turbine blades.

A 70m blade with a large distance between shear webs and load-carrying shell has been investigated and where the aft. shear starts at R11m, which is in the max chord region. Different damages were investigated as part of an elastic instability analysis. The models and damages investigated are:

- *Reference Model* - Intact, no damages/defects introduced
- *Disbond 1* - Disbonded Aft. SW from R11m (start) to R15m between PS panel and flange
- *Disbond 2* - Main SW disbonded from R0m to R8m between PS panel and flange
- *Face Sheet Debonding* - Outer face sheet debond from core between shear webs from 8m to 15m

In Figure 9, a section of the 70m blade is shown in the FEM environment. A coarse fish mouth has been added to the aft. shear web, which starts at R11m radially along the blade.



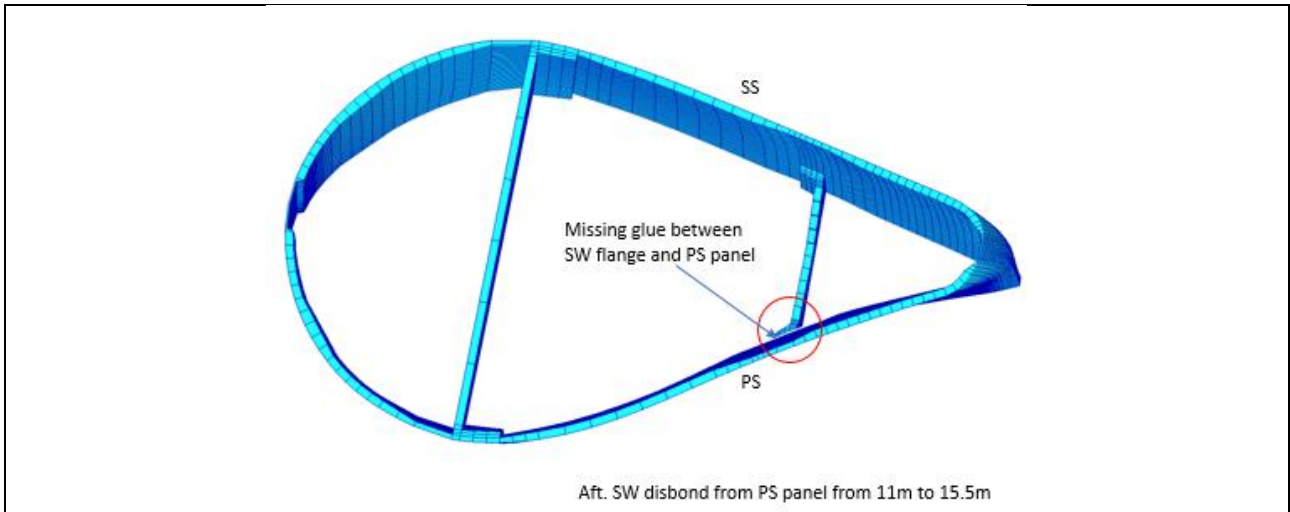


Figure 9: Illustration of aft. shear starting position at R11m and disbond between web and pressure side panel/shell (Disbond 1)

## Torsion - Influence of Damage

In the FEM model presented in Figure 9, the bondline (glue) has been removed between the aft. shear web and pressure side shell from R11m (start of aft. shear web) to R15m to simulate a shear web disbond from panel. This is a structural failure that is often seen in the field for load-carrying shell blade designs with rather large distance between the shear webs. A similar damage has been simulated for the same blade, however, the disbond is created between main shear web and pressure side panel from R0m to R8m.

Also, a debond damage has been simulated for the sandwich panel between the shear webs. Here the outer face sheet on the pressure side panel has been debonded/separated from the remaining sandwich panel from R8m to R15m. In Figure 10 the root torsional moment has been investigated for all 4 models (listed in top of this section).

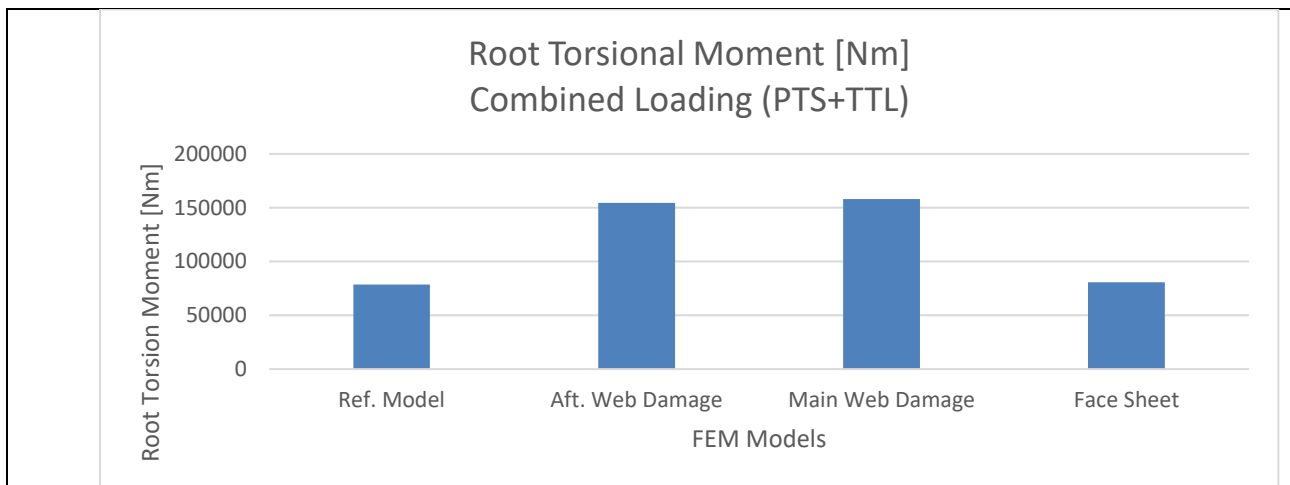


Figure 10: Root Torsional Moment for a 70m blade - both intact and various damages simulated

In Figure 10 it is seen that the shear web disbond damages affects the root torsional moment, whereas the debonded face sheet damage does not (almost) have an impact on the root torsional moment. The effect magnitudes are plotted in Figure 11, where the results are normalized towards the 'Intact/Reference' Model.

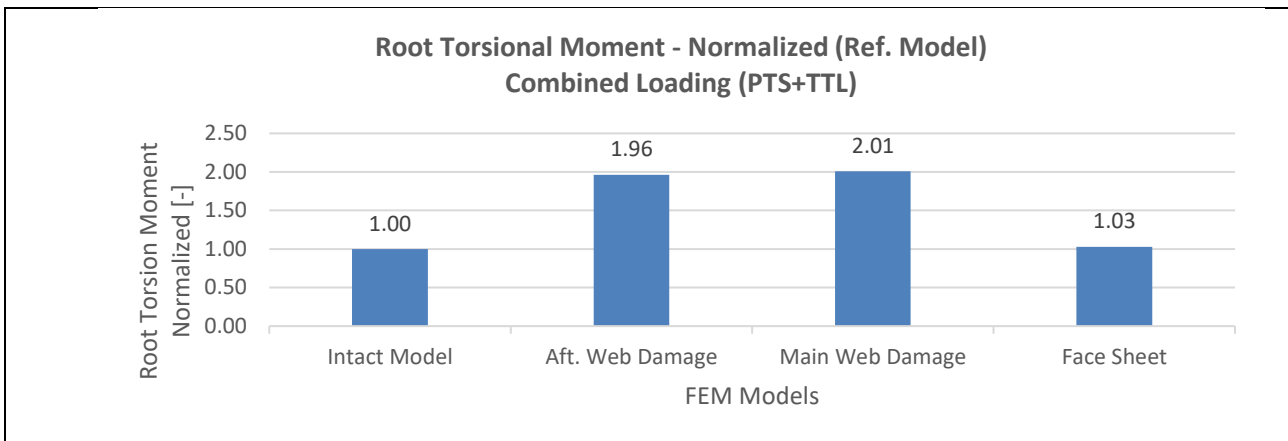


Figure 11: Root Torsional Moment normalized towards the 'Intact Model' and compared to all the damaged models.

The normalized comparison in Figure 11 shows, that the disbond damages between webs and pressure side panel affects the torsion loads in the blade, as the extracted torsional load increases by factor 2.0. A face sheet debond between shear webs from R8m to R15m does have an impact on the root torsional moment (only 3% percent difference for this simulation).

### Structural Behavior - Influence of Damage

#### Aft. Shear Web Disbond from Pressure Side Panel/Shell:

For the same blade (70m, load-carrying shell under PTS+TTL combined loading), the localized pressure panel deformation between trailing edge (TE) and main shear web, when aft. shear web is disbonded from panel from R11m (start) to R15m has been investigated. This is done by extracting the relative deformation between in the middle of the pressure side panel (PS2) and the 'rigid' points (PS1 and PS3), see Figure 12.

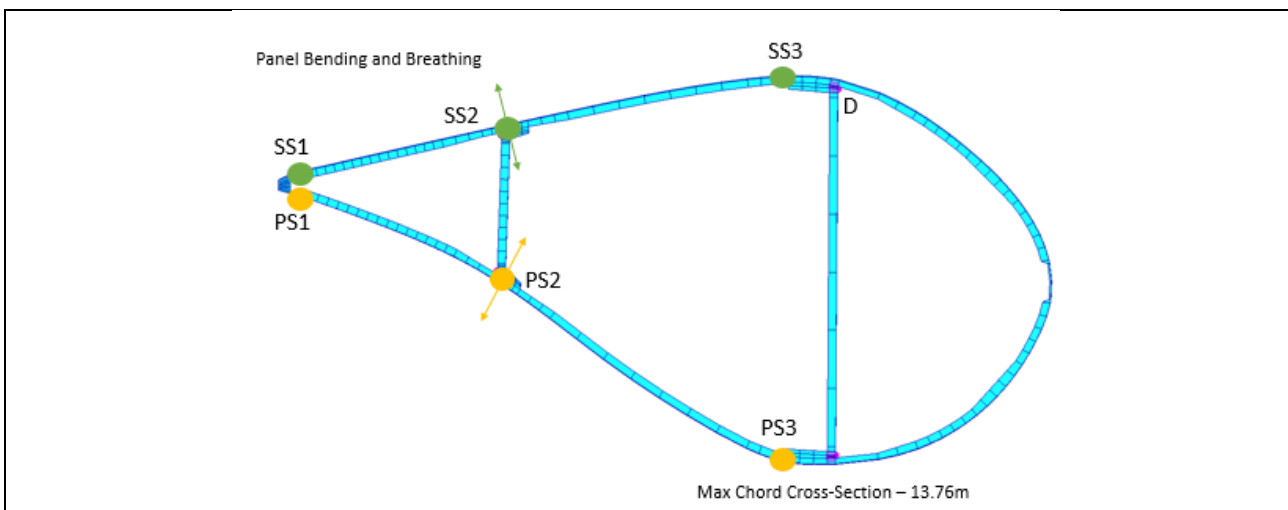


Figure 12: Illustration of extraction of breathing and panel bending. The breathing and panel bending are between the trailing edge and the main shear web. The position where the results are presented are at the aft. shear web (SS2 and PS2).

The blade is loaded in realistic combined load case (with loads applied near the aerodynamic center), with flapwise loading in PTS-direction and edgewise loading in TTL-direction. The localized pressure side panel deformation between trailing edge and main shear web (PS2 in Figure 12) has been extracted for both models and plotted in Figure 13.

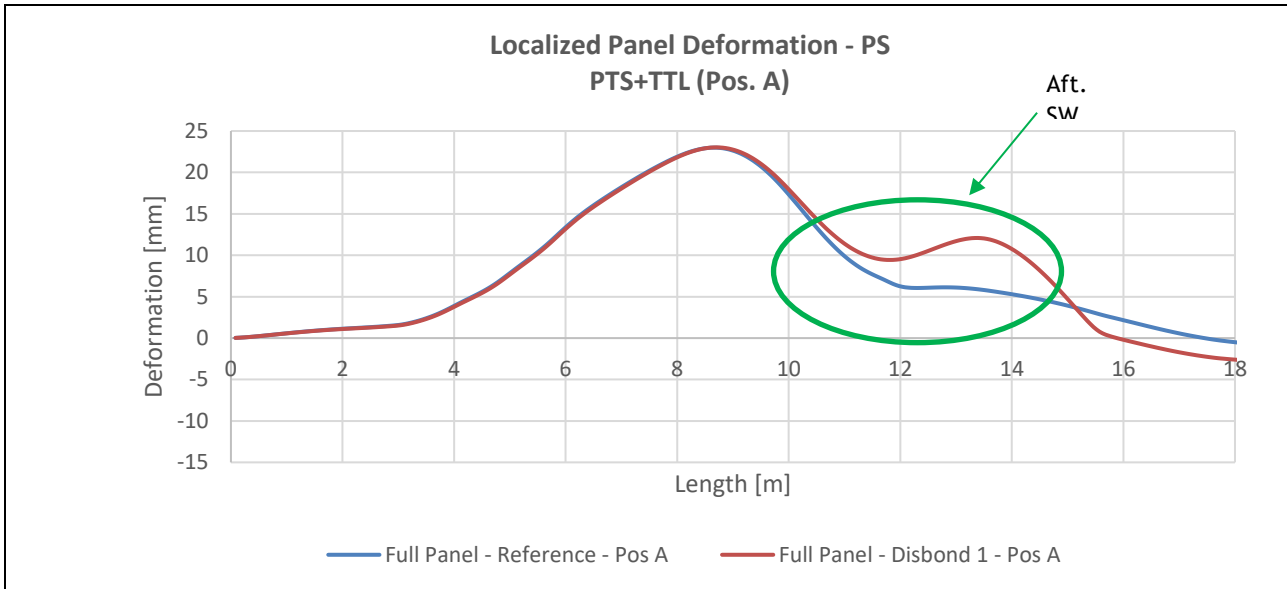


Figure 13: Pressure side panel localized out-of-plane deformation of 'Intact' and 'Aft. SW disbonded' 70m blade under combined loading (PTS+TTL)

The disbond between aft. shear web and pressure side panel/shell alternates the localized deformation of the pressure side panel for damaged mode (red curve).

## Outer Face Sheet (Skin) Debond from Core between Shear Webs at Pressure Side Panel/Shell:

For the same blade (70m, load-carrying shell under PTS+TTL combined loading), the localized pressure panel deformation between aft. shear web and main shear web, when outer face sheet (skin) is debonded from remaining sandwich panel (core and inner face sheet/skin) from R8m to R15m has been investigated. This is done by extracting the relative deformation between in the middle of the pressure side panel (PS2) and the 'rigid' points (PS1 and PS3), see Figure 14.

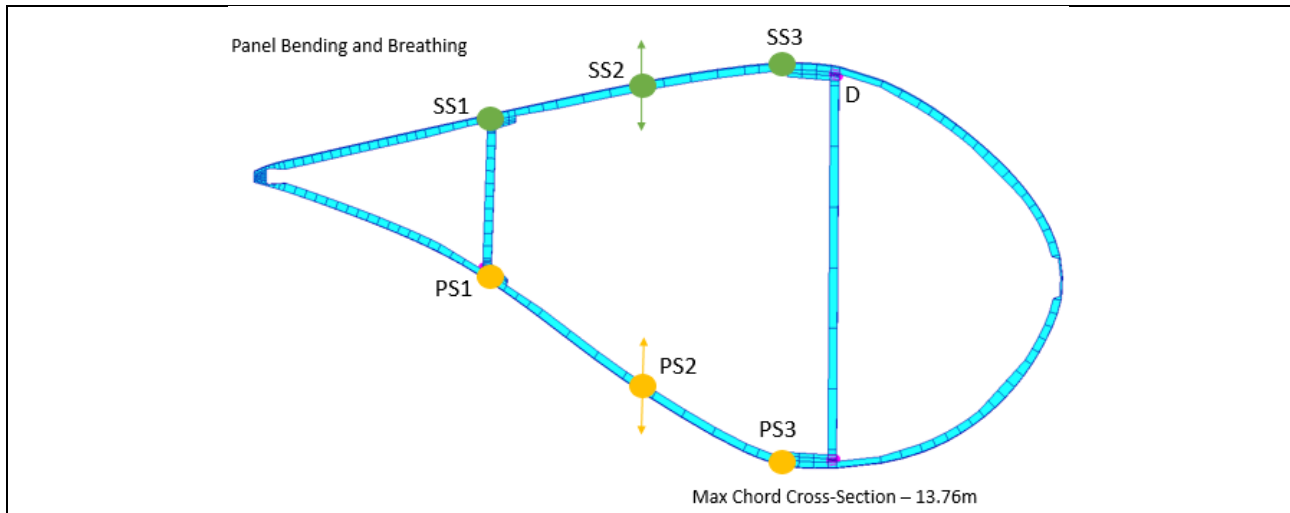


Figure 14: Illustration of extraction of breathing and panel bending. The breathing and panel bending are investigated at the panels located between the shear webs.

When the face sheet (skin) is debonded from the rest of the sandwich panel, the panel loses its local stiffness, and it is expected that the localized out-of-plane deformation increases, which causes higher interlaminar stresses between the different interfaces (plies in debonded face sheet and also interface between face sheet and core), see illustration in Figure 15.

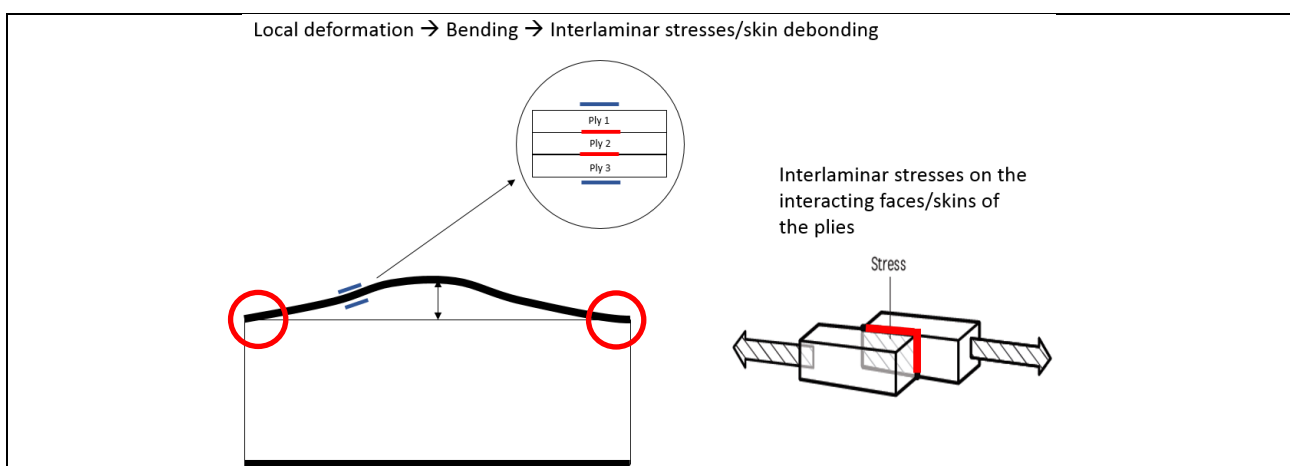


Figure 15: Interlaminar stresses between plies in debonded face sheet and also in interface between face sheet and core (red circles)

In Figure 16, deformation plots (scaled x20 for visualization purpose) are shown for the 'Intact' blade FEM model and the 'Debonded Face Sheet' FEM model.

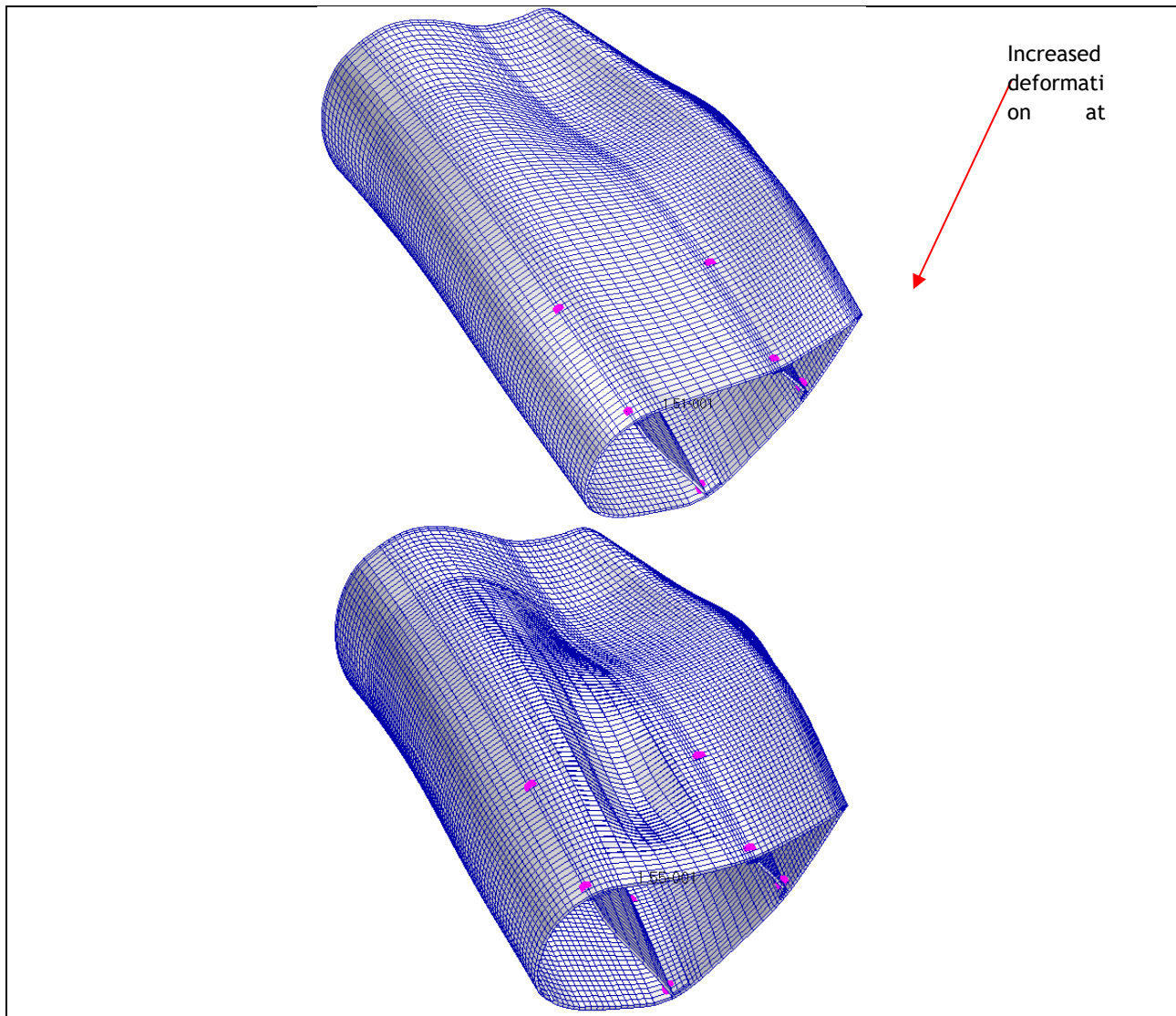


Figure 16: Left: Deformation of 'Intact' model (no defect/face sheet debond). Right: Deformation of 'Face Sheet Debond' model where the damage is located on the PS between the shear webs from 8m-15m. Deformation scaled x20 in the plot for visualization purpose.

From the upscaled deformation plot in Figure 16, it is clearly seen how the panel between shear webs undergoes a larger localized out-of-plane deformation (inwards, marked with arrow) for damaged (face sheet debond) model compared to the intact blade model. The debond damage has caused a local reduction in bending stiffness, which increases the local bending of the panel. The bending of face sheet and sandwich panel are the root cause for structural failures e.g. debond and transverse crack development. The localized out-of-plane deformation has been compared between the two models in Figure 17.

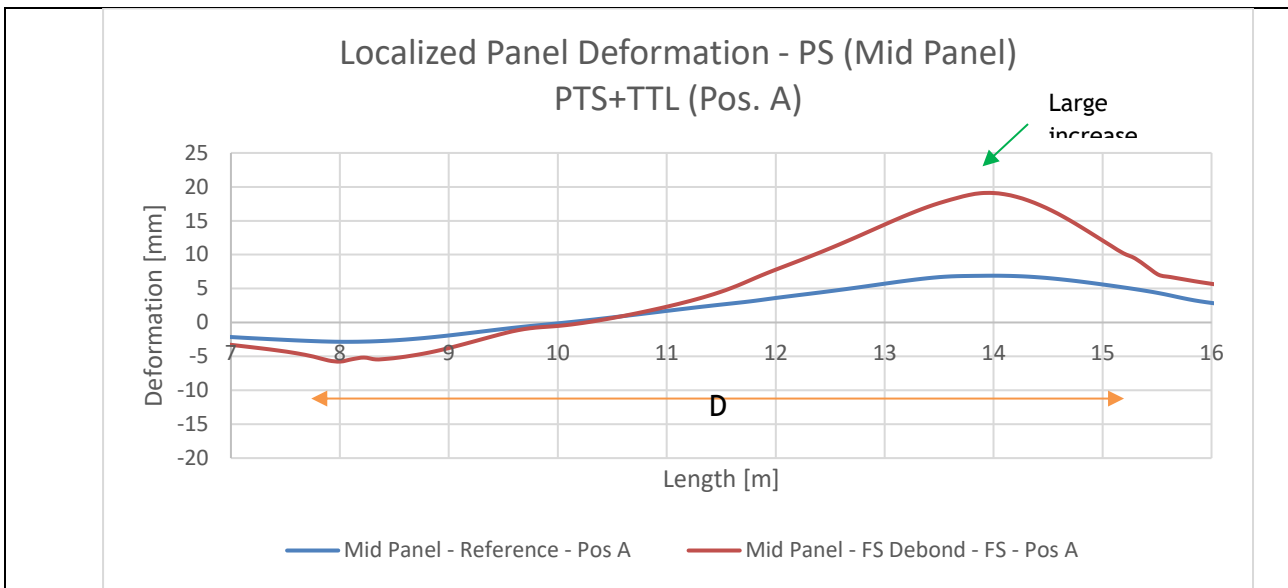


Figure 17: Localized out-of-plane deformation of pressure side mid-panel (between aft. shear web and main shear web)

Figure 17 shows localized (longitudinal) out-of-plane deformation of the middle of the pressure side sandwich panel (PS2 from Figure 14) between R7m to R16m (the debonded face sheet damage ranges between R8m to R15m).

Comparing the two curves, it is seen that localized deformation becomes approx. 2.8 times larger for the damaged blade (red curve) around R14m.

## References

- [2] DNVGL-ST-0376: Rotor Blades for Wind Turbine Blades, DNV GL, December 2015